Modelling and measurement of jet quenching in relativistic heavy-ion collisions at the LHC

ISBN: 978-94-6191-841-3

A catalogue record is available from the Utrecht University Library

Cover design: Hanne Kloosterboer

This work is licensed under a *Creative Commons Attribution-NonCommercial 3.0 Unported Licence (CC BY-NC 3.0)*

Modelling and measurement of jet quenching in relativistic heavy-ion collisions at the LHC

Modelleren en meten van jet quenching in relativistische kernbotsingen bij de LHC

(met een samenvatting in het Nederlands)

PROEFSCHRIFT

ter verkrijging van de graad van doctor aan de Universiteit Utrecht op gezag van de rector magnificus, G.J. van der Zwaan, ingevolge het besluit van het college voor promoties in het openbaar te verdedigen op maandag 7 oktober 2013 des ochtends te 12.45 uur

door

Marta Verweij

geboren op 31 maart 1983
te 's-Gravenhage

Promotores:	Prof. dr. R.J.M. Snellings
	Prof. dr. R. Kamermans †
Co-promotor:	Dr. ir. M. van Leeuwen

Dit werk maakt deel uit van het onderzoeksprogramma 'Hard Probes of the Quark Gluon Plasma at the LHC' dat (mede)gefinancierd is door de Nederlandse Organisatie voor Wetenschappelijk Onderzoek (NWO).

Contents

1 Introduction **1**

2 Theoretical Background **3**
2.1 QCD Phase Diagram and QGP 6
2.2 Relativistic Heavy-Ion Collisions 7
2.2.1 Initial State Hard Scatterings in Nuclear Collisions 8

3 Comparison of Parton Energy Loss Formalisms **13**
3.1 Parton Energy Loss Formalisms 13
3.1.1 Single Gluon Emission 14
3.1.2 Multiple Gluon Emission 15
3.2 Common Scale: Temperature 16
3.3 Energy loss in a Simple Geometry: the Brick Problem 19
3.3.1 Comparison at Fixed Temperature 19
3.3.2 Comparison at Fixed Suppression 23
3.4 Path Averaged Variables 27
3.5 Non-uniform Medium in GLV Energy Loss Kernel 28
3.5.1 Sensitivity to choice of density profile $\rho(z)$ 28
3.6 Energy Loss in a Heavy-Ion Collision Medium 32
3.6.1 Treatment of Medium Geometry 32
3.6.2 Scenarios Prior to Formation Time 33
3.6.3 Sampling Procedure 38
3.6.4 Nuclear Modification Factor R_{AA} 39
3.6.5 Di-Hadron Correlations 43
3.6.6 Parton Energy Loss at the LHC 47
3.7 Conclusion 51

4 Experimental Setup **53**
4.1 The Large Hadron Collider 53
4.2 The ALICE detector 54
4.2.1 Time Projection Chamber (TPC) 55
4.2.2 Inner Tracking System (ITS) 56
4.2.3 Zero Degree Calorimeters (ZDC) 58
4.2.4 VZERO 58

4.2.5 Detectors for Particle Identification . . . 58
4.3 Analysis Framework . . . 59
4.3.1 ROOT . . . 59
4.3.2 AliRoot . . . 59
4.3.3 GRID and AliEn . . . 59
4.4 MC Generators . . . 60
4.4.1 PYTHIA . . . 60
4.4.2 HIJING . . . 61
4.4.3 Detector Simulation . . . 61
4.5 Tracking . . . 61
4.5.1 Reconstruction of the Primary Vertex . . . 61
4.5.2 Charged Track Reconstruction . . . 62

5 Data Samples and Selection Criteria 65
5.1 Data Samples . . . 65
5.2 Event Selection . . . 66
5.2.1 On-line and Off-line Event Selection . . . 66
5.2.2 Centrality Determination . . . 66
5.3 Track Selection and Quality Assurance . . . 68
5.3.1 Tracking Transverse Momentum Resolution . . . 71
5.3.2 Tracking Efficiency . . . 71

6 Data Analysis Strategy 75
6.1 Jet Algorithms . . . 75
6.1.1 Anti-k_{T} and k_{T} Jet Algorithm . . . 75
6.1.2 Jet Area . . . 78
6.2 Jets in Heavy-Ion Events . . . 78
6.3 Background Fluctuations . . . 79
6.4 Unfolding Algorithms . . . 79
6.4.1 χ^2 Minimization . . . 80
6.4.2 Bayesian Approach . . . 81
6.4.3 Singular Value Decomposition . . . 81

7 Jet Reconstruction and Performance 83
7.1 Jet Reconstruction . . . 83
7.2 Background Fluctuations . . . 86
7.2.1 Sources of Background Fluctuations . . . 87
7.2.2 Fluctuations versus Jet Resolution Parameter . . . 92
7.2.3 Fluctuations with Jet Finding . . . 93
7.2.4 Impact on Jet Spectrum . . . 98
7.2.5 Summary Background Fluctuations . . . 98
7.3 Combinatorial Jets . . . 99
7.4 Detector Effects . . . 100
7.4.1 Jet Reconstruction Performance . . . 100

8 Unfolding Pb–Pb Jet Spectra **107**
8.1 Problem to solve . . . 107
8.2 Caveats . . . 108
8.2.1 Acceptance . . . 108
8.2.2 δ-Function Solution . . . 108
8.2.3 Combinatorial Jets . . . 109
8.3 Unfolding Method . . . 111
8.3.1 Optimization of Regularization Parameter . . . 112
8.4 Unfolding Ranges . . . 112
8.4.1 Transverse Momentum Range to optimize . . . 112
8.4.2 Transverse Momentum Range of Unfolded . . . 112
8.5 Response Matrix . . . 113
8.6 Combined Jet Performance . . . 116
8.7 Validation of Unfolding Method(s) . . . 117
8.7.1 Folding Model . . . 117
8.7.2 Heavy-Ion Background Model . . . 119
8.8 Flow Bias . . . 122
8.9 Statistical Uncertainties . . . 124
8.10 Systematic Uncertainties . . . 125
8.10.1 Regularization Strength β . . . 125
8.10.2 Minimum p_{T} of Unfolded Jet Spectrum . . . 127
8.10.3 Minimum p_{T} of Measured Jet Spectrum . . . 127
8.10.4 Unfolding Method . . . 127
8.10.5 Prior . . . 129
8.10.6 Extraction of δp_{T}-distribution . . . 129
8.10.7 Tracking Efficiency and Resolution . . . 130
8.10.8 Flow Bias Correction . . . 130
8.10.9 Centrality Determination . . . 131
8.10.10 Total Systematic Uncertainty . . . 132
8.11 Jet Spectrum in Heavy-Ion Collisions . . . 134

9 Results and Discussion **139**
9.1 Jet Suppression . . . 139
9.1.1 Comparison to Single Hadron Nuclear Modification Factor 141
9.1.2 Comparison to Calorimetric Jets . . . 143
9.1.3 Simplified Energy Loss Model . . . 143
9.2 Hard Jet Fragments . . . 145
9.3 Soft Jet Fragments . . . 147
9.3.1 Low p_{T} jet constituents . . . 147
9.4 Model Comparison . . . 151

10 Outlook **153**

Samenvatting **155**

Summary **157**

Appendices

A Hybrid Track Selection Criteria **159**

B Jet R_{CP} for leading track biased jets **161**

Bibliography **163**

Acknowledgements **171**

Curriculum Vitae **173**

1. Introduction

In collisions between relativistically accelerated lead ions a dense medium is formed: the *Quark Gluon Plasma* (QGP). The QGP consists of quarks and gluons which can move freely at these high temperatures. The QGP has a shear viscosity which is very close to the lowest possible value predicted by the quantum mechanical uncertainty principle. For this reason the QGP is often referred to as the perfect liquid. The QGP only lives for a very short period after it has formed. After the medium cools down the particles hadronize. The hadrons in final state can be observed with specialized particle detectors.

The exact properties, such as the equation of state, of the QGP are unknown. The measurement of hard processes in heavy-ion collisions is one of the possibilities to map out the properties of the QGP. In a hard scattering between incoming partons highly energetic partons, quarks and gluons, are created. The partons will radiate gluons which then split into quarks and anti-quarks. This process is known as jet fragmentation and emerges as a collimated spray of detectable hadrons (pions, kaons, protons). When a parton traverses a strongly interacting medium it exchanges momentum with the medium and the gluon radiation is enhanced with respect to the vacuum: this is called *jet quenching* [1, 2]. Due to the interaction of high energy partons with the hot and dense medium, it is expected that the fragmentation of highly energetic partons is modified leading to changes in the energy and structure of jets in heavy-ion collisions with respect to jets in pp collisions in which no QGP is created.

In this thesis, a phenomenological study of jet quenching as well as a measurement of the inclusive jet spectrum in heavy-ion collisions is presented.

In Chapter 3 different model implementations of the parton energy loss due to medium-induced gluon radiation are discussed and compared. For each model the parton energy loss is calculated in a simple medium geometry allowing for a detailed comparison of the impact of specific assumptions in each model. In this chapter parton energy loss calculations are also compared in an evolving medium which is closer to the situation in heavy-ion collisions. The models are compared to experimental observables of jet quenching like single hadron production and back-to-back di-hadron correlations in heavy-ion collisions.

In the experiment, hard scatterings are measured by grouping the detected hadrons in clusters with a jet algorithm [3, 4]. The kinematic properties of the jets can be associated to the kinematic properties of the original parton from the

hard process. In the presence of a medium a jet is quenched which can result in a broadening of the jet profile and out-of-cone jet radiation. A schematic view of both effects is shown in Figure 1.1. In case the gluons are radiated inside the jet cone, the constituents of the jet are expected to be softer and have a broader density profile compared to jets in vacuum. When significant energy is radiated out-of-cone the total jet energy will be reduced with respect to the jet energy in pp collisions [5, 6]. This results in a smaller jet yield

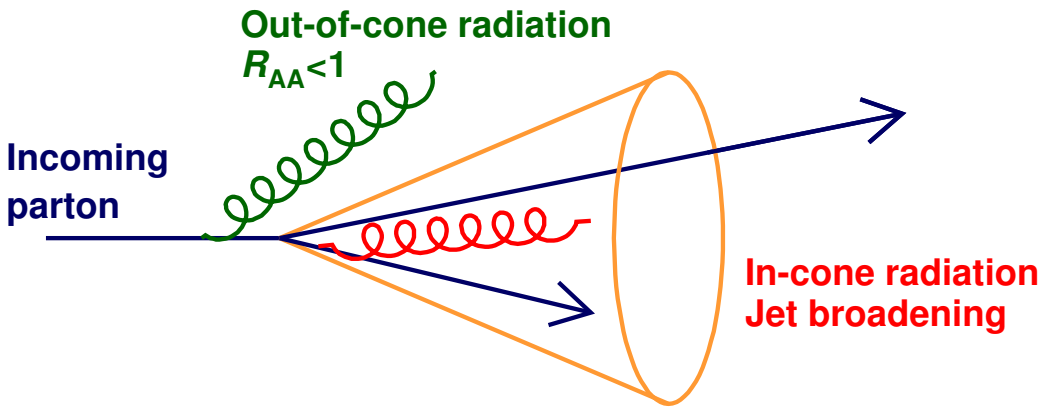

Figure 1.1: Schematic view of gluon radiation due to jet quenching inside and outside of the jet cone.

at a given jet energy in a quenched scenario compared to the vacuum case. Experimentally this is measured by taking the ratio between the jet spectrum measured in heavy-ion collisions and in proton-proton collisions scaled by the number of binary collisions. This ratio is called the nuclear modification factor R_{AA}. In the absence of nuclear effects, e.g. no jet quenching, R_{AA} is equal to one by construction. In case of out-of-cone radiation the R_{AA} will be smaller than one. In the second part of this thesis, chapters 5-9, a measurement of the inclusive transverse momentum spectrum of jets in Pb–Pb collisions at $\sqrt{s_{\mathrm{NN}}} = 2.76$ TeV with ALICE is presented.

2. Theoretical Background

The Standard Model describes the fundamental interactions of elementary particles. It is a quantum field theory in which the elementary particles and their interactions are described by using the principles of quantum mechanics and special relativity. The dynamics and kinematics of the theory are controlled by a Lagrangian. The standard model consists of an electroweak and strong sector.

The electroweak sector gives a unified description the electromagnetic and weak nuclear force between quarks and leptons. This is accomplished with a spontaneously broken $SU(2) \times U(1)$ gauge theory. The carriers of the electromagnetic and weak force, the gauge particles, between quarks and leptons are the charged W^+ and W^-, and the neutral Z^0 and γ bosons.

The strong nuclear force between quarks and gluons is described by Quantum Chromodynamics (QCD), the quantum field theory of the strong interaction [7–10]. The underlying gauge symmetry in QCD is $SU(3)$ with the color charge as a locally conserved quantity. Gluons are the mediators of the strong interaction. There are eight parameters in a general $SU(3)$ transformation, resulting in eight massless gluons mediating the strong interactions. The gluons do not only interact with color-charged quarks but also with themselves since they carry the quantum number color as well.

Hadrons (protons, pions, etc.) are the colorless asymptotic states of the theory at low temperatures and densities. The building blocks of hadrons are quarks and anti-quarks. Anti-quarks have the same spin and mass as the quarks, but with opposite electric charges. Hadrons are grouped into baryons and mesons. Baryons consist of three quarks or anti-quarks, qqq or $\bar{q}\bar{q}\bar{q}$, (e.g. protons) while mesons consist of a quark anti-quark pair, $q\bar{q}$, (e.g. pions).

The QCD Lagrangian is given by a term for the interaction between quarks and one for the self-interaction of gluons:

$$\mathcal{L}_{\text{QCD}} = \mathcal{L}_q + \mathcal{L}_g = \bar{\psi}(i\not{D} - m)\psi - \frac{1}{4}(F^a_{\mu\nu})^2, \tag{2.1}$$

The first term $\bar{\psi}(i\not{D} - m)\psi$ describes the coupling between quarks and gluons by the strong force where ψ is the quark field. The covariant derivative of the invariant local color transformation is

$$D_\mu = \partial_\mu - ig_s A^a_\mu t^a, \tag{2.2}$$

where A^a_μ is the four-component vector potential representing the gluon field and g_s is the strong coupling constant. A quark can change its color by emitting or absorbing a gluon of color a through the generator t^a.

$F^a_{\mu\nu}$ is the gauge-invariant gluon field strength tensor

$$F^a_{\mu\nu} = \partial_\mu A^a_\nu - \partial_\nu A^a_\mu - g_s f_{abc} A^b_\mu A^c_\nu, \tag{2.3}$$

where f_{abc} indicate the structure constants of the $SU(3)$ group. In addition to the two partial derivatives which are associated with the coupling between a quark and a gluon, there is an additional term containing the third and fourth order in the gauge field A^a_μ. The additional term corresponds to the self-interaction of the gluons in three- and four-gluon couplings.

The key difference between the electroweak and strong sector is that in QCD the mediators, gluons, interact with themselves giving rise to important properties of QCD: color confinement, asymptotic freedom and chiral symmetry breaking [7, 10].

Color confinement means that the color-charged objects, quarks and gluons, cannot exist as isolated particles. Color is confined in regions smaller than the typical QCD scale resulting in colorless objects in asymptotic states. This can be further understood by looking at the coupling strength between two interacting quarks which increases with the distance. The potential between the $q\bar{q}$ pair can be approximated by:

$$V(r) = -\frac{4}{3}\frac{\alpha_s}{r} + \kappa r, \tag{2.4}$$

with α_s the coupling strength, κ the string tension and r the distance between the quarks. If the distance between quarks in a hadron increases, the field strength increases which prevents the quarks from separating. At some point, if the energy in the field (a meson) keeps increasing, it is energetically preferred to create a new $q\bar{q}$ pair from the vacuum which then can couple to the already existing $q\bar{q}$ pair resulting in the formation of two new mesons.

Asymptotic freedom is a property of the theory where the coupling strength becomes asymptotically weaker at small distances or large momentum transfers. The coupling strength in QCD can be shown to have the following scale dependence at first order [11]

$$\alpha_s(\mu) = \frac{2\pi}{\beta_0 \ln(\mu/\Lambda_{\mathrm{QCD}})}, \tag{2.5}$$

where $\beta_0 = 11 - \frac{2}{3}N_f$ with N_f the number of active quark flavors and Λ_{QCD} sets the characteristic energy scale of QCD.

The quark anti-quark term in β_0, $-\frac{2}{3}N_f$, scales with the number of quark flavors and is negative like in QED. The other term in β_0, 11, originates from the non-linear self-interactions of the gluons. In case the number of flavors is not too large, α_s approaches 0 when $\mu \to \infty$: often referred to as the anti-screening effect. The strong coupling strength at a given momentum transfer scale Q can be be determined from experiments. High-energy experiments have verified the

predicted behavior of the strong coupling by measuring α_s as function of the momentum transfer Q, see Figure 2.1.

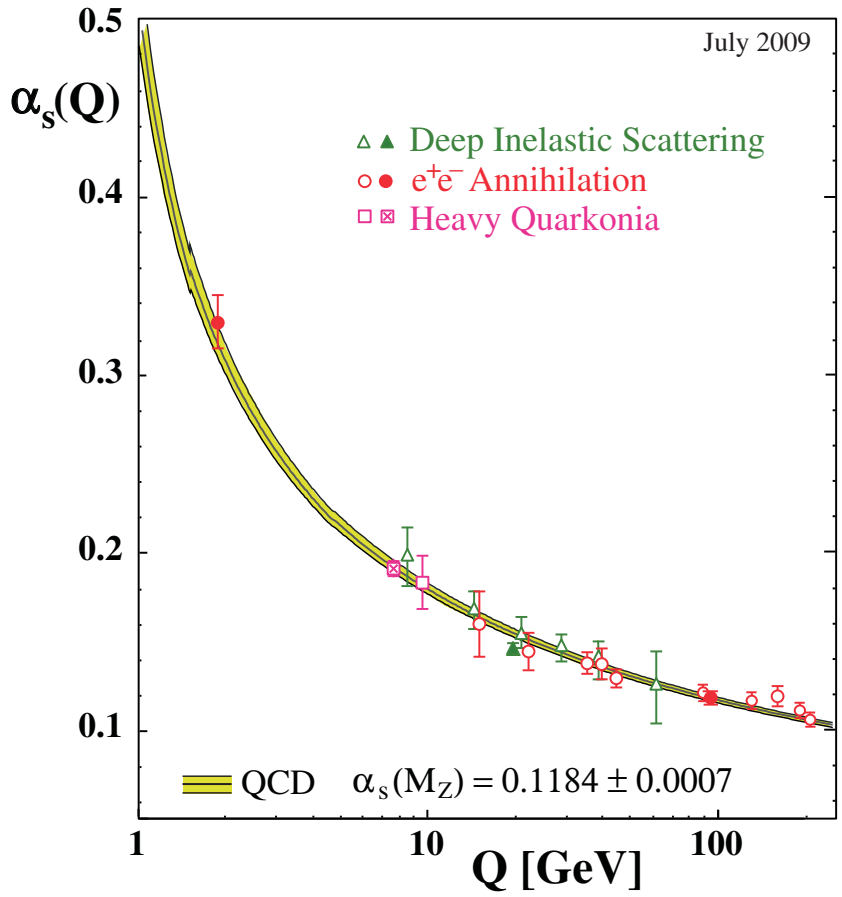

Figure 2.1: Strong coupling constant as function of the running scale Q [11].

Another fundamental phenomenon in QCD is chiral symmetry breaking. The breaking of chiral symmetry in the ground state of QCD is a non-perturbative phenomenon responsible for most of the visible mass in our universe. The mass of a proton, approximately 1 GeV/c^2, is larger than what one would expect by adding the masses of the three light quarks which each have a mass of a few MeV/c^2. The generation of the additional mass in bound states is associated with the spontaneous breaking of the chiral symmetry. At sufficiently high temperatures it is expected that chiral symmetry is restored and the quark masses are reduced to their bare Higgs masses.

There are different theoretical techniques to describe the processes involving quarks and gluons:

- Lattice QCD: This is the most established non-perturbative approach to QCD because it does not rely on small parameter expansions. It uses a discrete lattice of space-time coordinates. The uncertainty of the prediction

comes from limitations of the lattice spacing and the size of the lattice. Expanding the size is limited by computing power.

- Perturbative QCD (pQCD): This approach is based on asymptotic freedom using a perturbative expansion in series of the strong coupling constant α_s It allows to accurately calculate measurements from experiments performed at high energies. This technique is applicable if $\alpha_s \ll 1$, i.e. for large Q^2.

- Effective theories: These models provide a phenomenological description of physical processes and are used for specific problems but at the same time are not able to reproduce all the QCD properties. An example of such a theory is chiral field theory in which calculations are performed through a low energy expansion based on chiral symmetry breaking in QCD.

2.1 QCD Phase Diagram and QGP

Ordinary matter consists of quarks and gluons, confined into hadrons by the strong nuclear force. At high temperatures, $T \gg \Lambda_{\mathrm{QCD}}$, the formation of a quark-gluon plasma (QGP) is expected based on the asymptotic freedom property of QCD. In the QGP, quarks and gluons can move freely over long distances because the hadron wave functions in the QGP overlap: deconfinement. In addition, at some temperature $T_c \sim \Lambda_{\mathrm{QCD}}$ a transition from a broken chiral symmetry state to a chiral symmetric equilibrium is expected. In the QGP, the hadron wave functions overlap and the color quantum numbers are not longer conserved in the volume of the hadron. Such a plasma phase of matter is likely to have existed right after the Big Bang, when the temperature and density in the universe was high.

The key features of the QCD phase diagram as a function of temperature and baryo-chemical potential (μ_B) are shown in Figure 2.2. Depending upon the temperature T and on the chemical potential μ_B, the strongly interacting matter is expected to exist in different stable thermodynamic states. The exact locations of transitions from one phase to another are not exactly known. Ordinary matter exists at low temperature and at a baryo-chemical potential $\mu_B \simeq 940$ MeV. A resonance gas is formed by compression (i.e. increasing μ_B) or heating (i.e. increasing T). In such a gas nucleons interact strongly and at first instance form pions and exited states of the protons and neutrons (the Δ resonances). At even higher temperature or baryo-chemical potential the transition to the QGP takes place. Calculations on the lattice predict the phase transition to occur at $T_c \sim 155$ MeV, corresponding to an energy density of $\epsilon_c \simeq 1$ GeV/fm^3 [13]. This is a temperature that could be reached experimentally at low μ_B with relativistic heavy-ion collisions at RHIC and LHC. The high T and low μ_B is also the region of interest in cosmology.

The high μ_B and low T region is indirectly investigated by astrophysical studies.

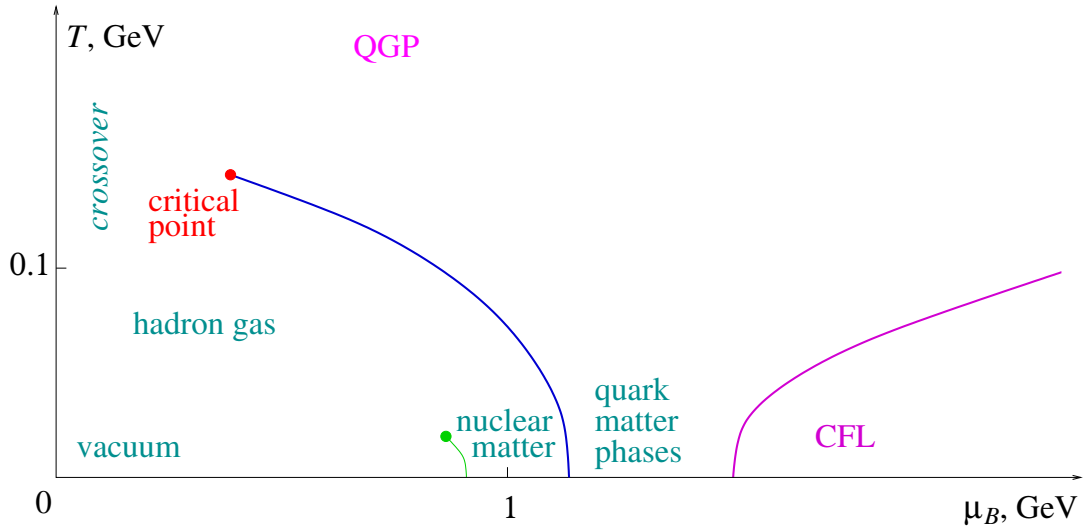

Figure 2.2: Schematic phase diagram of nuclear matter [12].

2.2 Relativistic Heavy-Ion Collisions

The Quark Gluon Plasma (QGP), a fundamentally new state of matter, is experimentally accessible in the laboratory by colliding heavy ions at high energies. Heavy-ion collisions provide a tool to study the equation of state of matter at high temperature and density. The first relativistic heavy-ion collisions were performed at the Bevelac experiment at the Lawrence Berkeley National Laboratory and at the Joint Institute for Nuclear Research in Dubna at energies up to 1 GeV per nucleon. The first dedicated program to create a QGP in heavy-ion collisions was at the fixed target heavy-ion collider SPS (Super Proton Synchrotron) at CERN. At the SPS Pb ions were collided at center of mass energy per nucleon between 8 and 17.3 GeV. Two years after the start of the SPS heavy-ion program in 1984 the Alternating Gradient Synchrotron (AGS) began operation colliding ions ranging in mass between the proton and ^{32}S with a fixed target at energies up to 28 GeV. In 1991 it was modified to allow ions up to ^{197}Au which are collided head-on in the Relativistic Heavy Ion Collider (RHIC) at center of mass energies from 3.85 GeV to 200 GeV.

A good understanding of the evolution of the system created in heavy-ion collisions is necessary to reveal the existence and properties of the QGP reliably from the various experimental observables. Just after the heavy-ions collide there is a pre-equilibrium stage in which the emerging partons start to interact. After some time, $\tau = \tau_0 < 1$ fm/c, a plasma in thermal equilibrium, the QGP, is formed. The plasma immediately starts to cool down due to the expansion of the system. The mean free path in the interacting system is expected to be small compared to the system size, making a description of the evolution using hydrodynamics possible. When the QGP has cooled down to the critical temperature T_c, a phase transition into a hadronic phase takes place. This phase

transition corresponds to a change in the effective degrees of freedom (from partons to hadrons). The hadronic phase is still in a local thermal equilibrium in which inelastic interactions take place. The system continues evolving and will reach the chemical freeze-out temperature at which the inelastic interactions cease. Finally, at thermal freeze-out, $\tau = \tau_f$, the hadrons leave the equilibrium state. This is when the kinematic properties of the hadrons are defined. The assumption that the system can be described with relativistic hydrodynamics is supported by measurements of the magnitude of the azimuthal modulation of particle production as a function of their p_{T}, elliptic flow, by RHIC and LHC experiments [14–16].

In a system where no QGP is formed, like in pp collisions, the partons directly freeze-out into a hadron phase. A comparison of the kinematic properties and chemical composition of the produced particles in the two systems gives information about the QGP produced in heavy-ion collisions.

2.2.1 Initial State Hard Scatterings in Nuclear Collisions

Hard scatterings occur in the early phase of the collisions by a large momentum transfer (large Q^2) well above the QCD scale ($\Lambda_{\mathrm{QCD}} \approx 0.2$ GeV) between the partonic constituents of the colliding nucleons. In hadronic collisions, elastic or inelastic scattering between two partons of the colliding hadrons or nuclei results in the production of two or more partons in the final state. The cross-sections of high energy parton production can be calculated with pQCD. The outgoing partons have large energy (called virtuality) which is reduced by radiating gluons and by $g \rightarrow q\bar{q}$ splitting. For jet production in the vacuum the only relevant initial state information is the probability to find suitable hard partons in the proton wave functions to undergo a perturbatively calculable hard scattering. This probability is given by the parton distribution functions. The evolution of the parton branchings in vacuum is very well understood in perturbation theory and implemented in Monte Carlo event generators. Quantum interference between successive splittings dictates that the shower follows an angular ordered pattern with decreasing emission angles. The QCD radiation probabilities are formulated by the Dokshitzer-Gribov-Lipatov-Altarelli, DGLAP, equations down to virtualities $\mathcal{O}(1\ \mathrm{GeV}^2)$. After this all the produced partons fragment non-perturbatively into final state hadrons. The collimated spray of hadrons resulting from the fragmentation of an outgoing parton is called a *jet*.

The development of a jet in heavy-ion collisions is schematically shown in Figure 2.3. In heavy-ion collisions the initial hard parton scattering occurs when the nuclei collide while the formation a thermalized medium takes some time. It is assumed that the probability to find a suitable hard parton in the nuclear wave functions can be included in the parton distribution functions by constructing nuclear parton distribution functions (nPDFs). These nPDFs are constructed from global fits to measurements of deep inelastic ℓ+A scattering at NMC and SLAC, neutrino + A at NuTeV, Drell-Yan di-lepton production in p+A collisions

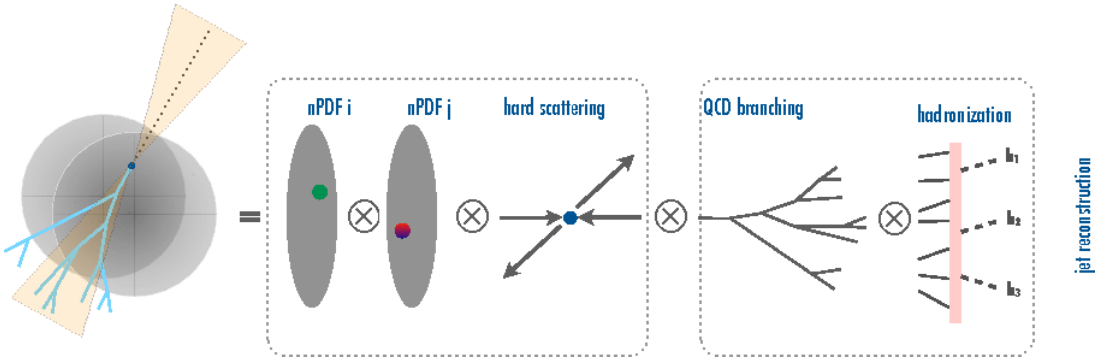

Figure 2.3: The successive stages of jet production in the presence of a medium [17].

at Fermilab, and inclusive pion production in d+Au and p+p collisions at RHIC [18]. At small x, the uncertainties on the nPDF's are large, especially for the gluon distribution. As in the vacuum case, the hard partonic cross section can be computed to any order in pQCD.

The scattered partons probe the evolution of the later thermalized stages of large color density created in heavy-ion collisions. Interactions of the partons with the medium induce additional gluon radiation resulting in a modification of the parton shower with respect to the vacuum parton shower, this is called *jet quenching* [1, 2]. The modication of the subsequent jet fragmentation process compared to the QCD vacuum can be measured and used to characterize the properties of the QCD medium.

Experimental evidence for jet quenching was first established by measurements in which the production of high p_{T} hadrons in nuclear collisions is compared to the same observable in pp collisions in which no nuclear or QCD medium effects are present. The modified evolution of the parton shower is expected to result in a suppression of hadronic spectra at high p_{T}. The suppression of high p_{T} processes is measured by calculating the nuclear modification factor R_{AA}. R_{AA} defined as the ratio between the particle yield in heavy-ion collisions scaled by the number of binary nucleon-nucleon collisions N_{coll} and pp collisions:

$$R_{\mathrm{AA}}(p_{\mathrm{T}}) = \frac{\mathrm{d}N/\mathrm{d}p_{\mathrm{T}}\,|_{\mathrm{AA}}}{N_{\mathrm{coll}}\,\mathrm{d}N/\mathrm{d}p_{\mathrm{T}}\,|_{\mathrm{pp}}}. \tag{2.6}$$

The nuclear modification factor for various mesons as measured at RHIC, shown in the upper panel of Figure 2.4, shows a strong suppression ($R_{\mathrm{AA}} \approx 0.2$) of high p_{T} particle production in central Au–Au collisions. Since the medium affects the shower of the high momentum parton and not only the final state leading hadron the details of the energy loss mechanism are hard to extract from the high-p_{T} single hadron R_{AA} measurement.

Another high p_{T} experimental observable is the production of di-jets. The $2 \rightarrow 2$ hard parton scattering process can be measured in the experiment by observing two jets pointing in opposite azimuthal direction. The total momentum balance of these two jets contains information about the primary hard QCD

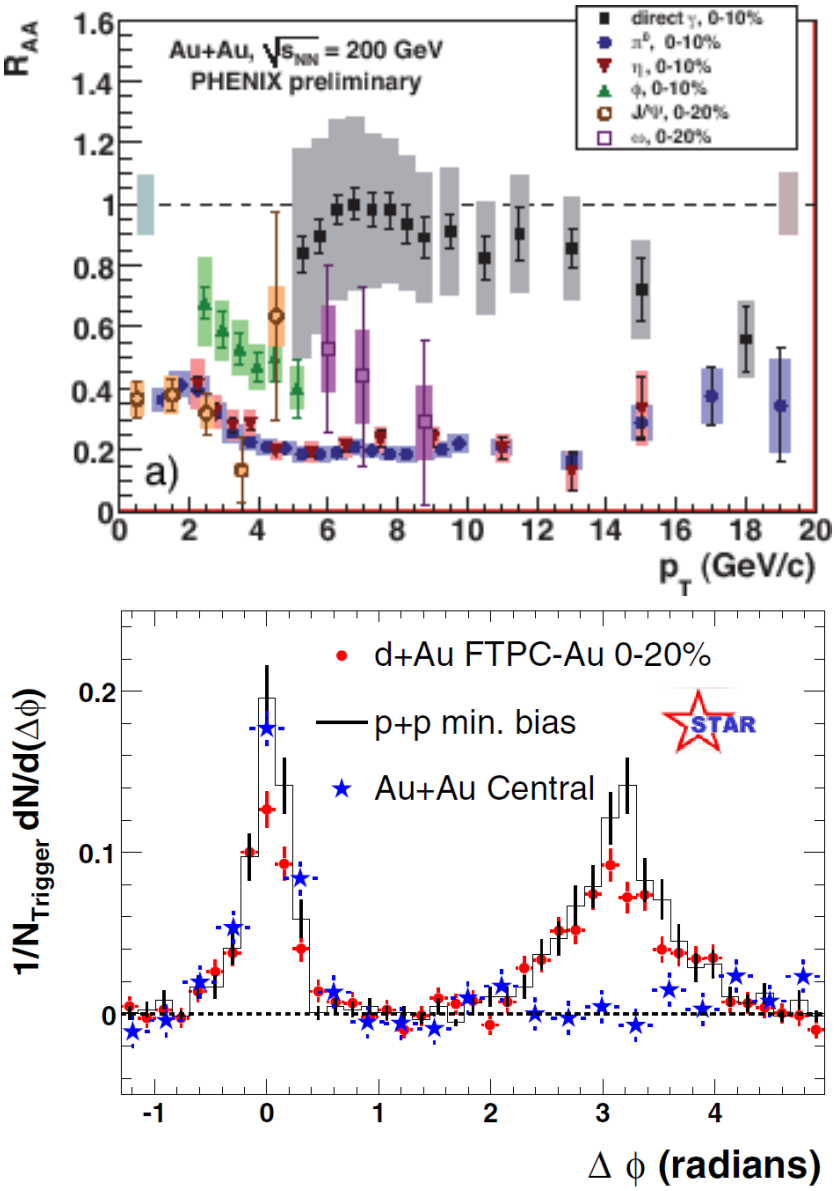

Figure 2.4: High-p_{T} jet quenching measurements at RHIC. Upper panel: Nuclear modification factor for direct photons various mesons in central Au–Au collisions at RHIC [19]. Bottom panel: Azimuthal angle distribution of associated particles with $p_{\mathrm{T}} > 2$ GeV/c with respect to trigger particles of $4 < p_{\mathrm{T}} < 6$ GeV/c. Results from Au-Au collisions (stars) are compared to reference data from p+p (line) and d+Au (circles) [20].

process whereas the momentum distribution of hadrons inside each of the jets contains information about the partonic shower, hadronization and any medium modication. Di-jet production can be measured with di-hadron correlations triggered by a the presence of a high p_{T} hadron in the event. The bottom panel of Figure 2.4 shows the di-hadron correlation as function of the angle between a

trigger particle and all measured particles in the event $\Delta\varphi$. In pp collisions two peaks at $\Delta\varphi = 0$ and $\Delta\varphi = \pi$ are clearly visible. The peak at $\Delta\varphi = 0$ is called the near-side peak representing the jet to which the trigger particle belongs to. The away-side peak at $\Delta\varphi = \pi$ is the second jet of the $2 \rightarrow 2$ hard parton scattering process.

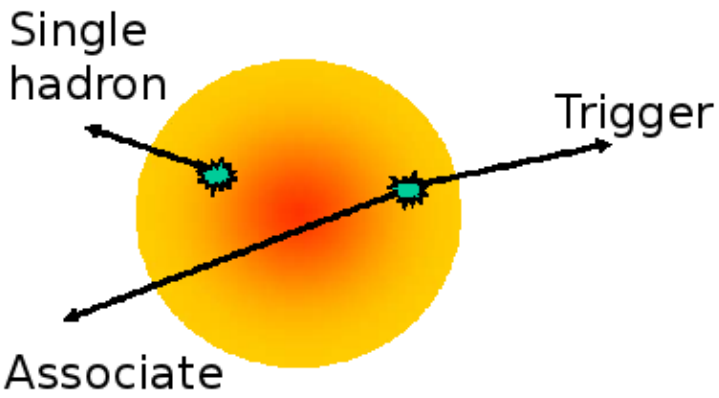

Figure 2.5: Schematic picture of single hadron and di-hadron production in a medium.

By selecting a high p_{T} hadron trigger in heavy-ion collisions it is expected that the parent parton of this trigger is created at the surface of the medium resulting in small energy loss, see the schematic picture in Figure 2.5. This results in a long path length through the medium for the corresponding away-side parton. It is expected that the amount of medium-induced radiation scales quadratically with the path length of the parton through the medium. With the measurement of di-hadron correlations the path length dependence of the in-medium energy loss can be probed. The trigger condition provides information about the hard process whereas the medium modication of the associated particle distribution is inferred from the recoiling (away-side) parton remnants. The production of hadrons associated with a high p_{T} hadron is studied in pp, dAu and Au–Au collisions at RHIC, see Figure **??**. The production of hadrons at the near-side of the trigger hadron is similar in the three collisions systems confirming the surface bias and small energy loss for the trigger. A strong decrease of the production of associated hadrons on the away-side is observed in Au–Au collisions with respect to pp and dAu collisions. This decrease is attributed to the medium modification due to jet quenching of the away-side jet.

In Chapter 3 of this thesis various analytic formalisms describing parton energy loss are discussed and compared to jet quenching measurements at RHIC and LHC.

3. Comparison of Parton Energy Loss Formalisms

In this chapter a side-by-side comparison of commonly used formalisms to calculate the energy loss of partons traversing a dense medium is presented. A systematic study with a simple geometry as well as more realistic scenarios are discussed.

3.1 Parton Energy Loss Formalisms

Radiative energy loss of a high-energy parton in a strongly interacting medium occurs due to QCD bremsstrahlung in combination with momentum exchanges between the parton and the radiated gluons with the medium. Figure 3.1 shows a schematic picture of the gluon radiation process. The incoming parton exchanges momentum with the dense medium. While the gluon is radiated off the hard

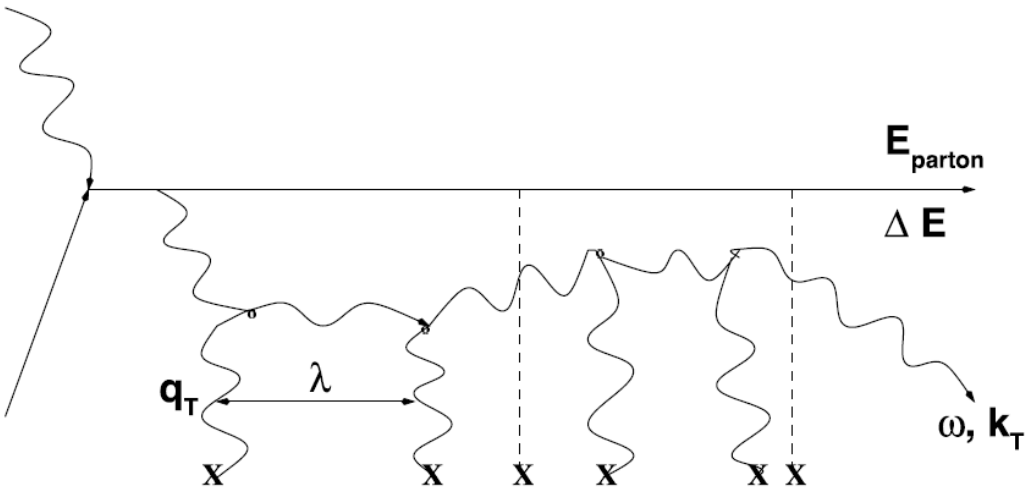

Figure 3.1: Schematic view of a hard parton interacting with the medium and radiating a gluon. Figure adapted from [21].

parton it undergoes multiple inelastic scatterings with the medium. The gluon radiation can start before or after the parton enters the medium. The interaction

of the hard parton and the gluon with the medium of certain length L can be calculated with pQCD. In calculations of medium-induced energy loss the scattering centers in the medium are assumed to be uncorrelated: the mean free path λ between the scattering centers is much larger than the Debye screening length $1/m_D$.

In this work four parton energy loss formalisms which, used frequently in comparisons to experimental observables, are compared:

- Multiple soft scattering approximation BDMPS-Z (ASW-MS) [22–25];
- Thermal effective theory formulation AMY [26, 27];
- Opacity Expansion ((D)GLV/WHDG and ASW-SH) [25, 28–31];
- Higher Twist [32, 33];

In the following sections similarities and differences between the models will be discussed.

3.1.1 Single Gluon Emission

All medium-induced parton energy loss models start from a description of the medium-induced single gluon radiation due to multiple scatterings. All models assume that both the parton and the radiated gluon are on eikonal trajectories: $E_{\text{parton}} \gg q_\perp$ and $\omega \gg q_\perp$ where $q_\perp$ is the momentum exchange of the incoming parton with the medium, ω is the energy of the radiated gluon and E_{parton} is the energy of the incoming parton. The eikonal approximation allows to neglect changes to the parent trajectory due to multiple scatterings with the medium in the calculation. It is also assumed that the parton and the radiated gluon travel along similar paths. If the formation time of the gluon is larger than the mean free path in the medium, destructive interference between all gluon emissions from scatterings takes place: this is known as the Landau-Pomeranchuk-Migdal effect. In the LPM regime not all collisions radiate a gluon but the medium acts as a single scattering center, leading to a suppression of the gluon emissions. The total energy the parton loses depends on the number of radiated gluons and the number of scatterers each gluon encounters in the medium. Both of these effects are proportional to the length of the medium that the parton traverses. This results in a quadratic in-medium length dependence of the energy loss. The single gluon spectrum, $dI/d\omega$, gives the probability that a parton radiates a gluon with a certain energy ω.

The interference between radiation due to the hard scattering in which the leading parton is created and the radiation induced by the medium is included in most formalisms. All treated models, except AMY, include also the destructive interference with the vacuum radiation.

In the multiple soft scattering approximation a path integral which resums multiple scatterings on heavy colored scattering centers is used to describe gluon

radiation off a hard parton. All the interference terms are summed while the hard scattering tail is neglected. The elastic scattering cross section is assumed to be Gaussian, resulting in a description of the single gluon radiation cross section which depends on one parameter called the transport coefficient $\hat{q}$ (defined in section 3.2).

The AMY formalism is based on thermal effective field theory in which it is assumed that the medium consists of quasi-particles with thermal masses of $\sim gT$. The momentum exchanges are dominated by soft multiple scatterings. The formulation is constructed in the $T \to \infty$ limit and then applied at realistic temperatures. The gluon splitting process $g \to gg$ is removed from the calculation in the comparisons presented here because none of the other models incorporate splittings of the radiated gluons.

In the opacity expansion formalisms (GLV and ASW-SH) used in this work one hard scattering is considered ($N = 1$) neglecting interferences between multiple scattering centers. The first order of opacity gives a similar energy loss as all orders of opacity for a thin medium, see for more details discussion around Figure 3.4. In the opacity expansion, the medium is modelled as separated heavy scattering centers with color screened Yukawa potentials. The Debye mass m_D screens the scattering potential of the medium. The other parameter in this model is the mean free path λ.

The Higher Twist approach is similar to the GLV description of the energy loss at the level of the single gluon radiation.

3.1.2 Multiple Gluon Emission

To obtain a description of multiple gluon radiation a transition by iteration from the single gluon cross section to a multiple gluon probability distribution has to be made. For the multiple soft scattering approximation and the opacity expansion the multi-gluon spectrum is obtained by a Poisson convolution of the single gluon spectrum. This results in an energy loss probability distribution $P(\Delta E)$, also called *quenching weight*, for a hard parton to lose energy ΔE. $P(\Delta E)$ consists of a discrete part p_0 and a continuous part $p(\Delta E)$:

$$P(\Delta E) = p_0\delta(\Delta E) + p(\Delta E) \tag{3.1}$$

Each gluon emission is assumed to be independent and the mean number of radiated gluons is given by integrating the single gluon spectrum $N_{\text{gluons}} = \int \mathrm{d}\omega dI/\mathrm{d}\omega$ (dI/dx in the (D)GLV description). The discrete part is a δ-function which gives the probability not to lose any energy: $p_0 = e^{-N_{\text{gluons}}}$. The Poisson convolution does not depend on the energy of the parton and therefore it is possible to lose more energy than the parton initially has. This is interpreted as absorption of the parton by the medium. The focus of these calculations is on the hard parton and the emitted gluons are not tracked.

In the Higher Twist calculation multiple gluon emission is done with a modified Dokshitzer-Gribov-Lipatov-Altarelli-Parisi (DGLAP) virtuality evolution.

The vacuum splitting function is replaced by an in-medium splitting function. A hard parton propagating through the medium gains virtuality by collisions and loses virtuality by emitting gluons.

AMY uses rate equations to obtain multiple gluon emissions in which the multiple emissions are treated by evolving the momentum distribution of the hard parton which traverses the medium.

3.2 Common Scale: Temperature

In order to compare different energy loss models the relation of the model parameters with the characteristics of the medium have to be understood. The basis for all model input parameters is the differential scattering rate which is known in two limits of the momentum $q_\perp$ exchanged between the parton and the medium [34]:

$$\frac{d\Gamma_{el}}{d^2q_\perp} \simeq \frac{C_R}{(2\pi)^2} \times \begin{cases} \dfrac{g^2\,T\,m_D^2}{\mathbf{q}_\perp^2(\mathbf{q}_\perp^2+m_D^2)} & \text{if } |\mathbf{q}_\perp| \ll T \\ \dfrac{g^4\,\mathcal{N}}{\mathbf{q}_\perp^4} & \text{if } |\mathbf{q}_\perp| \gg T, \end{cases} \tag{3.2}$$

in which T is the temperature of the medium, C_R the gluon color factor ($C_R = C_A = 3$), g the coupling constant ($g^2 = 4\pi\alpha_s$), and m_D the Debye screening mass:

$$m_D^2 = (1 + \frac{1}{6}N_f)g^2T^2, \tag{3.3}$$

where N_f is the number of quark flavors. The soft limit of Equation 3.2 uses Hard Thermal Loop (HTL) field theory to screen the soft divergences in the regime of $q_\perp \ll T$.

A colorless density $\mathcal{N}$ is defined as [34]:

$$\mathcal{N} = \frac{\zeta(3)}{\zeta(2)}(1 + \frac{1}{4}N_f)T^3, \tag{3.4}$$

in which $\zeta(2)$ and $\zeta(3)$ are Riemann $\zeta(n)$ functions.

The following expression for the differential scattering rate provides a smooth transition between the low and high energy limit of Equation 3.2:

$$\frac{d\Gamma_{el}}{d^2q_\perp} \simeq \frac{C_R}{(2\pi)^2} \times \frac{g^4\mathcal{N}}{\mathbf{q}_\perp^2(\mathbf{q}_\perp^2+m_D^2)} \tag{3.5}$$

In the high energy limit this approaches Equation 3.2 (in the limit $|\mathbf{q}_\perp| \gg T$) and it deviates in the soft region due to the difference in the numerator by 17%. The differential scattering rate as function of $q_\perp$ is shown in Figure 3.2. The curve

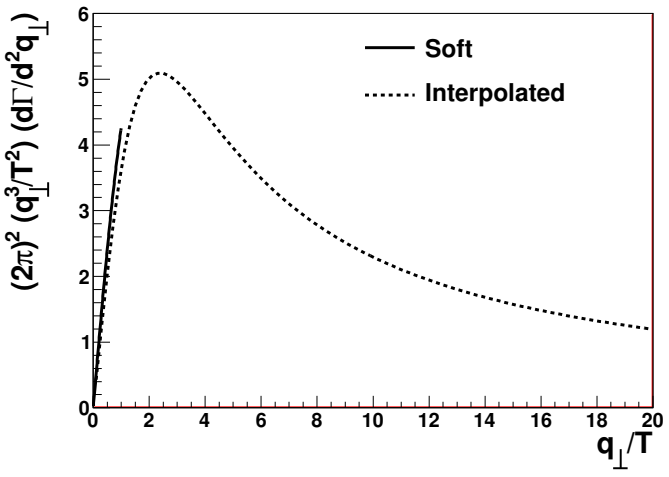

Figure 3.2: Differential elastic cross-section as function of $q_\perp$ for the different energy limits. The curve labeled with *Interpolated* correspond to the expression given in Equation 3.5. The curve labeled with *Soft* correspond to the low energy limit in Equation 3.2. See also [35].

labeled with *Interpolated* corresponds to the expression in Equation 3.5 and the curve labeled *Soft* corresponds to the low energy limit of Equation 3.2.

For the multiple soft scattering approximation the calculation of the energy loss depends on the transport coefficient $\hat{q}$ of the medium and length L traversed by the parton in the medium. The transport coefficient is defined as the mean squared momentum $\langle \mathbf{q}_\perp^2 \rangle$ per unit length:

$$\hat{q}(q_{\max}) = \int_0^{q_{\max}} d^2q_\perp \frac{d\Gamma_{el}}{d^2q_\perp} \mathbf{q}_\perp^2, \tag{3.6}$$

in which Γ_{el} is the rate for elastic collisions in the plasma, $\mathbf{q}_\perp$ is the transverse momentum imported by the medium to the radiated gluon in a collision and $q_{\max}$ is the ultraviolet cut-off.

The calculation of the medium temperature dependent transport coefficient is now straightforward using equations 3.5 and 3.6:

$$\hat{q}(T) = \frac{C_R g^4 \mathcal{N}(T)}{4\pi} \ln\left(\frac{q_{\max}^2(T)}{m_D^2(T)} + 1\right). \tag{3.7}$$

In the high energy limit the constant in the argument of the logarithm is negligible but in the low energy limit its presence is crucial since otherwise unphysical negative values for $\hat{q}$ are possible. In a realistic medium created in a heavy-ion collision naturally both cases are present.

The value at which $q_{\max}$ should be chosen is process dependent. In the high energy limit the cross-section describes collisions with static scattering centers as has been argued in [36] and references therein. Therefore in calculations that

will follow the upper integration limit for the calculation of $\hat{q}$ in Equation 3.6 is set at $q_{\max} = g(ET^3)^{1/4}$ which introduces a dependence on the energy E of the incoming parton.

In previous work the particles in the plasma are often approximated as static scattering centers for analytical convenience by using for the following rate for elastic scatterings:

$$\frac{d\Gamma_{el}}{d^2q_\perp} \simeq \frac{C_R}{(2\pi)^2} \times \frac{g^4\mathcal{N}}{(\mathbf{q}_\perp^2 + m_D^2)^2}. \tag{3.8}$$

The transport coefficient is calculated assuming that the mean squared momentum exchange per scattering is equal to m_D^2 resulting in:

$$\hat{q} \simeq m_D^2 \int_0^\infty d^2q_\perp \frac{d\Gamma_{el}}{d^2q_\perp} = m_D^2\Gamma_{el} = \frac{m_D^2}{\lambda} = \frac{C_R g^4 \mathcal{N}}{4\pi}, \tag{3.9}$$

in which the scattering rate as given in Equation 3.8 is used. In this case the transport coefficient does not depend on the energy of the incoming parton. Figure 3.3 compares the energy-dependent and independent calculation of $\hat{q}$.

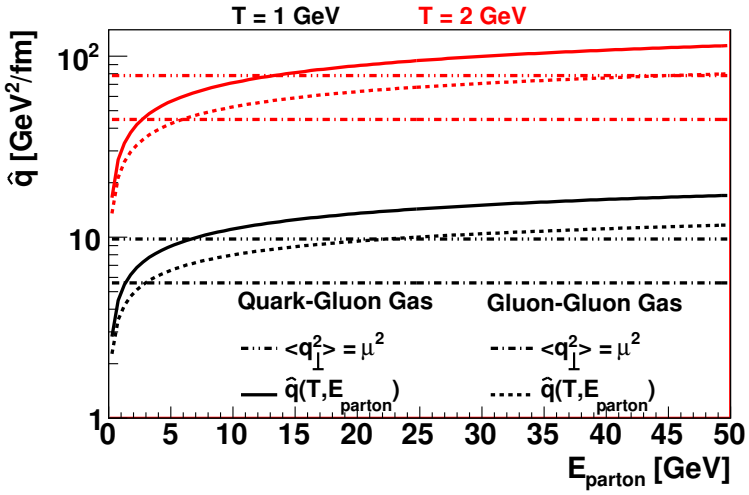

Figure 3.3: The transport coefficient as function of the energy of the parton traversing a medium of different temperatures. The transport coefficient is calculated in the hard thermal loop formalism as in Equation 3.7. See also [35].

In the opacity expansion formalism the particles in the plasma are approximated as static scatterers. This leads to the following expression for the number of scattering centers encountered by the parton traversing the medium:

$$\frac{L}{\lambda} = L \int d^2q_\perp \frac{d\Gamma_{el}}{d^2q_\perp} = 4\pi C_R \mathcal{N} \frac{\alpha_s^2}{m_D^2} L. \tag{3.10}$$

In this case the number of scatterings depends on the temperature of the medium but not on the energy of the incoming parton.

3.3 Energy loss in a Simple Geometry: the Brick Problem

Energy loss models are compared in a medium of fixed length L and temperature T: the *brick*. A highly energetic quark is propagated through the brick and the energy loss is calculated with several formalisms. The goal is to get more insight about the validity of models on the market and how similar or different their implementations of in-medium energy loss are. Outgoing radiated gluon and quark distributions of the radiative energy loss implementations are compared. A brick suppression factor, similar to the experimental measurement of the nuclear modification factor R_{AA}, is introduced, which allows to compare the medium densities needed to reach the same suppression in each formalism. Discussion and figures presented in this section are published in [35] where additional details can be found.

3.3.1 Comparison at Fixed Temperature

In this section a systematic comparison of the different radiative energy loss formalisms in a brick at a fixed medium temperature is presented. Figure 3.4 shows the emission rate of a gluon with $\omega = 3$ GeV of a incoming quark with $E = 16$ GeV as function of the medium length for different energy loss formulations and a full calculation. The full calculation is a numerical solution of the Zakharov

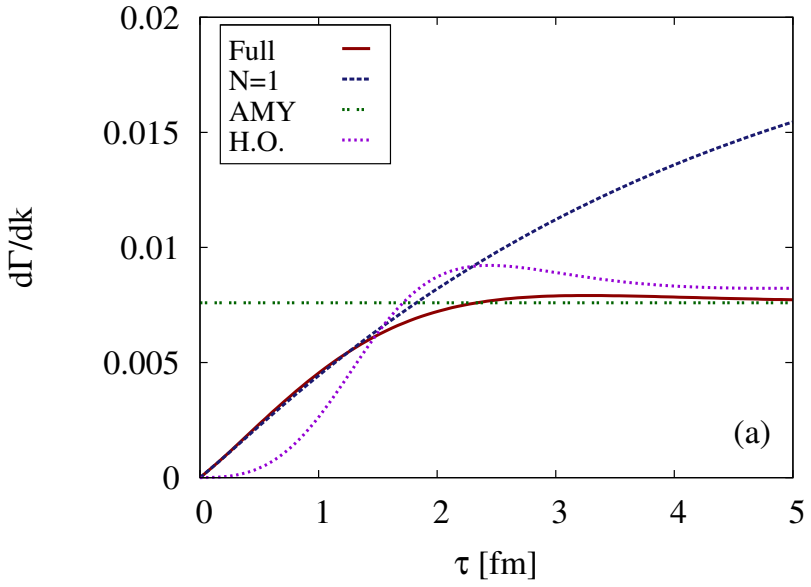

Figure 3.4: Radiation rate for a 3 GeV gluon from a 16 GeV quark as a function of traveled length τ through a brick of $T = 200$ MeV [37].

path integral [37, 38] which is the starting point for the considered energy loss implementations (ASW-MS, ASW-SH, DGLV/WHDG and AMY). The different

formalisms apply approximations to obtain an analytical solution which makes them differ from the full solution at different length scales. The radiation rate in AMY does not depend on the length of the medium because destructive interference with vacuum radiation is not implemented. The consequence is that AMY overestimates the radiation rate for short L. For large L, AMY gives the same result as the full calculation. The curve labeled with 'H.O' corresponds to the multiple soft scattering approximation. This formulation gives too little radiation at small L because the hard tail in the scattering potential is ignored in the derivation of the single gluon emission. GLV, labeled as $N = 1$, is accurate for small L but at larger lengths the first order opacity expansion overestimates the energy loss. At leading order no interference between scattering centers is present resulting in a large radiation rate. The suppression of the radiation due to the LPM effect, as discussed in section 3.1.1, is present in in the higher orders of the opacity expansion which is not calculated here. Each model is valid for different medium lengths: for small lengths the interference between vacuum and medium radiation is dominant while at large lengths the radiation is determined by the LPM interference between in-medium radiation.

Single gluon emission spectra for a parton propagating through a brick with fixed length $L = 2$ and 5 fm and a fixed temperature $T = 300$ MeV are shown in Figure 3.5 for four different formalisms. A hierarchy in the amount of radiation can be observed: AMY gives the largest amount of radiation of all models while the multiple soft scattering approximation, ASW-MS, and the two opacity expansions, ASW-SH and DGLV, give less radiation. For high gluon energies ω all models approach a similar radiation rate. For small gluon energies, large differences between the models are observed. ASW-MS gives the smallest amount of radiation while also for the opacity expansions the radiation is smaller compared to AMY. The observed differences in the radiation spectrum between AMY and the other models for small L are caused by ignoring finite-length effects in the AMY formalism. The opacity expansion at first order, $N = 1$, does not incorporate interferences between multiple scattering centers resulting in a larger radiation rate compared to ASW-MS. This effect is naturally larger for a brick with $L = 5$ fm than for the short brick with $L = 2$ fm.

In the two implementations of the opacity expansion different approximations are taken when going from the differential expression for the radiation spectrum to the integrated gluon distribution. In particular the treatment of large angle radiation has a significant effect on the single gluon distribution. In both implementations the phase space of the perpendicular component of the gluon momentum k_T is limited by a maximum value $k_{\max}$. For small x, k_{max} differs by a factor two resulting in more soft radiation for WHDG. For large x, the cut-off $k_{\max}$ also regulates large angle radiation. In WHDG large angle radiation is smoothly cut-off to no radiation at $x = 1$ while in ASW-SH the radiation at $x = 1$ is finite. The effect of other less dominating approximations like the inclusion of thermal gluon masses is discussed in [35, 39].

Comparisons of the outgoing quark distributions are presented in Figure 3.6

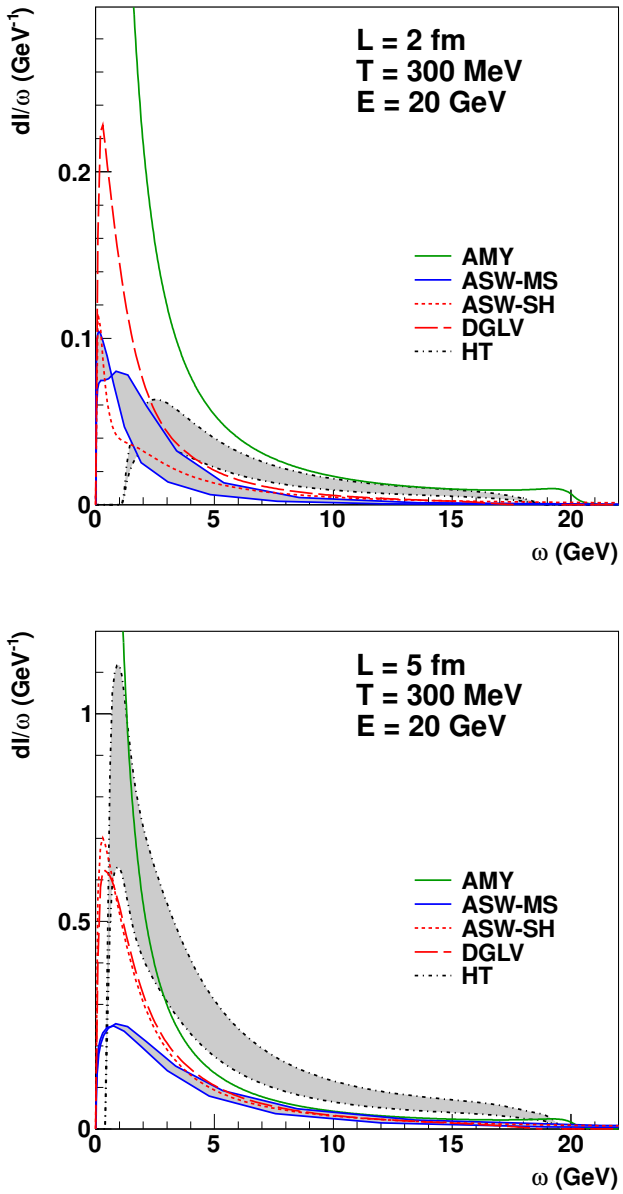

Figure 3.5: Single gluon emission spectrum bricks of length $L = 2$ and $L = 5$ fm and temperature $T = 300$ MeV. See also [35].

for the two considered L. For the models using a Poisson ansatz for the multiple gluon emissions, symbols at $x_E = 0$ and $x_E = 1$ indicate the probability that a quark is absorbed by the medium and the probability to not emit any gluon in the medium respectively. These numbers can also be found in Table 3.2 with p_0 being the probability to not radiate a gluon and p_1 the probability to absorb the incoming parton. The probability to not radiate a gluon is larger at both L for ASW-MS than for the opacity expansions. For $L = 5$ the probabilities to not

lose any energy for the opacity expansions are 0.12 and 0.14 and for ASW-MS it is 0.31 which is combined with a large probability to radiate a small amount of energy $x_E > 0.8$. For small L, finite small energy losses are reduced but still very sizable while the probability to pass untouched through the brick is larger than 0.6 for all models. The behavior of the quark propagating through a short brick is dominated by the probability to lose no energy.

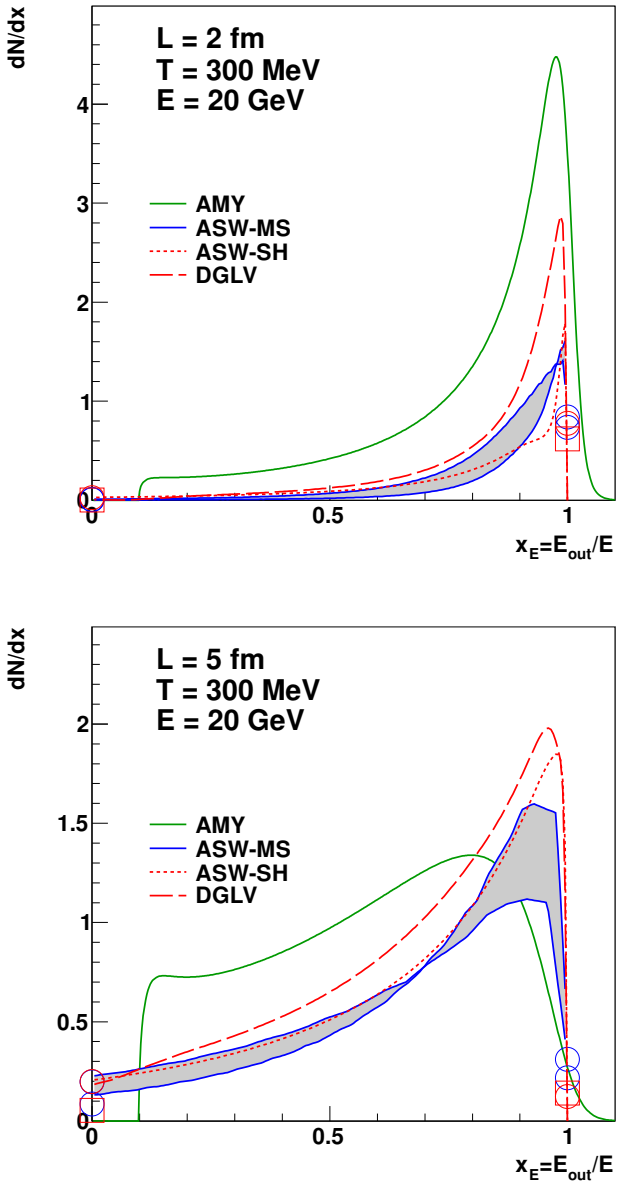

Figure 3.6: Outgoing quark distributions for bricks of length $L = 2$ and $L = 5$ fm and temperature $T = 300$ MeV. Symbols at $x_E = 0$ and $x_E = 1$ indicate the probability that a quark is absorbed by the medium and the probability to not emit any gluon in the medium respectively. See also [35]

3.3.2 Comparison at Fixed Suppression

Suppression in a Brick

Energy loss formalisms are compared by calculating a brick suppression factor as an approximation for the nuclear modification factor R_{AA}. Consider a simple scenario where the energy of each hadron is reduced by a fraction ϵ due to parton energy loss. The hadron momentum after energy loss then can be expressed as $p'_{\mathrm{T}} = (1-\epsilon)p_{\mathrm{T}}$. Measured hadron spectra at RHIC follow a power law shape: $\frac{dN}{dp_{\mathrm{T}}} = Ap_{\mathrm{T}}^{-n}$ with A a constant factor. The spectrum with fractional energy loss for the hadrons is given by:

$$\frac{\mathrm{d}N}{\mathrm{d}p'_{\mathrm{T}}} = A\frac{(1-\epsilon)^n}{p_{\mathrm{T}}^n}\frac{\mathrm{d}p_{\mathrm{T}}}{\mathrm{d}p'_{\mathrm{T}}} = A\frac{(1-\epsilon)^{n-1}}{p_{\mathrm{T}}^n}. \tag{3.11}$$

The nuclear modification factor R_{AA} is then equal to $(1-\epsilon)^{n-1}$. By taking the appropriate weighted average over $P(\epsilon)$ a brick suppression factor is obtained:

$$R_n = \int_0^1 d\epsilon (1-\epsilon)^{n-1} P(\epsilon), \tag{3.12}$$

where $\epsilon = \Delta E/E$. Since for RHIC energies, the hadron p_{T}-dependence of the cross-section can be approximated by a power law with $n = 6.5$ for $p_{\mathrm{T}} > 2$ GeV/c [40], R_7 will be used as an approximation for R_{AA} in a brick.

The brick suppression factor R_7, calculated as function of medium density $\hat{q}$, is shown in Figure 3.7. The suppression increases with increasing $\hat{q}$. For a given value of $\hat{q}$ the models give a different suppression factor. AMY gives the largest suppression (smallest R_7) at a fixed medium density while the multiple soft scattering approximation is the least suppressed of all compared models. For each model the required $\hat{q}$ to have a suppression of $R_7 = 0.25$ is determined by the crossing point of the model curves with the horizontal dotted line at $R_7 = 0.25$ in Figure 3.7. The medium properties for this typical suppression are reported in Table 3.1. The AMY formalism needs the smallest $\hat{q}$ to generate the typical suppression. For small L the differences in $\hat{q}$ at $R_7 = 0.25$ between the models goes up to a factor ~ 8 while for $L = 5$ fm the maximum is difference is a factor ~ 5.

In Figure 3.8 the models are compared at the same suppression by studying the single gluon and outgoing quark distributions. When all models are tuned to the same suppression factor, the single gluon and outgoing quark distribution of the models are quite different. To quantify the differences, some quantities characterizing the energy loss distributions are reported in Table 3.2. The mean energy loss for the incoming parton is calculated from the energy loss probability distribution $P(\Delta E)$:

$$\langle \Delta E \rangle = \int_0^{E_{\mathrm{parton}}} d(\Delta E) P(\Delta E). \tag{3.13}$$

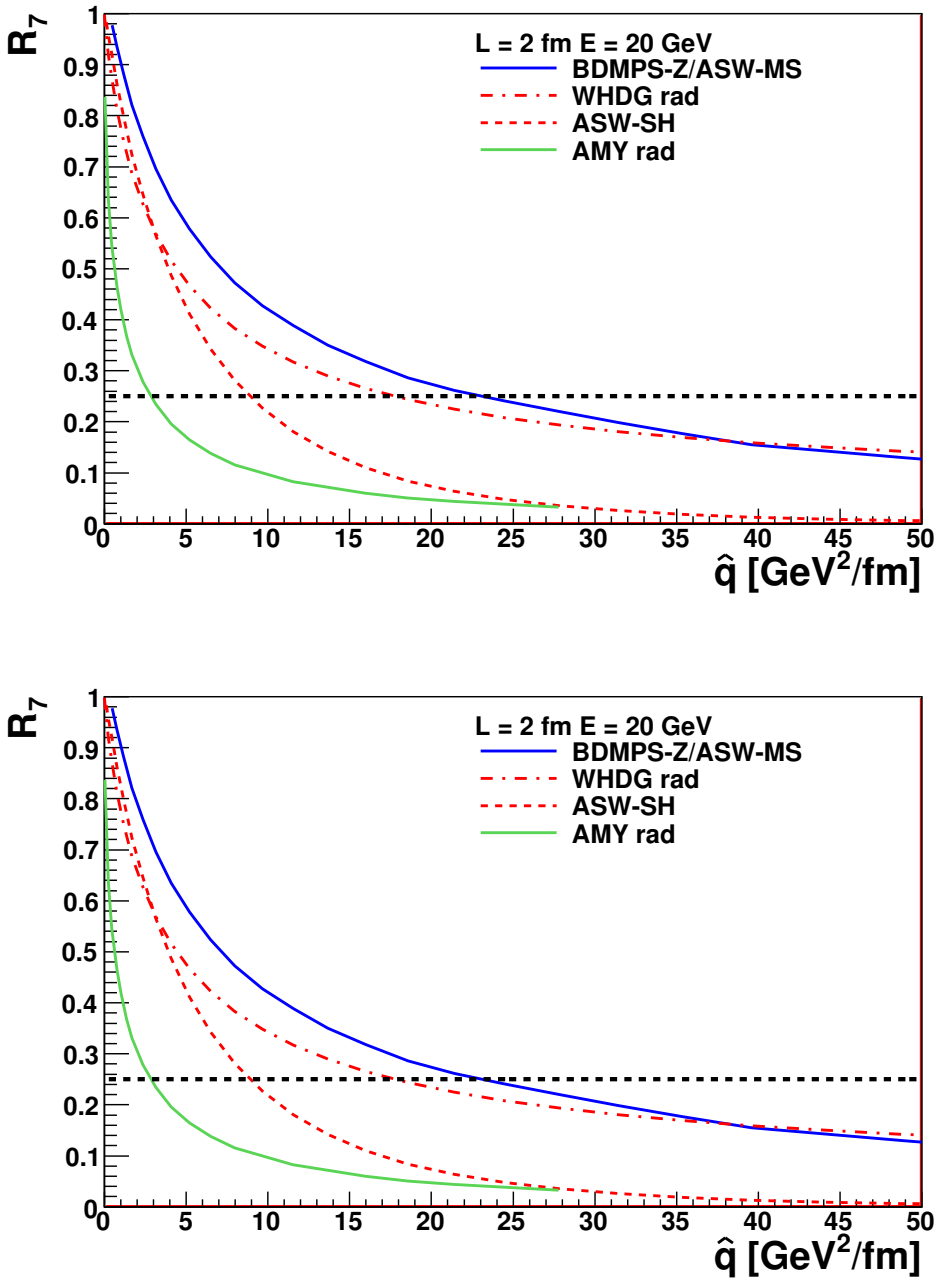

Figure 3.7: Correlation between brick suppression factor R_7 and medium density $\hat{q}$ for a primary quark with $E = 20$ GeV for different energy loss formalisms. The horizontal dashed line indicates $R_7 = 0.25$. See also [35]

At the same suppression the mean energy loss is very different for all models. The probabilities for no interaction and absorption at the typical suppression are largest for ASW-MS while the probability for fractional energy loss, $0 < x_E < 1$,

$R_7 = 0.25$		T (MeV)	$\hat{q}$ (GeV^2/fm)	ω_c or $\frac{L}{\lambda}\bar{\omega}_c$ (GeV)	R or $\frac{L}{\lambda}\bar{R}$ (GeV fm)	L/λ	m_D (GeV)
$L = 2$ fm	ASW-MS	1030	23.2	236	2393	-	-
	WHDG rad	936	17.8	105	1063	6.25	1.82
	ASW-SH	727	8.86	49.0	500	4.85	1.41
	AMY rad	480	2.7	-	-	-	-
$L = 5$ fm	ASW-MS	434	2.11	134	3401	-	-
	WHDG rad	358	1.23	36.5	925	5.97	0.69
	ASW-SH	326	0.95	27.6	702	5.44	0.63
	AMY rad	235	0.4	-	-	-	-

Table 3.1: Values of the model parameters required to reach the typical suppression of $R_7 = 0.25$.

is much smaller than for AMY and the opacity expansions. The large x cut-off in the single gluon spectra in WHDG/DGLV leads to a lower probability to absorb the parton in the medium.

The number of radiated gluons is very different for the models at fixed temperature. In case the suppression is fixed the number of radiated gluons is similar. This indicates that the suppression is dominated by the probability to not interact with the medium ($p_0 = e^{-N_{gl}}$).

		$T = 300$ MeV				$R_7 = 0.25$			
		$\langle N_{gl}\rangle$	$\langle \Delta E\rangle$	p_0	p_1	$\langle N_{gl}\rangle$	$\langle \Delta E\rangle$	p_0	p_1
$L = 2$ fm	ASW-MS	0.17	0.3	0.84	0.01	1.58	5.9	0.2	0.46
	WHDG rad	0.48	1.24	0.62	0.00	1.94	7.7	0.14	0.14
	ASW-SH	0.25	0.93	0.78	0.03	1.92	6.9	0.15	0.35
$L = 5$ fm	ASW-MS	0.12	3.95	0.31	0.08	1.83	6.4	0.16	0.33
	WHDG rad	1.96	5.63	0.14	0.05	2.44	7.3	0.09	0.11
	ASW-SH	2.09	5.76	0.12	0.2	2.47	6.7	0.08	0.26

Table 3.2: Table of different quantities characterizing the energy loss distribution for the different energy loss models. Left columns: for $T = 300$ MeV. Right columns: for fixed suppression factor $R_7 = 0.25$.

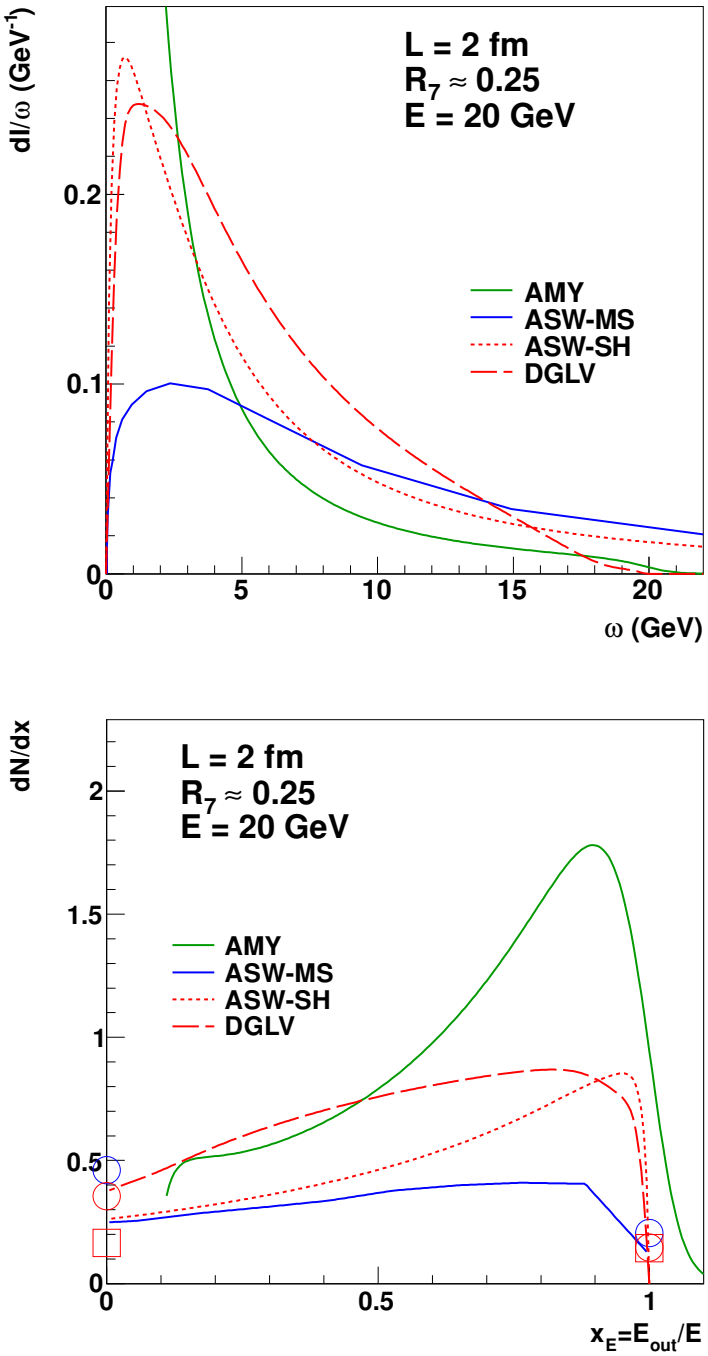

Figure 3.8: Single gluon radiation spectrum and outgoing quark distribution for a brick of length $L = 2$ fm and a suppression of $R_7 = 0.25$ for all models. See also [35]

3.4 Path Averaged Variables

In the studies presented in the previous section, the energy loss is calculated for a parton propagated through a simple medium of fixed length and density. In heavy-ion collisions the medium is non-uniform and evolves with time. To calculate the energy loss in a realistic scenario, average model parameters along the path of the parton through the medium are calculated.

The medium temperature T is used as the starting point from which the quantities characterizing the energy loss for each formalism are calculated. The relation between the temperature and model parameters is presented in section 3.2. A path integral $J_n^{(m)}$ along the trajectory of the parton through the medium is defined:

$$J_n^{(m)} = \int \mathrm{d}\tau \tau^n \, T^m. \tag{3.14}$$

For the multiple soft scattering approximation J_0^3 and J_1^3 are used in which T^3 is replaced by the local $\hat{q}(T)$. The two path integrals provide an effective length and $\hat{q}$:

$$L_{\text{eff}} \propto \frac{2J_1^{(3)}}{J_0^{(3)}} \text{ and } \hat{q}_{\text{eff}} \propto \frac{J_0^{(3)} \cdot J_0^{(3)}}{2J_1^{(3)}}. \tag{3.15}$$

Note that for a static medium, $J_0^{(3)}$ and $J_1^{(3)}$ are equivalent to the path integrals I_0 and I_1 as used in the Parton Quenching Model [41] and jet quenching studies presented in [42].

The input parameters of the multiple soft scattering approximation can also be expressed as:

$$\omega_{c,\text{eff}} = \frac{1}{2}\hat{q}_{\text{eff}} L_{\text{eff}}^2 \propto T^3 L^2 \propto J_1^{(3)} \text{ and } R_{\text{eff}} = \omega_{c,\text{eff}} L_{\text{eff}} \propto J_1^{(3)} \frac{2J_1^{(3)}}{J_0^{(3)}}. \tag{3.16}$$

For the opacity expansion the input parameters to calculate the single gluon radiation spectrum $dI/d\omega$ are:

$$\bar{\omega}_{c,\text{eff}} \propto T^2 L \propto J_0^{(2)}, \ \left.\frac{L}{\lambda}\right|_{\text{eff}} \propto TL \propto J_0^{(1)} \text{ and } \bar{R}_{\text{eff}} \propto \bar{\omega}_c L \propto T^2 L^2 \propto J_0^{(2)} \frac{J_1^{(m)}}{J_0^{(m)}}. \tag{3.17}$$

One should note that in this approach there is freedom in the choice of defining $\bar{R}$. All the results showed in this thesis are obtained with a definition of $\bar{R}$ in which the effective path length L_{eff} is proportional to $J_1^{(2)}/J_0^{(2)}$:

$$\bar{R}_{\text{eff}} = \frac{1}{2} m_{\text{D}}^2 L^2 \propto \frac{1}{2} T^2 L^2 \propto J_1^{(2)}. \tag{3.18}$$

In case $\bar{\omega}_c$, L/λ and $\bar{R}$ are known, m_{D} can be calculated as well.

The input parameters of the multiple soft scattering approximation and the opacity expansion are related since $\omega_c \simeq \frac{m_{\text{D}}^2}{\lambda} L^2 = \bar{\omega}_c \frac{L}{\lambda}$ and $R = \omega_c L = \bar{R}\frac{L}{\lambda}$.

3.5 Non-uniform Medium in GLV Energy Loss Kernel

In analytical derivation of the gluon emission rate a given shape of the distribution between scattering centers is assumed. For the GLV [29] solution this is an exponentially decaying distribution while for the multiple soft scattering approximation the distance between scatterers is assumed to be uniform [25,43]. In this section, the influence of homogeneous and non-homogeneous medium profiles in the GLV framework is studied with a numerical calculation[1]. The medium-induced gluon emission spectrum at first order of opacity in the GLV model can be written as [37]:

$$x\frac{dN_g}{dx} = \frac{C_R C_g g^2}{2\pi^3}\int \frac{d^2\mathbf{q}}{(2\pi)^2} d^2\mathbf{k}\; dz\; C(\mathbf{q},z)\times \mathcal{K}(\mathbf{k},\mathbf{q},z), \tag{3.19}$$

in which $\mathbf{k}$ is the transverse momentum of the emitted gluon and $\mathbf{q}$ the transverse momentum exchanged with a scattering center in the medium. The interference kernel $\mathcal{K}(\mathbf{k},\mathbf{q},z)$ is

$$\mathcal{K}(\mathbf{k},\mathbf{q},z) = \frac{\mathbf{k}\cdot\mathbf{q}(\mathbf{k}-\mathbf{q})^2 - \beta^2\mathbf{q}\cdot(\mathbf{k}-\mathbf{q})}{[(\mathbf{k}-\mathbf{q})^2+\beta^2]^2(\mathbf{k}^2+\beta^2)} \times \left[1-\cos\left(\frac{(\mathbf{k}-\mathbf{q})^2+\beta^2}{2Ex}z\right)\right], \tag{3.20}$$

and the scattering rate $C(\mathbf{q},z)$ is

$$C(\mathbf{q},z) = \frac{1}{C_R}(2\pi)^2\frac{d^2\Gamma_{el}(\mathbf{q},z)}{d^2\mathbf{q}}. \tag{3.21}$$

In the original GLV publications, the scattering rate $C(\mathbf{q},z)$ is separated into three terms: the number of scattering centers L/λ, a normalized Yukawa potential and a normalized density profile $\rho(z)$.

The scattering rate per unit path length $\frac{d^2\Gamma_{el}(\mathbf{q},z)}{d^2\mathbf{q}}$ encodes the dynamical properties of the medium.

3.5.1 Sensitivity to choice of density profile $\rho(z)$

In the original GLV implementation the distance between scattering centers is assumed to be an exponentially decaying distribution, $\rho(z) = \frac{2}{L}e^{-2z/L}$. Another widely used choice for the density of scattering centers is a uniform density (brick): $\rho(z) = \frac{1}{L}\theta(L-z)$ if $z \le L$. Figure 3.9 shows the single gluon emission spectrum for these two density profiles. The dashed-dotted curve corresponds to the WHDG calculation [30], which uses a variable shift $\mathbf{q} \to \mathbf{q}+\mathbf{k}$ and the approximation $\mathbf{k} \gg \mathbf{q}$ for analytical convenience, for more details see [39]. The dashed curve uses the same exponentially decaying function for $\rho(z)$ but without

[1] Text and Figures in this section are published in Hard Probes 2010 conference proceedings [44]

the variable substitution (unshifted). The solid curve shows the gluon emission spectrum for a uniform distribution between scattering centers without applying the variable shift. The three curves show a similar radiation spectrum. Within the GLV formalism the total energy loss does not strongly depend on the exact shape of $\rho(z)$.

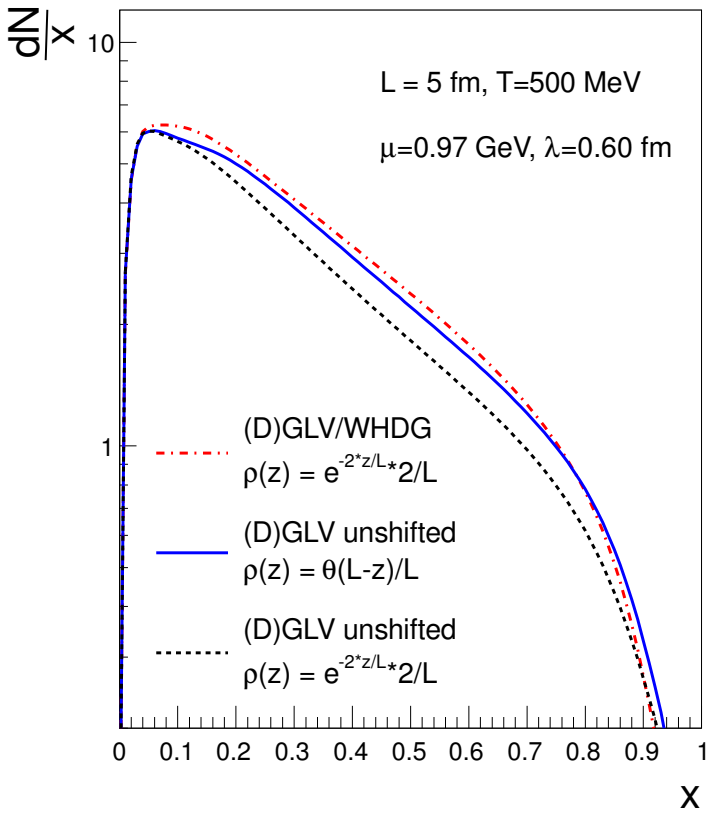

Figure 3.9: Single gluon spectrum for GLV and WHDG implementation at same medium temperature. Normalized Yukawa potential and $\rho(z)$.

With the numerical calculation of the GLV energy loss kernel the energy loss can also be evaluated with a scattering rate which depends on the local density profile encountered by the parton on its path through the medium. A Bjorken-expanding-Glauber profile is implemented and all temperature dependent variables evolve following this profile. The position dependent temperature profile enters the scattering rate $\frac{d\Gamma_{el}}{d^2q_\perp}$ from Equation 3.5 via the density $\mathcal{N}$ (as defined in Equation 3.4) and expands with $1/\tau^2$. The density at the local position of the parton in the medium is calculated from the local temperature at

[2] A detailed description of the medium model and its evolution is discussed in Section 3.6.1

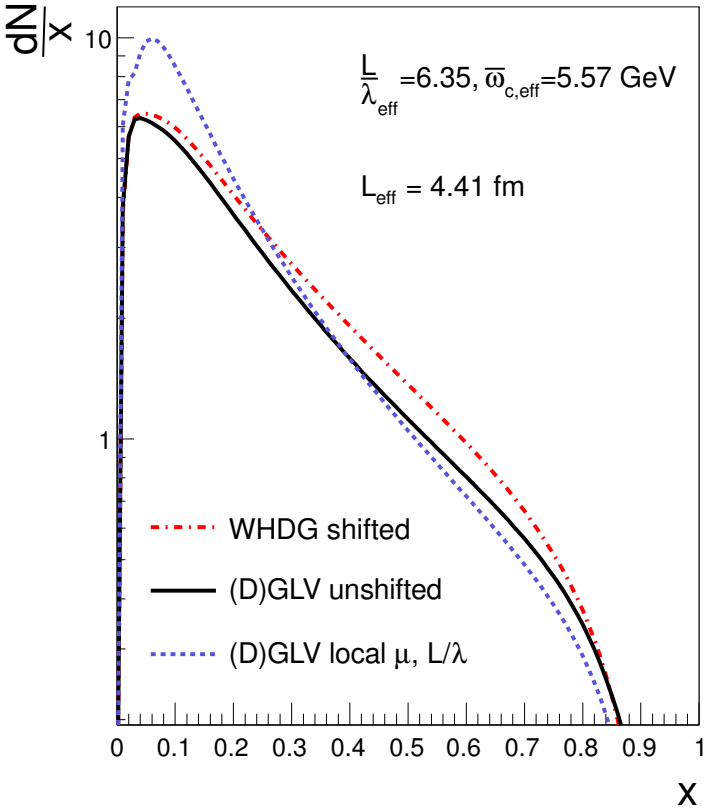

Figure 3.10: Single gluon spectrum for GLV and WHDG implementation at same medium temperature. Normalized Yukawa potential and $\rho(z)$.

that position, see Equation 3.4 for the relation between $\mathcal{N}$ and T. In Figure 3.10 the single gluon spectrum is shown for a parton which starts in the center of the medium and moves radially outwards. The result is compared with the calculation based on an effective medium density, which is calculated using Equation 3.17: $L/\lambda = 6.35$, $\bar{\omega}_c = 5.57$ GeV and $L = 4.41$ fm. Taking into account the local temperature of the medium there is more soft gluon radiation compared to the corresponding brick as is illustrated in Figure 3.10.

In Figure 3.11 the path length dependence of the brick suppression factor R_7, see Equation 3.12, is shown for different parton trajectories. A parton is created at x_0 and travels in the positive direction on the x-axis. The suppression factor is given as function of the starting position of the parton. For short path lengths ($x_0 > 2$ fm) the temperature dependent description agrees with the corresponding brick. For large path lengths however the suppression of the brick is much larger than for the temperature dependent calculation. Using average medium parameters for an evolving medium overestimates the energy loss for long

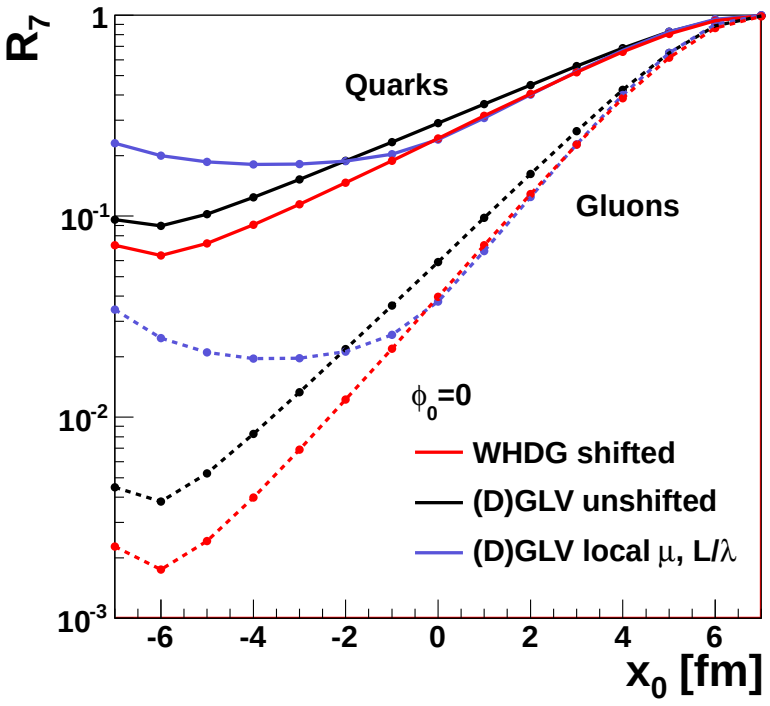

Figure 3.11: Suppression factor, R_7, as function of the starting point x_0 of parton for temperature dependent distribution of scattering centers and equivalent brick

parton trajectories. In heavy-ion collisions the number of partons with long path lengths is small compared to the number of partons with intermediate or short trajectories. Therefore using average medium parameters to model inclusive measurements will have a minimal effect but special care must be taken when more differential measurements, in which the parton path length is maximized, are modelled.

3.6 Energy Loss in a Heavy-Ion Collision Medium

In this section two radiative energy loss models, the multiple soft scattering approximation (ASW-MS) and the opacity expansion formalism (ASW-SH and (D)GLV/WHDG[3]), are compared to measured high p_{T} observables. In relativistic heavy-ion collisions, the medium evolves dynamically together with the propagation of the parton through the medium. In this work a time-dependent temperature profile is used to characterize the medium. The energy loss for each jet quenching formalism is calculated as function of the temperature of the medium. Leading partons fragment into hadrons assuming that this happens in the vacuum. The initial density profile is tuned such that each jet quenching model describes the measured single hadron suppression R_{AA} at RHIC. The di-hadron recoil suppression I_{AA} is also simulated and compared to data. Due to several biases, both measurements probe a different part of the medium. The relation between R_{AA} and I_{AA} provides information about what kind of energy loss is dominant: fractional energy loss or absorption of the parton in the medium.

R_{AA} and I_{AA} are also calculated at LHC energies and compared to recent measurement from ALICE and CMS.

3.6.1 Treatment of Medium Geometry

All the relevant parameters for the parton energy loss calculation, scale with a power of the temperature T, see equations 3.3, 3.7 and 3.10. In order to calculate the energy loss, effective quantities describing the medium density and the length of the medium as seen by the parton are obtained by averaging along the path of the parton through the medium. For this work the medium is modelled as a quark-gluon gas with three flavors: $N_f = 3$. In the model the parton does not interact with the medium if the temperature is lower than the freeze-out temperature which is when the transition from a quark-gluon gas to a hadron gas takes place. A freeze-out temperature of 150 MeV is used in the simulations, resulting in no medium induced energy loss after freeze-out. For the initial temperature profile of the medium an optical Glauber which scales with the number of wounded nucleons is used:

$$\rho_{\mathrm{WNS}} = \kappa \int d\vec{s}\ \Big\{ T_A(\vec{s} - \tfrac{1}{2}\vec{b}) \left(1 - e^{-\sigma_{NN} T_B(\vec{s}+\frac{1}{2}\vec{b})}\right) + T_B(\vec{s} + \tfrac{1}{2}\vec{b}) \left(1 - e^{-\sigma_{NN} T_A(\vec{s}-\frac{1}{2}\vec{b})}\right) \Big\}, \tag{3.22}$$

with $T_{A,B}$ the thickness functions of the nuclei, σ_{NN} the total hadronic cross section, $\vec{b}$ the impact parameter of the collisions, $\vec{s}$ the distance between the colliding nucleon and the center of the nucleus, and κ is a constant scaling factor. The initial temperature profile of the medium can be scaled to any value with the constant scaling factor κ.

[3]Only radiative and not elastic energy loss is modelled.

α_s	0.3
N_f	3
τ_0	0.6 fm
$T_{\mathrm{Freeze-Out}}$	150 MeV

Table 3.3: Model parameters for RHIC energies.

A Bjorken-expanding colorless density which depends on the spatial position in the medium and the time which has passed after the medium is created is defined as

$$\mathcal{N}(\tau) = \rho_{\mathrm{WNS}}(x, y)\frac{\tau_0}{\tau}, \tag{3.23}$$

in which τ is the time the parton has traveled in the medium, τ_0 the formation time of the medium and (x, y) the local coordinates in the medium. The production points, (x_0, y_0), of high energy partons are generated following a binary collisional density profile computed through the product of the profile function of two nuclei. The local coordinates in the medium (x, y) will then be given by the flight direction of the parton ϕ_0 and the time τ the parton has traveled through the medium: $(x, y) = (x_0 + \tau\cos\phi_0, y_0 + \tau\sin\phi_0)$. The local temperate is calculated from $\mathcal{N}(\tau)$ using Equation 3.4.

3.6.2 Scenarios Prior to Formation Time

Different scenarios for the parton energy loss prior to the formation time of the medium are considered:

- **Parton created at formation time τ_0;**
  In this scenario it is assumed that the parton and medium are created at the same time. This approach is independent from the value of the formation time.

- **Parton created at $\tau = 0$;**
  In this case the parton is created at $\tau = 0$ and propagates through space before the medium is created at formation time τ_0. For the period before formation time two extreme scenarios are studied:

  - **No medium interaction before formation time;**
    $\mathcal{N}(\tau) \propto \hat{q} = 0$ for $\tau < \tau_0$.
  - **Constant medium density before formation time;**
    $\mathcal{N}(\tau) = \mathcal{N}(\tau_0) \propto \hat{q}_0$ for $\tau < \tau_0$, in which $\hat{q}_0$ is the initial density at $\tau = \tau_0$ of the medium.

The different scenarios are illustrated in Figure 3.12 where the local $\hat{q}$ is shown as function of the position of the parton in the medium. The gray dashed line

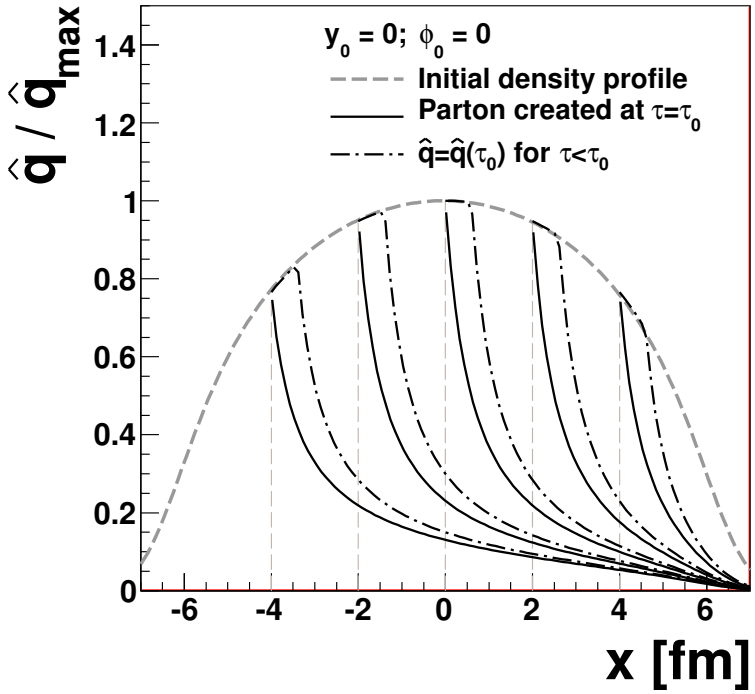

Figure 3.12: Local $\hat{q}$ as function of space-time coordinate x. Curves are shown for the initial medium density at $\tau = \tau_0$ and for a parton propagating along the x-axis through the medium with starting points at $x = -4$, -2, 0, 2 and 4 fm. Partons propagate in positive x direction.

is the initial density profile which expands with $1/\tau$. The local $\hat{q}$ which partons experience while moving through the medium for different production points x_0 is shown for partons created at the formation time by the black solid curves and for partons created at $\tau = 0$ with a static medium prior to formation time by the dashed-dotted curve. In the scenario with a constant medium density before formation time, the partons experience the very dense initial medium for a longer period.

In Figure 3.13 $\hat{q}_{\text{eff}}$ and L_{eff} are shown as function of the production point of the parton in the medium for the three different treatments of the parton energy loss before formation time. The partons travel radially through the medium in positive x direction (to the right in the figure). The effective $\hat{q}$ is largest in case there is a static medium density before formation time. In case the parton experiences no medium interaction before formation time, the effective $\hat{q}$ is smaller compared to the scenario in which the parton is created at formation time because the mean free path is larger and the average medium density is decreased by the absence of a medium prior to formation time. However note

that the energy loss scales with the characteristic gluon energy $\omega_c \propto \hat{q}L^2$ which results in similar energy loss for the two cases in which the parton exists before the formation time of the medium, see Figure 3.13(c). Because in one case L_{eff} is increased compared to the case where partons are created at formation time, and in the other case $\hat{q}_{\text{eff}}$ is increased, the energy loss is larger for the same medium conditions.

The energy loss in the opacity expansion scales with $\Delta E \propto \bar{\omega}_c \frac{L}{\lambda}$ which like ω_c in the multiple soft scattering approximation has an L^2 dependence. As discussed earlier, in section 3.4, the input parameters of the multiple soft scattering approximation and the opacity expansion are related since $\omega_c \simeq \frac{m_{\text{D}}^2}{\lambda} L^2 = \bar{\omega}_c \frac{L}{\lambda}$ and $R = \omega_c L = \bar{R} \frac{L}{\lambda}$. In an evolving medium the temperature and length are averaged along the trajectory of the parton in the medium, as is described in section 3.4. In this implementation this results in a difference between ω_c and $\bar{\omega}_c \frac{L}{\lambda}$ since $\omega_c \propto \langle T^3 L^2 \rangle$ while $\bar{\omega}_c \frac{L}{\lambda} \propto \langle T^2 L \rangle \langle T L \rangle$. This is because in the opacity expansion $\bar{\omega}_c$ and $\frac{L}{\lambda}$ are separated. Figure 3.14 shows the effective input parameters $\bar{\omega}_{c,\text{eff}}$, $\frac{L}{\lambda}|_{\text{eff}}$ and $\bar{\omega}_{c,\text{eff}} \frac{L}{\lambda}|_{\text{eff}}$ used for the opacity expansion.

While for the multiple soft scattering approximation, the energy loss with and without interaction with the medium before formation is time is approximately the same, in the opacity expansion the energy loss with a static medium before formation time is larger than with $\hat{q} = 0$ prior to formation time.

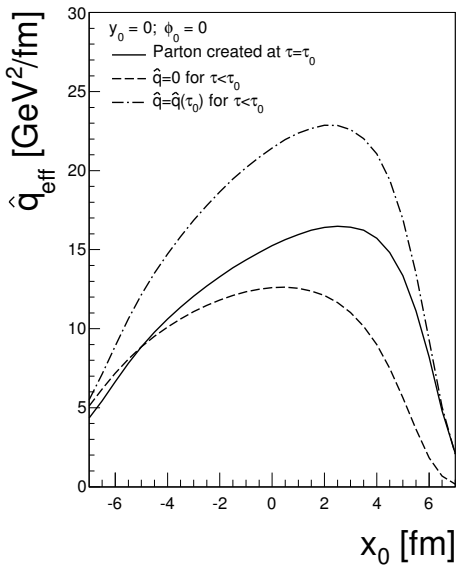

(a) $\hat{q}_{\mathrm{eff}}$

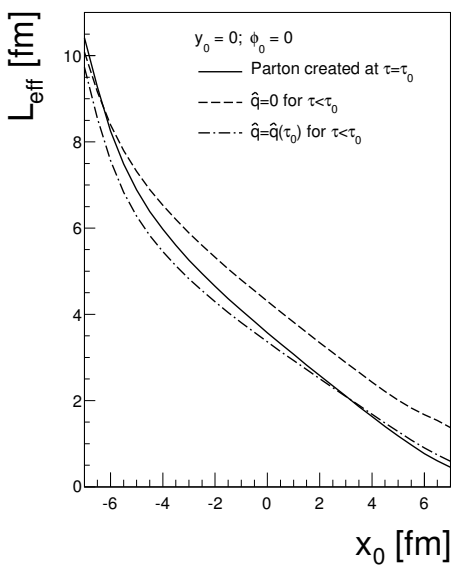

(b) L_{eff}

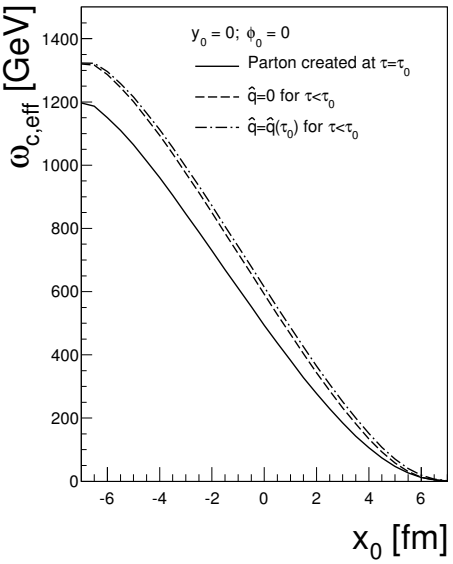

(c) $\omega_{\mathrm{c,eff}}$

Figure 3.13: Effective input parameters of the multiple soft scattering approximation for partons with $p_{\mathrm{T}} = 20$ GeV/c propagating along the x-axis through the medium. x_0 on the x-axis indicates the starting point of the parton. Partons propagate in positive x direction.

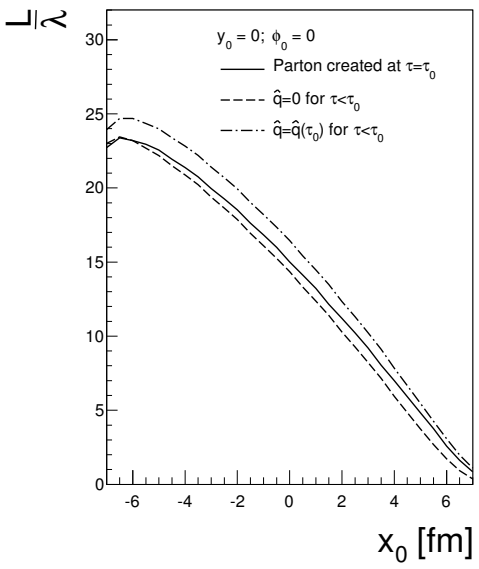

(a) $\left.\frac{L}{\lambda}\right|_{\text{eff}}$

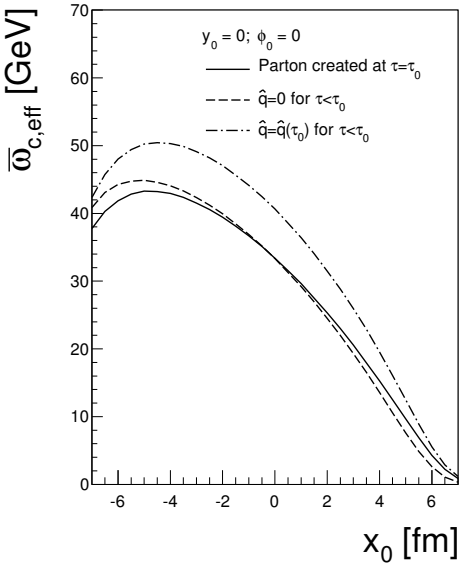

(b) $\bar{\omega}_{\text{c,eff}}$

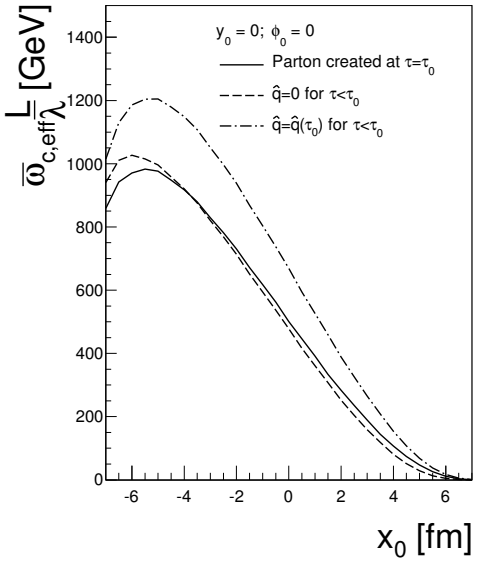

(c) $\bar{\omega}_{\text{c,eff}} \left.\frac{L}{\lambda}\right|_{\text{eff}}$

Figure 3.14: Effective input parameters of the opacity expansion for partons propagating along the x-axis through the medium. x_0 on the x-axis indicates the starting point of the parton. Partons propagate in positive x direction.

3.6.3 Sampling Procedure

Partons, light quarks (u,d and s) and gluons, are created at random positions (x, y) following a binary density profile and travel in a random direction φ in the (x, y)-plane. The partons are generated according to the LO pQCD cross-section which is calculated following the prescriptions in [45–49]. The LO cross-section is evaluated for RHIC and LHC collision energies, $\sqrt{s_{\rm NN}}$ = 200 GeV and $\sqrt{s_{\rm NN}}$ = 2.76 TeV, as function the rapidity and transverse momentum of the outgoing hard partons[4]. Figure 3.15 shows in the left panel the inclusive production of quarks and gluons as function of $p_{\rm T}$ and in the right panel the cross-section for back-to-back pair production as function of rapidity y for $p_{\rm T}^{\rm parton} > 2$ GeV/c. For the pair production one of the two partons is required to be in the acceptance, $|y| < 0.55$. Gluon production at $\sqrt{s_{\rm NN}} = 200$ GeV is dominant for

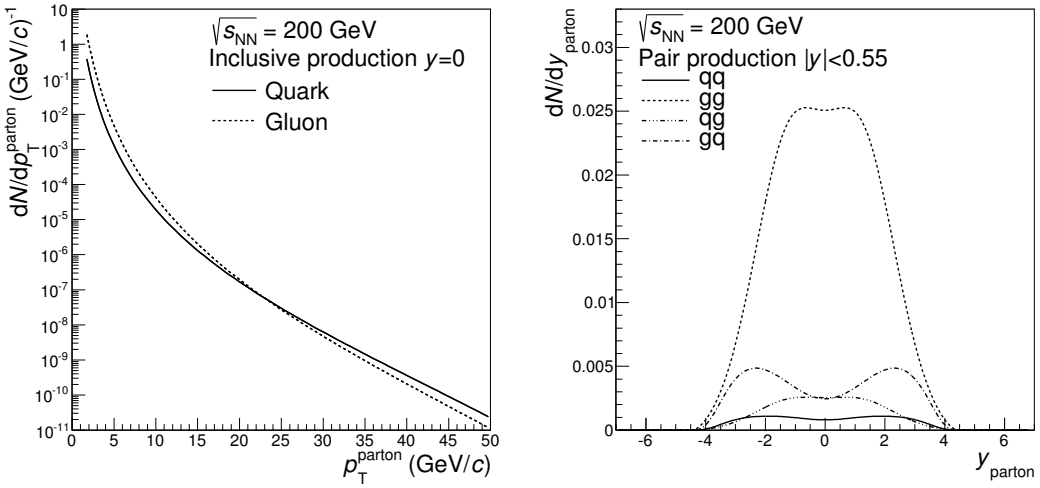

(a) Lower order pQCD production of inclusive partons and gluons at $y = 0$.

(b) Lower order pQCD production of parton pair production of which one of the partons is at rapidity $|y| < 0.55$ (the parton type listed first in the legend) and $p_{\rm T}^{\rm parton} > 2$ GeV/c.

Figure 3.15: Lower order pQCD parton production at $\sqrt{s_{\rm NN}} = 200$ GeV. Calculation based on [47].

$p_{\rm T}^{\rm parton} < 20$ GeV/c while for higher momenta more quarks are produced. The majority of the gluons originates from the $gg \rightarrow gg$ process. At LHC energies gluon production is the dominant process up to $p_{\rm T}^{\rm parton} \simeq 250$ GeV/c as is shown in Figure 3.16.

Partons propagate through the medium in which they lose energy by radiating gluons. The amount of radiated energy ΔE is drawn randomly from the probability distribution $P(\Delta E)$. $P(\Delta E)$ is calculated for each model based on

[4]For the calculation the CTEQ6.1 free parton distribution functions [50] are used. For the factorization scale $Q^2 = p_{\rm T}^2$ is utilized.

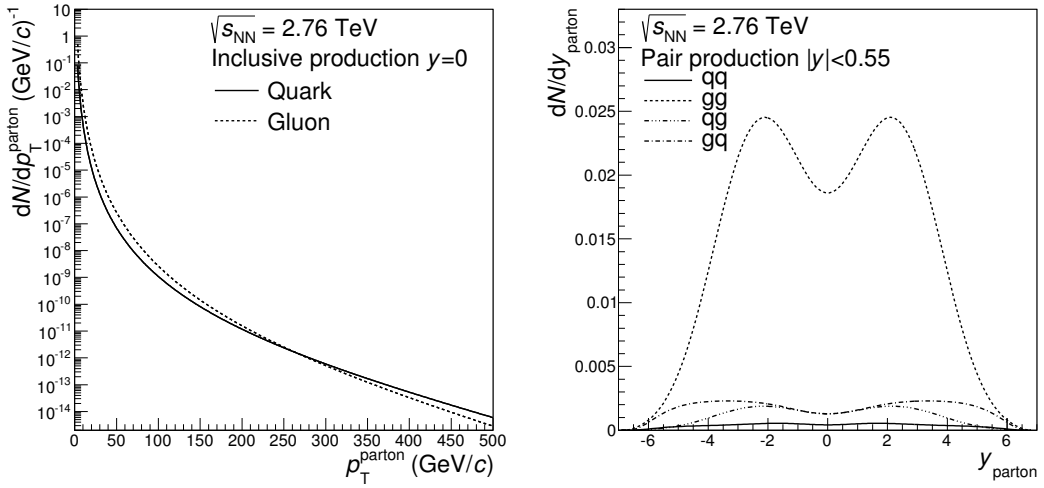

(a) Lower order pQCD production of inclusive partons and gluons at $y = 0$.

(b) Lower order pQCD production of parton pair production of which one of the partons is at rapidity $|y| < 0.55$ (the parton type listed first in the legend) and $p_{\mathrm{T}}^{\mathrm{parton}} > 2$ GeV/c.

Figure 3.16: Same as Figure 3.15 at LHC kinematics with c.m.s. $\sqrt{s_{\mathrm{NN}}} = 2.76$ TeV.

the effecting parameters for the parton trajectories discussed in 3.4. After the hadronization of the medium the partons fragment into hadrons as in vacuum using KKP fragmentation [51]. In this model the radiated gluons are assumed to be lost and do not contribute to the final hadron spectrum. For the reference spectrum the partons are propagated through the vacuum resulting in a final hadron spectrum without energy loss simulating the situation in pp collisions in which no medium is formed.

3.6.4 Nuclear Modification Factor R_{AA}

Charged particle production with and without energy loss is compared by calculating R_{AA}, which is the ratio between the charged particle spectrum with energy loss and the charged particle spectrum without energy loss. The Monte Carlo model as described in Section 3.6.3 allows to calculate the single hadron spectrum which is a convolution of the production of high p_{T} partons, the energy loss probability distribution and the fragmentation function $D(z)$:

$$\frac{\mathrm{d}N}{\mathrm{d}p_{\mathrm{T}}^{\mathrm{hadron}}} = \frac{\mathrm{d}N}{\mathrm{d}p_{\mathrm{T}}^{\mathrm{parton}}} \otimes P(\Delta E) \otimes D(z). \tag{3.24}$$

For the calculation in vacuum, the probability to radiate a medium-induced gluon is zero: $P_{\mathrm{vacuum}}(\Delta E) = \delta(0)$ which is equivalent to just removing $P(\Delta E)$ from Equation 3.24. The model is compared in the 0–5% centrality interval to the π^0 suppression measurement from the PHENIX experiment [52]. The

model is tuned by varying the initial scale κ of the medium temperature profile in Equation 3.22. The best fit for each energy loss formalism is estimated by minimizing the modified χ^2 which accounts for systematic effects, see [53, 54] for details of the calculation. The uncorrelated systematic uncertainty of the π^0 $R_{\rm AA}$ measurement is assumed to be anti-correlated: if the points at low $p_{\rm T}$ go down the points at high $p_{\rm T}$ go up and vice versa. The medium is characterized by reporting values for the maximum local transport coefficient $\hat{q}_0$ and the maximum initial temperature T_0 at $\tau = \tau_0$ in the medium. Medium characteristics for the best fits can be found in Table 3.4 with a 1σ uncertainty range around the best fit. The extracted medium properties are given for the three different scenarios prior to formation time. ASW-MS gives the largest values for the medium density while ASW-SH the smallest values. The estimates for the medium density in terms of $\hat{q}_0$ differ up to a factor 6 between the multiple soft scattering approximation and the opacity expansion formalism. The two opacity expansion formalisms, ASW-SH and WHDG, give a different estimate of $\hat{q}_0$ due to the large x gluon radiation treatment in WHDG, see for more details also the brick studies in section 3.3.

	Parton created at τ_0		$\hat{q} = 0$ for $\tau < \tau_0$		$\hat{q} = \hat{q}_0$ for $\tau < \tau_0$	
	$\hat{q}_0$	T_0	$\hat{q}_0$	T_0	$\hat{q}_0$	T_0
	(GeV^2/fm)	(MeV)	(GeV^2/fm)	(MeV)	(GeV^2/fm)	(MeV)
ASW-MS	$19^{+2.3}_{-2.3}$	953^{+37}_{-40}	$15^{+0.7}_{-5}$	884^{+14}_{-52}	17^{+2}_{-1}	926^{+26}_{-28}
ASW-SH	$3.3^{+0.3}_{-0.3}$	531^{+13}_{-13}	$3.6^{+1.5}_{-0.3}$	544^{+68}_{-25}	$2.7^{+0.4}_{-0.2}$	502^{+22}_{-16}
WHDG rad	$5.2^{+0.3}_{-0.3}$	618^{+10}_{-10}	$5.7^{+0.8}_{-0.3}$	638^{+27}_{-10}	$5.2^{+0.5}_{-0.8}$	618^{+19}_{-32}

Table 3.4: Best fit parameters for the different energy loss models fitted to the π^0 $R_{\rm AA}$ measurement for 5% most central events.

Figure 3.17 shows the charged particle $R_{\rm AA}$ curves as function of $p_{\rm T}$ for the best fit of each formalism in case a static medium is assumed prior to formation time. The shaded areas are the 1σ uncertainty bands of the fits as reported in Table 3.4. ASW-SH shows an increase of the $R_{\rm AA}$ as function of $p_{\rm T}$ which describes the measured points well. The multiple soft scattering approximation (ASW-MS) shows a milder increase with $p_{\rm T}$. Considering the statistical and systematic uncertainties on the measurement ASW-MS is compatible with data. The $R_{\rm AA}$ from WHDG does not increase but decreases slightly with $p_{\rm T}$ for low transverse momenta and is flat for $p_{\rm T} > 10$ GeV/c resulting in a poor fit to the data. The average energy loss in WHDG for low parton energies is smaller due to the high x cut-off in the calculation of the single gluon emission spectrum, resulting in a decrease of the $R_{\rm AA}$ at low hadron $p_{\rm T}$. In previous work it has been shown that by including the elastic energy loss, a good description of the $p_{\rm T}$-dependence of the single hadron $R_{\rm AA}$ is achieved with the WHDG model [30].

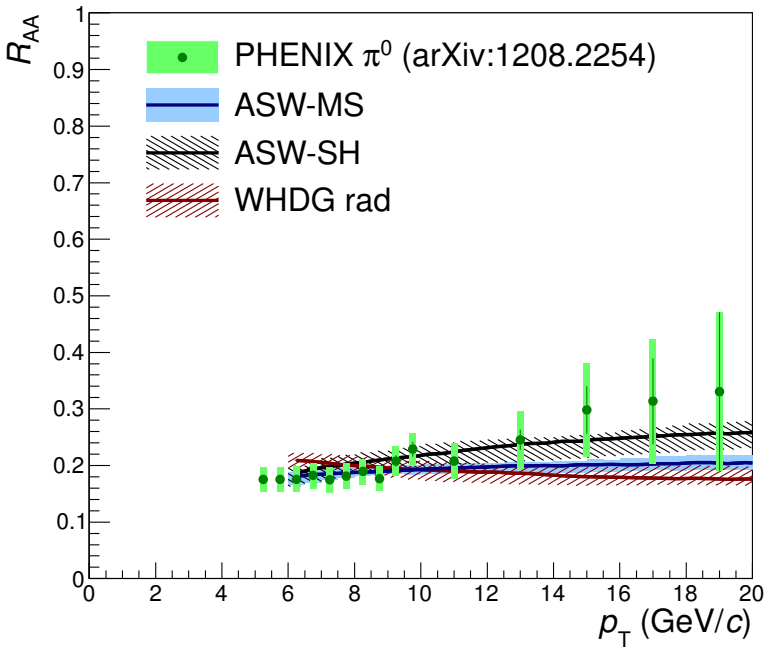

Figure 3.17: Single hadron suppression in models fit to RHIC data. Shaded and dashed bands indicate 1σ uncertainty bands of the modified χ^2 fit. Centrality: 0–5%. PHENIX data from [52].

To visualize the medium as seen by the parton, all parton trajectories in the (ω_c, L)-plane are shown in Figure 3.18. Each parton which is generated experiences an effective $\hat{q}$ and length on its path through the medium. The characteristic gluon energy $\omega_c \propto \hat{q}L^2$ experienced by the parton, relates the medium geometry to the energy radiated off the parton. For the opacity expansion the average energy loss scales with $\frac{L}{\lambda}\bar{\omega}_c$ in which $\frac{L}{\lambda}$ is the number of scattering centers and thus the number of emitted gluons. The typical energy of one radiated gluon is $\bar{\omega}_c$.

Several cases can be identified in the (ω_c, L)-plane. One of them is the earlier discussed case in which a parton travels along the x-axis through the medium, see Figure 3.13. This is a subset of all the generated partons in the $(\omega_c(\text{ or } \frac{L}{\lambda}\bar{\omega}_c), L)$-plane. Partons with a small $\omega_c(\text{ or } \frac{L}{\lambda}\bar{\omega}_c)$ and small length are created at the surface of the medium and emitted radially outward which results in small energy loss. Partons with a typical effective length (~ 2 fm) and typical ω_c (or $\frac{L}{\lambda}\bar{\omega}_c$), corresponding to large $\hat{q}$, are emitted radially outward at intermediate r. Partons which travel from one side to the other side of the medium (radially inward) experience a relatively low effective medium density. When they arrive at the most dense part of the medium (the center) the medium already cooled down due to the Bjorken expansion. Their effective length is very large which then finally results in large energy loss.

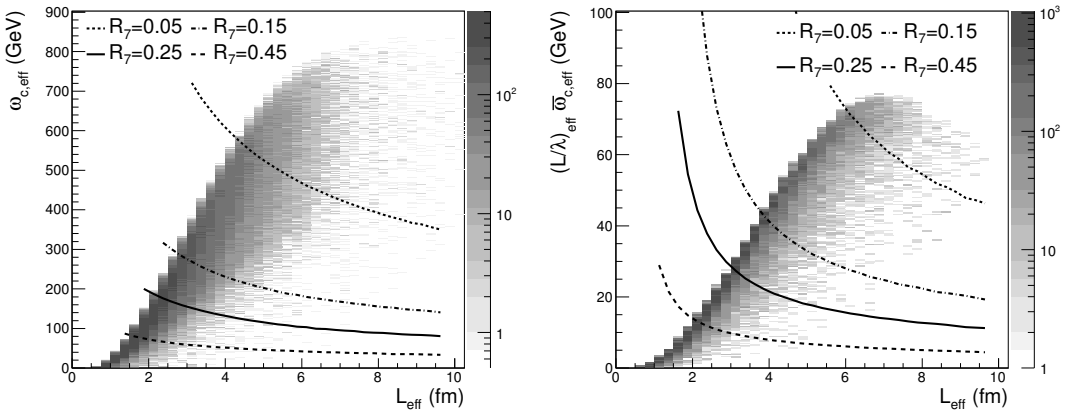

(a) ASW-MS (b) WHDG-rad

Figure 3.18: Effective typical gluon energy $\omega_{c,\mathrm{eff}}$ (or $\frac{L}{\lambda}|_{\mathrm{eff}}\bar{\omega}_{c,\mathrm{eff}}$) as function of effective length L_{eff} with brick isolines corresponding to the typical brick suppression R_7.

The correlation between $\frac{L}{\lambda}\bar{\omega}_c$ and L (Figure 3.18(b)) is stronger than the correlation between ω_c and L (Figure 3.18(a)). The main difference between the two correlations is the log from the hard thermal loop approximation which depends on the initial energy of the parton, see Equation 3.7, which in the multiple soft scattering approximation comes in through $\hat{q}$ and for the opacity expansions is inside the energy loss kernel.

For each combination of ω_c and L (or $\bar{\omega}_c$, L/λ and $\bar{R}$ in the opacity expansions) the typical brick suppression R_7, see Section 3.3.2, is calculated. Figure 3.18 shows isolines for $R_7 = 0.05, 0.15, 0.25$ and 0.45. The full geometry consists of a sum of several typical suppression factors R_7 given by the effective $\hat{q}$ and L resulting finally in a suppression of the inclusive single hadron spectrum with a factor 5.

The energy loss in the presented model calculations is a combination of fractional energy loss and total absorption by the medium of the parton. Since the observed suppression is approximately a factor 5, the energy loss must be large and total absorption of partons plays an important role. There is a clear difference between the survival rates of the different models after tuning the medium density for each model to describe the experimentally measured π^0 R_{AA}. In WHDG, 73% of the partons with $p_{\mathrm{T}}^{\mathrm{parton}} > 3$ GeV/c survive while in ASW-MS and ASW-SH only 16% do. The much larger survival probability in the WHDG formalism is explained by the large x cut-off in the GLV single gluon spectrum which limits the possibility to radiate a hard gluon. In the WHDG formalism more partons end up in the continuous part of the energy loss distribution: 51% in WHDG versus 5% and 6% in ASW-MS and ASW-SH respectively. In ASW-MS the average number of radiated gluons is larger, resulting in a smaller probability to not lose any energy : 11% for ASW-MS versus 22% for WHDG. For higher parton energies, the number of surviving partons increases for the ASW

formalisms: 24% for ASW-MS and 30% for ASW-SH for parton with $p_{\mathrm{T}}^{\mathrm{parton}} > 10$ GeV/c. In WHDG however, the survival rate decreases to 47% because for highly energetic partons the kinematic large x cut-off has a smaller effect. The differences in survival rate imply that WHDG is dominated by fractional energy loss while the ASW implementations are more a *black-white* scenario in which a parton survives untouched or is absorbed in the medium. The first case results in a shift of the transverse momentum towards lower values and the absorption case in a decrease of the hadron yield at given p_{T} resulting in a downward shift of the inclusive hadron spectrum. In the ASW-MS formalism only partons generated at the surface of the medium survive while the WHDG formalism partons from deeper in the medium lose a certain fraction of their energy instead of being absorbed.

The observation of the large absorption rates, makes one question the validity of these models. The analytical expressions describing the probability to radiate a single gluon is derived in the the soft eikonal limit. A parton can be absorbed by radiating a large number of gluons with small x but also large angle radiation could potentially give a significant contribution. Large angle radiation, however, is not correctly described by the energy loss kernels in the considered models.

For the continuous part of the energy loss distribution ASW-SH radiates more soft gluons than ASW-MS resulting in a larger p_{T} dependence of R_{AA}. Note that R_{AA} does not indicate how many partons survived and neither if they lost only a fraction of their energy.

The very different absorption and survival rates for the models show that their respective energy loss probability distributions, $P(\Delta E)$, are very different. Nevertheless they all give a reasonable description of the R_{AA}. Due to the limited kinematic reach at RHIC in combination with the averaging procedure over the full medium geometry and the full initial parton spectrum, only a limited range of the energy loss probability distribution $P(\Delta E)$ is probed [55,56]. It is possible to obtain the same inclusive hadron R_{AA} with jet quenching models pocessing very different properties. The magnitude of the observed inclusive hadron suppression gives an indication about how much energy is lost in total but does not reveal what kind of energy loss mechanism is causing this.

3.6.5 Di-Hadron Correlations

In di-hadron studies, azimuthal 2-particle correlations are studied. For this analysis a high p_{T} particle is selected as a trigger and correlated to all other particles with lower p_{T} in the event. In this correlation at the near and away side in $\Delta\varphi$ of the trigger particle a jet structure is visible: di-jet production. The production of back-to-back partons is modelled in vacuum and in the presence of a medium after which the production of associated particles per trigger at the away side is studied and compared to the recoil suppression, I_{AA}, as measured by the STAR

collaboration [57]. The recoil suppression I_{AA} is defined as:

$$I_{\mathrm{AA}}(z_{\mathrm{T}}) = \frac{\frac{1}{N_{\mathrm{trig,AA}}}\frac{dN_{\mathrm{AA}}^{\mathrm{assoc}}}{dz_{\mathrm{T}}}}{\frac{1}{N_{\mathrm{trig,pp}}}\frac{dN_{\mathrm{pp}}^{\mathrm{assoc}}}{dz_{\mathrm{T}}}}, \tag{3.25}$$

where $z_{\mathrm{T}} = p_{\mathrm{T}}^{\mathrm{assoc}}/p_{\mathrm{T}}^{\mathrm{trig}}$.

Di-hadron correlations are modelled by generating back-to-back partons which are propagated through the medium. After hadronization all hadrons within the requested trigger p_{T} interval, $8 < p_T^{\mathrm{hadron}} < 15$ GeV/c, are assigned as a trigger particle. The associated particles on the away side are traveling in opposite direction in φ with respect to the azimuthal orientation of the trigger particle: $\Delta\varphi = \varphi_{\mathrm{trig}} - \varphi_{\mathrm{assoc}} \simeq \pi$. The triggered parton survives by definition and the associated parton may or may not be absorbed by the medium, depending on the total energy which is lost.

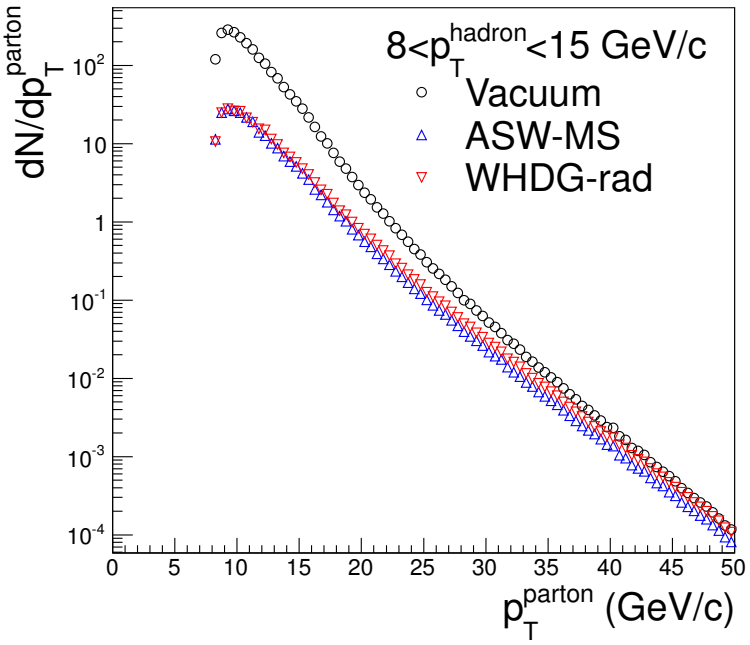

Figure 3.19: Original parton spectra resulting in hadrons with $8 < p_T^{hadron} < 15$ GeV/c for without (vacuum) and with (ASW-MS/WHDG) radiative energy loss.

Kinematic Bias The trigger particles determine the parton pairs and therefore define which part of the inclusive parton spectrum is probed. In case the parton loses energy due to jet quenching before fragmenting into a hadron it will need a larger parton p_{T} to be selected as a trigger. Figure 3.19 shows the p_{T} distribution of partons from which the selected triggers originate. The shape of the parton

spectra are flatter if the parton is affected by jet quenching. The result is a different event sample in the numerator and denominator of I_{AA} while for the R_{AA} measurement the event sample is the same for both. The bias towards higher parton energies is expected to decrease the suppression compared to the single hadron suppression measurement.

Surface Bias In Figure 3.20 the distributions of the effective path lengths of all selected triggers and corresponding associated particles are shown.

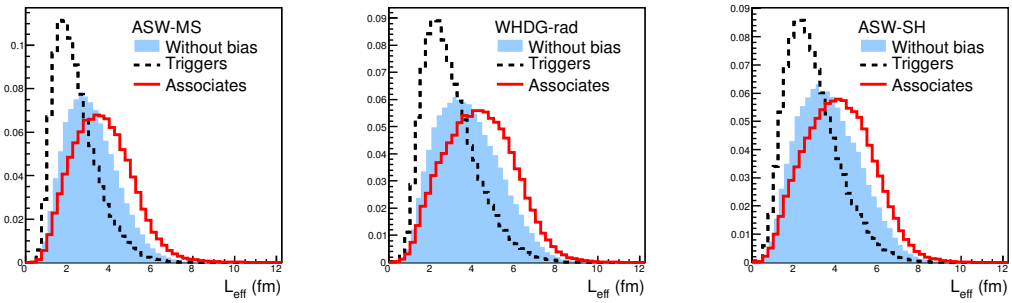

Figure 3.20: Effective lengths for inclusive hadrons, trigger hadrons and associate hadrons. Selection criteria for trigger and associate particles: $8 < p_{\mathrm{T}}^{\mathrm{trig}} < 15$ GeV and $p_{\mathrm{T}}^{\mathrm{trig}} > p_{\mathrm{T}}^{\mathrm{assoc}}$.

As a reference the length distribution without a bias (like in the R_{AA} measurement) is also shown. By selecting a trigger, the event sample is biased towards production points of the partons at the surface of the medium since those partons loose less energy. And by requiring that the trigger has larger energy than the associated particle, the associates are biased towards longer path lengths and thus larger energy loss. As discussed in the previous section the multiple soft scattering approximation is more a *black-white* scenario than the WHDG. From this, one would expect to observe a stronger surface bias and thus longer path lengths while looking at the away side for ASW-MS. In the three panels of Figure 3.20 the path length distributions for the three models are shown. The small differences observed between the different models are due to the slightly different definition of L_{eff} for the multiple soft scattering approximation and the opacity expansions, see section 3.4.

The discussed biases, kinematic bias of parton p_{T} and surface bias, work in opposite directions: the first one decreases the suppression while the path length bias results in a larger suppression with respect to the inclusive R_{AA} measurement.

Fragmentation Bias Another bias due to the selection of a high p_{T} trigger is a bias on the particle type which can be a quark or a gluon. In the process with the same type of outgoing particles, $X \rightarrow qq, q\bar{q}, gg$, this bias does not

exist, but for the process in which a quark and a gluon are produced back-to-back it is more likely that the quark is selected as a trigger. This is already the case in the vacuum since the fragmentation of quarks is harder than for gluons. In the vacuum for 80% of the cases the quark is selected as a trigger. Jet quenching is stronger for gluons than for quarks due to the larger number of color configurations possible for gluons. Therefore the effect of selecting the quark as a trigger is enhanced in the presence of a medium to 90–93% of all the qg productions.

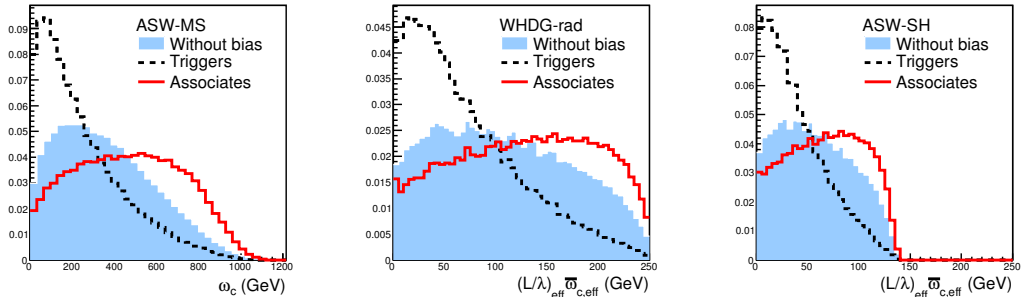

Figure 3.21: Effective characteristic gluon energy $\omega_c(\frac{L}{\lambda}\bar{\omega}_c)$ for inclusive hadrons, trigger hadrons and associate hadrons. Selection criteria for trigger and associate particles: $8 < p_{\mathrm{T}}^{\mathrm{trig}} < 15$ GeV and $p_{\mathrm{T}}^{\mathrm{trig}} > p_{\mathrm{T}}^{\mathrm{assoc}}$.

To give an indication about the magnitude of the energy loss of the associated partons with respect to the trigger, the path averaged values of ω_c for triggers, associated and inclusive (without bias) particles are shown in Figure 3.21. These distributions contain the $\hat{q}L^2$ dependence of the energy loss. Since in the multiple soft scattering approximation the average ΔE for a fixed medium density is much smaller than in the opacity expansion formalism, a larger medium densities is needed to get to the same hadron suppression. Therefore the ω_c distribution for ASW-MS (left panel in Figure 3.21) goes up to much larger values than $\frac{L}{\lambda}\bar{\omega}_c$ for the opacity expansions.

The trigger particles are selected in a high p_{T} interval, $8 < p_T^{\mathrm{trig}} < 15$ GeV/c, and for the associated particles the interval $3 < p_T^{\mathrm{assoc}} < p_T^{\mathrm{trig}}$ GeV/c is used. These trigger and associated p_{T} ranges corresponds to the di-hadron measurement from STAR. Figure 3.22 compares the calculated I_{AA} to the experimental data from STAR [57]. The medium density corresponds to the best fit with the π^0 R_{AA} data as reported in Table 3.4 and the shaded areas are the 1σ uncertainty of the fit. While all the models fit the single hadron R_{AA} at this specific medium density, they all underestimate the measured away side yield. WHDG shows the highest I_{AA} but still strongly overestimates the suppression on the away side. In order to describe the data points, $\hat{q}$ needs to be decreased. At least a decrease of a factor four in medium density is needed to give a reasonable description of the measured hadron recoil suppression I_{AA}.

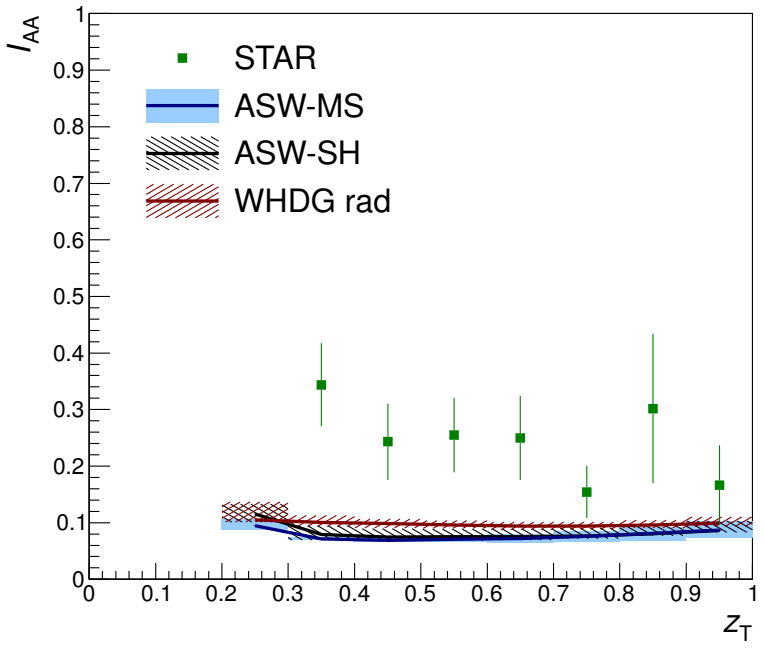

Figure 3.22: Recoil hadron suppression in models with medium density calibrated to the single hadron R_{AA} at RHIC. Curves are for the case where a static medium is present prior to formation time. Shaded and dashed bands indicate 1σ uncertainty bands of the modified χ^2 fit. Centrality: 0–5%. STAR data from [57].

Extending the study with a more realistic medium geometry would be beneficial. It is expected that the use of a hydrodynamically evolving medium constrained against bulk observables, significantly increases I_{AA} while calibrating the model on the measured single hadron suppression [56]. In [58] it has been shown that different assumptions for the initial and final medium conditions, equations of state and viscosity of the medium model, affect the parton energy loss. The differences in the jet quenching observables calculated with a simple medium geometry as used here and a hydrodynamically evolving medium become large if the variable of interest is correlated with the reaction plane. I_{AA} will be affected since the away-side suppression of hard back-to-back correlations is sensitive to the path length dependence of parton energy loss.

3.6.6 Parton Energy Loss at the LHC

One of the first measurements in Pb–Pb collisions at the LHC, has been the R_{AA} of inclusive charged particles [59,60]. Using the same modelling framework as for the parton energy calculation at RHIC kinematics, the energy loss is modelled at LHC Pb–Pb collision energy $\sqrt{s_{NN}} = 2.76$ TeV. The parton cross-section of inclusive and pair production is calculated numerically, see Section 3.6.3. The formation time τ_0 is set to 0.2 fm in the Monte Carlo simulation. The relation

between the initial $\hat{q}$ at RHIC and LHC is given by:

$$\hat{q}_0^{\mathrm{LHC}}(\tau_0 = 0.2) = n \times \hat{q}_0^{\mathrm{RHIC}}(\tau_0 = 0.6), \tag{3.26}$$

with n a scaling factor for the density profile. Note that the medium formation times for the two simulations are different. Before formation time the density profile is assumed to be static. All other parameters like α_s and the number quark flavors, are kept the same as in the simulations for RHIC kinematics, see Table 3.3.

The single hadron suppression R_{AA} is first evaluated for the same medium density as obtained by fitting the π^0 RHIC suppression, see Table 3.4. In Figure 3.24 the resulting R_{AA} is shown for each model for values of $\hat{q}_0$ ranging between the same $\hat{q}_0$ as at RHIC to a four times larger medium density than at RHIC. Note that $\hat{q}_0^{\mathrm{RHIC}}$ is different for each model. With the extended p_{T} reach, all models show a R_{AA} which increases with p_{T}. For the same medium density as at RHIC (labeled with $1 \times \hat{q}_0^{\mathrm{RHIC}}$) the suppression is larger for ASW-MS and WHDG compared to WHDG. Since the particle multiplicity increases with a factor 2.2, one naively expects that the medium density increases with the same factor. For ASW-SH the curve with twice the $\hat{q}$ as at RHIC gives a good description of the measured R_{AA} at high p_{T}. ASW-MS and WHDG both overestimate the suppression with the expected increase of medium density. Both models suggest that the medium density at RHIC and LHC are similar. ASW-SH shows a similar p_{T} dependence to the data measured with ALICE [59] and CMS [60] while ASW-MS and WHDG show a flatter R_{AA}.

The suppression of charged hadrons recoiling from a high momentum particle is also simulated and compared to a measurement from ALICE [61]. I_{AA} is measured as function of the p_{T} of the associated particles recoiling from hadrons with $8 < p_{\mathrm{T}} < 15$ GeV/c. A similar picture as for the jet quenching simulations at RHIC kinematics arises: I_{AA} in the model is smaller than observed in data. The same caveats regarding the medium model as discussed earlier in the last paragraph of section 3.6.5 are present.

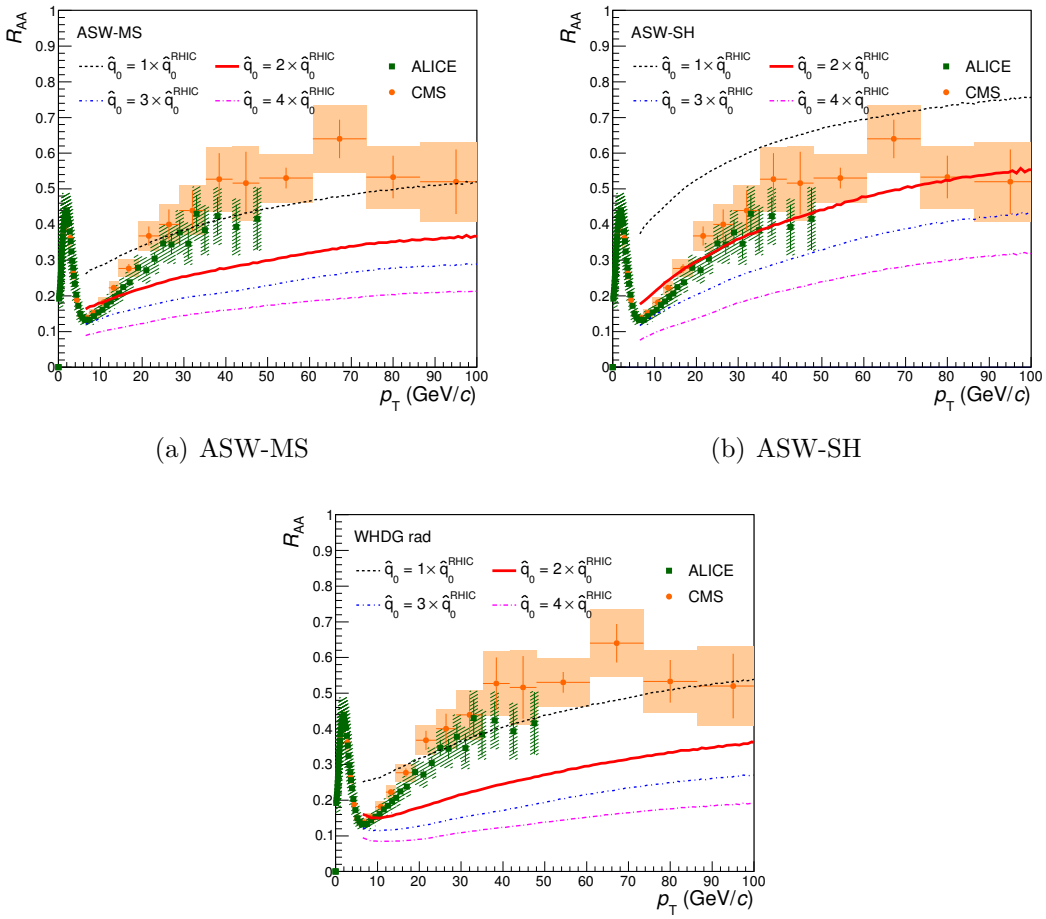

(a) ASW-MS

(b) ASW-SH

(c) WHDG radiative

Figure 3.23: Charged particle R_{AA} for different values of $\hat{q}$ at LHC energy and comparison to the suppression measured at the LHC with ALICE [59] and CMS [60]. Centrality: 0–5%.

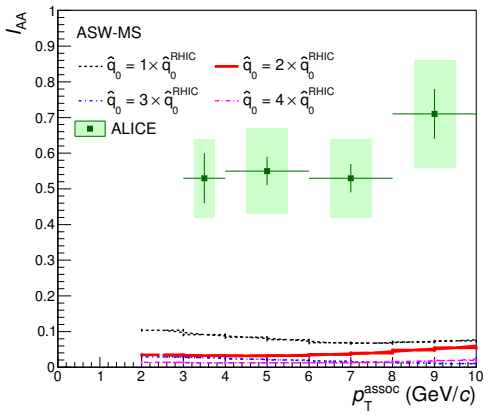

(a) ASW-MS

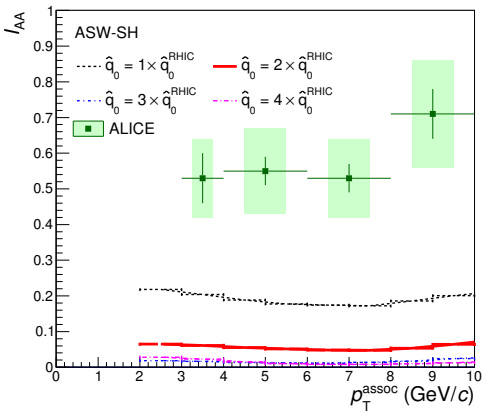

(b) ASW-SH

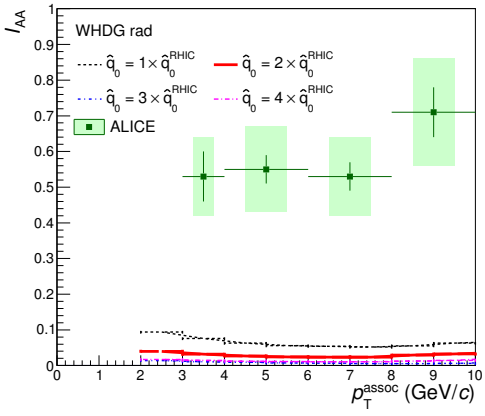

(c) WHDG radiative

Figure 3.24: I_{AA} as function of associated p_{T} for different values of $\hat{q}$ at LHC energy and comparison to the suppression measured at the LHC with ALICE [61]. Centrality: 0–5%.

3.7 Conclusion

Parton energy loss formalisms describe the process of gluon radiation of a hard parton which traverses a hot and dense medium. A selection of commonly used parton energy loss models is studied in a simplified and a realistic medium geometry. High-p_{T} measurements at RHIC and LHC are compared to model calculations. The medium geometry for the comparison with data is modelled with a variant of the Bjorken model in which an initial Glauber profile with participant scaling expands longitudinally with $1/\tau$. The initial medium temperature is calibrated for each model to the nuclear modification factor, R_{AA}, of high p_{T} hadrons. All models describe the single hadron R_{AA} relatively well but the estimated initial medium temperature of the models are significantly different. This is due to different approximations in the parton energy loss implementations. A full calculation of the parton energy loss without mentioned approximations in a uniform medium shows that each model is accurate for different medium lengths. In reality however a parton can have a short, intermediate and long path lengths depending on its production point and flight angle through the medium. In addition, a parton encounters various medium densities along its trajectory through the medium. This results in a broad range of medium lengths and densities experienced by all partons. A full calculation of the parton energy loss within an evolving medium is at present not feasible but might be possible with a Monte Carlo implementation of jet quenching. In addition to the suppression of the inclusive hadron production the model calculations have been compared to a coincident measurement of two high momentum hadrons probing di-jet production. When the initial medium temperature is calibrated for each model to the single hadron suppression, the suppression of the associated particles in a di-hadron correlation is overestimated. A more sophisticated medium model is needed to describe multiple observables simultaneously.

4. Experimental Setup and Analysis Framework

4.1 The Large Hadron Collider

The Large Hadron Collider (LHC) is a particle accelerator at the European Center of Particle Physics CERN located at the French-Swiss border on the edge of Geneva. The LHC is an underground circular accelerator of 27 km long. The LHC is designed to accelerate and collide proton bunches at a center of mass energy of 14 TeV and heavy-ion (Pb) bunches at 5.5 TeV per nucleon pair. The protons or ions are accelerated in two rings in opposite direction and are held in orbit by superconducting magnets with magnetic fields up to 8.33 T. Until the

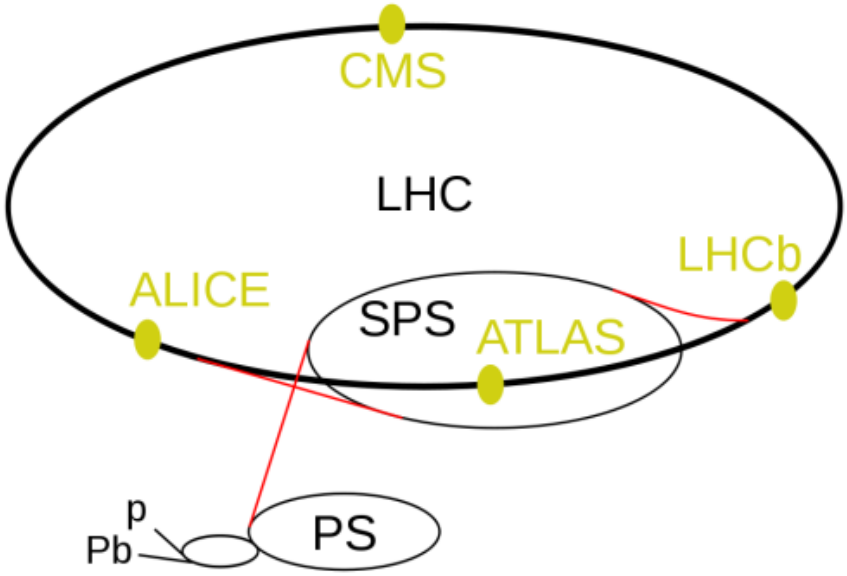

Figure 4.1: Schematic of the LHC accelerator.

long shutdown starting in 2013 the LHC delivered collisions at half of the nominal energy: $\sqrt{s} = 7$ TeV for pp collisions and $\sqrt{s_{\mathrm{NN}}} = 2.76$ TeV for Pb–Pb collisions. In 2012 the collision energy was increased to $\sqrt{s} = 8$ TeV for pp collisions. In

addition, in 2012 and 2013 also for the first time proton-lead, p–Pb, collisions at $\sqrt{s} = 5.02$ TeV were performed.

At several locations of the accelerator experiments are placed: ATLAS (A Toroidal LHC Apparatus) [62], ALICE (A Large Ion Collider Experiment), CMS (Compact Muon Solenoid) [63], LHCb (Large Hadron Collider beauty) [64], TOTEM (TOTal Elastic and diffractive cross section Measurement) [65] and LHCf (Large Hadron Collider Forward) [66]. ATLAS and CMS are multi-purpose detectors designed for the study of the Higgs boson and physics beyond the Standard Model, e.g. supersymmetry in proton-proton collisions. LHCb studies the difference between matter and anti-matter through precision measurements of beauty quarks. The main focus of ALICE is to investigate strongly interacting matter at very high densities created in collisions between lead nuclei.

4.2 The ALICE detector

The ALICE detector is designed to reconstruct particles in an extremely high particle density environment: up to 8000 charged particles per unit of rapidity. The ALICE set-up consists of a central part and a forward part on one side to measure muons. In total the ALICE detector contains 18 subdetector which are shown in Figure 4.2.

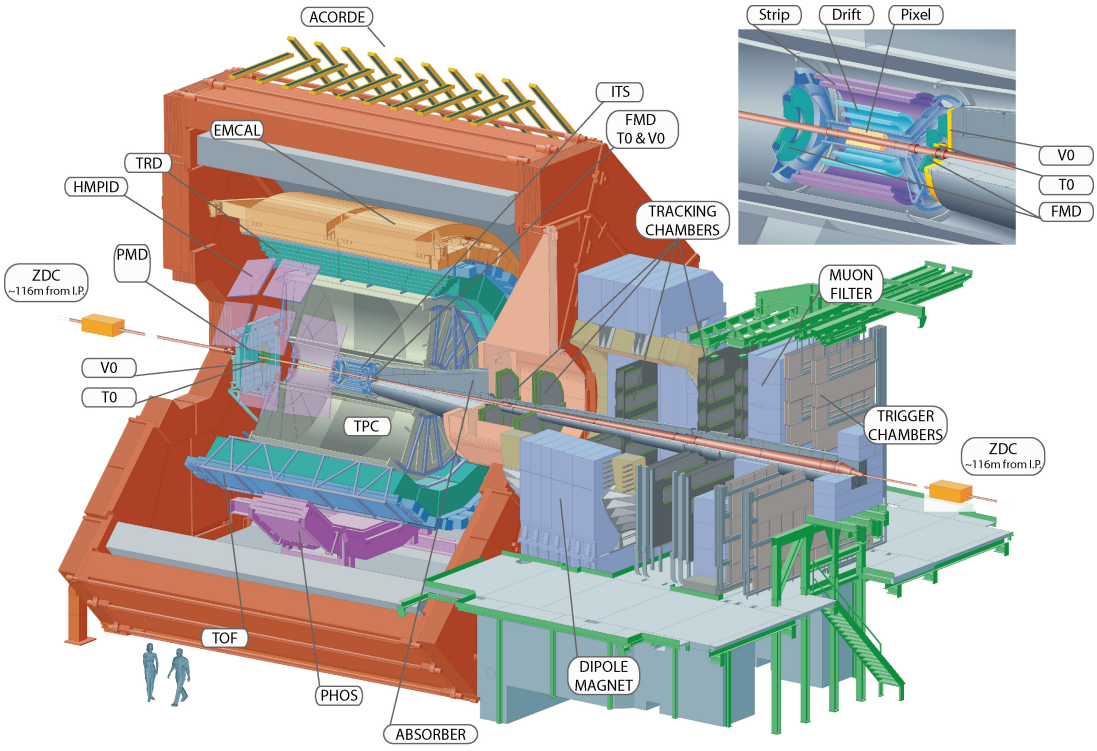

Figure 4.2: Schematic of the ALICE detector.

In the local coordinate system of the experiment, the origin of the Cartesian

coordinates is located at the nominal bunch-crossing point in the center of the L3 magnet. The magnet of the L3 experiment at the Large Electron-Positron collider (LEP) is reused in ALICE. The x-axis of the Cartesian coordinate system points to the the center of the LHC beam circuit. The y-axis points upwards, and the z-axis points along beam direction away from the muon-arm (see Figure 4.2).

Cylindrical coordinates are used to indicate positions in the ALICE detector. The azimuthal angle φ is the angle in the (x,y)-plane and is zero when pointing along the x-axis. The pseudo-rapidity is given by:

$$\eta = -\ln\left(\tan\frac{\theta}{2}\right), \tag{4.1}$$

where θ is the polar angle with the z-axis. The pseudorapidity can also be written as function of the momentum, p, and the longitudinal momentum, p_L, of the particle:

$$\eta = \frac{1}{2}\ln\frac{p+p_L}{p-p_L}. \tag{4.2}$$

The central detectors are inside the L3 magnet. The magnet provides a magnetic field between 0.2 T and 0.5 T (default), parallel to the beam axis. The acceptance of the central detector system covers the full azimuth and pseudorapidity within $\mid \eta \mid < 1$. Charged particles follow a curved trajectory due to the magnetic field which allows for a precise measurement of their transverse momentum ($p_{\mathrm{T}} = 0.3BR$ where B is the magnetic field and R the measured track curvature). The muon arm covers the full azimuth at $2.4 < \eta < 4$. The ALICE collaboration consists of more than 1,000 scientists and engineers from all over the world.

In the following sections the four subdetectors used for the jet analysis presented in this thesis will be discussed while for the other subdetectors a short overview will be given.

4.2.1 Time Projection Chamber (TPC)

The main tracking device in ALICE is the Time Projection Chamber (TPC) [67]. The TPC detects charged particles in the transverse momentum range $0.1 < p_{\mathrm{T}} < 100$ GeV/c. The TPC covers the full azimuth. The pseudorapidity coverage is $\mid \eta \mid < 0.9$ for tracks traversing the full TPC. For partial tracking (tracks which do not reach the outer part of the TPC) an acceptance up to $\mid \eta \mid < 1.5$ is accessible with a reduced momentum resolution. The TPC also identifies particle types by using $\mathrm{d}E/\mathrm{d}x$ measurements.

The TPC is cylindrical in shape with an active gas volume that ranges from 84.1 cm to 246.6 cm, in the radial direction, and has a length of 500 cm along the beam direction. Charged particles traversing the TPC ionize the gas mixture with which the TPC is filled, leaving a long trace along the trajectory of the particle. The diffusion constant is one of the essential parameters for choosing

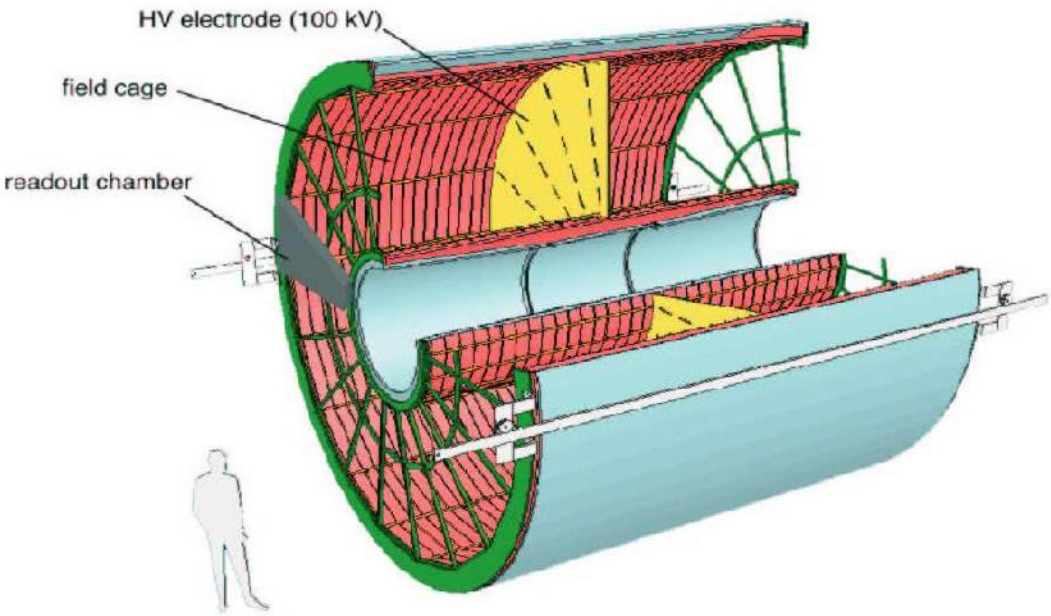

Figure 4.3: Schematic of the Time Projection Chamber.

the gas mixture. This the gas mixture used for the ALICE TPC is Ne/CO_2 which is a so-called cold gas. The used gas meets the requirements of low diffusion and large ion mobility to achieve a good momentum resolution and high rate capability.

The volume of the TPC is divided in two by a high voltage central electrode which is held at 100 kV with respect to the end plates 2.5 m away. The electrons freed by the ionization of the gas are transported towards the end plates at either side of the volume. Their maximum drift time is 90 μs. At the end plates a signal from the electrons is received by multi-wire chambers with cathode pad readout which are mounted in 18 trapezoidal sectors on each side of the TPC. Between the sectors there are small insensitive areas in the TPC azimuthal acceptance (10% of the full azimuth). The curvature of the tracks in the TPC is used to determine the charge and momentum of the particles. Charged particles are reconstructed with a maximum of 160 clusters and the particle type can be determined from the deposited energy in the detector.

Details on the TPC can be found in the TPC Technical Design Report [67].

4.2.2 Inner Tracking System (ITS)

The detector closest to the interaction point is the Inner Tracking System (ITS) which consists of six concentric layers of silicon detectors [68]. The location close to the interaction point allows to precisely measure the location of primary and secondary vertices. The first two layers are highly granular pixel layers which

are located in the central barrel at radii of 3.9 and 7.6 cm from the beam line. These two inner layers are called the Silicon Pixel Detector (SPD). The SPD reconstructs primary and secondary vertices with high precision and is used in the global tracking. The third and fourth layer is the Silicon Drift Detector (SDD) which surrounds the pixel layers at radii of 15.0 and 23.9 cm from the beam line. The four innermost layers are two-dimensional devices, so that they can handle the high particle density up to 90 tracks per cm^2. The two outer layers of the ITS are the Silicon Strip Detectors (SSD) which are located at radii of 38.0 and 43.0 cm where the track density is smaller than one track per cm^2. The SSD are double-sided microstrip detectors which are important for the connection of tracks from the ITS to the TPC.

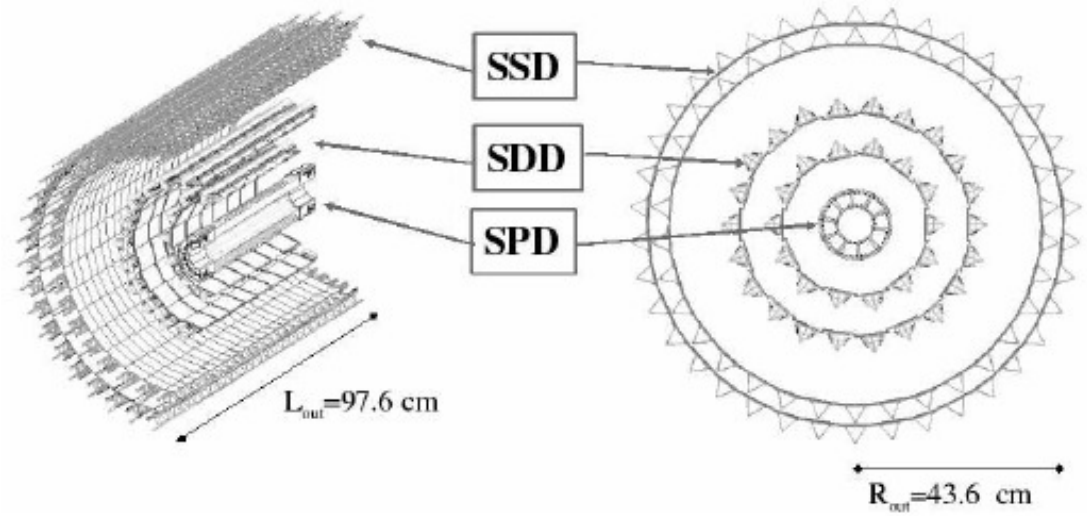

Figure 4.4: Layout of the Inner Tracking System.

The acceptance of the ITS covers the full azimuth and pseudorapidity within $|\eta| < 0.9$ for all vertices located in the region of the interaction diamond ($-5.3 < z < 5.3$ cm along the beam direction). The first pixel layer has a larger range of rapidity coverage, $|\eta| < 1.98$ for collisions taking place at $z = 0$ cm.

With the high spatial resolution of the ITS the interaction vertex and decay vertices, required for the detection of hyperons and particles with open charm and beauty, are reconstructed. The ITS also can identify the particle type of low momentum particles, $p < 100 - 200$ MeV/c, passing through the silicon layers with $\mathrm{d}E/\mathrm{d}x$ measurements in the SDD and SSD. These low momentum tracks do not reach the TPC due to the curvature induced by the magnetic field. Furthermore, the ITS improves the momentum resolution for high momentum particles which also traverse the TPC by increasing the lever arm of the track with additional measured space points in the ITS to the track trajectory. Tracks which fall in the insensitive regions of the TPC are recovered and identified by the ITS. With these improvements on the global tracking and momentum resolution

the ITS is beneficial for the study of many physics topics which are addressed by the ALICE experiment. For the analysis presented in this thesis, the main use of the ITS is the improvement of the global tracking at high p_{T}.

A full description of the ITS can be found in the ITS Technical Design Report [68].

4.2.3 Zero Degree Calorimeters (ZDC)

The ZDCs [69] are calorimeters consisting of four modules at 115 m from the interaction point on the beam axis. On each side two modules are situated of which one is for the detection of protons and the other one to detect neutrons. The ZDCs are used to determine the centrality in heavy-ion collisions by measuring the nucleons which did not interact in the collision: the so-called spectators. If the number of spectators is large, the overlap between the colliding ions is small. The centrality measure of the ZDC has a resolution of $\sim 1\%$ in the most central collisions and 3% in mid-central collisions [70].

4.2.4 VZERO

The VZERO detector [71] consists of two rings of segmented scintillator counters around the beam pipe on both sides of the central barrel detectors in the forward direction at pseudorapidity $-3.7 < \eta < -1.7$ (V0C) and $2.8 < \eta < 5.1$ (V0A). Charged particles traversing the VZERO counters deposit energy which allow to record the amplitude and timing of charged particles. The deposited energy is proportional to the number of particles traversing the VZERO. Each set of VZERO counters contains 32 elementary counters arranged in 4 rings and 8 sectors of 45°.

The VZERO counters serve as an online trigger firing when one of the two counters detects more energy than the threshold. The VZERO is also used to determine the centrality in Pb–Pb collisions, see Section 5.2.2, and to measure the momentum asymmetry in Pb–Pb collisions.

4.2.5 Detectors for Particle Identification

One of the strengths of ALICE lies in identifying particles of a broad range in p_{T} by using signals from different detectors. Detectors used for particle identification, PID, are the ITS, TPC, TOF (acronym for Time Of Flight detector), HMPID (acronym for High Multiplicity Particle Identification), the EMCal (acronym for Electromagnetic Calorimeter) and the TRD (Transition Radiation Detector). The TOF detector provides particle identification in the intermediate transverse momentum range, $0.5 < p_{\mathrm{T}} < 4$ GeV/c, overlapping with the identification in the TPC and extending the p_{T} reach. The HMPID is used for particle identification at high momenta between $p_{\mathrm{T}} = 3$ GeV/c and $p_{\mathrm{T}} = 5$ GeV/c. The EMCal identifies electrons and neutral pions through their two photon decay.

In addition, the EMCal is used to measure the neutral constituents of jets and also provides an on-line jet trigger. The TRD enables electron-pion separation at transverse momenta larger than one GeV/c. The TRD can also be used as high p_{T} hadron trigger for jets and electrons from heavy quarks.

4.3 Off-Line Analysis Framework

4.3.1 ROOT

ROOT is an Object Oriented data analysis framework written in the `C++` computing language [72]. ROOT provides packages for event generation, detector simulation, event reconstruction, data acquisition, data visualization etc. ROOT provides a set of functionalities to handle and analyze large amounts of data in an efficient way. It provides several ways of user interaction: graphic interface, command line or batch scripts.

4.3.2 AliRoot

The software environment AliRoot [73] is a complete experimental framework to reconstruct and analyze simulated and real data from recorded collisions in the ALICE detector. AliRoot is based on the ROOT framework. AliRoot consists of several modules providing software for detector simulation, event generation, event reconstruction and data analysis.

The output of the global reconstruction of real and simulated data is detector independent and is stored in the ESD (Event Summary Data) output file. ESDs are used as a starting point for the analysis. To increase the computing speed of the physics data analysis, ESDs are filtered into AODs. In AODs collision candidates are stored while events from beam-gas interactions are rejected. Also a standard quality selection on the reconstructed tracks is applied.

4.3.3 GRID and AliEn

The Large Hadron Collider produces several Petabytes of data on annual basis. The Grid, a large-scale distributed data processing facility across many different institutes and countries, is essential to make the analysis of these data possible. The GRID is a parallel implementation of a computing infrastructure capable of dealing with such amounts of data.

The ALICE Off-Line collaboration has developed a tool called AliEn (ALICE Environment) to access data on the GRID. The recorded data is reconstructed on the grid and is available to all collaborators. Through the AliEn environment, event simulations are produced centrally and used for analysis. AliEn provides authentication, virtual file catalogue and job management. Jobs that are submitted are sent to a central queue. The computer centers which satisfy

the specific requirements given by the user, pull down the job from the central queue to execute it locally.

The status of the connected computing centers and submitted jobs are monitored and visualized to all users through MonaLisa (acronym for "MONitoring Agents using a Large Integrated Services Architecture") which is accessible through a simple web interface[1].

4.4 Monte Carlo Simulations

In particle physics experiments the simulation of events is used to compare the recorded data to expectations. The simulation chain consists of the generation of an event, the simulation of the detector, digitization and reconstruction in the same way as for the recorded data. The generated events with all its particles are stored as Monte Carlo truth. Each reconstructed particle is stored after passing it through the full detector simulation chain and can be traced back to its corresponding Monte Carlo truth particle or to an interaction with the material of the detector. For this thesis two Monte Carlo (MC) event generators, PYTHIA and HIJING, were used.

4.4.1 PYTHIA

PYTHIA is an event generator of high-energy collisions [74]. In this thesis PYTHIA is used to simulate the evolution of collision between to protons into a complex multi-hadronic final state. The program contains theory and models for a number of physics aspects, including hard and soft interactions, parton distributions, initial- and final-state parton showers, multiple interactions, fragmentation and decay. The generator includes analytical results and QCD-based models because not all the physics processes can be calculated perturbatively. PYTHIA is a leading order generator while parameters for initial and final state radiation are tuned as much as possible to describe the next-to-leading-order pQCD predictions.

PYTHIA has many free parameters which must be tuned to obtain a good description of the experimental data. The parameters tune the perturbative parton cascade and also the non-perturbative hadronization process. Most of the parameters are related to the non-perturbative processes which are phenomenological. This includes parameters for e.g. the kinematic distribution of the transverse momentum in hadron fragmentation and baryon- to meson-ratios. Also the modeling of the underlying event depends heavily on phenomenological assumptions like the parton distribution functions inside the colliding hadrons and the mechanism of multiple parton interactions. A great effort has been done to tune PYTHIA to experimental observables at the Tevatron and LHC [75]. In this thesis the Perugia tunes described in [75] will be used.

[1] http://alimonitor.cern.ch/map.jsp

4.4.2 HIJING

HIJING (Heavy Ion Jet Interaction Generator) is the generator specific for the simulation of nucleus-nucleus collisions [76]. A nucleus-nucleus collision simulated by HIJING consists of multiple underlying p-p collisions. A nucleon of one nucleus can collide with many nucleons in the other nucleus which will deposit a large amount of energy in the collision region. HIJING combines a QCD-based model of jet production with the Lund string model for jet fragmentation. Multiple interactions are calculated using the Woods-Saxon geometry of multiple collisions which provides a quantitative description of the geometry of the nuclei when they collide. Parton shadowing is taken into account by a parametrization of the parton distribution function for the nucleus. HIJING events are a superposition of p-p events and therefore they do not contain any collective effects like elliptic flow.

4.4.3 Detector Simulation

To model the propagation of final state particles through the detector, an accurate description of the ALICE detector is needed. ALICE uses GEANT3 to model the interactions of the produced particles with the different detector materials within the magnetic field that is present in ALICE [77]. The detector simulation includes potential decays of the particles. The energy loss of each particle is modeled depending on the particle type and the material it traverses.

In the digitization process the response of the detector material is modeled. From this an electronic signal of each particle, equivalent to what is recorded in data, is simulated.

4.5 Track Reconstruction and Vertexing

When a charged particle traverses the detector it leaves a trace of discrete signals in the detector modules. Track reconstruction takes place in different steps:

1. cluster finding;
2. reconstruction of the position of the interaction vertex;
3. track reconstruction;

4.5.1 Reconstruction of the Primary Vertex

The primary vertex reconstruction is done separately for the z-coordinate along the beam line and the position in the x, y-plane.

To find a first estimate of the z-coordinate of the primary vertex in Pb-Pb collisions, all the measured space points in the first and second pixel layer are used. The distribution of all the z coordinates in the pixel layers is symmetric

around a certain value of z. This value is the first roughly estimated value of the z-coordinate of the primary vertex. If the interaction point is far away of the center of the detector, $z > 12$ cm, the estimated z-coordinate is inaccurate because too many particles are produced outside the detector acceptance. However, in the next step the vertex position can still be recovered by including more information. In the next step the vertex reconstruction will take into account the correlation between the measured space points in the two pixel layers and the previously found estimate of the z-coordinate is only used to reduce the background of uncorrelated hits. Pairs of measured space points in the pixel layers corresponding to the same particle are selected by requiring that they lie within a small azimuthal window $\Delta\varphi$. These pairs are called tracklets. The selected tracklets point to the interaction vertex and from this the final primary vertex position is calculated.

A similar approach is used to calculate the primary vertex coordinate in the transverse plane. The pixel layers are located close to the interaction vertex and the tracks can be considered to follow a straight trajectories from the interaction point to the second pixel layer. Pairs that point to the beam-axis and intersect the beam-axis within $4\sigma_z$ around the estimated z-coordinate are taken into account. Also a $\Delta\varphi$ cut is applied. This way the centroid of the x and y distribution is selected and the primary vertex is reconstructed in three dimensions.

4.5.2 Charged Track Reconstruction

The signals particles leave in the detectors on their trajectory are collected by a cluster finder. Each found cluster is characterized by a spatial position of a hit and an estimate of the error on this point. Once the primary vertex is reconstructed, it is used to reconstruct tracks from the clusters with a Kalman filter method [78]. The Kalman filtering algorithm finds and fits multiple tracks simultaneously. The clusters close to the outer wall of the TPC (low occupancy) and the position of the primary vertex are used as seeds for the Kalman filtering.

The track reconstruction starts from the outer wall of the TPC and the fit is performed by extrapolating to smaller radii. Using the space points in the TPC the track is prolongated to the inner wall of the TPC. The resolution of the track parameters improve when more points are added. It is allowed to use the same cluster for multiple tracks. To avoid multiple partial reconstruction of the same physical track, a maximum threshold on the number of shared clusters between a pair of tracks is applied. Tracks which have less than 20 clusters assigned or less than 50% of the expected clusters are rejected. Once the inner wall of the TPC is reached the track parameters are stored and this type of track is referred to as TPC-only track. After this the track is matched first to the outer SSD layer and then propagated through the whole ITS until the first SPD layer. The next step is to restart the tracking from the point of closest approach from the primary vertex for each track and propagate back through the ITS and TPC. After reaching the outer wall of the TPC the tracks are prolongated and matched

to the clusters in the outer detectors (e.g. TRD, EMCal and TOF). For tracks which get TRD clusters assigned the momentum resolution at high p_{T} is further improved. For the last step of the track reconstruction the track is propagated again inward starting from the outer wall of the TRD. At this tracking pass the tracks are refitted with the previously found clusters by the Kalman filter.

Each reconstructed track is described by of a set of five parameters, such as curvature and the angles with respect to the coordinate axes. The primary vertex is computed again from the reconstructed tracks providing the optimal resolution. The track parameters and primary vertex are finally stored in the Event Summary Data (ESD) which is used for physics data analysis. The matching efficiency between between the TPC and ITS is $\sim 97\%$ for tracks with at least two hits in the ITS and $p_{\mathrm{T}} > 100$ MeV/c in pp and Pb–Pb collisions. For tracks with at least 1 hit in the ITS the matching efficiency is $\sim 85\%$ in pp collisions and $\sim 80\%$ in Pb–Pb collisions.

The track finding procedure is described in detail in chapter 5 of the ALICE Physics Performance Report [79] and in [80].

5. Data Samples and Selection Criteria

5.1 Data Samples

Collisions between lead ions recorded by the ALICE detector in the fall of 2010 during the first Pb–Pb run at a collision energy of $\sqrt{s_{\mathrm{NN}}} = 2.76$ TeV are used for this analysis. The total number of Pb–Pb events used in this analysis is 12.8 million after applying the event selection discussed in section 5.2. The data sample is divided in four classes of centrality intervals ranging from very central to peripheral events: 0-10%, 10-30%, 30-50% and 50-80%.

To model the corrections for detector effects, Monte Carlo event generators (PYTHIA for pp collisions and HIJING for Pb–Pb collisions) are used. The detector response of all generated particles is modeled with a full GEANT [77] description of the ALICE detector. Simulations are anchored to real data runs who define what kind of detector configuration and beam vertex condition is used. For the simulations used in this analysis anchor runs from the 2010 Pb–Pb run are used. No correction for hadronization effects is applied since the relation between parton and particle level is unknown in heavy-ion collisions.

In the PYTHIA simulations each generated event contains a jet within a specified acceptance interval. This is done by forcing hard parton interactions from $2 \rightarrow 2$ processes during the event generation. Event samples are produced for 10 different intervals in the exchanged momentum between two scattered partons, which is called $p_{\mathrm{T}}^{\mathrm{hard}}$. The division in $p_{\mathrm{T}}^{\mathrm{hard}}$ bins provides high statistics for a wide range in jet p_{T}. For each $p_{\mathrm{T}}^{\mathrm{hard}}$ bin the average cross-section $\sigma_{p_{\mathrm{T}}^{\mathrm{hard}}}$ and the total number of generated events N_{trials} is stored in order to scale each $p_{\mathrm{T}}^{\mathrm{hard}}$ bin to their contribution to a minimum bias event sample. The scale factor used for the event weighting is:

$$w_{p_{\mathrm{T}}^{\mathrm{hard}}} = \frac{\sigma_{p_{\mathrm{T}}^{\mathrm{hard}}}}{N_{\mathrm{trials}}}. \tag{5.1}$$

Only one anchor run which gives a good representation of the full Pb–Pb data set is used for the PYTHIA simulation. Simulating PYTHIA jet samples for all runs is not possible due to limitations in computational costs and disk space. The PYTHIA tunes used for these productions are Perugia-0 and Perugia-2011

[75]. The Perugia-0 tune is a pre-LHC tune based on describing data from LEP, Tevatron and SPS. By varying theoretical parameters (soft, hard, parton density, and color structure parameters) systematically a prediction is made for the charged track multiplicity in inelastic, nondiffractive minimum-bias events at the LHC. The Perugia-2011 tune takes into account early LHC data.

The HIJING event sample is a minimum bias event sample for which all used Pb–Pb runs are used as anchor runs. The used HIJING sample contains 850 thousand events between 0% and 80% centrality.

5.2 Event Selection

5.2.1 On-line and Off-line Event Selection

The analysis presented in this thesis uses minimum-bias events, triggered online by the two forward VZERO counters and the Silicon Pixel Detector (SPD). The VZERO detector selects events from real collisions and rejects interactions of the beam with the gas in the beam pipe. The two VZERO detectors, V0A and V0C, measure the time at which particles arrive with respect to the time when the bunches crossed the nominal interaction point in ALICE. The difference between arrival time of particles from beam-beam interactions and particles from beam-gas interactions allows to efficiently select pp and Pb–Pb collisions.

The online minimum-bias trigger used by ALICE in Pb–Pb collisions requires that at least two out of the following three conditions are satisfied:

- two pixel chips hit in the outer layer of the SPD,
- a signal in V0A,
- a signal in V0C.

The trigger efficiently selects hadronic events in Pb–Pb collisions. In addition an off-line selection is applied in which the online trigger is validated and remaining background events from beam-gas and electromagnetic interactions are rejected.

To ensure a high tracking efficiency for all considered events, the primary vertex is required to be within $|z_{\mathrm{vertex}}| < 10$ cm and $r_{\mathrm{vertex}} < 1$ cm from the center of the detector.

5.2.2 Centrality Determination

Measurements in heavy-ion collisions are often reported as function of the collision centrality. In case two nuclei collide head-on thousands of particles are created while for collisions in which the nuclei only overlap partially the event multiplicities are much smaller. Head-on collisions are referred to as *central* collisions while the collisions in which the nuclei have a partial overlap are called *peripheral*. Since nuclei are constituted of nucleons, it is natural to ask how many

nucleons are involved in a collision. Theoretical techniques allow to estimate quantities like the number of participating nucleons $\langle N_{\mathrm{part}} \rangle$ and the number of binary nucleon-nucleon collisions $\langle N_{\mathrm{coll}} \rangle$. For this the Glauber model is used [81] in which nuclear collisions are described as multiple collisions of individual nucleons on straight-line trajectories. In Monte-Carlo Glauber simulations the spatial position of the incoming nuclei is modeled according to a modified Wood-Saxon function describing the nuclear density distribution of the lead nucleus [82]. The parameters are based on data from low energy electron-nucleus scattering experiments [83]. Nucleons from the two nuclei are assumed to collide in case the crossing distance between them is less than 0.4 fm. The collisions are treated as independent binary nucleon-nucleon collisions. For a given impact parameter b the average overlap (called the thickness function T_{AA}), the number of participants and the number of binary collisions are estimated. The extracted geometrical values for the centrality classes considered in the analysis presented in this thesis are reported in Table 5.1.

Centrality	b_{min} (fm)	b_{max} (fm)	N_{part}	N_{coll}	T_{AA}
0–10%	0	4.91	356.5 ± 3.3	1502.7 ± 169.9	23.5 ± 1.0
10–30%	4.91	8.51	223.8 ± 4.4	743.1 ± 79.4	11.6 ± 0.5
30–50%	8.51	10.97	107.2 ± 3.0	247.7 ± 24.4	3.9 ± 0.2
50–80%	10.97	13.89	32.5 ± 1.5	46.0 ± 4.2	0.7 ± 0.05

Table 5.1: Geometrical values characterizing the centrality classes used in the jet analysis.

The centrality of a Pb–Pb collisions can be obtained experimentally by measuring the particle multiplicity or the deposited energy in a detector. In ALICE several approaches were developed to determine the centrality of a collision. The charged particle multiplicity, measured by the VZERO, the SPD, and the TPC, scales with the centrality of a collision. Another approach is to measure the number of spectators which are the particles not participating in a collision. In peripheral collisions the number of spectators is large while for central collisions it is small. The nucleon spectators are measured with the ZDC.

For the jet analysis presented in this thesis, the centrality estimate of the VZERO detectors is used [70]. The distribution of the measured VZERO signal amplitude, which is proportional to the event multiplicity, is shown in Figure 5.1. The Glauber model is fit to the VZERO amplitude after which the centrality classes are determined from the measured distribution. The centrality percentiles are also indicated in Figure 5.1 as function of the measured VZERO amplitude.The resolution of the centrality determination with the VZERO is $\sim 0.5\%$ for the centrality range 0–20% and increases for more peripheral collisions remaining always below 2% for the 20–80% centrality class.

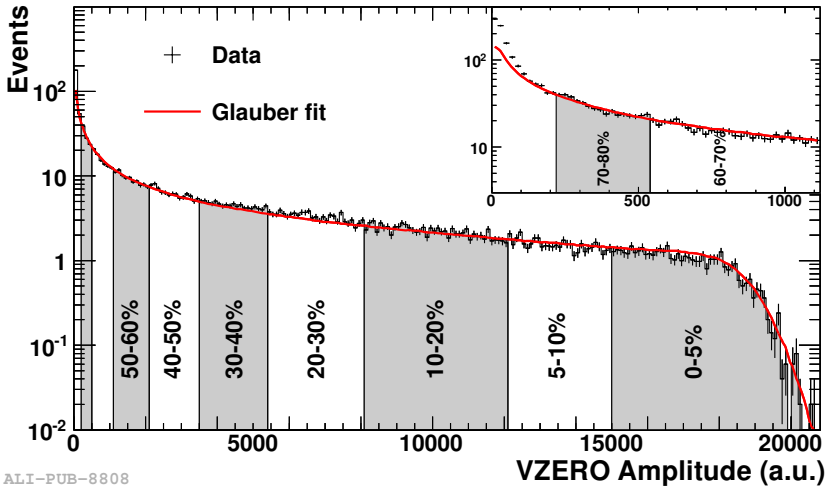

Figure 5.1: Distribution of summed amplitudes measured in the VZERO detector for minimum bias events. Centrality classes are based on a Glauber model. Figure taken from [70].

5.3 Track Selection and Quality Assurance

The track selection has been optimized to avoid biases in the jet clustering by ensuring a uniform acceptance of reconstructed tracks in η and φ.

The clustering of the event is strongly effected by particles with high transverse momentum. This is the desired behavior in case the high momentum track originates from a hard collision, but in case the high momentum reconstructed track has a bad resolution this will bias the jet measurement. The track selection is tuned to reduce the number of outliers at the prize of a lower efficiency at low p_{T}. Outliers are tracks which have low generated p_{T} but are reconstructed at very large p_{T}.

Since some parts of the SPD ladders were switched off during many run periods, inefficient regions in the global track reconstruction are present. To ensure uniform distributions in the (η,φ)-plane, an approach of hybrid tracks of the following types is used:

- global tracks with measured space points in the SPD and a good fit in the full ITS
- global tracks without any space points in the SPD but with a good fit through the remaining ITS layers; track is constrained to the primary vertex
- global tracks with a poor fit through the measured space points in the ITS (typically less than three ITS space points); track is constrained to the primary vertex

As far as available tracks of first type with ITS information are used. Those give the best resolution in transverse momentum p_{T}. Tracks of the second and

third type are constrained to the primary vertex of the event to improve the p_{T} resolution in spite of a missing hit in the SPD or failing the refit in the ITS. Figure 5.2 shows the azimuthal distribution of the three hybrid track categories. In addition the figure also shows the sum of the hybrid tracks resulting in a uniform azimuthal track multiplicity distribution. The primary vertex is estimated from all tracks in the event with SPD hits. A less good p_{T} resolution for some tracks, the ones without ITS refit, needs to be accepted in favor of high and homogeneous tracking efficiency when all types of tracks are combined.

In the total track sample 79% of the tracks is from the first unconstrained category. The remaining 21% are constrained to the primary vertex of which 6% have less than three measured space points in the ITS which causes the ITS refit to fail (the third category).

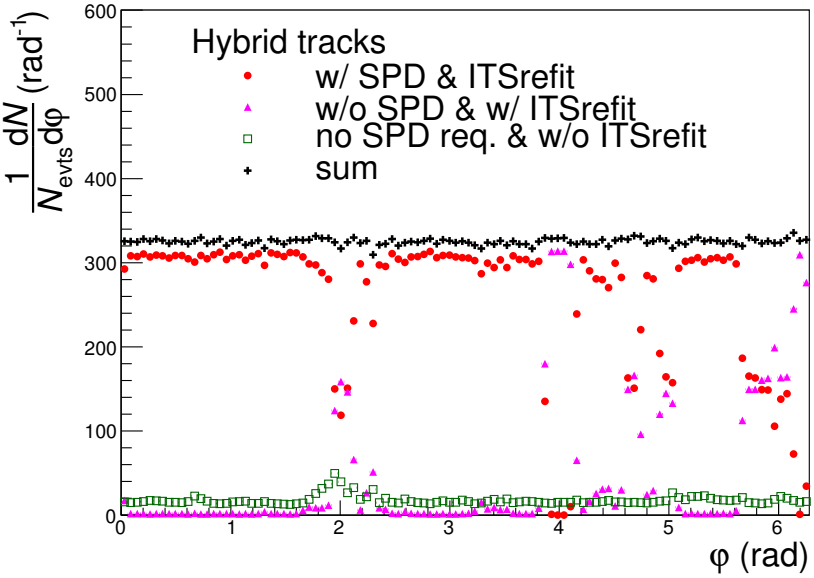

Figure 5.2: Azimuthal distribution of hybrid tracks in 10% most central Pb–Pb collisions.

In the following paragraphs the most important track selection criteria are described. A complete list of track selection criteria can be found in Appendix A.

Number of TPC clusters Tracks of unreasonable high reconstructed p_{T} are rejected by a minimum number of TPC clusters assigned to a track. The maximum number of clusters which can be assigned to a track is 160 which is the total number of pad rows in the TPC. A charged particle traversing the TPC leaves a signal in each pad row it crosses. If this signal is above a certain threshold a cluster is assigned from which the tracks are reconstructed. The number of clusters of a track is related to the track length. Low momentum tracks might curl out of the TPC acceptance never reaching the outer wall of the TPC. Tracks with

a large uncertainty on the estimated p_{T} typically have a low number of clusters assigned at the first tracking pass. Also fake tracks, tracks which do not originate from a particle created by the collision, have a low number of clusters. Tracks are only selected if they have a large number clusters assigned to it at the the first tracking pass. For tracks with $p_{\mathrm{T}} > 20$ GeV/c a minimum number of 100 clusters is required. For tracks with $p_{\mathrm{T}} < 20$ GeV/c a minimum of 70 clusters is required at $p_{\mathrm{T}} = 0$ GeV/c and increases linearly with p_{T}: $N^{\mathrm{iter\,1}}_{\mathrm{clusters,TPC}} > 70 + 1.5p_{\mathrm{T}}$.

χ^2 of TPC track For each reconstructed track in the TPC the χ^2 between the helix of the track and the clusters assigned of the track is calculated. Fake tracks typically have a much larger χ^2 than real well reconstructed tracks. In case $\chi^2/N_{\mathrm{clusters,TPC}}$[1] is larger than four the track is rejected.

TPC and ITS refit During the last tracking pass, propagation towards the primary vertex starts at the outer part of the TRD inward, the tracks are refitted with the previously found clusters in the TPC and ITS. In case the refit fails the tracks are flagged as such. The momentum resolution of tracks with a TPC and ITS refit is significantly better than when one or both of the refits fails. For all tracks used in the analysis a TPC refit is required. From the total hybrid track population 6% fails the ITS refit.

Distance of closest approach to primary vertex Each track is propagated to the closest position to the primary vertex. The distance between the track and the primary vertex is called the impact parameter of the track. Because the spatial resolution in the (x, y)-plane is better than in the direction of the beam line, this is done separately for the radial (x, y) and longitudinal (z) direction. The selection criteria for the two impact parameters are $d_{0,xy} < 2.4$ cm and $d_{0,xy} < 3.1$ cm. With this criterion tracks originating from the interaction of particles with the material are removed from the track sample and the number of secondaries from weak decays are reduced. Not all secondaries are removed from the sample, for $p_{\mathrm{T}} < 1$ GeV/c approximately 10% of the tracks originate from a weak decay. For larger transverse momenta the contribution of secondaries is negligible.

χ^2 between global and TPC-only track Outliers are identified by comparing the track parameters of the global (unconstrained) track to the TPC-only track when it is constrained to the primary vertex. The χ^2 between these two types of tracks is calculated with:

$$\chi^2_{\mathrm{TPC-ITS}} = (\mathbf{v}_{\mathrm{TPC}} - \mathbf{v}_{\mathrm{TPC-ITS}})^{\mathrm{T}} \cdot (\mathbf{C}_{\mathrm{TPC}} + \mathbf{C}_{\mathrm{TPC-ITS}})^{-\mathbf{1}} \cdot (\mathbf{v}_{\mathrm{TPC}} - \mathbf{v}_{\mathrm{TPC-ITS}}), \quad (5.2)$$

where $\mathbf{v}_{\mathrm{TPC}}$, $\mathbf{v}_{\mathrm{TPC-ITS}}$ represent the measured track parameter vectors $\mathbf{v} = (x, y, z, \theta, \varphi, 1/p_{\mathrm{T}})$ and $\mathbf{C}_{\mathrm{TPC}}$, $\mathbf{C}_{\mathrm{TPC-ITS}}$ their covariance matrices. Cases where

[1] The degrees of freedom of the fit is $2N_{\mathrm{clusters,TPC}} - 5$.

the total change in the track parameters is more than 6σ ($\chi^2 > 36$), the track is rejected from the sample.

In addition to all the mentioned track quality cuts, jets containing a track with $p_{\mathrm{T}} > 100$ GeV/c are tagged and rejected after performing the jet clustering.

5.3.1 Tracking Transverse Momentum Resolution

The transverse momentum resolution is estimated from the covariance matrix of each fitted track and validated by the position and width of the reconstructed $K^0_s \to \pi^+\pi^-$ peak in data and simulation. The momentum resolution extracted from the covariance matrix for the 10% most central Pb–Pb collisions is shown in Figure 5.3 as function of track p_{T}. The p_{T} resolution for hybrid tracks does

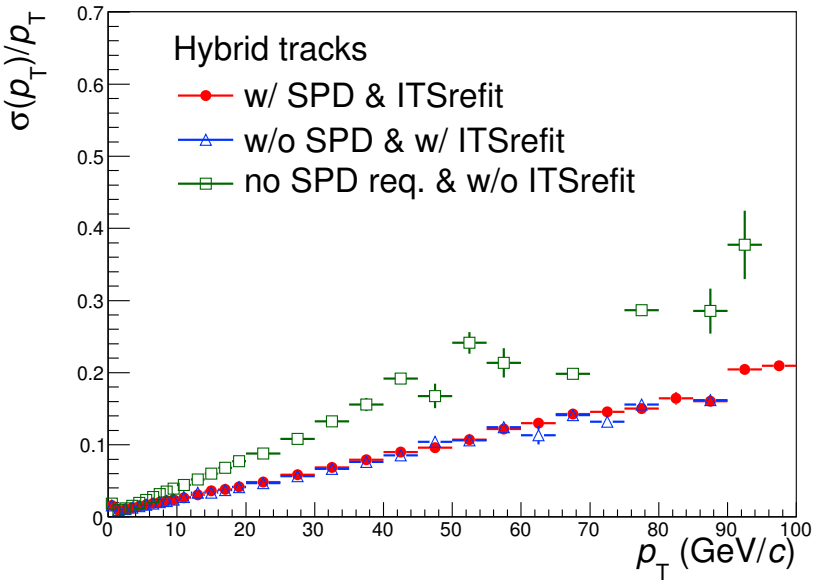

Figure 5.3: Transverse momentum resolution for different types of hybrid tracks. Centrality: 0-10%.

not vary with centrality. All track types have transverse momentum resolution of $\sigma(p_{\mathrm{T}})/p_{\mathrm{T}} \simeq 1\%$ at 1 GeV/c. For the majority of tracks the resolution at $p_{\mathrm{T}} = 50$ GeV/c is $\sigma(p_{\mathrm{T}})/p_{\mathrm{T}} \simeq 10\%$, only tracks having fewer than three reconstructed space points in the ITS have a resolution of $\sigma(p_{\mathrm{T}})/p_{\mathrm{T}} \simeq 20\%$ at 50 GeV/c.

5.3.2 Tracking Efficiency

The tracking efficiency for hybrid tracks reconstructed in the ITS and TPC is evaluated with event and detector simulations. The number of generated particles is defined as all the generated charged primary pions, protons, kaons, electrons and muons within $|\eta| < 0.9$. Reconstructed tracks are all tracks which pass

the track selection and originate from a primary particle. The ratio between the reconstructed and generated tracks gives the tracking efficiency:

$$\varepsilon(p_{\mathrm{T,gen}}) = \frac{\mathrm{d}N^{\mathrm{rec}}/\mathrm{d}p_{\mathrm{T,gen}}}{\mathrm{d}N^{\mathrm{gen}}/\mathrm{d}p_{\mathrm{T,gen}}}. \tag{5.3}$$

The tracking efficiency in HIJING events, shown in figure 5.4(a), is on average 4% lower compared to PYTHIA due to the different reconstruction settings for pp and Pb–Pb collisions and event multiplicities. For Pb–Pb collisions the tracking parameters are more restrictive to avoid a large number of multiple, split, and fake reconstructed tracks in the sample. The tracking efficiency increases rapidly for low transverse momenta, and is approximately constant at higher momenta. The tracking efficiency at intermediate p_{T}, $1 < p_{\mathrm{T}} < 3$ GeV/c, is a few percent larger than at high p_{T} due to an efficiency loss of high p_{T} tracks within the TPC sectors. Tracks with intermediate p_{T} have enough curvature to leave the insensitive regions between the TPC sectors while a high p_{T} track can traverse the full TPC in such an insensitive region. Peripheral collisions in HIJING have a 2% higher efficiency than central collisions in HIJING due to the lower track multiplicity, see Figure 5.4(b).

The largest uncertainty on the tracking efficiency originates from the exact number of clusters assigned to each track which depends on how well the gain in the TPC is modeled. By varying the cut on the number clusters up and down by 20%, the uncertainty on the tracking efficiency is estimated to be 4%.

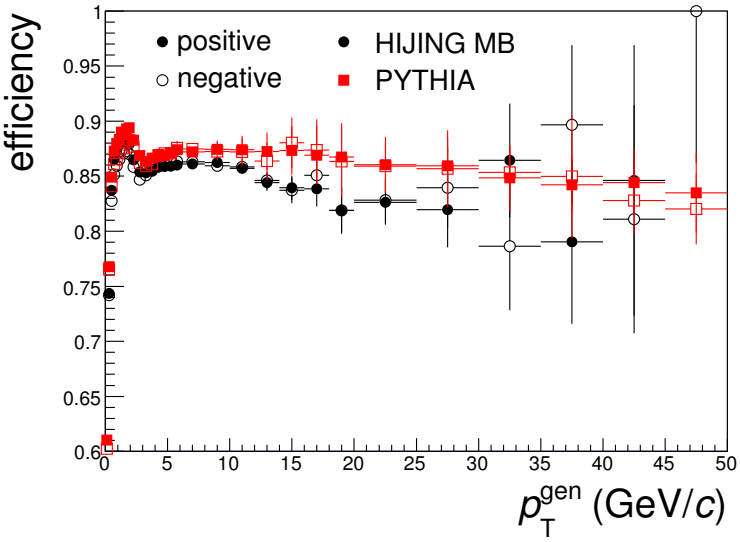

(a) Tracking efficiency of hybrid tracks with PYTHIA and HIJING simulations. HIJING corresponds to a minimum bias event sample here.

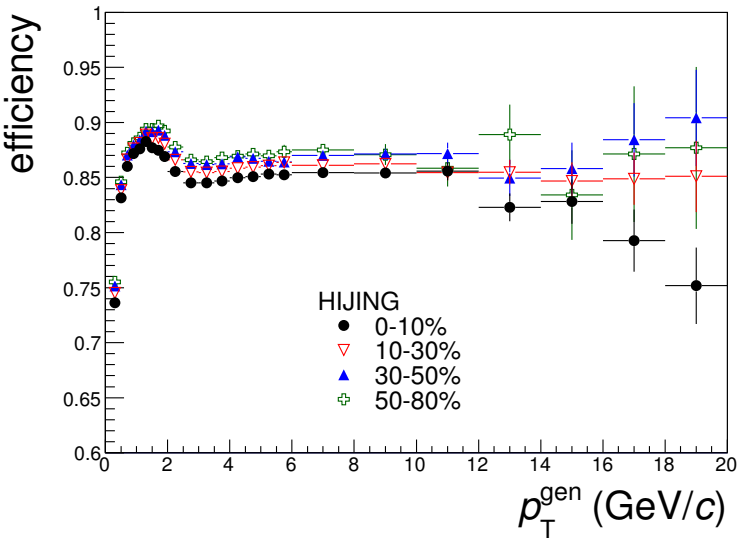

(b) Tracking efficiency of hybrid tracks for different centrality classes HIJING simulations.

Figure 5.4: Tracking efficiency extracted from event and detector simulations.

6. Data Analysis Strategy

The analysis of jet production in heavy-ion collisions consists of the following steps:

1) Jet finding;

2) Event-by-event background subtraction;

3) Quantifying effects distorting the reconstructed jet p_{T};

4) Correction of jet spectrum via unfolding;

6.1 Jet Algorithms

A jet is an object defined by the algorithm. High energy partons lead to collimated bunches of particles. A jet and a parton are not the same object, but their kinematic properties are related. A jet algorithm should not be sensitive to soft QCD effects to ensure that an experimentally observed jet can be related to a theoretically well-defined observable: infrared and collinear (IRC) safety. In an IRC safe algorithm, a collinear splitting or the emission of a soft gluon does not affect the clustering resulting in an unchanged set of hard jets found by the algorithm in the event. With a collinear safe jet algorithm, if configuration (a) in Figure 6.1 gives one jet, then the same configuration with a collinear splitting (b), should also lead to a single jet allowing for the cancellation of divergences in perturbative QCD. In a collinear unsafe algorithm the addition of a collinear splitting leads to the clustering of two jets as shown in (c,d) where the infinities do not cancel. An example of an infrared safe and unsafe algorithm is shown in Figure 6.2. In the illustration on the right (c), the addition of a soft gluon converts the event from having two jets to just one jet.

For the analysis presented in this thesis, jets are reconstructed with algorithms from the `FastJet` package [85, 86].

6.1.1 Anti-k_{T} and k_{T} Jet Algorithm

For this analysis the anti-k_{T} and (inclusive) k_{T} algorithm are used [86, 87]. The two algorithms are sequential recombination algorithms which group particles

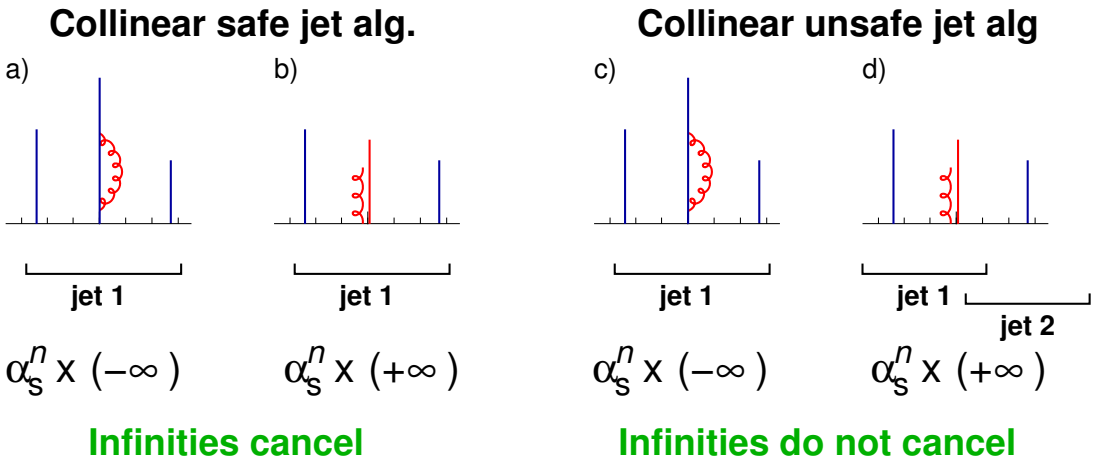

Figure 6.1: Illustration of collinear safety (left) and collinear unsafety (right) in a jet reconstruction algorithm. Particles are vertical lines, their height is proportional to their transverse momentum, and the horizontal axis indicates rapidity. Figure adapted from [84].

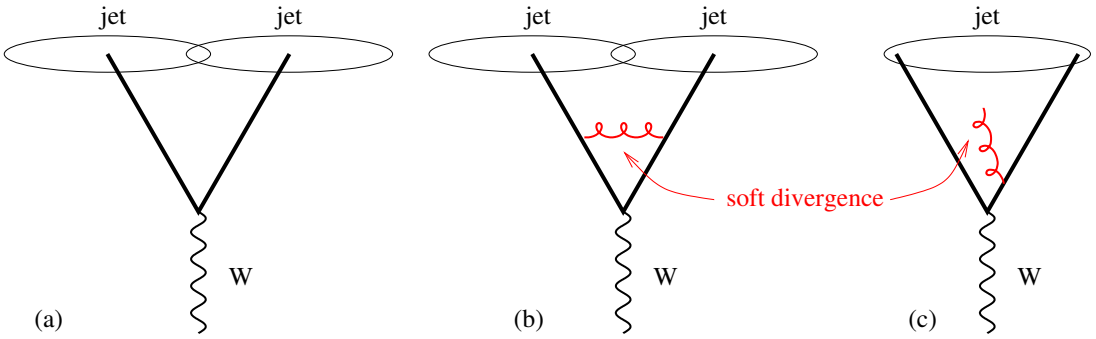

Figure 6.2: Illustration of infrared unsafety in events with a W boson and two hard partons. Figure shows angular structure of the particles and not p_{T} as a function of rapidity. Figure adapted from [84].

into jets based on their transverse momentum and angular distance between them. The k_{T} algorithm clusters the soft particles first resulting in jets with an irregular shape. k_{T} clusters are used in this analysis to estimate the average background in the event, see section 6.2. The anti-k_{T} algorithm starts clustering with the highest p_{T} particles in the event and produces jets with a stable circular area. For both sequential recombination algorithms the p_{T}-weighted distance between all particles in the event is calculated:

$$d_{ij} = \min\left[k_{\mathrm{T}i}^{2p}, k_{\mathrm{T}j}^{2p}\right] \frac{\Delta_{ij}^2}{R^2}, \tag{6.1}$$

in which $\Delta_{ij}^2 = (y_i - y_j)^2 + (\varphi_i - \varphi_j)^2$ is the distance between the pairs of particles i, j. R is the dimensionless angular radius in the η–φ plane which sets the minimal distance between jets in analogy with the radius of a cone. The

beam distance for a particle is

$$d_{iB} = k_{\mathrm{T}i}^{2p}. \tag{6.2}$$

For the k_{T} algorithm $p = 1$ is used while for the anti-k_{T} algorithm $p = -1$ is used. For all pairs of particles the values of d_{ij}, d_{iB} are calculated. In case d_{ij} is smaller than d_{iB} the two particles, i and j, are merged into a new pseudo-particle by summing their 4-momenta. If d_{iB} is smaller than d_{ij}, particle i is defined to be a final jet and is removed from the list. The clustering continues until the (pseudo-)particle list is empty resulting in a set of stable well-separated jets. Each particle is assigned to a unique jet and the stable jets have a well-defined particle multiplicity.

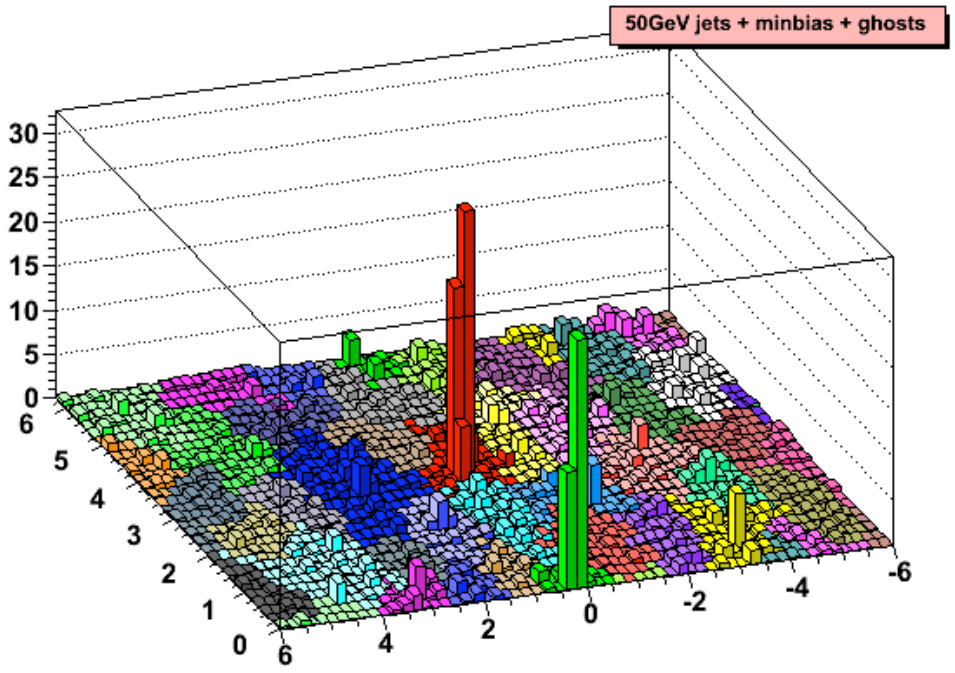

Figure 6.3: Event display of reconstructed jets from simulated events. [Cacciari et. al.]

The soft background present in heavy-ion collisions is estimated using the k_{T} clusters. The background is subtracted from anti-k_{T} jets on an event-by-event basis as will be explained in the following sections. Both the anti-k_{T} and the k_{T} algorithm are infrared and collinear safe to all orders in perturbative QCD meaning that if one adds a collinear splitting or a soft particle emission to the event the number of hard jets is unchanged.

6.1.2 Jet Area

The active area method from the `FastJet` package is used to estimate the area of a reconstructed jet [88]. A large amount of ghost particles with infinitesimal small p_{T} are randomly distributed in the event after which clustering is repeated. The number of ghost particles in a jet is used to determine the jet area. The precision of the area determination depends on the number of ghosts per unit area. This can be varied by changing the ghost area for the computation of the area of the jet. For a smaller ghost area, more ghost particles are used which increases the computation time and memory consumption since it scales with the numbers of particles to cluster. For this analysis a ghost area of 0.005 has been used.

6.2 Jet Reconstruction in Heavy-Ion Events

The average transverse-momentum density per unit area ρ is estimated following the `FastJet` scheme [89, 90]. For each signal jet j, ρA is subtracted from its 4-momentum to correct for the background contribution:

$$p_j^{\mu,\mathrm{sub}} = p_j^{\mu} - \rho A_j^{\mu}, \tag{6.3}$$

in which A_j^{μ} is the 4-vector area of the anti-k_{T} jet. In the case that $p_{\mathrm{T},j} < \rho A_j$ a correction to the jet's scalar p_{T} is performed to allow jets to also have 'negative' p_{T} after background subtraction:

$$p_{\mathrm{T},j}^{\mathrm{sub}} = p_{\mathrm{T},j} - \rho A_j, \tag{6.4}$$

in which A_j is the area of the jet instead of the 4-vector area used before.

The method with which ρ is calculated consists of calculating the median of the transverse momentum density of all k_{T} clusters in the event:

$$\rho = \mathrm{median}\left\{\frac{p_{\mathrm{T},i}}{A_i}\right\}, \tag{6.5}$$

in which i indicates the ith k_{T} cluster in the event, $p_{\mathrm{T},i}$ is the transverse momentum of the cluster and A_i is the area of the k_{T} cluster. Small area clusters do not appear with the k_{T} algorithm which makes this algorithm suitable to estimate the average p_{T} per unit area in an event. With the k_{T} algorithm an event consisting of a soft uniform background is naturally clustered into clusters with $A \sim \pi R^2$ with equal p_{T}. In practice the soft background fluctuates and p_{T}/A for each cluster will fluctuate around average p_{T} density ρ. By using the median and not the average to estimate ρ in the event the contribution from true hard jets to the background estimate ρ is reduced. To further reduce contributions from hard scatterings the two leading k_{T} clusters with highest p_{T} are excluded from the calculation of the median background energy ρ.

6.3 Method to measure Background Fluctuations

The underlying soft background fluctuates from point-to-point within each event due to statistical fluctuations and collective effects. This results in a local p_{T} density $\rho_{\mathrm{local}}(\eta, \varphi)$ which is not equal to the average p_{T} density ρ from equation 6.5. Background induced fluctuations on the measured jet signal and effects of the underlying event on the jet finding are studied by embedding well known probes into heavy-ion events. The difference between the transverse momentum of the background subtracted jet containing the probe is compared the originally embedded probe to quantify the influence of the soft background on the reconstructed jet p_{T}:

$$\delta p_{\mathrm{T}} = p_{\mathrm{T}}^{\mathrm{jet,rec}} - A^{\mathrm{jet,rec}} \cdot \rho - p_{\mathrm{T}}^{\mathrm{probe}}, \tag{6.6}$$

in which $p_{\mathrm{T}}^{\mathrm{jet,rec}}$ is the transverse momentum of the reconstructed anti-k_{T} jet, $A^{\mathrm{jet,rec}}$ is the area of the reconstructed anti-k_{T} jet and $p_{\mathrm{T}}^{\mathrm{probe}}$ is the embedded transverse momentum of the probe. A detailed study of the magnitude and sources of background fluctuations in the measurement of jets with ALICE is presented in Chapter 7.

6.4 Unfolding Algorithms

In this section the unfolding algorithms which are used in the data analysis are discussed. Unfolding algorithms are used to correct measured data for resolution effects, resulting in bin migrations of the true value to the measured observable. The measured distribution $f(y)$ is given by:

$$f(y) = \int \mathrm{d}x \; G(y, x) \; g(x), \tag{6.7}$$

where y is the measured quantity and x is the true variable of interest. The resolution function $G(y, x)$ represents the distortion of variable x into observable y. Comparison to theory can be done by folding the theory curve with the response function and comparing the folded theory to the measurement. For a comparison between various experiments or in case the theory is unknown the true distribution is needed. The goal is to extract the true distribution $g(x)$ from the measured distribution $f(y)$. Both approaches require knowledge about the resolution function $G(y, x)$. For the analysis presented in this thesis, the true jet spectrum is obtained by unfolding the measured jet spectra.

Since measured data is binned and not a continuous curve, a numerical approach is used. Equation 6.7 is written as a matrix equation with a finite number of parameters:

$$\mathbf{y} = \mathbf{G}\mathbf{x}, \tag{6.8}$$

where $\mathbf{y}$ and $\mathbf{x}$ are vectors of the measured and true distributions and $\mathbf{G}$ is the resolution function, also called response matrix. A direct solution of the problem can be obtained by inverting the response matrix: $\mathbf{x} = \mathbf{G^{-1}y}$. In practice the result from a matrix inversion is only satisfactory for a response matrix $\mathbf{G}$ with dominating diagonal, e.g. almost no bin migrations. In experiment however bin migrations due to the detector response can be very sizable. This results in negative off-diagonal elements and very large diagonal elements in $\mathbf{G^{-1}}$. Multiplication of $\mathbf{G^{-1}}$ with measured distribution gives then a highly fluctuating solution which is not physical. This is known as the so-called *discrete ill-posed problem* and occurs in all experiments. Standard methods in numerical linear algebra cannot be used to solve the problem. Instead, more sophisticated methods must be used to restore the true distribution. This is done with unfolding algorithms which apply a regularization to suppress the non-physical fluctuating solutions. There are many regularization methods available. For this work three unfolding methods with different regularization schemes are considered: regularized χ^2 minimization, Bayesian approach and a matrix inversion by singular value decomposition.

6.4.1 χ^2 Minimization

The χ^2 minimization method [91] minimizes the difference between the refolded and measured distribution. The refolded distribution is the unfolded solution convoluted with the response matrix:

$$y_i^{\text{refolded}} = \sum_j^{n_j} G_{ij} y_j^{\text{unfolded}}. \tag{6.9}$$

The χ^2 function to be minimized indicates how well the refolded distribution describes the measured distribution:

$$\chi^2_{\text{fit}} = \sum_i^{n_i} \left(\frac{y_i^{\text{refolded}} - y_i^{\text{measured}}}{\sigma_i^{\text{measured}}} \right)^2, \tag{6.10}$$

in which y is the yield of the refolded or measured distribution and σ_{measured} the statistical uncertainty on the measured distribution. The minimization of Equation 6.10 in which the uncertainty on the measurement for each bin is taken into account, is called a weighted least square problem. The lowest χ^2_{fit} is generally obtained with a strongly fluctuating solution. To suppress these fluctuations a constraint which favors a certain shape for the unfolding distribution is added to the χ^2 function:

$$\chi^2 = \sum_i^{n_i} \left(\frac{y_i^{\text{refolded}} - y_i^{\text{measured}}}{\sigma_i^{\text{measured}}} \right)^2 + \beta P(y_i^{\text{unfolded}}), \tag{6.11}$$

where y^{unfolded} is the unfolded distribution. $\beta P(y^{\text{unfolded}})$ in equation 8.4 is the penalty term which regularizes the unfolded distribution. The strength of the

applied regularization is given by β and $P(y^{\text{unfolded}})$ is the regularization term favoring a certain shape. The choice of the regularization function is based on what kind of shape is expected for the solution. Sensitivity of the unfolded distribution to this particular choice of regularization can be tested by varying the regularization strength β and by comparing the unfolded distribution to a solution with a different shape for the regularization function.

In case the regularization is dominant the penalty term is similar or larger than the χ^2_{fit} between the refolded and measured distribution. In this case the refolded distribution does not describe the measured distribution and the χ^2_{fit} between the refolded and measured distribution is large.

In case the regularization is too weak or too strong, all bins of the unfolded distribution will be strongly correlated. This is visible in very pronounced off-diagonal correlations in the Pearson coefficients which can be extracted from the covariance matrix in the following way:

$$\rho(x, y) = \frac{\text{cov}(x, y)}{\sigma_x \sigma_y}, \tag{6.12}$$

where $\text{cov}(x, y)$ indicates the covariance between bin x and y, and $\sigma_{x,y}$ is the statistical uncertainty of bin x or y.

6.4.2 Bayesian Approach

In the Bayesian unfolding method Bayes theorem is used to invert the response matrix. The implementation of the Bayesian method [92] in the `RooUnfold` package is used [93]. The response matrix is inverted by applying Bayes' theorem iteratively. The unfolded distribution, $\hat{n}(C_i)$, is result of applying the unfolding matrix, M_{ij}, to the measured distribution, $n(E_j)$:

$$\hat{n}(C_i) = \sum_{j=1}^{n_E} M_{ij} n(E_j), \quad \text{where} \quad M_{ij} = \frac{P(E_j|C_i) n_0(C_i)}{\epsilon_i \sum_{l=n}^{n_C} P(E_j|C_l) n_0(C_l)}. \tag{6.13}$$

$P(E_j|C_i)$ is the response matrix previously called G and gives the probability of the true value C_i conditional to the measured quantity The efficiency is given by ϵ_i for each unfolded bin i, and $n_0(C_l)$ is the prior distribution. The prior is initially arbitrary and updated in each iteration. For the initial prior it is common to use a flat distribution, the measured distribution or the observable in a MC model. The solution is regularized by aborting after a certain number of iterations before the true but wildly fluctuating inverse is reached. For most problems the solution does not depend strongly on the choice of number of iterations and the prior.

6.4.3 Singular Value Decomposition

In this method the unfolding is regularized with a singular value decomposition (SVD) based approach [94]. The SVD implementation in the `RooUnfold` package

is used [93]. The response matrix is inverted by decomposing the singular values. The equation that is minimized is Equation 6.10 which can be rewritten en a more general form:

$$(\hat{G}_{ij} y_j^{\text{unfolded}} - \hat{y}_i^{\text{measured}})^T C^{-1} (\hat{G}_{ij} y_j^{\text{unfolded}} - \hat{y}_i^{\text{measured}}) = \min, \tag{6.14}$$

with $\hat{G}_{ij}$ the response matrix normalized by the uncertainty of the measurement $(G_{ij}/\sigma_i^{\text{measured}})$, $\hat{y}_i^{\text{measured}} = y_i^{\text{measured}}/\sigma_i^{\text{measured}}$ and C^{-1} covariance matrix of the measurement. All equations in the problem are rotated and rescaled such that the covariance matrix equals the unit matrix. The rescaling is done by dividing the unfolded vector with some prior: $w_j = y_j^{\text{unfolded}}/y_j^{\text{prior}}$.

The SVD of a response matrix G is $G = U\Sigma V^T$ where U and V are orthogonal matrices and Σ is a diagonal matrix with non-negative elements. The diagonal elements of Σ are the singular values s_i of the response matrix. For ill-posed problems the singular values decrease gradually to zero. Small values s_i correspond to high-frequency fluctuations ($1/s_i$ becomes large). For smooth measured distributions, only the first few terms (often called k) of the decomposition are statistically significant. Regularization is applied by using a smooth cut-off on small singular value contributions ($s_i^2 \rightarrow s_i^2/(s_i^2 + s_k^2)$) suppressing highly fluctuating solutions.

7. Jet Reconstruction and Performance

In a collision experiment the measured hadrons are grouped together by a jet algorithm. The kinematic properties of the jets reflect the kinematic properties of the original hard partons produced by the hard process. The challenge in heavy-ion collisions is to disentangle the soft background from the bulk from the jet fragments created by the parton shower following a hard scattering.

7.1 Jet Reconstruction

Signal jets are reconstructed with the anti-k_{T} jet algorithm. The jets are only accepted in case they are fully contained in the acceptance in which tracks are measured: full azimuth and $|\eta_{\mathrm{jet}}| < 0.5$ where η_{jet} refers to the pseudo-rapidity of the jet axis. Jets with a small area are rejected. The minimum required area for jets with radii $R = 0.2$, 0.3 and 0.4 is 0.07, 0.2 and 0.4 respectively. This selection mostly removes jets that are at very low transverse momentum $p_{\mathrm{T,ch\,jet}} < 20$ GeV/c where $p_{\mathrm{T,ch\,jet}}$ refers to the transverse momentum of the charged jet after background subtraction.

The average background transverse momentum density per unit area is estimated per event as explained in Section 6.2. In Figure 7.1 the correlation between the charged average p_{T} density ρ_{ch} and the uncorrected charged particle multiplicity is shown. The k_{T} clusters from which ρ_{ch} is estimated include charged constituents with $p_{\mathrm{T}} > 150$ MeV/c within the ALICE acceptance ($|\eta| < 0.9$ and full azimuth). The magnitude of ρ_{ch} scales linearly with the charged particle multiplicity of the event. The linear dependence in figure 7.1 is consistent with an average track momentum $\langle p_{\mathrm{T}} \rangle$ of 700 MeV/c. For the 10% most central events the mean p_{T} density $\langle \rho_{\mathrm{ch}} \rangle$ is equal to 138.3 GeV/c. For jet radii of 0.2, 0.3 and 0.4 the average underlying background $\rho_{\mathrm{ch}} \cdot A_{\mathrm{jet}}$ for 10% most central events is 17, 39 and 69 GeV/c respectively for which it is assumed that the jets are circular with area $A_{\mathrm{jet}} = \pi R^2$. In case the minimum p_{T} threshold for the constituents is increased, the underlying background becomes smaller since the multiplicity is reduced. In Table 7.1 an overview of $\langle \rho_{\mathrm{ch}} \rangle$ is given for central and semi-peripheral events with a minimum p_{T} requirement on the constituents of

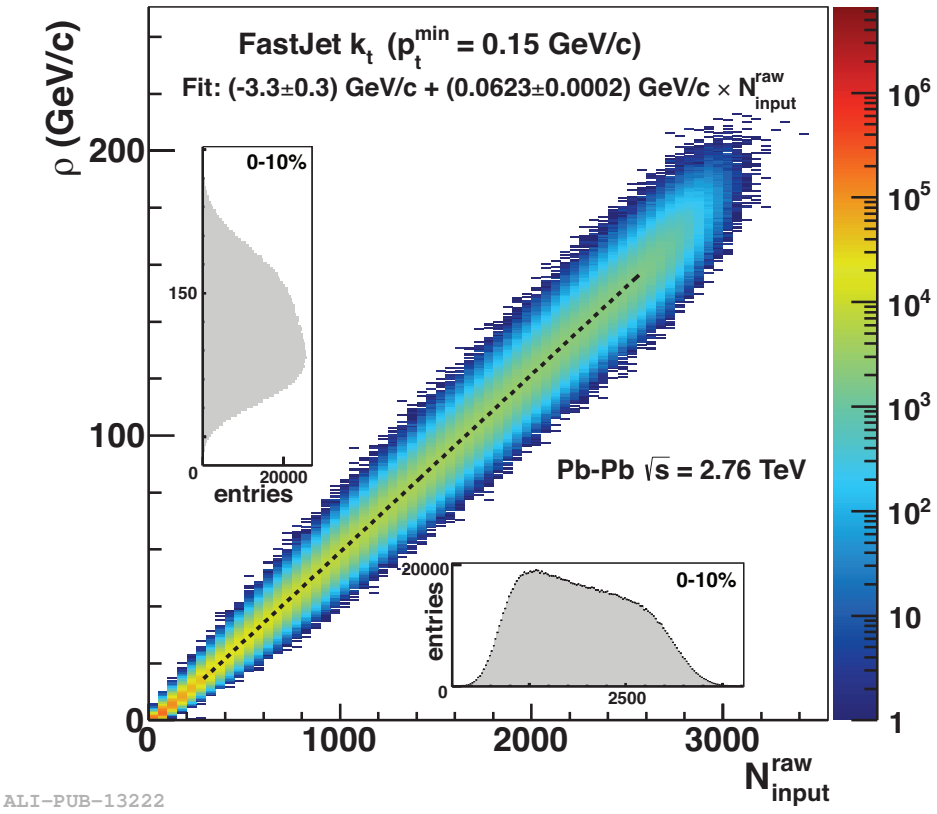

Figure 7.1: Charged transverse momentum background density per unit area ρ_{ch} as function of the uncorrected multiplicity. See also [95].

$p_{\mathrm{T}}^{\mathrm{min}}$ (GeV/c)	$\langle\rho_{\mathrm{ch}}\rangle$ (GeV/c)	$\sigma(\rho_{\mathrm{ch}})$ (GeV/c)
0-10%		
0.15	138.32 ± 0.02	18.51 ± 0.01
1.00	59.30 ± 0.01	9.27 ± 0.01
2.00	12.28 ± 0.01	3.29 ± 0.01
50-60%		
0.15	12.05 ± 0.01	3.41 ± 0.01
1.00	4.82 ± 0.01	1.77 ± 0.01
2.00	4.41 ± 0.05	0.92 ± 0.04

Table 7.1: Average and standard deviation of the event-wise charged particle p_{T} density per unit area ρ_{ch} for three choices of minimum particle p_{T} and two centrality bins. The quoted uncertainties are purely statistical. See also [95]

0.15, 1 and 2 GeV/c. In Table 7.1 the event-by-event spread of the background density $\sigma(\rho_{\mathrm{ch}})$ is also reported. Both the average density and the spread of the average density decrease with centrality.

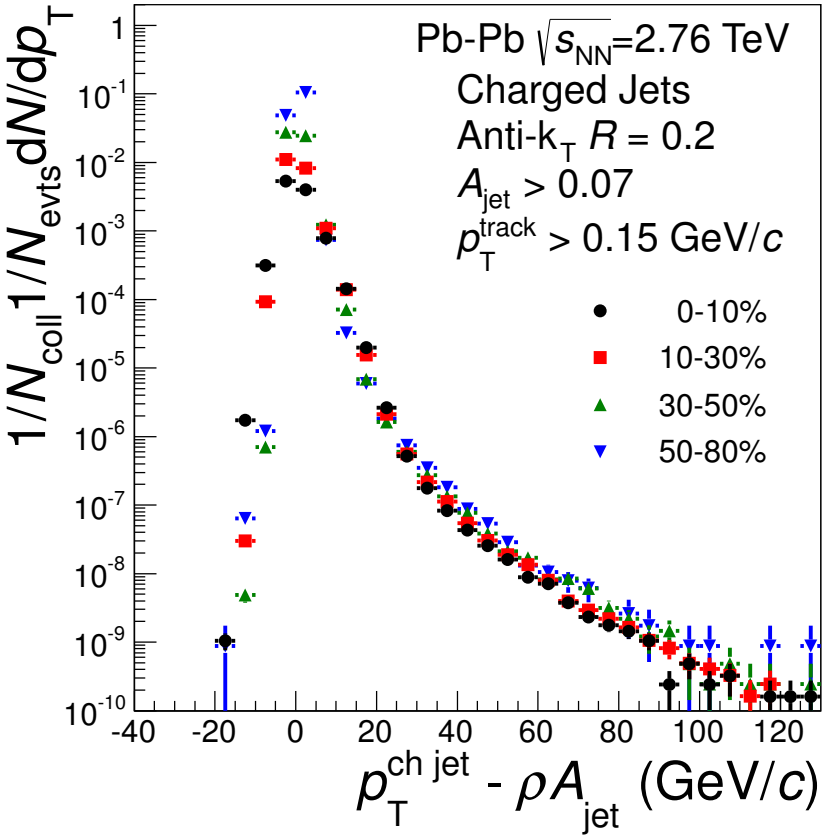

Figure 7.2: Uncorrected jet spectrum reconstructed from charged particles with $R = 0.2$ and $p_{\mathrm{T}}^{\mathrm{track}} > 150$ MeV/c.

Figures 7.2 and 7.3 show the measured p_{T} jet spectra of the background subtracted jets. If the average background is larger than the reconstructed jet p_{T} the jet has a *negative* transverse momentum. The uncorrected jet spectrum for jets with resolution parameter $R = 0.3$, see Figure 7.3, is broader than the jet spectrum with $R = 0.2$. The deviations of the local background p_{T}-density from the average background ρ_{ch} increase with the jet area. These fluctuations of the background affecting the reconstructed jet momentum need to be corrected for.

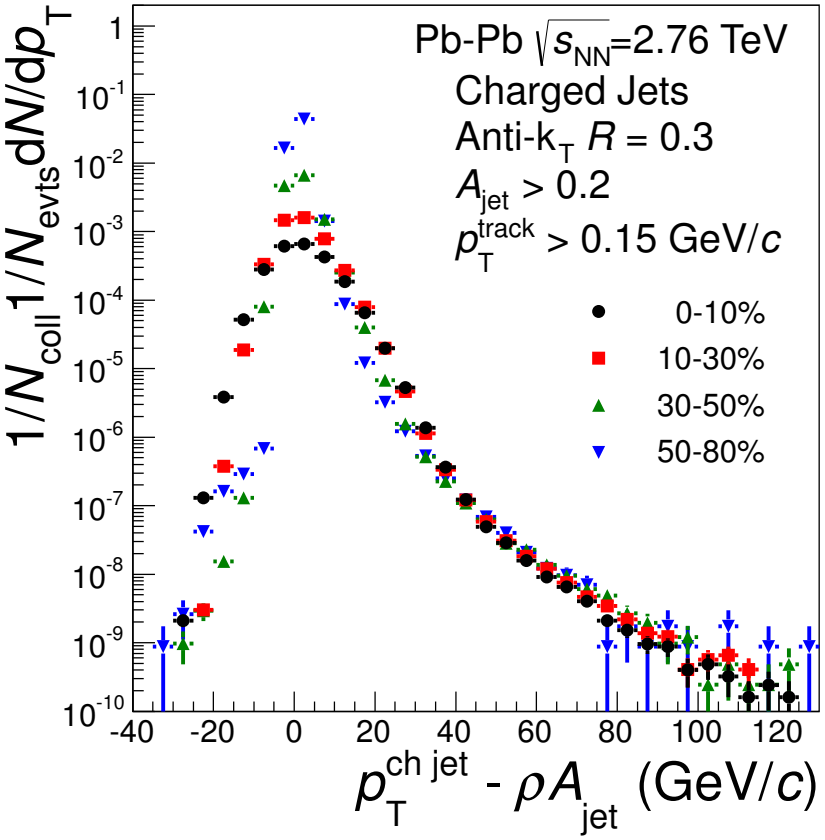

Figure 7.3: Uncorrected jet spectrum reconstructed from charged particles with $R = 0.3$ and $p_{\mathrm{T}}^{\mathrm{track}} > 150$ MeV/c.

7.2 Background Fluctuations

The background in heavy-ion collisions fluctuates from region-to-region from the average subtracted background $\rho_{\mathrm{ch}} A_{\mathrm{jet}}$. One could consider using a local range to estimate ρ_{ch} to reduce sensitivity to long-range correlations. Since the soft particle distribution for $|\eta| < 0.9$, the track acceptance for this analysis, is uniform there is no need to estimate ρ_{ch} as function of η. The modulation of soft particles in φ due to collective flow is hard to disentangle from the back-to-back production of jets in φ. The acceptance in which ρ_{ch} is calculated A_ρ has to contain enough background clusters to extract a reliable median: typically $A_\rho > 10 A_{\mathrm{jet}}$. Considering the enhanced bias one would get from jet fragments and the small number of background clusters one would have to work with in a local range in φ the global ρ_{ch} is used for the average background calculation with the price of a larger width of the background fluctuations.

Background fluctuations are studied by embedding three different probes into the measured Pb–Pb events:

- Rigid random cones
- Single high p_{T} particles
- Simulated PYTHIA jets

7.2.1 Sources of Background Fluctuations

The contribution to the background fluctuations of different sources are studied by placing rigid cones with radius $R = 0.4$ in the measured Pb–Pb event at a random position in η and φ while the cone is fully contained in the detector acceptance. The fluctuations of the background are characterized by looking at the difference between the summed p_{T} of all the particles in the random cone (RC) and the estimated background:

$$\delta p_{\mathrm{T}} = \sum_{i}^{\mathrm{RC}} p_{\mathrm{T,i}} - A \cdot \rho_{\mathrm{ch}}, \tag{7.1}$$

where A is the area of the cone $A = \pi R^2$. In contrast to what happens when clustering jets with an algorithm, the position and area of the random cones are not influenced by the structure of the event. Figure 7.4 shows the normalized δp_{T} distribution of random cones for central events and $p_{\mathrm{T}}^{\mathrm{const}} > 0.15$ GeV/c in the filled red circles. The distribution shows the probability that the p_{T} of a jet fluctuates up or down with $p_{\mathrm{T}} = \delta p_{\mathrm{T}}$. The fluctuations are centered around zero indicating that on average the p_{T} density ρ_{ch} is estimated correctly. The background fluctuations are characterized by the width of the measured distribution $\sigma(\delta p_{\mathrm{T}})$, which for this radius, $R = 0.4$, and p_{T} constituent cut, $p_{\mathrm{T}}^{\mathrm{const}} > 0.15$ GeV/c, is 11 GeV/c. The δp_{T} distribution is asymmetric with an enhanced probability for positive fluctuations: the high p_{T} tail. The left-hand-side can be described with a Gaussian. To obtain a stable result a Gaussian fit is done iteratively in the range $[\mu^{\mathrm{LHS}} - 3\sigma^{\mathrm{LHS}}, \mu^{\mathrm{LHS}} + 0.5\sigma^{\mathrm{LHS}}]$ with the mean μ^{LHS} and standard deviation σ^{LHS} from the previous iteration. Iterations continue until the change in μ^{LHS} is less than 0.01 GeV/c resulting in a robust result of the fit. As can be seen in Figure 7.4 the Gaussian fit describes the δp_{T} distribution for $\delta p_{\mathrm{T}} < 0$ GeV/c very well. The width of the Gaussian fit, $\sigma^{\mathrm{LHS}} = 9.7$ GeV/c, is smaller than the width of the full distribution due to the asymmetric shape of the δp_{T} distribution for $\delta p_{\mathrm{T}} > 0$ GeV/c.

The background fluctuations reported are detector specific since they are not corrected for tracking efficiency and momentum resolution. The δp_{T} distribution is measured to acquire knowledge about the influence of the background on reconstructed jets. The measured fluctuations will be used to correct the jet measurement.

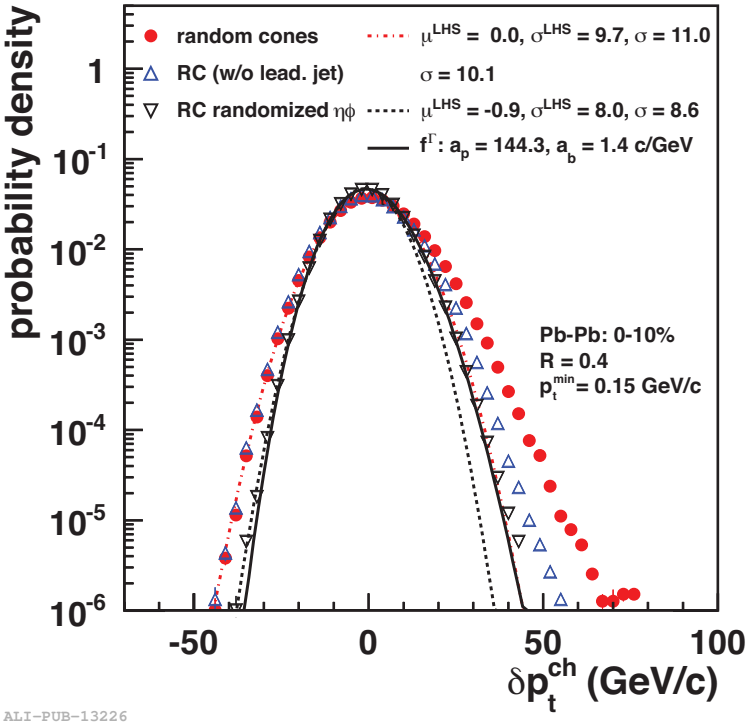

Figure 7.4: $\delta p_{\mathrm{T}}$from three different types of rigid random cones with radius $R = 0.4$ in 10% most central events. Minimum p_{T} of tracks is $p_{\mathrm{T}} > 0.15$ GeV/c. The left-hand-side has been fitted with a Gaussian as explained in the text. See also [95].

Statistical Fluctuations

The contribution to the background fluctuations from statistically independently emitted particles is studied by obtaining the δp_{T} distribution in randomized events. In randomized events region-to-region correlations in the event are removed by assigning a random η and φ to each measured track in the Pb–Pb events while keeping the p_{T} of the tracks as measured. The δp_{T} distribution from randomized events is shown in figure 7.4 by the open black triangles. It can be observed that random event-by-event $\langle p_{\mathrm{T}} \rangle$ fluctuations do not have a symmetric Gaussian shape. This is due to the non-Gaussian shape of the single particle p_{T} and multiplicity distributions. The δp_{T} distribution for a model with independent particle emission can be described by a Gamma function with parameters a_p and a_b [96, 97]:

$$f^{\Gamma}(\delta p_{\mathrm{T}}, a_p, a_b) = A \cdot a_b/\Gamma(a_p) \cdot (a_b \delta p_{\mathrm{T}} + a_p)^{a_p - 1} \cdot e^{-(a_b \delta p_{\mathrm{T}} + a_p)}, \qquad (7.2)$$

in which the mean has been shifted with $-a_p/a_b$ and the standard deviation is $\sigma = \sqrt{a_p}/a_b$. The Gamma distribution gives the statistical Poissonian limit of the background fluctuations. This limit is compared in Figure 7.4 to background fluctuations measured in randomized events which are expected to approach the Poissonian limit. The distribution of Poissonian fluctuations is narrower than the fluctuation distribution of the unmodified event pointing to the presence

of region-to-region fluctuations in addition to the statistical fluctuations in the measured Pb–Pb events. The Gamma distribution gives a good description of the randomized δp_{T} distribution. High momentum tracks originating from a hard process are still present in the randomized events causing a slightly larger probability for positive fluctuations compared to the Poissonian limit.

By placing the random cones far away from the hardest subtracted anti-k_{T} jet (distance $D > 1$) the influence of true jets to the background fluctuations is removed. It is observed that avoiding overlap with the hardest anti-k_{T} jet reduces the upward fluctuations in the δp_{T} distribution as is shown in Figure 7.4 with the points labeled 'RC (w/o leading jet)'. The left-hand-side of the distribution is unmodified by this requirement. The width of the distribution is reduced from 11.0 to 10.1 GeV/c.

Correlated Fluctuations

A source of non-Poissonian correlated fluctuations is the collective flow of particles induced by the anisotropy in coordinate space of the nuclear overlap. Due to multiple interaction this anisotropy is transferred to momentum space. The anisotropy is orientated with respect to the reaction plane of the collision. The experimental measure of the asymmetry of the event is calculated from the azimuthal distribution of all tracks in each event resulting in an orientation of the event plane Ψ_{EP}. The azimuthal particle distribution is characterized by a Fourier analysis of the particle flow. The leading term is the second moment of the Fourier expansion, elliptic flow v_2 [98]. Odd Fourier components like v_3 driven by the initial state fluctuations can have a significant impact on the azimuthal distribution of particles in an event.

For the determination of the event plane, tracks reconstructed in the TPC with $|\eta| < 0.8$ and $p_{\mathrm{T}} > 0.15$ GeV/c are used. The tracks are weighted with their p_{T} or with a constant weight factor 2 in case $p_{\mathrm{T}} > 2$ GeV/c to limit the influence of hard processes to the event plane calculation. Random cones are sampled with respect to the event plane orientation Ψ_{EP}. The angle between a random cone and the event plane is $\Delta\varphi = \varphi_{\mathrm{RC}} - \Psi_{\mathrm{EP}}$ in which φ_{RC} is the azimuthal orientation of the cone axis. Three categories are defined:

- 'in-plane': $\Delta\varphi < 30^o$,
- 'intermediate': $30^0 < \Delta\varphi < 60^o$, and
- 'out-of-plane': $\Delta\varphi > 60^o$.

The δp_{T} distributions for in-plane, intermediate and out-of-plane orientation to the event plane are shown in the upper panel of Figure 7.5. The left-hand-side mean of a Gaussian fit μ^{LHS} for in-plane and out-of-plane is shifted by 5.4 and -4.5 GeV/c respectively. This indicates that the average background momentum density in-plane is larger than the average momentum density of the full event. In case of out-of-plane too much background has been subtracted pointing to a

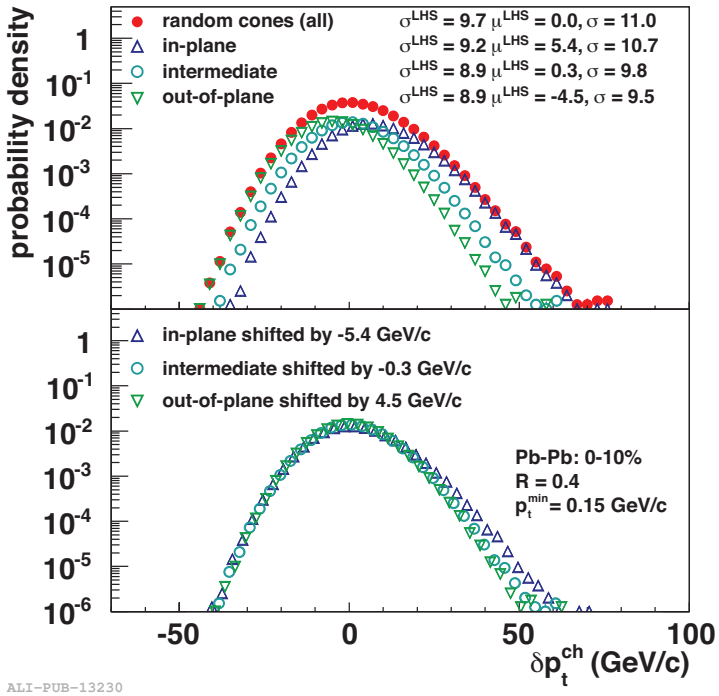

Figure 7.5: δp_{T} distribution from rigid random cones with radius $R = 0.4$ in 10% most central events for 3 different orientations to the event plane. Minimum p_{T} of tracks is $p_{\mathrm{T}} > 0.15$ GeV/c. In the bottom panel the distributions have been shifted such that the mean of the left-hand-side fit, μ^{LHS}, is situated at zero. See also [95].

lower momentum density perpendicular to the event plane orientation. For the intermediate region μ^{LHS} is 0.3 GeV/c indicating that the average background in that region is similar to the average background of the full event. The left-hand-side widths of the δp_{T} distributions for the different orientations to the event plane as reported in the legend of the upper panel in Figure 7.5, are not significantly different. This is also visualized in the lower panel of Figure 7.5 in which the distributions are shifted such that the mean of the left-hand-side fit μ^{LHS} is situated at zero. The figure also shows that the probability for large upward fluctuations is larger in-plane than out-of-plane. This could point to a dependence of jet production to the orientation of the reaction plane. However there is also a contribution of auto-correlation since the event plane is calculated with the same tracks as considered for the random cones. The event plane can also be measured with the VZERO detectors situated at large rapidity ($-3.7 < \eta < -1.7$ and $2.8 < \eta < 5.1$) which would reduce the auto-correlation with the random cones measured at mid-rapidity. The resolution of the VZERO event plane however is worse which makes the interpretation difficult.

The width of the measured fluctuations from purely random Poissonian fluctuations can be estimated from the width and mean p_{T} of the single particle p_{T} spectrum assuming that there is no correlation between the particle multiplicity

and the mean p_{T} [79]:

$$\sigma(\delta p_{\mathrm{T}}) = \sqrt{N_{\mathrm{A}}\ \sigma^2(p_{\mathrm{T}}) + N_A\ \langle p_{\mathrm{T}}\rangle^2}, \tag{7.3}$$

in which N_A is the expected track multiplicity in the cone, $\langle p_{\mathrm{T}}\rangle$ is the mean p_{T} of the single particle p_{T} spectrum and $\sigma(p_{\mathrm{T}})$ indicates the width of the single particle p_{T} spectrum. Non-Poissonian fluctuations from local variations of the average multiplicity can be added by calculating the non-Poissonian standard deviation $\sigma_{\mathrm{NP}}(N_{\mathrm{A}})$:

$$\sigma(\delta p_{\mathrm{T}}) = \sqrt{N_{\mathrm{A}}\ \sigma^2(p_{\mathrm{T}}) + (N_{\mathrm{A}} + \sigma^2_{\mathrm{NP}}(N_{\mathrm{A}}))\ \langle p_{\mathrm{T}}\rangle^2}, \tag{7.4}$$

Figure 7.6 shows the width of the δp_{T} distribution as function of the track

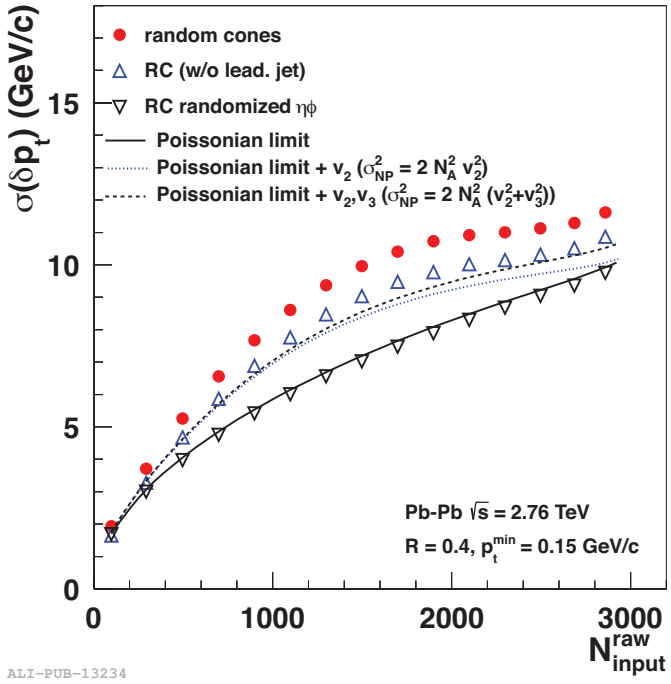

Figure 7.6: Width of δp_{T} distributions from rigid random cones with radius $R = 0.4$ as function of the raw charged track multiplicity. Comparison of measured data points with the Poissonian limit and contribution from elliptic and triangular flow. See also [95].

multiplicity for the three types of considered random cones. The width of random cones in randomized events is well described by the expression in Equation 7.3 for purely statistical fluctuations. Non-Poissonian fluctuations from elliptic flow and triangular flow scale with multiplicity and can be described as

$$\sigma^2_{\mathrm{NP}}(N_{\mathrm{A}}) = 2N^2_{\mathrm{A}}(v_2^2 + v_3^2), \tag{7.5}$$

in which v_2 and v_3 are added in quadrature since they are not correlated via a common plane of symmetry. In Figure 7.6 the expected Poissonian fluctuations

with only a contribution of elliptic flow and including both elliptic and triangular flow are shown. For v_2 the p_{T}-integrated value in the range $0.2 < p_{\mathrm{T}} < 5.0$ GeV/c as measured by ALICE is used [15]. Triangular flow has only a weak dependence on centrality and is approximated for this work as constant: $v_3 = 2.4\%$. Only including elliptic flow underestimates the width of the measured background fluctuations for central events. Including v_3 as well gives a reasonable agreement with the measured background fluctuations in which the hardest jet is excluded. Contributions of remaining jet fragments resulting in upward fluctuations are not taken into account in the parametrization of the fluctuations in equation 7.4. Also flow-induced changes of $\langle p_{\mathrm{T}} \rangle$ and $\sigma(p_{\mathrm{T}})$ are not considered.

7.2.2 Fluctuations versus Jet Resolution Parameter

Background fluctuations are smaller in case the multiplicity within the jet cone is reduced, see Equations 7.3 and 7.4. In figure 7.7(a) the δp_{T} distributions from random cones for three different jet radii (0.2, 0.3 and 0.4) are shown for events with 0-10% centrality [1]. The background fluctuations are characterized by the standard deviation of the δp_t distributions in the legend. For the typically used jet resolution parameter $R = 0.4$ the fluctuations are 10.18 GeV/c while this reduces to 4.47 GeV/c for R=0.2. In Figure 7.7(b) the width of the measured

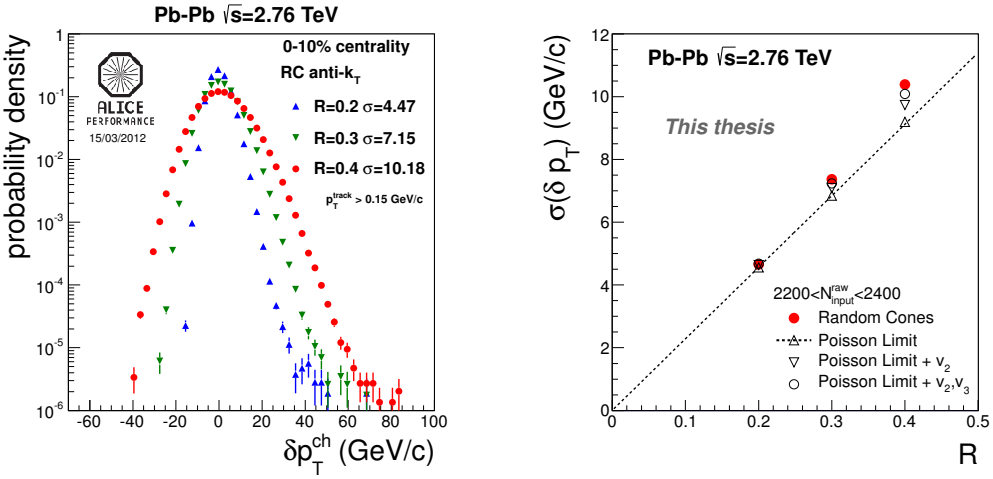

(a) Background fluctuations measured with random cones for three different radii: $R = 0.2$, $R = 0.3$ and $R = 0.4$.

(b) Width of background fluctuations for random cones for typical multiplicity for 10% most central events compared to Poissonian limit and Poissonian limit with flow contribution.

Figure 7.7: Jet area dependence of background fluctuations.

[1] The width for $R = 0.4$ cones is a bit smaller here compared to what is reported in Figures 7.4, 7.5 and 7.6 due to an additional high p_{T} track quality cut applied which reduces the raw event multiplicity by a few percent.

background fluctuations for the three considered radii is compared to the Poissonian limit and the Poissonian limit with flow contributions as in Equations 7.3 and 7.4. The absolute contribution from region-to-region fluctuations becomes larger for larger jet areas since they scale quadratically with jet resolution parameter R, $\sqrt{N} \propto R$, while the statistical fluctuations scale linearly with R.

7.2.3 Fluctuations with Jet Finding

The influence of background fluctuations on the p_{T} of the reconstructed anti-k_{T} jets is studied by embedding high transverse momentum probes into measured Pb–Pb events. To account for the response of a jet finder in a heavy-ion environment the embedded probes are reconstructed with the same jet finder and settings as used in data analysis. Three types of high p_{T} probes are embedded in the measured heavy-ion events:

- single high p_{T} particles,
- anti-k_{T} pp jets generated with PYTHIA,
- anti-k_{T} quenched jets generated with Q-PYTHIA [99].

The main difference between the probes is their fragmentation pattern. Ideally the jet finder response should not depend on the jet fragmentation pattern since it is potentially modified by the presence of a dense medium in the heavy-ion collision. Considering a single high p_{T} particle is an extreme not very realistic scenario for the fragmentation function but conceptually similar to a particle carrying a transverse momentum larger than the typical particle p_{T} in the heavy-ion event. In this case the anti-k_{T} jet finder will reconstruct a circular jet with radius R around the embedded particle.

The probes are embedded in the heavy-ion events at random position in (η, φ) within the jet acceptance ($|\eta_{\mathrm{jet}}| < 0.5$ and full azimuth). The response to probes in the momentum range $60 < p_{\mathrm{T}} < 100$ GeV/c is studied.

After matching the reconstructed jets from the events with the embedded probe to the embedded high p_{T} probe. The difference between the background subtracted reconstructed jet and the embedded probe is the background fluctuation δp_{T}:

$$\delta p_{\mathrm{T}} = p_{\mathrm{T,ch\,jet}}^{\mathrm{det}} - A^{\mathrm{jet,rec}} \cdot \rho_{\mathrm{ch}} - p_{\mathrm{T}}^{\mathrm{probe}}, \tag{7.6}$$

in which $p_{\mathrm{T,ch\,jet}}^{\mathrm{det}}$ is the transverse momentum of the reconstructed anti-k_{T} jet, $A^{\mathrm{jet,rec}}$ is the area of the reconstructed anti-k_{T} jet and $p_{\mathrm{T}}^{\mathrm{probe}}$ is the embedded transverse momentum of the probe.

When embedding simulated PYTHIA and quenched jets the constituents of these jets become important. Not all constituents of an embedded probe jet will be necessary found back in one reconstructed heavy-ion jet. In order relate the embedded probe and reconstructed jet a matching condition is used. The algorithm to connect a reconstructed jet with the embedded probe requires that

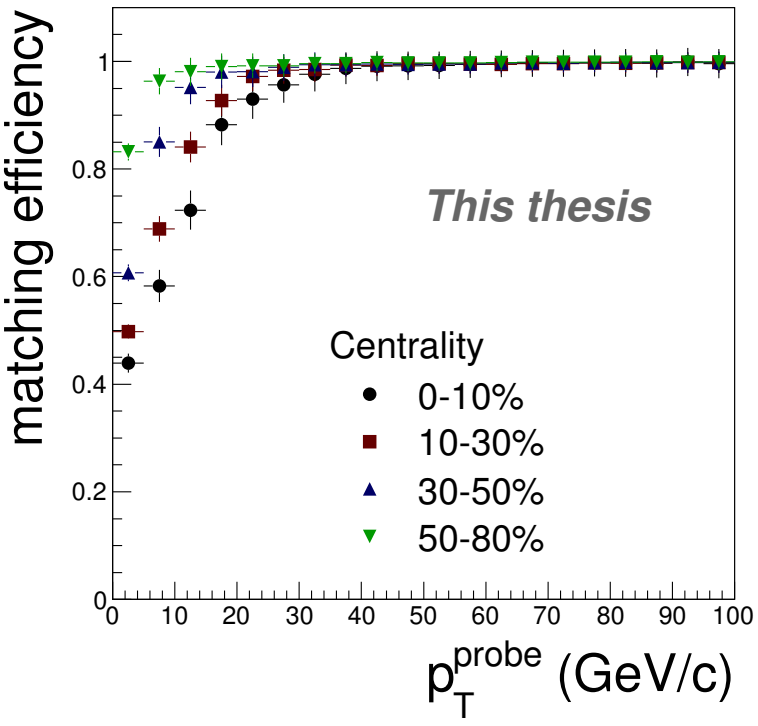

Figure 7.8: Matching efficiency of embedded PYTHIA jets in Pb–Pb events.

the reconstructed jet carries at least 50% of the originally embedded transverse momentum. In case of embedding single high p_T particles the p_T found back in a reconstructed jet is 100% by definition since each particle can only belong to one anti-k_T jet. Requiring at least half of the transverse momentum of the embedded probe jet in the reconstructed jet guarantees an unique matching. In case a reconstructed jet is paired to two or more embedded probe jets it is matched to the probe jet with highest p_T and the other probe jets are considered as lost. The matching efficiency as shown in Figure 7.8 for 0-10% central events is larger than 90% for $p_T^{probe} > 30$ GeV/c. For events with 30-100% centrality the matching efficiency is larger than 98% for $p_T^{probe} > 20$ GeV/c. For quenched jets produced with the Q-PYTHIA event generator no significant decrease of the matching efficiency is observed.

In Figure 7.9 the δp_T distribution of the background fluctuations obtained from embedding single high p_T particles and PYTHIA jets are compared to the background fluctuations obtained from random cones. The background fluctuations are extracted for three different minimum p_T values on the constituents of the reconstructed jets: $p_{T,track}^{min} > 0.15$ GeV/c, 1 GeV/c and 2 GeV/c. The single track embedding gives very similar results to the distributions obtained from random cones. Due to the jet area resolution of the k_T and anti-k_T jet finder the width of the distribution is slightly wider: 11.19 ± 0.01 GeV/c for single track

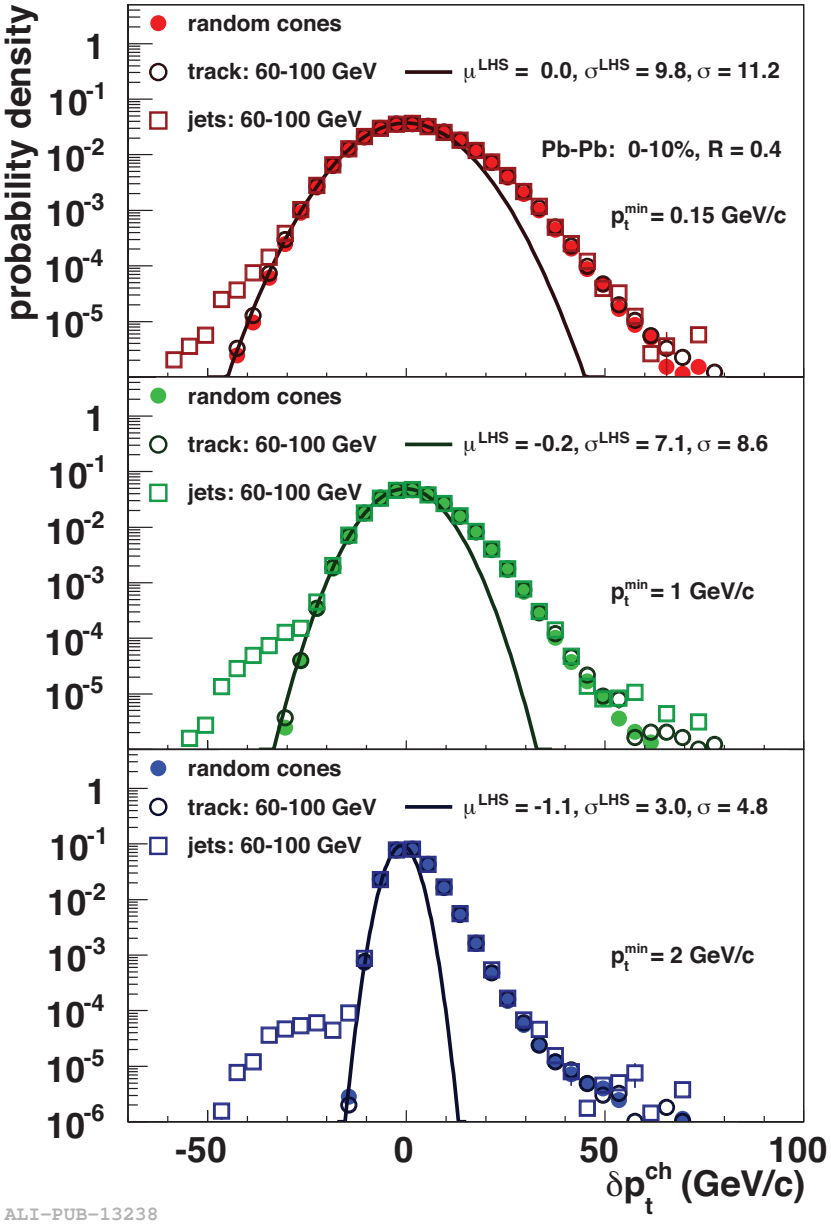

Figure 7.9: Width of δp_{T}distributions from three different type of probes (random cones and embedded high p_{T} particles and PYTHIA jets) with radius $R = 0.4$ for 10% most central Pb–Pb events. The three panels show the fluctuations for $p_{\mathrm{T,track}}^{\mathrm{min}} > 0.15$ GeV/c, 1 GeV/c and 2 GeV/c. See also [95].

embedding and 10.98 ± 0.01 GeV/c for random cones for $p_{\mathrm{T,track}}^{\mathrm{min}} > 0.15$ GeV/c. The width obtained from single track embedding reduces when the ghost area is reduced, reaching a lower limit which is expected to be very close to the width of the random cones for infinitely small ghost area.

The width of the δp_{T} distribution obtained from embedding jets is 11.34 ± 0.02 GeV/c, see Table 7.2, which is $\sim$ 150 MeV/c larger than the width obtained

	σ (GeV/c)	σ^{LHS} (GeV/c)	μ^{LHS} (GeV/c)
$p_{\mathrm{T}}^{\mathrm{min}} = 0.15$ GeV/c			
random cones	10.98 ± 0.01	9.65 ± 0.02	-0.04 ± 0.03
track emb.	11.19 ± 0.01	9.80 ± 0.02	0.00 ± 0.03
jet emb.	11.34 ± 0.02	9.93 ± 0.06	0.06 ± 0.09
$p_{\mathrm{T}}^{\mathrm{min}} = 1$ GeV/c			
random cones	8.50 ± 0.01	7.08 ± 0.01	-0.22 ± 0.02
track emb.	8.61 ± 0.01	7.11 ± 0.01	-0.25 ± 0.02
jet emb.	8.78 ± 0.02	7.25 ± 0.04	-0.08 ± 0.08
$p_{\mathrm{T}}^{\mathrm{min}} = 2$ GeV/c			
random cones	4.82 ± 0.01	3.41 ± 0.01	-0.01 ± 0.01
track emb.	4.88 ± 0.01	3.05 ± 0.01	-0.92 ± 0.01
jet emb.	5.03 ± 0.01	3.52 ± 0.01	0.01 ± 0.02

Table 7.2: Background fluctuations in central events as obtained from different types of probes for the three $p_{\mathrm{T,track}}^{\mathrm{min}}$-cuts. Comparison of the Gaussian fit to the left-hand-side of the δp_{T}-distributions and the standard deviation in central Pb–Pb collisions. The quoted uncertainties are purely statistical. See also [95].

from embedding single particles. In the δp_{T} distribution an enhancement of large negative fluctuations is observed in case of jet embedding. This structure is caused by probe jets with large area (A^{probe}) which are reconstructed with the anti-k_{T} jet finder in case two high p_{T} particles at a distance $\sim R$ are present in the event. The cones around the two seeds are merged resulting in a final jet with an area larger than the typical area of πR^2 [87]. These large area pp jets occasionally split in a heavy-ion environment resulting in two similar reconstructed jets with a reduced area ($A^{\mathrm{rec}} \approx 0.3$–$0.5$) and a large shift $\Delta d \approx 0.2$ of the jet axis. This feature gets more pronounced if the minimum p_{T} of the jet constituents is increased because the rate at which the jet splitting happens does not depend on the soft particle multiplicity while the common background fluctuations decrease if the multiplicity is reduced.

Response to Low p_{T} Probes

The response of low p_{T} probes to the heavy-ion environment is studied by investigating the response of embedded single particles with $p_{\mathrm{T}} < 20$ GeV/c. Embedding a high p_{T} probe changes the way a heavy-ion event is clustered with the anti-k_{T} jet algorithm. The high p_{T} probe will function as a seed moving all background clusters to a different position. In case a very low p_{T} probe is

embedded the structure of the event is unmodified and will not influence the jet clustering. The low p_{T} probe will be matched to the cluster where it is geometrically placed in. Many of these clusters are background clusters with smaller area than the typical area for a high p_{T} signal [100]. Figure 7.10 shows the correlation between δp_{T} and the reconstructed jet area for 4 different embedded p_{T} ranges in central Pb–Pb events. The average width of the δp_{T} distribution for low p_{T} probes, $p_{\mathrm{T}} < 10$ GeV/c, is narrower than for the high p_{T} probes. For probes with transverse momenta larger than 10 GeV/c the width of the background fluctuations has been found to be constant. Small area jets with small background fluctuations exist also in heavy-ion events. These jets, however, do not originate from a hard process and can be rejected by requiring a minimum area for the considered jets.

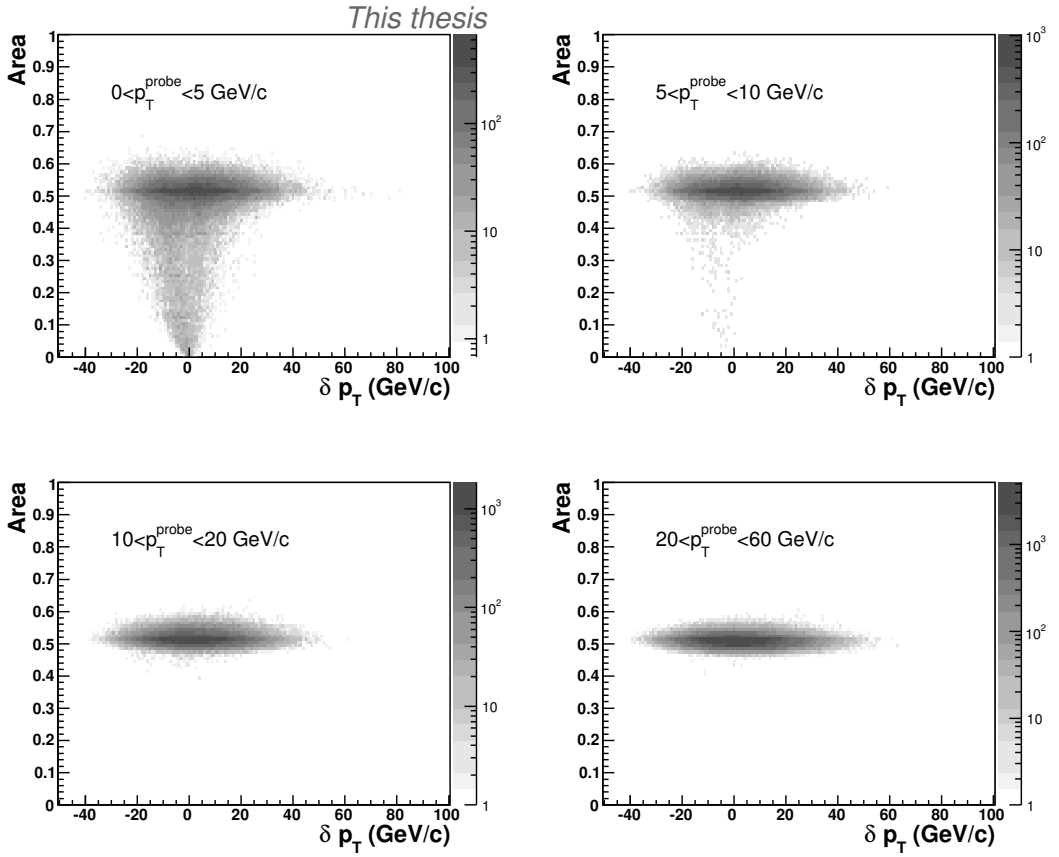

Figure 7.10: Correlation between the reconstructed jet area and δp_{T} for single embedded particles reconstructed with anti-k_{T} jet finder with radius $R = 0.4$ for 10% most central Pb–Pb events. The panels show the correlation for different embedded p_{T} ranges.

7.2.4 Impact on Jet Spectrum

In this section the impact of background fluctuations on the reconstructed jet energy is discussed. In order to quantify how large the effect of background fluctuations is on a steeply falling spectrum, a distribution with a power law shape, $f(p_{\mathrm{T}}) = 0.7/(0.7 + p_{\mathrm{T}}^5)$, is smeared with the measured background fluctuations. The power law spectrum is folded with the background fluctuations corresponding to jets with resolution parameter $R = 0.4$ in central events for a minimum p_{T}-cut on the constituents of 0.15 GeV/c and 2 GeV/c. Since a *true* jet spectrum at low p_{T} in heavy-ion collisions is not meaningful due to the finite size of jets and number of particles, the power law spectrum is only considered for $p_{\mathrm{T}} > 4$ GeV/c. In addition, the jet spectrum is not well described by a power law at low p_{T}. The δp_{T} distribution gives the probability that the p_{T} of a true jet is smeared by δp_{T}.

The result of this folding exercise is reported in Table 7.3 as the yield increase relative to the yield of the unsmeared spectrum in a high p_{T} bin ($60 < p_{\mathrm{T}} < 68$ GeV/c). For the lower $p_{\mathrm{T}}^{\mathrm{min}}$ cut corresponding to $\sigma(\delta p_{\mathrm{T}}) \approx 11$ GeV/c a relative increase of a factor 10 is observed. In case of a 2 GeV/c cut on the constituents the background fluctuations are narrower, $\sigma(\delta p_{\mathrm{T}}) \approx 5$ GeV/c and a milder relative increase of the jet yield is observed: 1.3–1.6. The variations of the δp_{T} distributions from the different studied probes have an effect on the folded spectrum which is smaller than the statistical uncertainty. The finite probability for upward fluctuations have a large impact on the increase of the jet yield. For comparison, in Table 7.3 the increase of the jet yield with a Gaussian smearing of the jet energy is also reported. The two widths of the applied Gaussian smearings are equal to the widths of the considered δp_{T} distributions with as the main difference that the Gaussian distribution does not have a high p_{T} tail. It is found that the impact of the asymmetric δp_{T} smearing on a steeply falling spectrum is many times larger than for a symmetric Gaussian smearing: a factor 10 versus a factor 1.8.

7.2.5 Summary Background Fluctuations

In this section the main points regarding background fluctuations on the reconstructed jet energy in heavy-ion collisions are summarized. Background fluctuations have a large impact on the measured jet spectrum due to the finite probability for positive fluctuations. The asymmetric shape of the δp_{T} distributions with a tail to positive fluctuations can not be ignored since it causes a very large increase of the measured yield on a steeply falling spectrum. The width of the background fluctuations depends strongly on the multiplicity of the soft particles originating from the bulk below the jet cone. As a result, consequently the magnitude of the background fluctuations depends on centrality, minimum p_{T} of the jet constituents and also collective region-to-region effects like flow. Only a minor dependence on the fragmentation pattern for the background fluctuations

$f(p_{\mathrm{T}})$ folded with	relative yield for $p_{\mathrm{T}} = 60$–$68\,\mathrm{GeV}/c$		
δp_{T}	random cones	tracks	jets
$p_{\mathrm{T}}^{\mathrm{min}} = 0.15\,\mathrm{GeV}/c$	9.8 ± 1.7	11.4 ± 1.1	10.9 ± 3.4
$p_{\mathrm{T}}^{\mathrm{min}} = 2\,\mathrm{GeV}/c$	1.30 ± 0.02	1.31 ± 0.02	1.65 ± 0.25
Gauss			
$\sigma = 11\,\mathrm{GeV}/c$	1.82 ± 0.04		
$\sigma = 5\,\mathrm{GeV}/c$	1.05 ± 0.01		

Table 7.3: Yield modification for power law spectrum. Relative to true yield in the bin $p_{\mathrm{T}} = 60$–$68\,\mathrm{GeV}/c$ for a power law spectrum ($f(p_{\mathrm{T}}) = 0.7/(0.7 + p_{\mathrm{T}}^5)$ and $p_{\mathrm{T}} > 4\,\mathrm{GeV}/c$), folded with the different δp_{T} distributions for 0-10% centrality and with a Gaussian, where the width is similar to the standard deviation of the δp_{T} distributions. See also [95].

is found. Background fluctuations are very specific for each experiment since the measured multiplicity is influenced by the detector performance.

7.3 Combinatorial Jets

Jet algorithms cluster all particles in the event into candidate jets. In heavy-ion collisions the full η–φ acceptance is filled with particles created in the collisions but not all of them originate from a hard process. There will be candidate jets which consist of a random combination of background particles from the bulk: combinatorial jets. The distinction between jets originating from a hard parton and combinatorial jets is not a matter of first principles, and thus requires a pragmatic definition. At very high p_{T}, it is clear that all jet clusters originate from a parton fragmentation process, while at low and intermediate p_{T}, clusters can be formed that contain fragments from multiple partons or even from the hadronization of the soft matter. Combinatorial jets and background fluctuations are intimately related: very low energy jets, for example with a momentum below 5 GeV/c, are are also subject to background fluctuations and appear at relatively high p_{T} (well above 20 GeV/c). Such jets are mostly background energy, and thus background fluctuations give rise to combinatorial jets.

A large fraction of the combinatorial jets have a low jet p_{T} and on average a smaller area than signal jets. In the analysis combinatorial jets are removed by a minimum reconstructed jet p_{T} and area requirement. Combinatorial jets can be further excluded from the measurement by requiring a minimum p_{T} for the leading particle in the jet [101]. The leading particle requirement introduces a bias to harder fragmentation. Jets with a soft fragmentation pattern are removed from the sample when a high p_{T} leading particle is required. Jet spectra are

measured with and without requiring a leading particle in the jet. Remaining contamination of combinatorial jets in the signal sample is taken care of during unfolding as explained in Chapter 8.

7.4 Detector Effects

Detector effects affecting the jet energy scale and resolution are the charged particle tracking efficiency and the transverse momentum resolution. Of these two effects, the tracking efficiency is the dominant contributor to the jet energy scale. If a particle is not reconstructed it will not be part of the reconstructed jet en therefore the jet energy will be underestimated. The finite tracking p_{T} resolution has a small effect on the jet energy scale since the majority of the constituents of a jet are of moderate p_{T} where the tracks only suffer from a mild p_{T} smearing, see Chapter 5. Corrections on the jet energy scale are determined by extracting the jet energy resolution and jet finding efficiency in simulation.

7.4.1 Jet Reconstruction Performance

The jet performance is evaluated using Monte Carlo event generators in combination with the ALICE detector simulation. Jets are reconstructed before and after applying detector effects. This results in two jet samples: 'particle level' jets and 'detector level' jets. For each event the particle level jets are geometrically matched to the detector level jets. The matching algorithm matches the closest detector level jet to a particle level jet, ensuring there is no other particle level jet closer to the detector level jet. This guarantees a that every detector level jet is matched to a particle level jet. Particles level jets not matched to a detector level jets are considered lost resulting in a jet finding inefficiency, see Section 7.4.1 for more details.

Jet Energy Resolution

The jet energy resolution depends on the jet finder settings like the jet resolution parameter R and p_{T} requirements on the jet constituents. The jet energy resolution is extracted from PYTHIA simulations followed by detector simulation with GEANT. For detailed information about the used Monte Carlo data samples see Chapter 5. The conditions of the detector applied in the simulations are always anchored to the detector performance of a specific run period. All simulations used are official productions generated by the ALICE collaboration.

In Figure 7.11 the distribution of relative p_{T} residuals after applying detector effects, $(p^{\mathrm{det}}_{\mathrm{T,ch\ jet}} - p^{\mathrm{part}}_{\mathrm{T,ch\ jet}})/p^{\mathrm{part}}_{\mathrm{T,ch\ jet}}$, for three different bins of generated jet p_{T}, $p^{\mathrm{part}}_{\mathrm{T,ch\ jet}}$, is shown. As can be seen from the peak around zero, the most probable scenario is that the measured detector level p_{T} is very close to the jet p_{T} on particle level. The probability to reconstruct a lower p_{T} than on particle level is

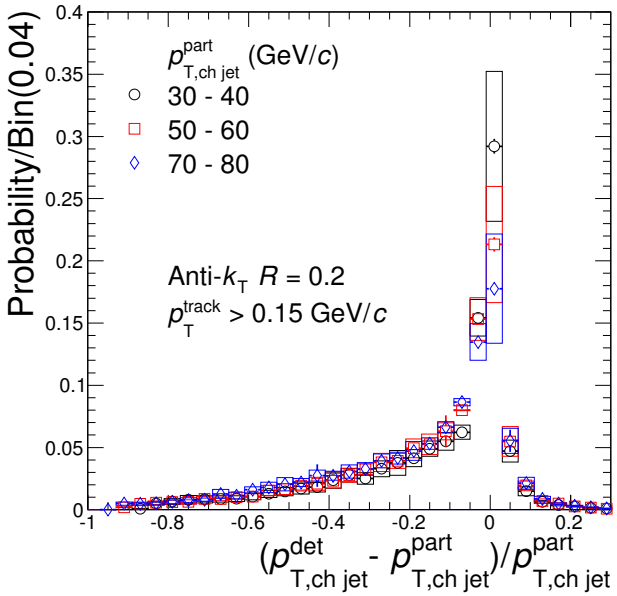

(a) Detector response for jets with resolution parameter $R = 0.2$

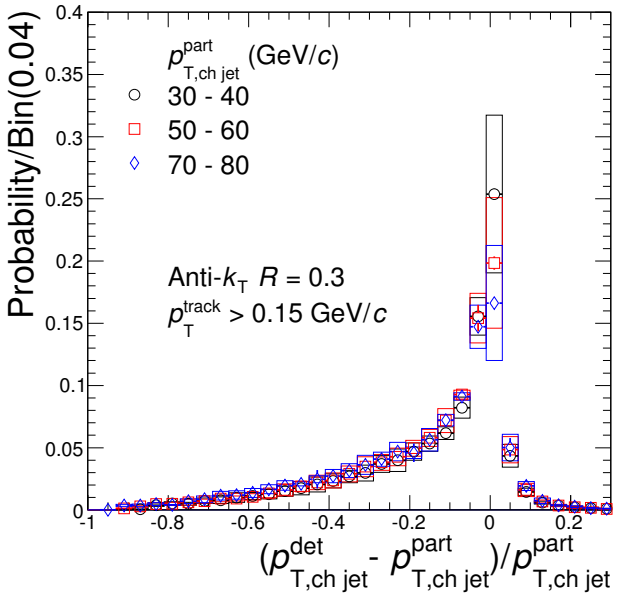

(b) Detector response for jets with resolution parameter $R = 0.3$

Figure 7.11: Simulated detector response for anti-k_T jets for three bins in generated jet p_T and two jet resolution parameters. Data points extracted from PYTHIA simulation in p_T hard bins with reduced tracking efficiency corresponding to the tracking efficiency in Pb–Pb multiplicity environment. The open boxes indicate the systematic uncertainty which is driven by the uncertainty on the tracking efficiency.

larger than a p_{T} smearing upwards. The 10-20% inefficiency in the charged particle reconstruction causes the detector level jet to have a lower momentum than the particle level jet, whereas momentum resolution effects and back-reaction can cause a detector level jet to have a higher momentum. The resulting smearing of the jet transverse momentum is strongly non-Gaussian, as can be observed in Figure 7.11.

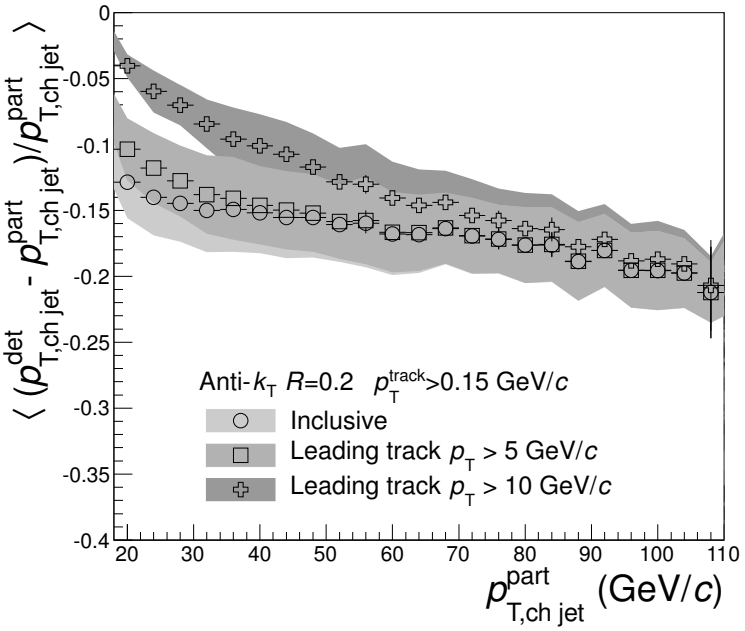

Figure 7.12: The mean of the jet response for charged jets with resolution parameter $R = 0.2$. Systematic uncertainty originates from uncertainty on tracking efficiency. Data points extracted from PYTHIA and full detector simulation in p_{T} hard bins. See text for details.

To characterize the detector response, the mean of the relative difference between $p_{\mathrm{T,ch\,jet}}^{\mathrm{det}}$ and $p_{\mathrm{T,ch\,jet}}^{\mathrm{part}}$ as a function of the jet momentum at particle level is shown in Figure **??**. A value of the mean which is close to zero, indicates that the jet p_{T}-resolution is very good. Without a leading track selection, the reconstructed jet momentum is on average ∼14–19% lower than the generated momentum, in the range $p_{\mathrm{T,ch\,jet}}^{\mathrm{part}} = 20 - 100$ GeV/c, with only a weak p_{T}-dependence. Jets with a larger radius have a slightly better p_{T}-resolution due to the larger average p_{T} of the jet constituents in the core of the jet. The mean of the jet response is also shown for jets selected by a 5 and 10 GeV/c leading track. If jets with a high p_{T} leading constituent are selected, the jet the resolution at low $p_{\mathrm{T}}^{\mathrm{jet}}$ improves because jets for which the leading track was not reconstructed are rejected from the sample. This results in a decrease of the jet finding efficiency which will be discussed in the next section. When jets with a high p_{T} leading track are selected the jet energy resolution evolves with p_{T}.

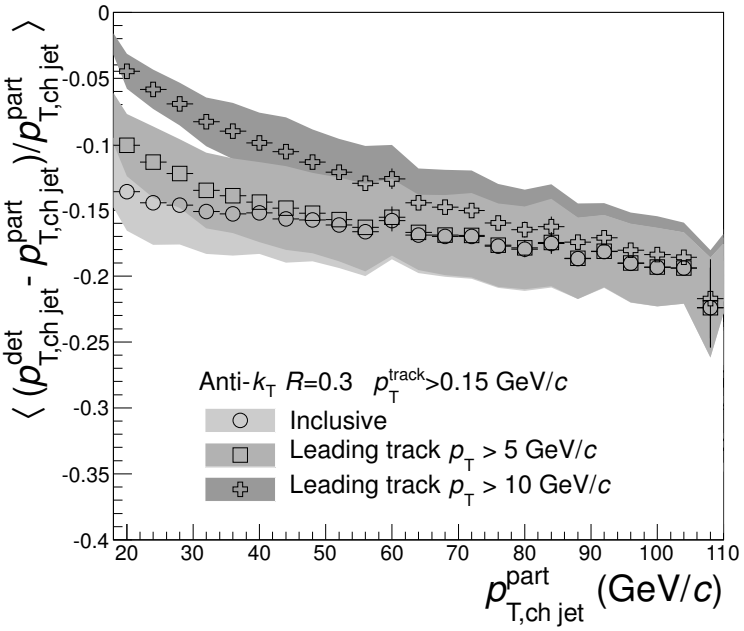

Figure 7.13: The mean of the jet response for charged jets with resolution parameter $R = 0.3$. Systematic uncertainty originates from uncertainty on tracking efficiency. Data points extracted from PYTHIA and full detector simulation in p_{T} hard bins. See text for details.

The total correction of detector effects is 10% on the jet transverse momentum which corresponds to a 40% correction on the jet yield assuming the jet spectrum scales with p_T^{-5}. The uncertainty on the tracking efficiency is estimated to be 4% motivated by the difference observed in PYTHIA and HIJING simulations, see Section 5.3. By varying the tracking efficiency in simulation with 4% two variations of the jet energy resolution are obtained. The extracted jet spectrum is corrected with the nominal jet energy resolution and compared to a corrected jet spectrum based on the jet energy resolution from the variation of the tracking efficiency. This results in a 3% uncertainty on the jet energy scale which is added to the systematic uncertainty of the jet spectrum measurement.

Jet Energy Scale

To further characterize the detector response to jets, the most probable value and the four quartiles of the distribution of the relative difference between $p_{\mathrm{T,ch\ jet}}^{\mathrm{part}}$ and $p_{\mathrm{T,ch\ jet}}^{\mathrm{det}}$ are shown as a function of $p_{\mathrm{T,ch\ jet}}^{\mathrm{det}}$ in Figures 7.14 and 7.15. The most probable value is determined by fitting a Gaussian function to the peak region, $-0.03 < (p_{\mathrm{T,ch\ jet}}^{\mathrm{det}} - p_{\mathrm{T,ch\ jet}}^{\mathrm{part}})/p_{\mathrm{T,ch\ jet}}^{\mathrm{part}} < 0.03$, of the jet response and reporting the mean of the fit. The most probable value of the detector level p_{T} is within 0.5% of $p_{\mathrm{T,ch\ jet}}^{\mathrm{part}}$ over the full p_{T} range.

Figures 7.14 and 7.15 also show the boundaries at 25%, 50% or 75% of the re-

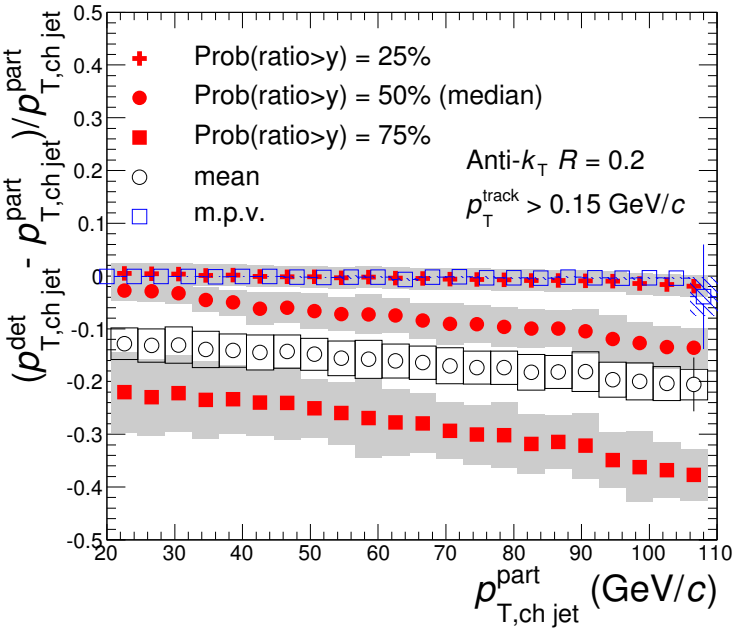

Figure 7.14: Integrated percentiles jet response, mean and most probable value for $R = 0.2$. Systematic uncertainties drawn as boxes around data points originate from uncertainty on tracking efficiency.

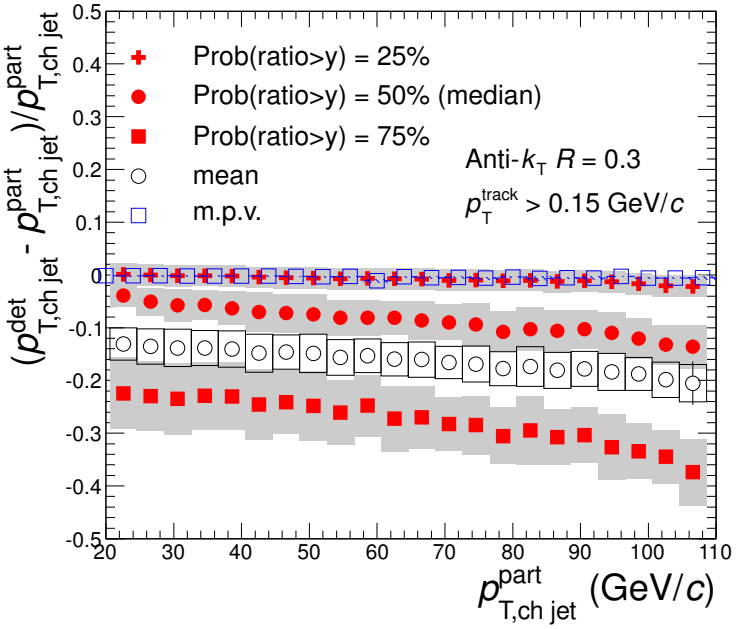

Figure 7.15: Integrated percentiles jet response, mean and most probable value for $R = 0.3$. Systematic uncertainties drawn as boxes around data points originate from uncertainty on tracking efficiency.

sponse distribution, integrating from the right $p_{\mathrm{T,ch\ jet}}^{\mathrm{det}} \to \infty$. Approximately 25% of the detector level jets has a larger jet momentum than the corresponding particle level jet, due to momentum resolution effects. The 50% percentile (median) correction is 5% at $p_{\mathrm{T,ch\ jet}}^{\mathrm{part}} = 20$ GeV/c and increases to 14% at $p_{\mathrm{T,ch\ jet}}^{\mathrm{part}} = 100$ GeV/c. For 75% of the jet population the correction for detector effects is smaller than 25% at low $p_{\mathrm{T}}^{\mathrm{jet}}$ and 40% at high $p_{\mathrm{T}}^{\mathrm{jet}}$.

Jet Finding Efficiency

The jet finding efficiency is defined as the ratio between the number of reconstructed matched jets and the number of particle level jets in the jet acceptance as function of the transverse momentum of the particle level jet $p_{\mathrm{T,ch\ jet}}^{\mathrm{part}}$:

$$\varepsilon_{\mathrm{jet}}(p_{\mathrm{T,ch\ jet}}^{\mathrm{part}}) = \frac{N_{\mathrm{matched}}}{N_{\mathrm{particle\ level}}^{|\eta_{\mathrm{gen}}|<0.5}}, \tag{7.7}$$

in which $N_{\mathrm{particle\ level}}^{|\eta_{\mathrm{gen}}|<0.5}$ is the total number of jets on generated particle level and N_{matched} refers to the particle level jets matched to a detector level jet. To

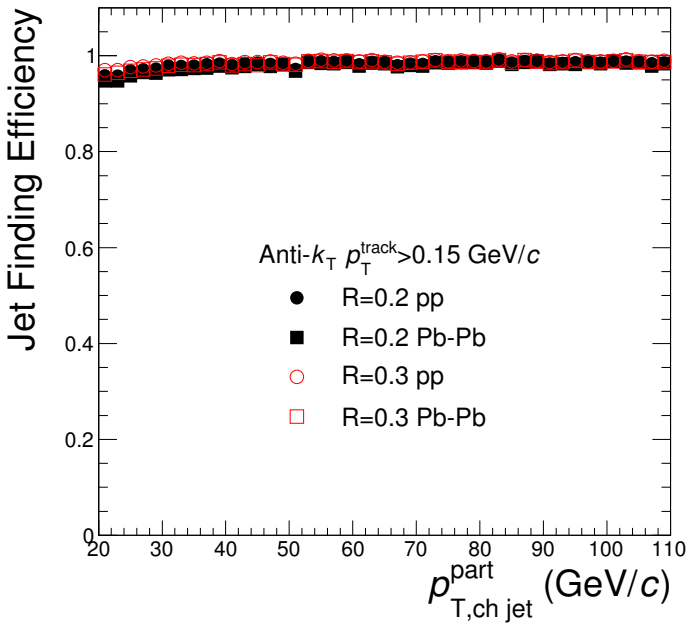

Figure 7.16: Jet finding efficiency for inclusive unbiased jets for pp and Pb–Pb reconstruction settings.

avoid an artificial decrease of the jet finding efficiency due to edge effects, in the definition of the jet finding efficiency only the generated jets are selected to be within the jet acceptance and no selection is applied on the reconstructed jets. This means that in case the reconstructed jet migrates outside acceptance, $|\eta_{\mathrm{rec}}| > 0.5$, it is not counted as lost.

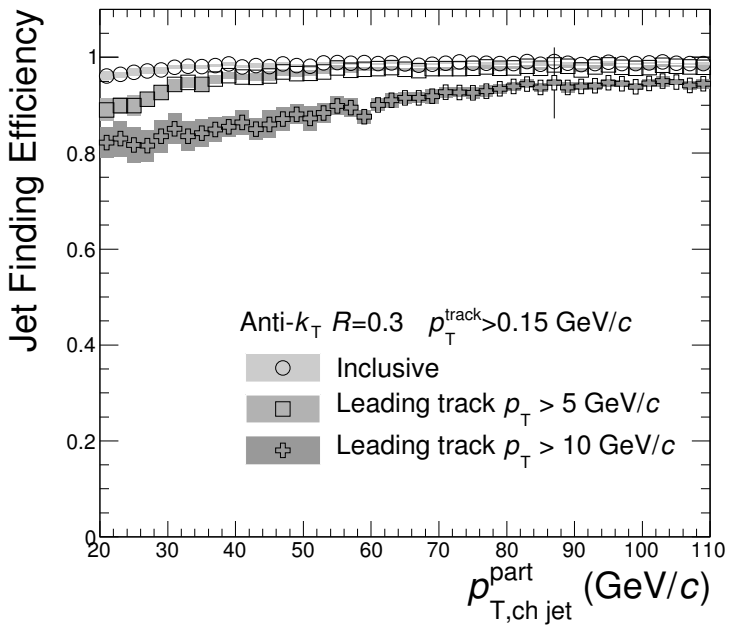

Figure 7.17: Jet finding efficiency for jets with radius parameters $R = 0.2$ and $R = 0.3$. Data points extracted from PYTHIA simulation in p_{T} hard bins with pp and Pb–Pb reconstruction settings. Systematic uncertainties drawn as boxes around data points in the right panel originate from uncertainty on tracking efficiency.

The jet finding efficiency for jets with resolution parameters $R = 0.2$ and $R = 0.3$ is fully efficient at high $p_{\mathrm{T}}^{\mathrm{jet}}$ and reduces to 95% at $p_{\mathrm{T,ch\ jet}}^{\mathrm{part}} = 20$ GeV/c, see Figure **????**. At low p_{T} the jet finding efficiency is reduced due to migration outside the jet η acceptance to an efficiency of ~ 0.9 at $p_{\mathrm{T,ch\ jet}}^{\mathrm{part}} = 10$ GeV/c. The jet finding efficiency for jets with radii of $R = 0.2$ and $R = 0.3$ differs a few percent at low p_{T} and is the same at high p_{T}. In general the jet finding efficiency is higher in pp compared to Pb–Pb driven by the higher multiplicity environment in Pb–Pb collisions. When jets are selected by requiring a high p_{T} leading track the jet finding efficiency is reduced since jets of which the leading particle is not reconstructed due to tracking inefficiency are lost, see Figure **????**. With the leading track requirement the jet finding efficiency increases with p_{T} reaching an efficiency of 0.95 at $p_{\mathrm{T,ch\ jet}}^{\mathrm{part}} \approx 30$ GeV/c for $p_{\mathrm{T}}^{\mathrm{leading\ track}} > 5$ GeV/c and at $p_{\mathrm{T,ch\ jet}}^{\mathrm{part}} \approx 60$ GeV/c for $p_{\mathrm{T}}^{\mathrm{leading\ track}} > 10$ GeV/c.

8. Unfolding Pb–Pb Jet Spectra

8.1 Problem to solve

The measured jet spectrum in heavy-ion collisions is distorted by fluctuations of the estimated jet transverse momentum. The task that needs to be accomplished is to infer the true hard jet spectrum from the measured one. In the presence of large bin migrations this is done by deconvoluting the measured distribution back to the true distribution: this procedure is known as *unfolding* [102–104]. The transverse momentum of each true jet $p_{\mathrm{T,ch\ jet}}^{\mathrm{part}}$ fluctuates to a different reconstructed value $p_{\mathrm{T,ch\ jet}}^{\mathrm{det}}$ due to background fluctuations and detector effects, as discussed in Chapter 7. The relation between the true and measured jet spectrum is given by:

$$M(p_{\mathrm{T,ch\ jet}}^{\mathrm{det}}) = \int \mathrm{d}p_{\mathrm{T,ch\ jet}}^{\mathrm{part}}\, G(p_{\mathrm{T,ch\ jet}}^{\mathrm{det}}, p_{\mathrm{T,ch\ jet}}^{\mathrm{part}})\, T(p_{\mathrm{T,ch\ jet}}^{\mathrm{part}})\, \varepsilon(p_{\mathrm{T,ch\ jet}}^{\mathrm{part}}), \tag{8.1}$$

in which $M(p_{\mathrm{T,ch\ jet}}^{\mathrm{det}})$ is the measured jet spectrum, $T(p_{\mathrm{T,ch\ jet}}^{\mathrm{part}})$ is the true jet spectrum, $\varepsilon(p_{\mathrm{T,ch\ jet}}^{\mathrm{part}})$ is the jet finding efficiency, and $G(p_{\mathrm{T,ch\ jet}}^{\mathrm{det}}, p_{\mathrm{T,ch\ jet}}^{\mathrm{part}})$ is the response function which encodes the effect of the fluctuating heavy-ion background and detector effects on the measured jet transverse momentum $p_{\mathrm{T,ch\ jet}}^{\mathrm{part}}$. It is assumed that the number of jets is conserved: each measured jet corresponds to a true jet. As discussed in section 7.2.3 the response to background fluctuations also depends on the area of the reconstructed jet. The area dependence can be included to Equation 8.1:

$$M(p_{\mathrm{T,ch\ jet}}^{\mathrm{det}}) = \int_0^{\infty} \mathrm{d}p_{\mathrm{T,ch\ jet}}^{\mathrm{part}} \int_{A_{\mathrm{C}}}^{A_{\mathrm{L}}} \mathrm{d}A_{\mathrm{S}}\, G(p_{\mathrm{T,ch\ jet}}^{\mathrm{det}}, p_{\mathrm{T,ch\ jet}}^{\mathrm{part}}, A_{\mathrm{B}}, A_{\mathrm{S}})\, T(p_{\mathrm{T,ch\ jet}}^{\mathrm{part}})\, \varepsilon(p_{\mathrm{T,ch\ jet}}^{\mathrm{part}}) \tag{8.2}$$

in which A_{S} and A_{B} are the area of the signal jet and the background. A_{C} is a low area cut–off discussed in Section 7.1 and A_{L} some large suitable cut-off area.

In practice the integral equation, Equation 8.1, is solved numerically by representing the spectra as histograms and the response function as a matrix:

$$\boldsymbol{M}_m = \boldsymbol{G}_{m,t} \cdot \boldsymbol{T}'_t \tag{8.3}$$

in which $\boldsymbol{T}'_t$ is the jet spectrum corrected for the p_{T} smearing. The true jet

spectrum is obtained by correcting for the jet finding efficiency: $\boldsymbol{T}_t = \boldsymbol{T}'_t \cdot \mathbf{1}/\boldsymbol{\varepsilon}_t$. $\boldsymbol{G}_{m,t}$ is the response matrix and $\boldsymbol{M}_m$ the binned measured jet spectrum.

8.2 Caveats

8.2.1 Acceptance

All particles in every event will always be clustered while only a maximum number of jets fits into the acceptance: $N_{\text{jets}}^{\text{max}} \approx \text{acceptance}/A$ in which A is the area of a jet. Due to this acceptance effect the assumption that the measured spectrum is a pp jet spectrum smeared with background fluctuations in Equation 8.1 cannot be correct at low transverse momenta.

8.2.2 δ-Function Solution

The measured jet spectrum and the δp_{T}-distribution have a very similar width and shape, see Figure 8.1, which makes unfolding particularly challenging. A δ-function at $p_{\text{T}} = 0$ GeV/c is a mathematically correct solution to the problem but not physical. This solution will need to be rejected by the unfolding algorithm which is described in section 6.4.

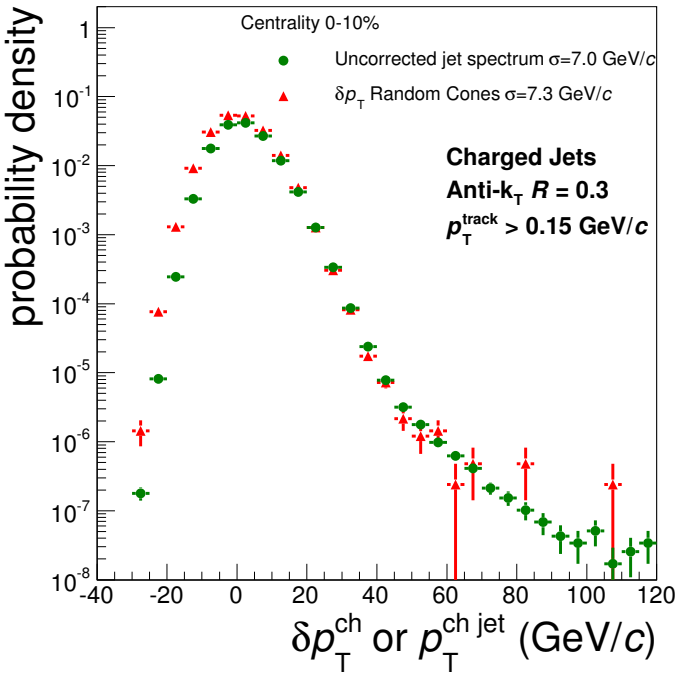

Figure 8.1: Shape comparison of uncorrected jet spectrum and δp_{T}-distribution from random cones. The uncorrected jet spectrum is normalized at $p_{\text{T}}^{\text{jet}} = 20$ GeV/c to the δp_{T}-distribution.

8.2.3 Combinatorial Jets

In heavy-ion collisions the full η–φ acceptance is filled with particles which are all clustered into jets by the jet algorithm. Not all of these jet candidates originate from a hard process. The distinction between jets originating from a hard parton and soft background containing mostly low momentum particles (*combinatorial jets*) requires a pragmatic definition. At very high p_{T}, it is clear that all jet clusters originate from a fragmentation process of a hard parton, while at low and intermediate p_{T}, clusters can be formed that contain fragments from multiple partons or from the hadronization of the soft matter.

Even jet clusters which originate from a hard scattering will contain a large amount of uncorrelated, mostly soft, background particles. The soft background is subtracted on an average basis even-by-event, but has large region-to-region fluctuations, see section 7.2. Also combinatorial jets appear at relatively high p_{T} (well above 20 GeV/c) since they are also subject to background fluctuations.

The contamination of combinatorial jets in the jet spectrum can be reduced by selecting jets with a high p_{T} leading track. Figure 8.2 shows the uncorrected jet spectra for different leading track selections. The jet yield is reduced at low jet p_{T} when a higher leading track p_{T} is required. In addition to combinatorial jet rejection, also jets with a soft fragmentation pattern are removed by the leading high p_{T} track selection.

The contribution of combinatorial jets is studied with respect to the jet spectrum with a 12 GeV/c leading track requirement. All jets containing such a high p_{T} leading track can be considered as true hard jets. In Figure 8.3 the increase of the number of reconstructed jets with radius $R = 0.3$ when the p_{T} of the leading track requirement is reduced is shown. The solid markers show the ratio of the $p_{\mathrm{T,ch\,jet}}^{\mathrm{det}}$ integrated Pb–Pb jet spectra from Figure **??** for three different minimum $p_{\mathrm{T,ch\,jet}}^{\mathrm{det}}$. For all minimum jet p_{T} the ratio becomes constant for $p_{\mathrm{T}}^{\text{leading track}} < 3$ GeV/c indicating that all jets in this region are dominated by combinatorial jets. The Pb–Pb data points in Figure 8.3 are compared to the effect of the fragmentation bias in PYTHIA represented by the lines passing through the open markers. It has to be noted that the jet p_{T} scale of Pb–Pb data is uncorrected while for the PYTHIA spectrum the true generated jet p_{T} is used. Feed-in and feed-out around the minimum reported jet p_{T} is expected for both the denominator and numerator. For $p_{\mathrm{T,ch\,jet}}^{\mathrm{det}} > 30$ GeV/c the difference between vacuum fragmentation and Pb–Pb data for $p_{\mathrm{T}}^{\text{leading track}} \leq 2$ GeV/c is a factor ~ 3.5 while for leading track selection with 5 GeV/c tracks this factor is reduced to ~ 1.6. In case the minimum jet p_{T} is increased the difference between PYTHIA and data becomes smaller since at higher jet p_{T} there are less combinatorial jets. For $p_{\mathrm{T}}^{\mathrm{jet}} > 40$ GeV/c the difference between the Pb–Pb and PYTHIA ratio is ~ 1.3 for the lowest leading track p_{T} selection. Almost no combinatorial jets are observed for $p_{\mathrm{T}}^{\mathrm{jet}} > 50$ GeV/c.

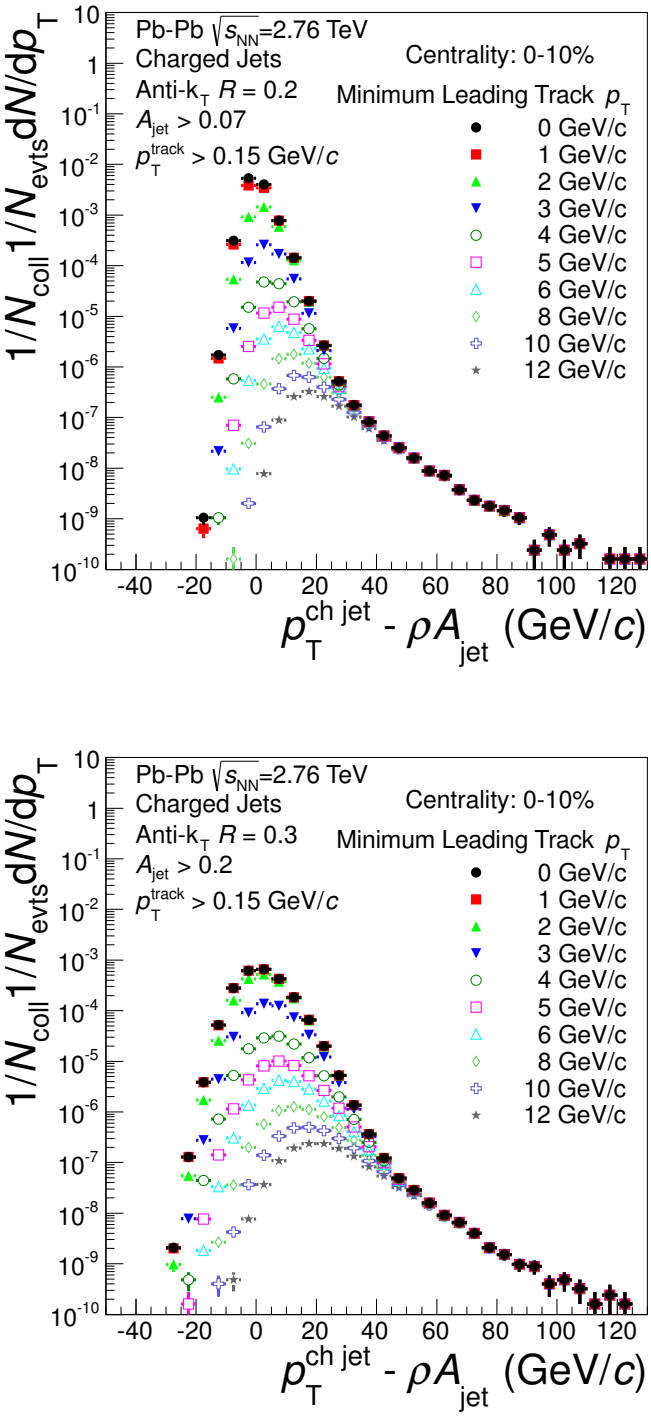

Figure 8.2: Uncorrected jet spectrum for 10% most central events reconstructed from charged particles with resolution parameters $R = 0.2$ and $R = 0.3$ and $p_{\mathrm{T}}^{\mathrm{min}} = 150$ MeV/c. Jet spectra are shown for different leading track triggers.

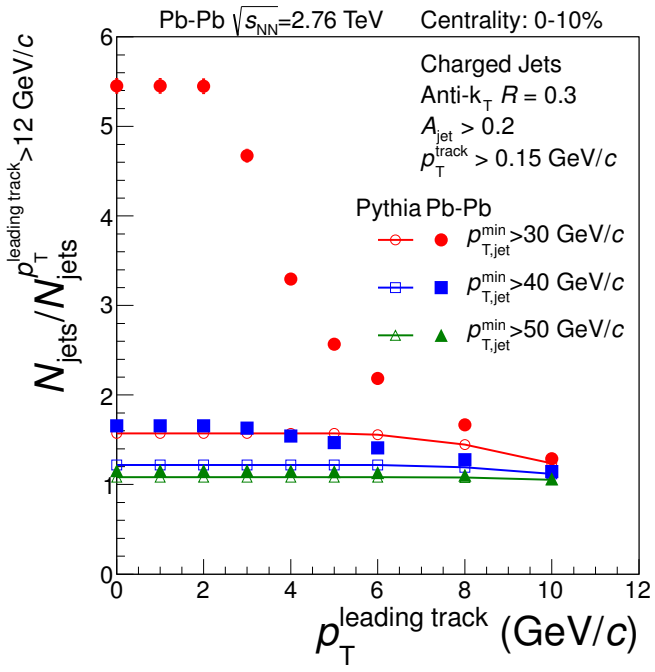

Figure 8.3: Increase of number of reconstructed jets with respect to the jet sample with a leading track of at least 12 GeV/c as function of leading track p_{T} requirement and low momentum cut-off on jet spectrum. Solid marker represent values determined from Pb–Pb jet spectra in central collisions. Open markers and lines correspond to vacuum fragmentation without soft heavy-ion background extracted from PYTHIA.

8.3 Unfolding Method

The jet spectra are unfolded with the χ^2 minimization method, see section 6.4.1. For the penalty term in Equation 6.11 which regularizes the unfolded solution a local power law is used resulting in the following χ^2 function:

$$\chi^2 = \sum_{\text{refolded}} \left(\frac{y_{\text{refolded}} - y_{\text{measured}}}{\sigma_{\text{measured}}} \right)^2 + \beta \sum_{\text{unfolded}} \left(\frac{\mathrm{d}^2 \log y_{\text{unfolded}}}{\mathrm{d} \log p_{\mathrm{T}}^2} \right)^2, \qquad (8.4)$$

in which y is the yield of the refolded, measured, or unfolded jet spectrum and σ_{measured} the statistical uncertainty on the measured jet spectrum. The first summation term of Equation 8.4 is the χ^2 between the refolded spectrum and the measured jet spectrum and will be referred to as χ^2_{fit}. The second summation term in Equation 8.4 regularizes the unfolded solution favoring a local power law which is calculated using finite differences.

As a prior the measured spectrum is used. The final corrected spectrum is y_{unfolded} from Equation 8.4 divided by the jet finding efficiency.

8.3.1 Optimization of Regularization Parameter

Without regularization the unfolded solution fluctuates heavily resulting in a non-physical shape of the spectrum. If the regularization is very strong the unfolded spectrum is too steep at low p_{T} and too flat at high p_{T}. The correct solution lies somewhere in between these two extreme regimes. The range of β with heavily fluctuating solutions is not considered. If β is too large the penalty term dominates and the refolded distribution deviates from the measured spectrum giving a large χ^2_{fit}. To prevent an over-regularized solution it is required that the penalty term is much smaller than χ^2_{fit}. In addition, when the unfolding is over-constrained, strong correlations between bins are present which are visible in the Pearson coefficients. The Pearson coefficients are obtained from the covariance matrix of the unfolded solution:

$$\rho(x, y) = \frac{\mathrm{cov}(x, y)}{\sigma_x \sigma_y} \tag{8.5}$$

8.4 Unfolding Ranges

8.4.1 Transverse Momentum Range to optimize

The measured spectrum is used between a minimum p_{T}, $p_{\mathrm{T}}^{\mathrm{min,meas}}$, and a maximum p_{T}, $p_{\mathrm{T}}^{\mathrm{max,meas}}$, which is given by the available statistics. The minimum p_{T} cut-off is introduced to suppress jet candidates which are dominated by background fluctuations or are purely combinatorial. The minimum p_{T} cut on the measured spectrum is typically $5\sigma(\delta p_{\mathrm{T}})$ in which $\sigma(\delta p_{\mathrm{T}})$ is the width of the δp_{T}-distribution. The optimal value of the minimum p_{T} cut-off has been studied in a model in which a PYTHIA jet spectrum is folded with the measured background fluctuations and with a heavy-ion background Monte Carlo model, see section 8.7. χ^2_{fit} is calculated between the minimum and maximum p_{T} range of the measured spectrum.

8.4.2 Transverse Momentum Range of Unfolded

The unfolded spectrum has bins below the minimum p_{T} cut-off of the measured spectrum to allow feed-in from $p_{\mathrm{T}} < p_{\mathrm{T}}^{\mathrm{min,meas}}$ into the region where the χ^2 is minimized. This is a significant effect since the spectrum falls steeply with $p_{\mathrm{T}}^{\mathrm{jet}}$. Feed-in from larger transverse momenta than the maximum measured momentum is also allowed by extending the reach of the unfolded spectrum to $p_{\mathrm{T}} = 250$ GeV/c.

The unfolding will break down if the fit gets too much freedom which is when the number of fit parameters, i.e. number of bins in the unfolded spectrum, is of the similar to or larger than the number of bins in the measurement.

In figure 8.4 the different p_{T} ranges for the measured and unfolded spectrum are illustrated. The unfolded spectrum has three bins below $p_{\mathrm{T}}^{\mathrm{min,meas}}$. In this

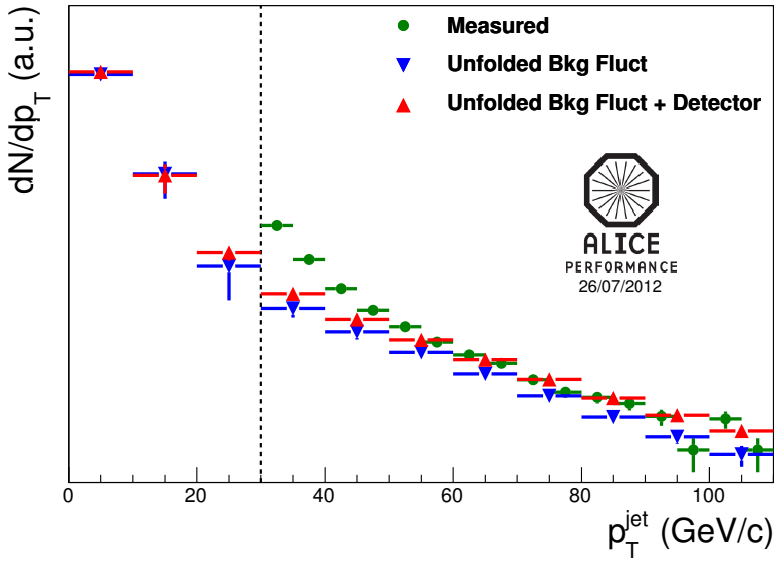

Figure 8.4: Unfolded spectra after correction for background fluctuations and the combined correction for background fluctuations and detector effects are shown. The dotted vertical line at $p_{\mathrm{T}} = 30$ GeV/c indicates the minimum p_{T} cut-off of the measured spectrum.

procedure, the combinatorial jets will emerge at (very) low p_{T}, while the spectrum is only reported above the p_{T} cut-off, thus effectively removing the combinatorial jets from the result. The extra bins allowing for feed-in from higher p_{T} are not shown in this figure.

8.5 Response Matrix

The response matrix incorporates the smearing of the jet p_{T} caused by detector effects and background fluctuations. Both effects are discussed in Chapter 7. The true jet spectrum $\boldsymbol{T}_t$ is distorted by the response of the detector effects $\boldsymbol{G}_{d,t}$ resulting in a jet spectrum $\boldsymbol{D}_d$:

$$\boldsymbol{D}_d = \boldsymbol{G}_{d,t} \cdot \boldsymbol{T}_t, \tag{8.6}$$

in which $\boldsymbol{T}_t$[1] is the true jet spectrum and $\boldsymbol{D}_d$ is the jet spectrum smeared by detector effects. In addition to the detector effects in heavy-ion collisions the background fluctuations are another source of p_{T} smearing. The largest effect of this smearing are low p_{T} clusters on top of upward fluctuations resulting in a high momentum jet in the measurement. Upward fluctuations are more likely than downward fluctuations due to the asymmetric high p_{T} tail of the δp_{T}-distribution. The measured spectrum can be written as

$$\boldsymbol{M}_m = \boldsymbol{G}_{m,d} \cdot \boldsymbol{D}_d, \tag{8.7}$$

[1]The jet finding efficiency is left out from the equations in this section.

in which $\boldsymbol{M}_m$ is the measured jet spectrum and $\boldsymbol{G}_{m,d}$ contains the smearing of background fluctuations.

Combining equations 8.6 and 8.7 leads to:

$$\boldsymbol{M}_m = \boldsymbol{G}_{m,d} \cdot \boldsymbol{G}_{d,t} \cdot \boldsymbol{T}_t = \boldsymbol{G}_{m,t} \cdot \boldsymbol{T}_t, \tag{8.8}$$

where $\boldsymbol{G}_{m,t}$ is the combined response matrix of background fluctuations and detector effects. A corrected jet spectrum can be obtained by performing a two-step correction procedure or by using the combined response matrix $\boldsymbol{G}_{m,t}$. Unfolding is used to obtain the true jet spectrum by solving Equation 8.8.

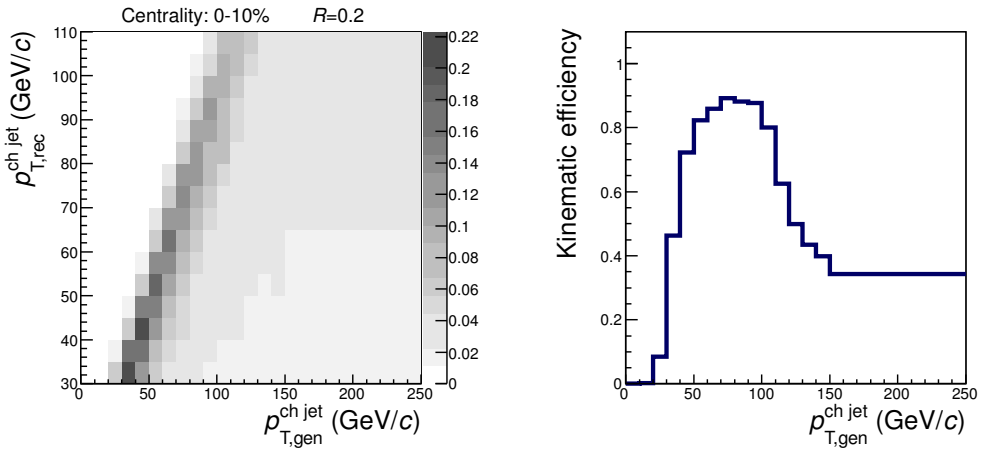

(a) Left panel: Combined response matrix $\boldsymbol{G}_{m,t}$ for $R = 0.2$ and centrality 0–10%. Right panel: Kinematic efficiency indicating which fraction of the yield is moved inside the selected window in $p_{\mathrm{T,ch\ jet}}^{\mathrm{det}}$ due to detector response and background fluctuations.

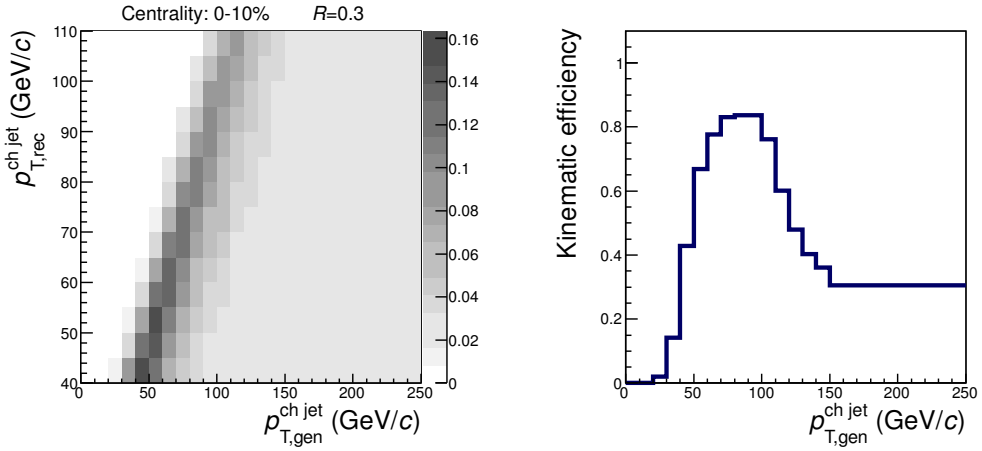

(b) Left panel: Combined response matrix $\boldsymbol{G}_{m,t}$ for $R = 0.3$ and centrality 0–10%. Right panel: Kinematic efficiency indicating which fraction of the yield is moved inside the selected window in $p_{\mathrm{T,ch\ jet}}^{\mathrm{det}}$ due to detector response and background fluctuations.

Figure 8.5: Response matrices and kinematic efficiencies for central collisions.

For the response matrix of background fluctuations $\boldsymbol{G}_{m,d}$ the δp_{T}-distributions of Figure 7.7(a) are used. Each slice in generated p_{T} of a two-dimensional response matrix with an arbitrarily fine binning is filled with the δp_{T} probability distribution. For high enough $p_{\mathrm{T,ch\ jet}}$ ($p_{\mathrm{T,ch\ jet}} > 10 - 20$ GeV/c) the δp_{T}-distribution does not vary with $p_{\mathrm{T,ch\ jet}}$. Since the measurement will not be done for jets with $p_{\mathrm{T}}^{\mathrm{jet}} < 20$ GeV/c the δp_{T}-distribution can be assumed to be constant over the full range of p_{T} for the measurement.

The correlation between the generated and measured jet p_{T} from detector effects is obtained from PYTHIA+GEANT simulations. Each slice in generated p_{T} (jet p_{T} on particle level) is normalized to a total probability of one. This gives the response matrix $\boldsymbol{G}_{d,t}$ with the p_{T} smearing from detector effects. This response matrix also has a fine binning with the dimensions $t \times d$ in which t and d are the same.

The two matrices $\boldsymbol{G}_{m,d}$ and $\boldsymbol{G}_{d,t}$ are multiplied to obtain the combined response matrix $\boldsymbol{G}_{m,t}$. The response matrix is rebinned to the coarse binning in which data is available. The statistics in the Pb–Pb data allows to measure the jet spectrum in bins with a width of 5 GeV/c. For accurate unfolding the bin width on the generated axis is twice as large (10 GeV/c). The generated axis of the response matrix defines the binning of the unfolded spectrum. It is ensured that the bin width of the unfolded spectrum is never smaller than the resolution. The coarse response matrix is obtained by merging slices of the fine response matrix. Each slice in generated p_{T} of the fine response matrix is weighted as function of a steeply falling spectrum. For this analysis a Tsallis function is used as weighting function:

$$f(p_{\mathrm{T}}) = p_{\mathrm{T}}(1 + \frac{1}{nT}p_{\mathrm{T}})^{-n}, \tag{8.9}$$

in which $n = 8$ and $T = 0.9$. This function describes the jet spectrum from PYTHIA simulation for $p_{\mathrm{T,ch\ jet}} < 120$ GeV/c. As long as a reasonable weighting function is used, the unfolded solution is not affected by this particular choice of weighting function. Without merging the narrow slices the resolution is underestimated. The combined response matrices for $R = 0.2$ and $R = 0.3$ jets in the 10% most central events are shown in the left panels of Figure 8.5. The p_{T}-axes of the response matrix are truncated according the p_{T} ranges chosen for the measurement, see section 8.4. Part of the yield for a given true jet p_{T} can be smeared to reconstructed p_{T} outside the p_{T}-reach of the response matrix. The fraction of jets which will be smeared outside the acceptance of the response matrix, is shown in the kinematic efficiency curve in the right panel of Figure 8.5 and is taken into account in the unfolding procedure. The generated p_{T}-axis of the response matrix reaches to higher p_{T} than the measurement to allow for feed-in into the measured p_{T} range.

8.6 Combined Jet Performance

Figure 8.6 shows the jet resolution in Pb–Pb collisions for the 0–10% centrality class. The resolution is extracted from the combined response matrix, see Figure 8.5. The resolution is defined as $\sigma(p_{\mathrm{T,ch\ jet}}^{\mathrm{det}})/p_{\mathrm{T,ch\ jet}}^{\mathrm{part}}$. The jet energy resolution is dominated at low $p_{\mathrm{T}}^{\mathrm{jet}}$ by the background fluctuations while at high p_{T} the detector effects become more important.

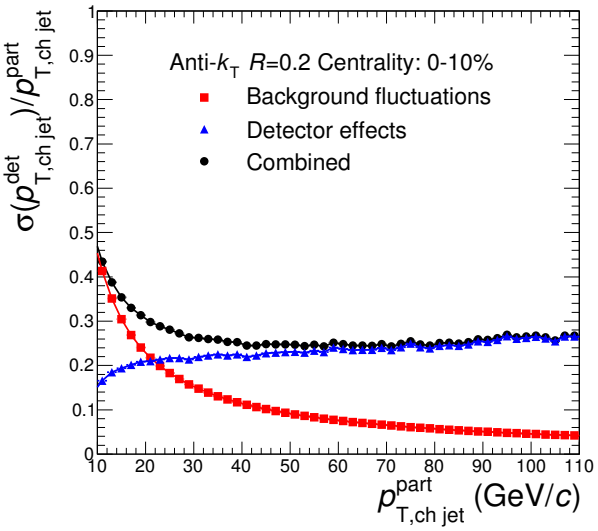

(a) Jet energy resolution for inclusive unbiased jets with $R = 0.2$.

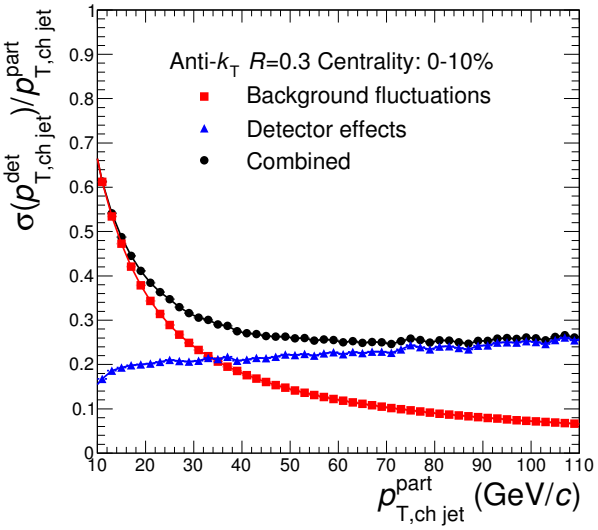

(b) Jet energy resolution for inclusive unbiased jets with $R = 0.3$.

Figure 8.6: Combined jet energy resolution from combined response matrix for two jet radii for 0–10% centrality class.

8.7 Validation of Unfolding Method(s)

In this section unfolding methods are evaluated in two models where the true distribution is known. In the first model which will be discussed, the assumption that the measured spectrum is the true spectrum times some response function is mathematically correct. Meaning that limitations due to acceptance and combinatorial jets are not present. The second model is an event generator based on independent particle emissions and provides a realistic picture including acceptance effects and combinatorial jets.

8.7.1 Folding Model

The unfolding method is tested with a simple model in which a PYTHIA jet spectrum on particle level is folded with the measured fluctuations as illustrated in Figure 8.7. The folded spectrum then represents the measured spectrum and is unfolded. Like in data a convex shape of the 'measured' spectrum is observed in the low p_{T} region where background fluctuations dominate. The corrected spectrum is obtained by unfolding and compared to the original PYTHIA jet spectrum. This folding exercise does not incorporate the presence of combinatorial jets, jet merging or acceptance effects in the measured spectrum. It allows to study the unfolding performance in case of a very broad response in combination with a steeply falling spectrum.

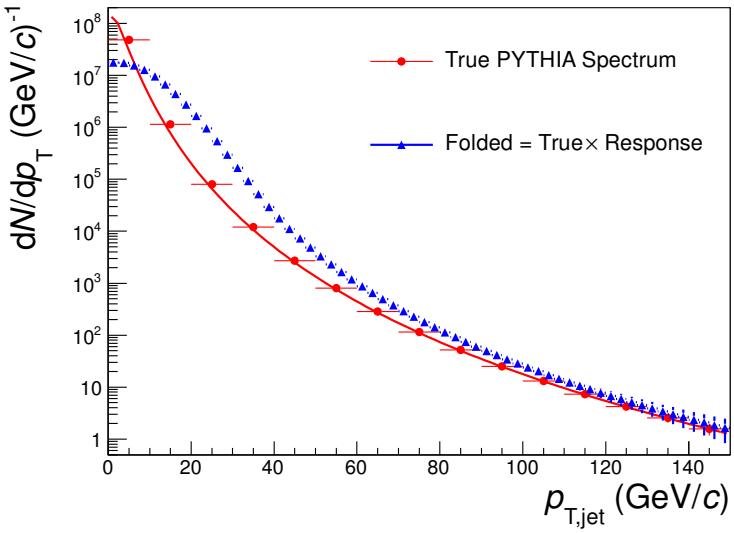

Figure 8.7: Example of folding exercise for radius $R = 0.3$ and background fluctuations corresponding to 0–10% in centrality. Red line: PYTHIA jet spectrum. Blue points: jet spectrum folded with δp_{T}-distribution.

For this exercise the maximum measured p_{T} is fixed to 110 GeV/c which corresponds to the p_{T} reach in Pb–Pb data. The minimum p_{T} cut-off in the

folded spectrum of the toy model has been varied to study the performance of the unfolding algorithm. The unfolding exercise is considered to be successful in case the unfolded spectrum is within 5% of the input PYTHIA jet spectrum.

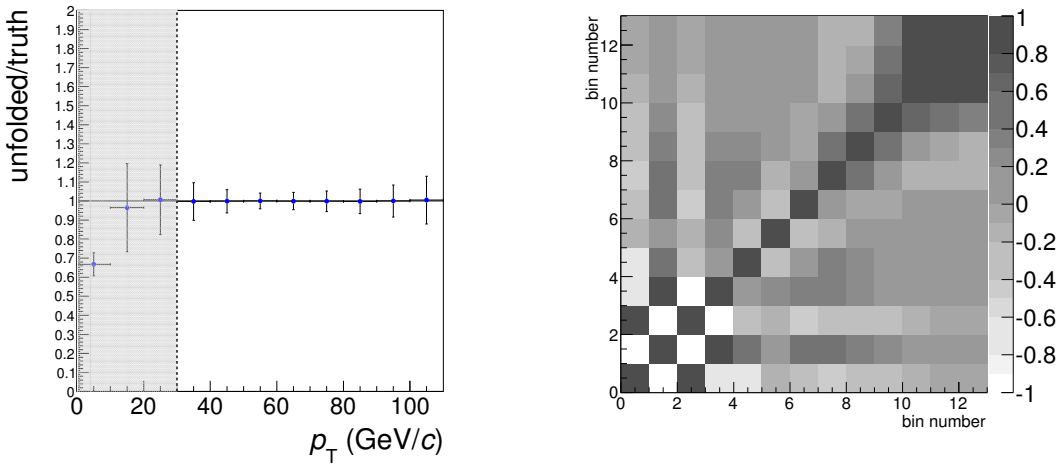

(a) Ratio between generated and unfolded spectrum.

(b) Pearson coefficients from covariance matrix after unfolding.

Figure 8.8: Control figures from folding exercise with $p_{\mathrm{T}}^{\mathrm{min}} = 30$ GeV/c.

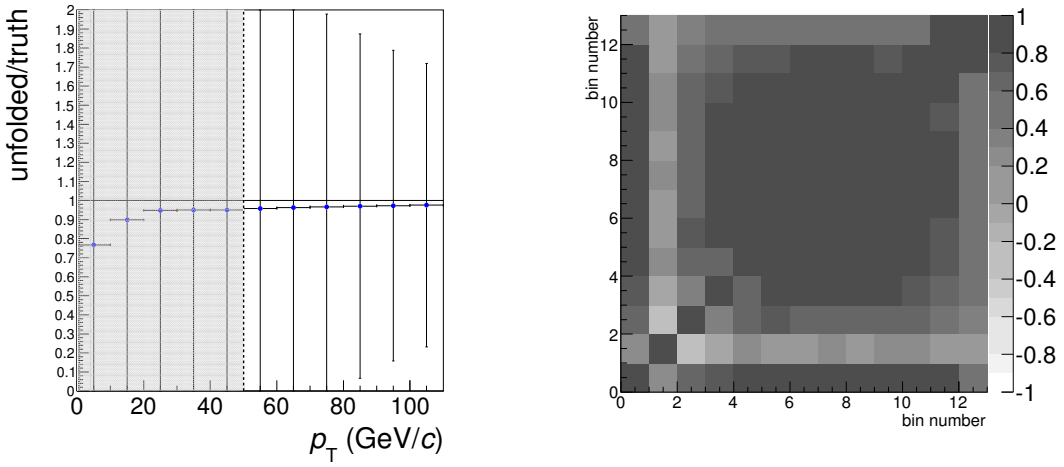

(a) Ratio between generated and unfolded spectrum.

(b) Pearson coefficients from covariance matrix after unfolding.

Figure 8.9: Control figures from folding exercise with $p_{\mathrm{T}}^{\mathrm{min}} = 50$ GeV/c.

The χ^2 minimization method is used to unfold the folded spectra. The regularization strength β is varied and the optimal unfolded solution is chosen based

on the Pearson coefficients: unfolded solution with strong off-diagonal correlations are not accepted. In Figure 8.8(a) the ratio between the generated input spectrum and the unfolded spectrum is shown for the case where the minimum measured p_{T} is 30 GeV/c. The unfolded and generated spectra agree perfectly. In Figure 8.8(b) the corresponding Pearson coefficients of this unfolded spectrum are shown. In Figure 8.9 the same two quality assurance figures in case the measured spectrum is only considered starting from 50 GeV/c, are shown. In this case the unfolding algorithm reproduces the generated jet spectrum as well but the Pearson coefficients show strong correlations with p_{T} bins far away. In this case the number of unfolded bins is similar to the number of measured bins. This gives too much freedom to the fit and it is impossible to reliably extract an unfolded spectrum.

8.7.2 Heavy-Ion Background Model

In this section a heavy-ion background model developed by G. Barros et al. [101] is used to study the unfolding performance. Soft particle production in the model follows a Boltzmann distribution with $\langle p_{\mathrm{T}} \rangle = 670$ MeV/c. The hard component is a power law, p_{T}^{-5}, which is normalized with $T_{\mathrm{AA}} \mathrm{d}\sigma/\mathrm{d}p_{\mathrm{T}}$ where $\mathrm{d}\sigma/\mathrm{d}p_{\mathrm{T}}$ is the charged jet cross-section. Events are generated by randomly picking particles following the single particle p_{T} spectrum and assigning them a random η and φ. The η acceptance is limited to $|\eta| < 1$ corresponding to the ALICE acceptance. The total multiplicity of the events is fixed to $M_{\mathrm{tot}} = 2200$ which is a typical value for the 10% most central collisions. The model gives a reasonable description of the uncorrected charged particle spectra measured by ALICE for this specific multiplicity bin. Although the model does not incorporate any collective effects the background fluctuations are in agreement with the background fluctuations measured ALICE since the dominant component originates from statistical fluctuations. In contrast to the folding model discussed in the previous section the heavy-ion background model incorporates overlapping and combinatorial jets. The hard signal consists of single high p_{T} particles without realistic fragmentation.

In Figure 8.10 the generated hard particle spectrum (Truth) is shown together with the reconstructed jet spectrum from the events generated by the model. Jet reconstruction and average background subtraction is done as in the Pb–Pb data analysis, see Chapter 6. The p_{T} distribution of all reconstructed jets and a subset of these jets selected by a 5 GeV/c constituent is shown. The jet yield at low p_{T} is reduced by a large factor when a leading high p_{T} constituent is required as is also observed in data, see Figure **??**.

The response matrix of the model contains only the p_{T} smearing from background fluctuations since detector effects are not modeled. The reconstructed jet spectra are unfolded with the same procedure as applied in data. The left panels in Figures 8.11 and 8.12 show the ratio between the unfolded jet spectrum and the true spectrum for $R = 0.3$ jets with and without a leading constituent

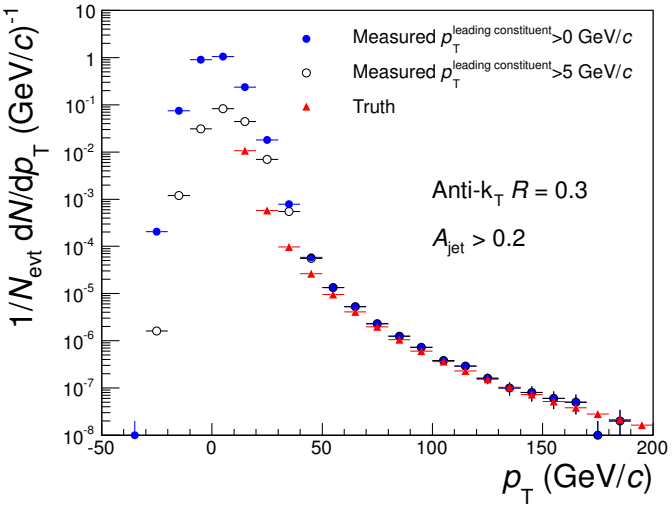

Figure 8.10: Generated and reconstructed jet spectrum with jet radius $R = 0.3$ in the heavy-ion background model.

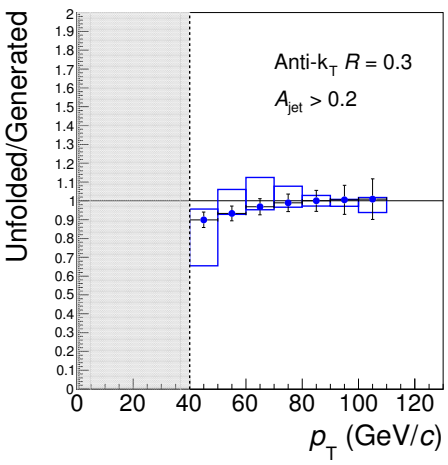

(a) Ratio between unfolded with χ^2 minimization method and true distribution. Boxes indicate systematic uncertainties from unfolding p_T ranges and regularization.

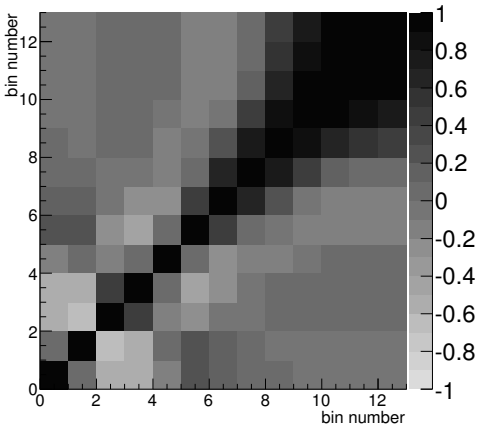

(b) Pearson coefficients.

Figure 8.11: Unfolding performance for jets without a leading constituent trigger.

requirement. The right panels show how the p_T bins are correlated by reporting the Pearson coefficients. The boxes in the ratio figures indicate systematic uncertainties from unfolding p_T ranges and regularization. The evaluation procedure of these systematic unfolding uncertainties is discussed in detail in Section 8.10. At high p_T the unfolded distribution coincides with the true distribution within

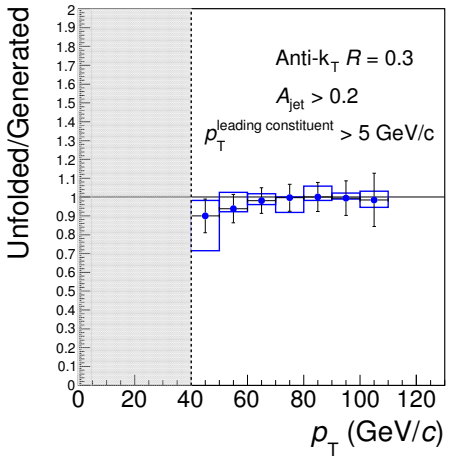

(a) Ratio between unfolded with χ^2 minimization method and true distribution. Boxes indicate systematic uncertainties from unfolding p_{T} ranges and regularization.

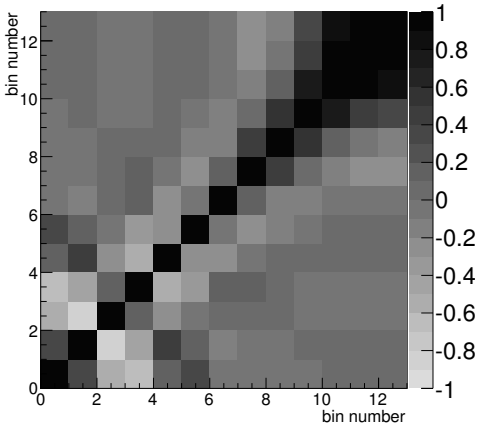

(b) Pearson coefficients.

Figure 8.12: Unfolding performance for jets with a constituent of at least $p_{\mathrm{T}} = 5$ GeV/c.

a few percent for both unfolded jet spectra. For the lowest p_{T} bin, $40 < p_{\mathrm{T}} < 50$ GeV/c, the central value of the unfolded yield underestimates the true yield by 10%. This difference is captured by the systematic uncertainty which is larger close to the minimum p_{T} cut-off than at high p_{T}. Although the contribution of combinatorial jets in the jet spectrum without a leading constituent requirement is larger, the unfolding performance is very similar to what is observed with a biased spectrum. Combinatorial jets are transported during the unfolding procedure to the unconstrained region below $p_{\mathrm{T}}^{\mathrm{min,meas}}$ not affecting the p_{T} range in which the measurement is reported.

Comparison of Unfolding Methods

In addition to the χ^2 minimization method also the Bayesian and SVD (Singular Value Decomposition) methods are evaluated. For both methods the measured spectrum is used as a prior. For the Bayesian method the 4th iteration is chosen as the most optimal one based on trending the Pearson coefficients. For the SVD method the regularization parameter is chosen based on the $|d_i^{k_{\mathrm{reg}}}|$ distribution, see section 6.4.3. The unfolded spectrum from the SVD unfolding method is similar to the solution of the χ^2 minimization method and close to the truth. The Bayesian solution is not smooth. The yield of the lowest p_{T} bin is too small (40% lower than the truth) causing an upward fluctuations with respect to the truth in a higher p_{T} bin. Increasing or decreasing the number of iterations does not provide an unfolded spectrum closer to the true spectrum.

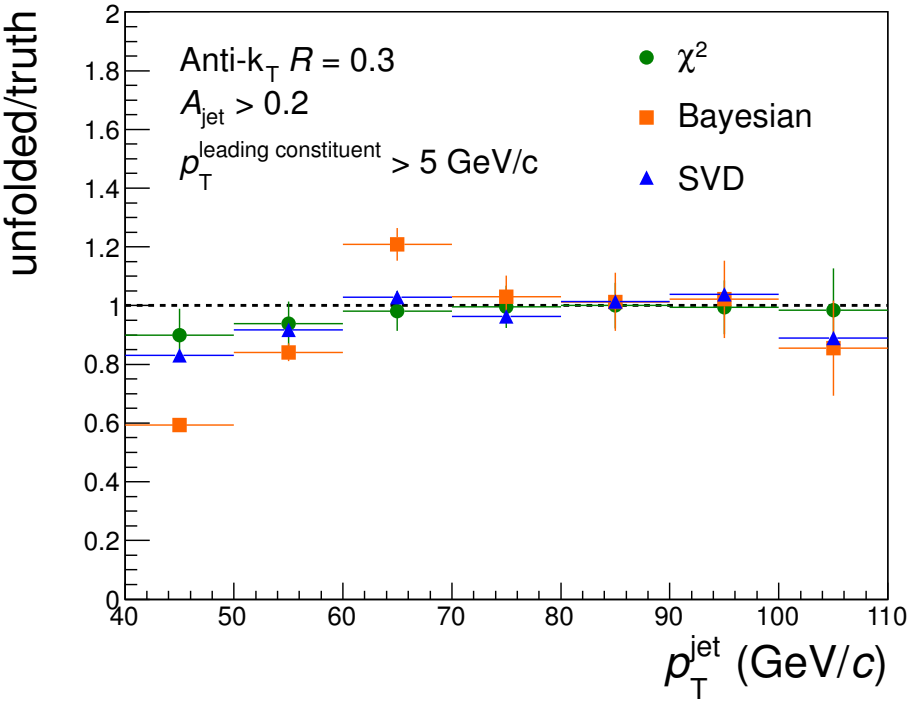

Figure 8.13: Ratio between unfolded and true spectrum for χ^2 minimization ($\beta = 0.013$), Bayesian ($N_{\text{iterations}} = 4$) and SVD method ($k_{\text{reg}} = 6$).

8.8 Flow Bias for Hadron Triggered Jet Spectra

Jets selected by a leading charged track are biased towards higher momentum density regions in the event. These regions are present due to collective effects like flow. The background which is subtracted on an event-by-event basis of each jet, is the average p_{T} density of the event multiplied by the area of the jet. It is expected that the background is underestimated for jets with a leading high p_{T} charged track: *flow bias*. The width of the δp_{T}-distribution is not expected to be significantly different, see Figure 7.5 where the δp_{T}-distribution for different orientations to the event plane is shown. The background bias introduced by a leading hadron trigger is studied by comparing the average density in different regions in the event, ρ_{region}, to the p_{T} density of the full event, $\rho_{\text{full event}}$. The average p_{T} density is calculated with respect to the orientation to the leading track in the event. Three regions with respect to the leading track in the event are defined:

1. near side $|\varphi_{\text{leading track}} - \varphi_{\text{bkg cluster}}| < \pi/4 - R$;
2. away side $|\varphi_{\text{leading track}} - \varphi_{\text{bkg cluster}} - \pi| < \pi/4 - R$;
3. two perpendicular regions $|\varphi_{\text{leading track}} - \varphi_{\text{bkg cluster}} - \pi/2| < \pi/4 - R$;

The regions are illustrated in Figure 8.14. The average p_{T} density in the different

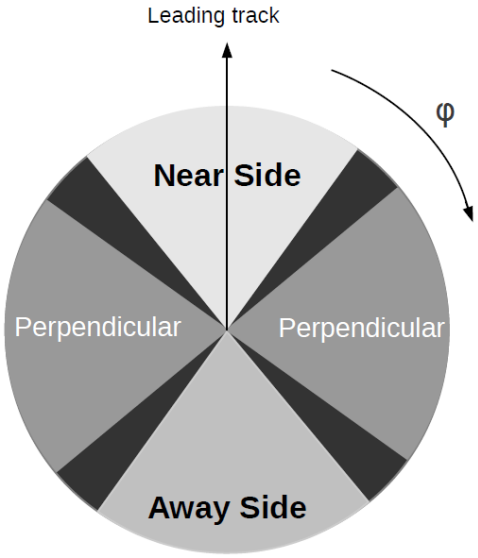

Figure 8.14: Illustration of different regions with respect to the leading track in the event.

regions and the full event is estimated using k_{T} clusters with distance parameter $R = 0.2$ while the two leading k_{T} clusters are excluded from the ρ calculation. The difference between the local p_{T} density and the p_{T} density of the full event

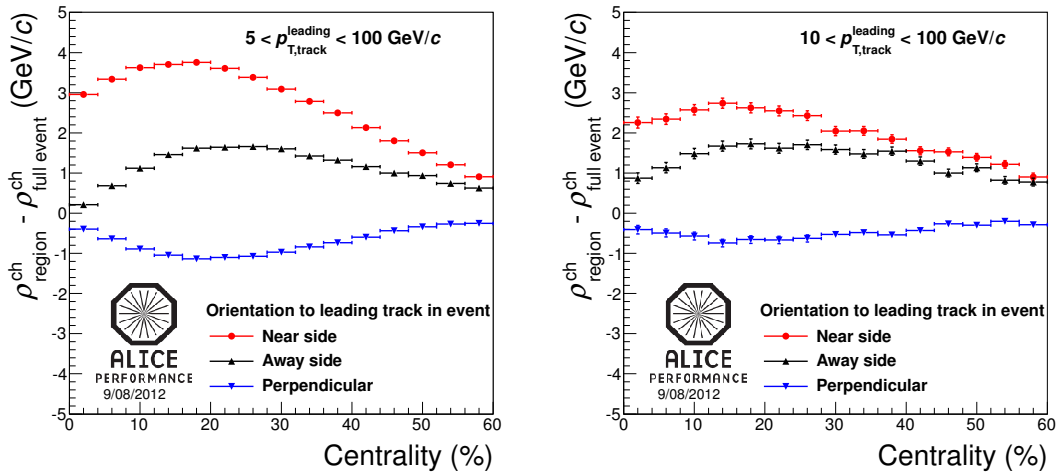

(a) $5 < p_{\mathrm{T}}^{\text{leading track}} < 100$ GeV/c. (b) $10 < p_{\mathrm{T}}^{\text{leading track}} < 100$ GeV/c.

Figure 8.15: Difference between local p_{T} density ρ_{region} and p_{T} density of the full event $\rho_{\text{full event}}$ for two leading track triggers.

is shown in figure 8.15 for two different leading track triggers: $p_{\mathrm{T,track}} > 5$ and $p_{\mathrm{T,track}} > 10$ GeV/c.

Centrality interval	$p_{\mathrm{T}}^{\text{leading track}}$ (GeV/c))	$\delta p_{\mathrm{T}}^{\text{shift}}(R=0.2)$ (GeV/c)	$\delta p_{\mathrm{T}}^{\text{shift}}(R=0.3)$ (GeV/c)
0-10%	5	0.19	0.43
	10	0.13	0.28
10-30%	5	0.22	0.49
	10	0.14	0.31
30-50%	5	0.13	0.28
	10	0.10	0.21
50-80%	5	0.06	0.14
	10	0.06	0.14

Table 8.1: Shifts of δp_{T}-distribution from underestimation of background momentum density due to flow bias in case a leading charged track in a jet is required.

For the analysis of jets selected by a high p_{T} leading hadron the relevant bias is at the near-side. For 0–10% centrality the difference between the local and full event average background density is 3 GeV/c for triggers of 5 GeV/c and 2 GeV/c for triggers of 10 GeV/c. These values are an upper estimate of the flow bias since there is a non-negligible contribution of jet constituents which are outside the $R = 0.2$ jet cluster. In the analysis the bias is assumed to be half of the upper estimate resulting in the values reported in Table 8.1 which represent the bias times the typical area of a jet with a certain resolution parameter: $\delta p_{\mathrm{T}}^{\text{shift}}(R)$. The influence of the flow bias correction on the jet energy has been studied by unfolding the jet spectrum with the inclusive δp_{T} response and a δp_{T}-distribution shifted with the values in Table 8.1. For shifts of 400 MeV/c or less the influence on the unfolded jet spectrum is negligible (less than 1% on the unfolded jet yield).

8.9 Statistical Uncertainties

Reported statistical uncertainties are the square root of the diagonal elements of the covariance matrix. As a cross check, the measured spectrum is randomized according to the statistical uncertainties in each bin. The measured yield in each bin is taken as the central value of a Gaussian function with a width equal to the statistical uncertainty for that specific $p_{\mathrm{T}}^{\text{jet}}$ bin. A random number from this Gaussian is picked to obtain the yield for a toy spectrum in this $p_{\mathrm{T}}^{\text{jet}}$ bin. Each p_{T} bin of the jet spectrum is randomized independently. This is repeated many times providing a sample of several hundreds of randomized measured spectra.

All these randomized spectra are unfolded and the spread of all these solutions is the statistical uncertainty on the measured spectrum which coincides with the diagonal elements from the covariance matrix.

8.10 Systematic Uncertainties

The systematic uncertainties originating from the unfolding procedure are estimated by varying the following settings of the unfolding algorithm:

1) regularization strength β;

2) minimum p_{T} of unfolded jet spectrum;

3) minimum p_{T} of measured jet spectrum;

4) prior;

5) δp_{T}-distribution from random cones and high p_{T} probe embedding;

6) unfolding method;

7) tracking efficiency and resolution;

8) correction for flow bias in case of hadron triggered jets;

9) centrality limits;

In this section the systematic uncertainties for the Pb–Pb jet spectrum in the 0–10% centrality class with resolution parameter $R = 0.3$ and without a requirement on the leading track is discussed. For a full overview of the systematic uncertainties for jet spectra in other centrality bins, jet radii of $R = 0.2$ and $R = 0.4$ and jets with a leading track requirement see Appendix **??**.

8.10.1 Regularization Strength β

The regularization strength β is varied between the region in β-space where fluctuating solutions dominate and the point where the unfolding gets over-constrained. The main effect of varying β is that the jet spectrum changes shape. If the regularization gets stronger the unfolded spectrum gets steeper at low p_{T} and flatter at high p_{T}. Figure 8.16 shows the unfolded and refolded inclusive jet spectra with $R = 0.3$ for different regularization parameters which are in the reliable range (β-space in which fluctuations are suppressed while the unfolding is not over-constrained). The minimum p_{T} cut-off on the measured spectrum is 40 GeV/c. The unfolded spectra fluctuate heavily in the unconstrained region $p_{\mathrm{T}}^{\mathrm{jet}} < 40$ GeV/c. Above this threshold the unfolded spectra are stable. The refolded spectra agree well with the measured jet spectrum as can be seen in the

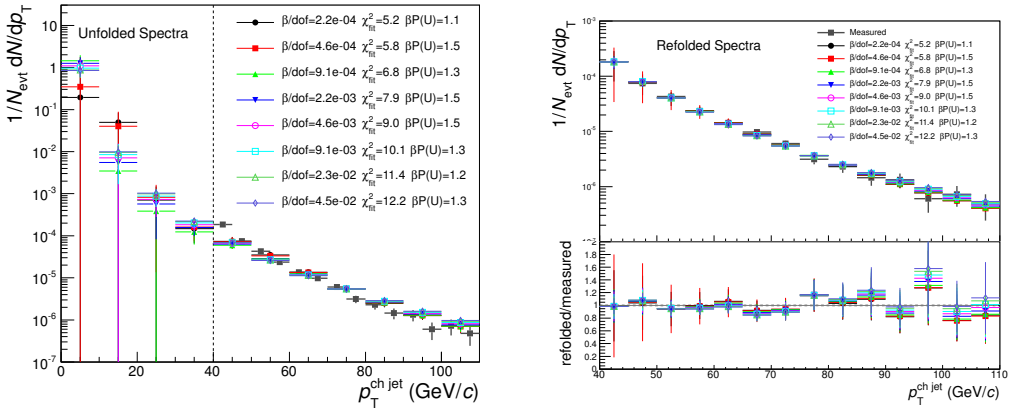

(a) Unfolded spectra for different values of β. The dotted vertical line indicates the minimum p_{T} cut-off on the measured jet spectrum.

(b) Upper panel: Refolded spectra for different values of β. Lower panel: Ratio between refolded and measured jet spectra.

Figure 8.16: Unfolded and refolded spectra as function of regularization parameter β. Inclusive $R = 0.3$ jets, no leading track requirement, 0–10% centrality.

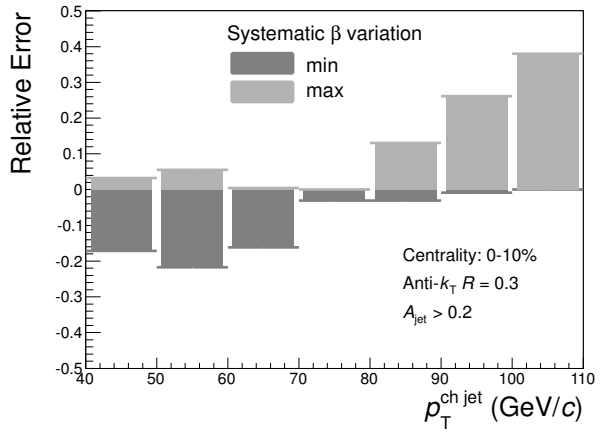

Figure 8.17: Systematic uncertainty from β variation for $R = 0.3$ jets without leading track requirement in 10% most central collisions.

ratio between the refolded and measured spectrum in the lower panel of 8.16(b).

Deviations of the yield for each p_{T} bin of the unfolded spectra within the reasonable range of β are included in the systematic uncertainty of the jet measurement. Figure 8.17 shows the relative difference between the default unfolded spectrum ($\beta/\mathrm{n_{bin}} = 9.1 \cdot 10^{-4}$ where the number of degrees of freedom, dof, is equal to the number of bins in the measured spectrum) and the largest deviation for each $p_{\mathrm{T}}^{\mathrm{jet}}$ bin when β is varied. The magnitude of this systematic uncertainty depends on jet p_{T}.

8.10.2 Minimum p_{T} of Unfolded Jet Spectrum

In the default configuration the unfolded spectrum starts at $p_{\mathrm{T}} = 0$ GeV/c. In order to estimate the influence on the unknown amount of soft jets to the region in which the χ^2 is minimized the first bin of the unfolded p_{T} range is removed. This removes one parameter from the χ^2 minimization. It results in an increase of the unfolded jet yield for $p_{\mathrm{T,ch\,jet}} > p_{\mathrm{T}}^{\mathrm{min,meas}}$ by a few percent depending on the centrality bin and jet radius which is used. This difference is included in the systematic uncertainty of the jet measurement. The contribution to the relative systematic uncertainty for $R = 0.3$ jets without a leading track requirement in central collisions is shown in Figure 8.18.

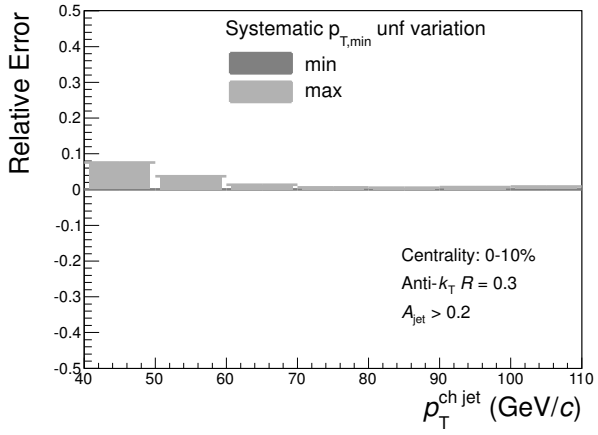

Figure 8.18: Systematic uncertainty from $p_{\mathrm{T}}^{\mathrm{min,unf}}$ variation for $R = 0.3$ jets without leading track requirement in 10% most central collisions.

8.10.3 Minimum p_{T} of Measured Jet Spectrum

The minimum p_{T} of the measured jet spectrum is varied with 10 GeV/c to lower and higher values. With the two variations the unfolding is performed again and the resulting difference between the unfolded spectra with the default unfolded spectrum is assigned as a systematic uncertainty. This systematic uncertainty is largest at low p_{T} in the region where the $p_{\mathrm{T}}^{\mathrm{min,meas}}$ cut-off is placed. Figure 8.19 shows the contribution of varying the $p_{\mathrm{T}}^{\mathrm{min,meas}}$ cut-off to the systematic uncertainty on the unfolded jet spectrum.

8.10.4 Unfolding Method

The unfolded spectrum of the χ^2 minimization method is compared to the result of unfolding with Bayesian and SVD unfolding methods. In Figure 8.20 the unfolded spectra of the three methods are shown in the left panel. In the right panel the difference between the Bayesian and SVD with respect to the

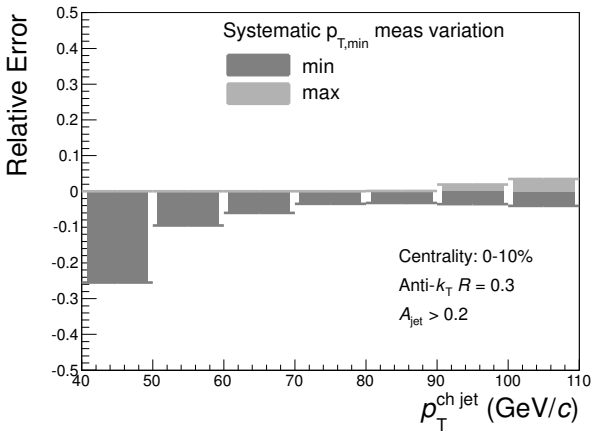

Figure 8.19: Systematic uncertainty from $p_{\mathrm{T}}^{\mathrm{min,meas}}$ variation for $R = 0.3$ jets without leading track requirement in 10% most central collisions.

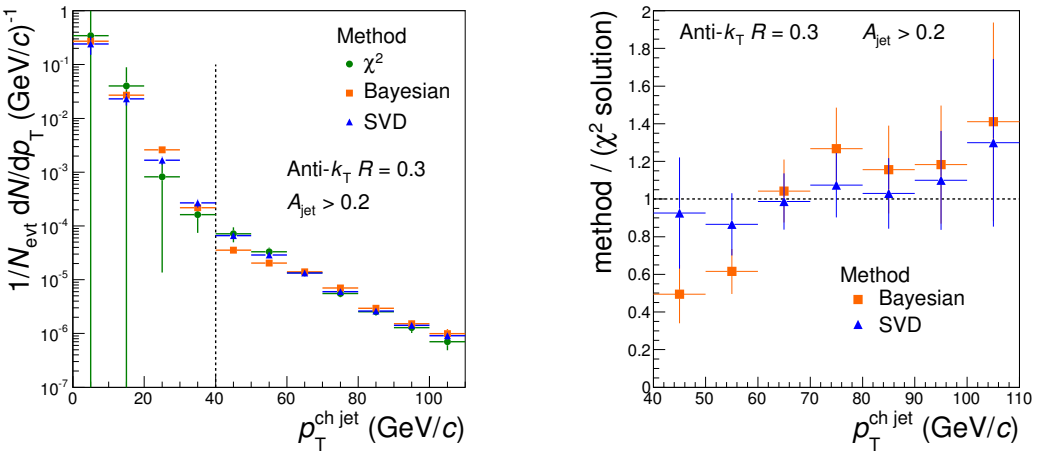

(a) Unfolded jet spectra for three unfolding methods. The dotted vertical line at $p_{\mathrm{T,ch\ jet}} = 40$ GeV/c indicates the minimum p_{T} cut-off on the measured spectrum.

(b) Ratio of Bayesian and SVD unfolded spectrum with respect to the χ^2 unfolded jet spectrum.

Figure 8.20: Comparison of unfolded spectra for $R = 0.3$ jets without leading track requirement in 10% most central collisions. $N_{\mathrm{iter}}^{\mathrm{Bayesian}} = 4$, $k_{\mathrm{reg}}^{\mathrm{SVD}} = 4$ and $\beta = 0.013$

χ^2 solution is shown. The χ^2 and SVD unfolded spectra agree within $\pm 10\%$. Deviations up to 50% at low p_{T} are observed for the Bayesian method. As can be seen in Figure 8.20 the Bayesian unfolded jet spectrum is not smooth. This is also observed in the validation studies with a heavy-ion background model in section 8.7.2. The Bayesian method has more difficulties removing fake jets from the unfolded jet spectrum in the optimized region ($p_{\mathrm{T}}^{\mathrm{jet}} > p_{\mathrm{T}}^{\mathrm{min,meas}}$). Figure 8.21 shows the comparison of unfolding methods for jet spectra with a 5 GeV/c

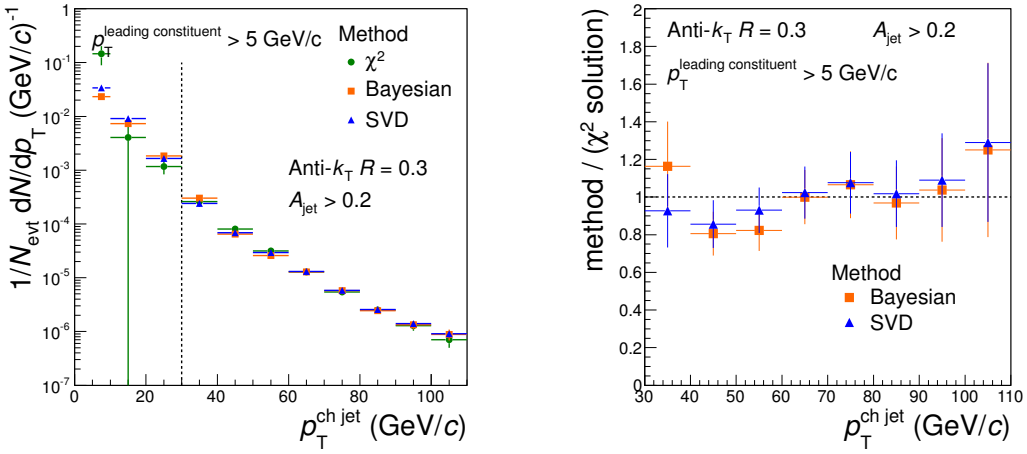

(a) Unfolded jet spectra for three unfolding methods. The dotted vertical line at $p_{\mathrm{T,ch\ jet}} = 30$ GeV/c indicates the minimum p_{T} cut-off on the measured spectrum.

(b) Ratio of Bayesian and SVD unfolded spectrum with respect to the χ^2 unfolded jet spectrum.

Figure 8.21: Comparison of unfolded spectra for $R = 0.3$ jets with 5 GeV/c leading track requirement in 10% most central collisions. $N_{\mathrm{iter}}^{\mathrm{Bayesian}} = 4$, $k_{\mathrm{reg}}^{\mathrm{SVD}} = 4$ and $\beta = 0.007$

leading track requirement in which the contamination of combinatorial fake jets is reduced. In this case the three unfolding algorithms give consistent results.

8.10.5 Prior

The measured jet spectrum is used as a prior. The sensitivity to the choice of prior is evaluated by changing the prior. In case the prior is far from the truth it takes more iterations to converge but eventually the same unfolded jet spectrum is obtained. The choice of prior has a negligible effect on the final unfolded spectrum with the χ^2 minimization method.

8.10.6 Extraction of δp_{T}-distribution

The δp_{T}-distribution obtained from embedding single high p_{T} tracks in measured Pb–Pb events is used as a variation to the δp_{T}-distribution of random cones. The width of the background fluctuations obtained from single track embedding is a few hundred MeV/c larger than for the random cones. The difference between the unfolded jet spectrum using the response from single track embedding is compared to the unfolded spectrum using the random cones δp_{T}-distribution. The difference is largest at low $p_{\mathrm{T}}^{\mathrm{jet}}$ as illustrated in Figure 8.22.

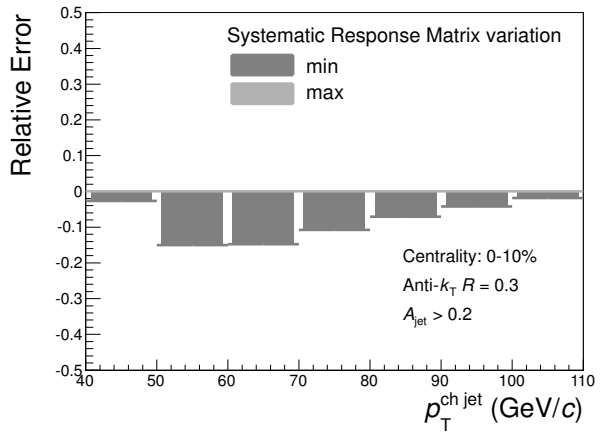

Figure 8.22: Systematic uncertainty from difference between δp_{T}-distribution extracted with random cones (default) and single track embedding for $R = 0.3$ jets without leading track requirement in 10% most central collisions.

8.10.7 Tracking Efficiency and Resolution

The uncertainty on the tracking efficiency is estimated to be 4% motivated by the difference observed in PYTHIA and HIJING simulations, see Section 5.3. The tracking efficiency is varied in a fast simulation by 4% giving a new response matrix for detector effects. The measured Pb–Pb spectrum is unfolded using these variations. The difference between the nominal unfolded solution and the unfolded spectra with a modified tracking efficiency response gives $\sim 20\%$ systematic uncertainty on the unfolded yield at $p_{\mathrm{T}}^{\mathrm{jet}} = 50$ GeV/c and decreases to $\sim 11\%$ at $p_{\mathrm{T}}^{\mathrm{jet}} = 100$ GeV/c. This corresponds to a 3–5% uncertainty on the jet p_{T}.

8.10.8 Flow Bias Correction

The flow bias correction only applies for jet spectra with a high p_{T} leading track selection. The uncertainty on this correction is estimated by shifting the applied δp_{T} shift to 0 and to the upper estimate discussed in Section 8.8: 3 GeV/c for ρ with 5 GeV/c leading track trigger and 2 GeV/c for a 10 GeV/c leading track trigger. Since the upper and lower variations of the flow correction are symmetric with respect to the default the systematic uncertainty is also symmetric, see Figure 8.23 in which the systematic uncertainty for $R = 0.3$ jets with $p_{\mathrm{T}}^{\text{leading track}} > 5$ GeV/c in 10% most central collisions is shown. The uncertainty due to the flow bias correction reduces with $p_{\mathrm{T}}^{\mathrm{jet}}$, for the illustrated example it is 9% at $p_{\mathrm{T}}^{\mathrm{jet}} = 40$ GeV/c and decreases to 4% at $p_{\mathrm{T}}^{\mathrm{jet}} = 100$ GeV/c.

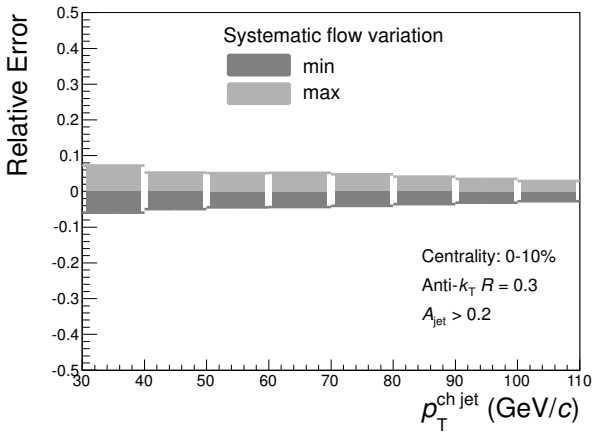

Figure 8.23: Systematic uncertainty from varying flow bias correction for $R = 0.3$ jets with $p_{\mathrm{T}}^{\text{leading track}} > 5$ GeV/c in 10% most central collisions.

8.10.9 Centrality Determination

The relative uncertainty on the the fraction of hadronic cross section used in the Glauber fit to determine the centrality classes is 1%. The contribution of this uncertainty on the jet spectrum is estimated by varying the limits of the centrality classes by ±1% (e.g. for the 10–30% centrality class, 9.9–29.7% and 10.1–30.3%). With the shifted limits of the centrality classes, the jet spectrum is compared to the nominal jet spectrum. The uncertainty is equivalent for the jet spectrum with different leading track biases and increases from central to peripheral events. For the 0–10% centrality class the uncertainty is less than 1% and in the peripheral centrality class 50–80% it is $\sim 2\%$.

In Tables 8.2 and 8.3 the systematic uncertainties in percentiles at low and high p_{T} for all sources are reported for jets without leading track bias and jets selected by a 5 GeV/c track.

Centrality class	Resolution parameter	$R = 0.2$		$R = 0.3$	
	p_{T}-interval (GeV/c)	40–50	70–80	40–50	70–80
0–10%	Regularization	$^{+2.0}_{-0.0}$	$^{+2.0}_{-1.5}$	$^{+3.3}_{-17.1}$	$^{+0.0}_{-3.1}$
	Unfolding method	$^{+1.9}_{-0.0}$	$^{+0.0}_{-3.7}$	$^{+0.0}_{-7.4}$	$^{+7.4}_{-0.0}$
	Minimum p_{T} unfolded	$^{+0.7}_{-0.0}$	$^{+0.2}_{-0.0}$	$^{+7.5}_{-0.0}$	$^{+0.6}_{-0.0}$
	Minimum p_{T} measured	$^{+4.2}_{-8.7}$	$^{+0.1}_{-0.4}$	$^{+0.0}_{-25.5}$	$^{+0.0}_{-3.5}$
	Prior	< 1			
	δp_{T}	$^{+0.0}_{-2.7}$	$^{+0.0}_{-2.3}$	$^{+0.0}_{-2.6}$	$^{+0.0}_{-10.7}$
	Detector effects	± 4.6	± 5.5	± 27.7	± 8.8
	Centrality determination	0.8			
	Total shape uncertainty	$^{+4.8}_{-9.1}$	$^{+2.0}_{-4.4}$	$^{+8.2}_{-30.8}$	$^{+7.4}_{-11.7}$
	Total correlated uncertainty	± 4.7	± 5.5	± 27	± 8.9
50–80%	Regularization	$^{+6.9}_{-0.0}$	$^{+25.5}_{-0.9}$	$^{+1.7}_{-0.0}$	$^{+2.7}_{-1.3}$
	Unfolding method	$^{+7.2}_{-0.0}$	$^{+0.0}_{-20.7}$	$^{+6.3}_{-0.0}$	$^{+0.0}_{-20.0}$
	Minimum p_{T} unfolded	$^{+0.1}_{-0.0}$	$^{+0.1}_{-0.0}$	$^{+0.7}_{-0.0}$	$^{+0.6}_{-0.0}$
	Minimum p_{T} measured	$^{+1.0}_{-0.0}$	$^{+0.0}_{-1.1}$	$^{+0.0}_{-1.7}$	$^{+0.0}_{-1.5}$
	Prior	< 1			
	δp_{T}	$^{+6.6}_{-0.0}$	$^{+2.3}_{-0.0}$	$^{+1.6}_{-0.0}$	$^{+2.3}_{-0.0}$
	Detector effects	± 4.7	± 7.1	± 2.1	± 5.4
	Centrality limits	1.9			
	Total shape uncertainty	$^{+9.8}_{-0.0}$	$^{+25.6}_{-20.7}$	$^{+6.5}_{-1.7}$	$^{+3.7}_{-20.1}$
	Total correlated uncertainty	± 5.1	± 7.3	± 2.8	± 5.7

Table 8.2: Overview of systematic uncertainties for unbiased jet spectra. Relative uncertainties are given in percentiles for two p_{T}-intervals.

8.10.10 Total Systematic Uncertainty

For the final jet cross-section measurement the systematic uncertainties are divided into two categories:

- Spectrum shape uncertainty;
- Correlated uncertainty;

Contributions to the systematic shape uncertainty are the regularization (variation of β and difference between χ^2, SVD solution and Bayesian solution if

Centrality class	Resolution parameter / p_{T}-interval (GeV/c)	$R = 0.2$ 30–40	$R = 0.2$ 70–80	$R = 0.3$ 30–40	$R = 0.3$ 70–80
0–10%	Regularization	$^{+3.4}_{-0.0}$	$^{+2.3}_{-0.3}$	$^{+9.9}_{-0.0}$	$^{+2.6}_{-6.7}$
	Unfolding method	$^{+0.0}_{-3.5}$	$^{+0.0}_{-1.1}$	$^{+0.0}_{-7.3}$	$^{+7.6}_{-0.0}$
	Minimum p_{T} unfolded	$^{+9.6}_{-0.0}$	$^{+0.3}_{-0.0}$	$^{+0.0}_{-5.9}$	$^{+0.0}_{-1.8}$
	Minimum p_{T} measured	$^{+1.7}_{-4.8}$	$^{+0.2}_{-0.3}$	$^{+0.0}_{-12.7}$	$^{+0.0}_{-2.1}$
	Prior	< 1			
	δp_{T}	$^{+0.0}_{-4.9}$	$^{+0.0}_{-2.1}$	$^{+0.0}_{-26.7}$	$^{+0.0}_{-4.6}$
	Detector effects	± 2.7	± 5.5	± 4.6	± 5.2
	Flow bias	$^{+0.9}_{-5.8}$	$^{+0.4}_{-4.1}$	$^{+7.3}_{-5.9}$	$^{+4.8}_{-4.1}$
	Centrality determination	0.8			
	Total shape uncertainty	$^{+10.4}_{-7.6}$	$^{+2.4}_{-2.4}$	$^{+9.9}_{-31.0}$	$^{+7.6}_{-8.6}$
	Total correlated uncertainty	$^{+2.9}_{-6.4}$	$^{+5.6}_{-6.9}$	$^{+8.6}_{-7.5}$	$^{+7.1}_{-6.6}$
50–80%	Regularization	$^{+0.0}_{-5.5}$	$^{+13.3}_{-4.1}$	$^{+0.1}_{-5.1}$	$^{+17.2}_{-2.2}$
	Unfolding method	$^{+2.1}_{-0.0}$	$^{+0.0}_{-19.8}$	$^{+2.3}_{-0.0}$	$^{+0.0}_{-20.0}$
	Minimum p_{T} unfolded	$^{+0.3}_{-0.0}$	$^{+0.1}_{-0.0}$	$^{+1.0}_{-0.0}$	$^{+0.6}_{-0.0}$
	Minimum p_{T} measured	$^{+9.3}_{-0.0}$	$^{+0.7}_{-0.4}$	$^{+7.5}_{-0.0}$	$^{+1.0}_{-0.0}$
	Prior	< 1			
	δp_{T}	$^{+8.2}_{-0.0}$	$^{+2.4}_{-0.0}$	$^{+3.0}_{-0.0}$	$^{+2.2}_{-0.0}$
	Detector effects	± 3.3	± 6.2	± 3.3	± 3.1
	Flow bias	$^{+1.9}_{-1.9}$	$^{+0.3}_{-0.3}$	$^{+0.4}_{-7.2}$	$^{+0.3}_{-4.0}$
	Centrality determination	1.9			
	Total shape uncertainty	$^{+12.6}_{-5.5}$	$^{+13.5}_{-19.8}$	$^{+8.5}_{-5.1}$	$^{+17.4}_{-20.0}$
	Total correlated uncertainty	$^{+4.2}_{-4.2}$	$^{+6.5}_{-6.5}$	$^{+3.8}_{-8.2}$	$^{+3.6}_{-5.4}$

Table 8.3: Overview of systematic uncertainties for jet spectra selected by charged track with $p_{\mathrm{T}} > 5$ GeV/c. Relative uncertainties are given in percentiles for two p_{T}-intervals.

available), extraction of δp_{T}-distribution (random cones versus single track embedding) and minimum p_{T} of the measured and unfolded spectrum. The uncertainties are added in quadrature. For the uncertainty from the regularization the maximum deviation of the variation of β or the difference with the SVD and Bayesian unfolded spectrum is taken.

Correlated uncertainties originate from the uncertainty on the knowledge of tracking efficiency and the flow bias in case of hadron triggered jets. The two contributions are added quadratically.

In Table 8.3 the systematic shape and correlated uncertainties are reported for the different p_{T}-jet intervals.

The systematic uncertainties from the unfolding method, which include regularization and variation of p_{T}-ranges, are not correlated from one unfolded jet spectrum to another. When a ratio between two unfolded jet spectra is taken all uncertainties are propagated fully.

The systematic uncertainties from the flow bias, the δp_{T}-distribution and the detector effects are highly correlated between unfolded spectra from different centrality classes, jet resolution parameters and leading track biases. The uncertainty on the tracking efficiency is the similar for all centrality classes. The flow bias depends on the p_{T} of the leading track, jet resolution parameter and centrality class but is correlated. As a consequence when a ratio is calculated the correlated systematic uncertainty partially cancels.

8.11 Jet Spectrum in Heavy-Ion Collisions

Jet spectra are measured with resolution parameters $R = 0.2$ and 0.3 in four centrality classes: 0–10%, 10–30%, 30–50% and 50-80%. Figure 8.24 shows all the measured Pb–Pb jet spectra with charged constituents with $p_{\mathrm{T}} > 0.15$ MeV/c. The upper panels show the inclusive jet spectra while for the central and lower panels jets are selected by a leading track with a transverse momentum of at least 5 and 10 GeV/c respectively. The markers represent the central values of the unfolded jet spectra which due to unfolding effects are correlated. The filled and open boxes indicate the corresponding shape and correlated systematic uncertainties discussed in previous sections of this chapter. The vertical error bars represent the statistical uncertainties which are correlated within bins since the measured yield migrates from point-to-point during the unfolding process.The statistical error bars correspond to the diagonal elements of the covariance matrix. From the covariance matrix the Pearson coefficients are calculated and shown in Figures 8.25, 8.26 and 8.27 for all unfolded jet spectra. The jet yield is given per event and normalized by the average number of nucleon-nucleon collisions N_{coll} corresponding to the given centrality interval, see Section 5.2.2. The markers shown below 20 GeV/c indicate the uncertainty on the extracted values of N_{coll}. The jet yield evolves with centrality: for more central collisions less jets are observed per N_{coll}.

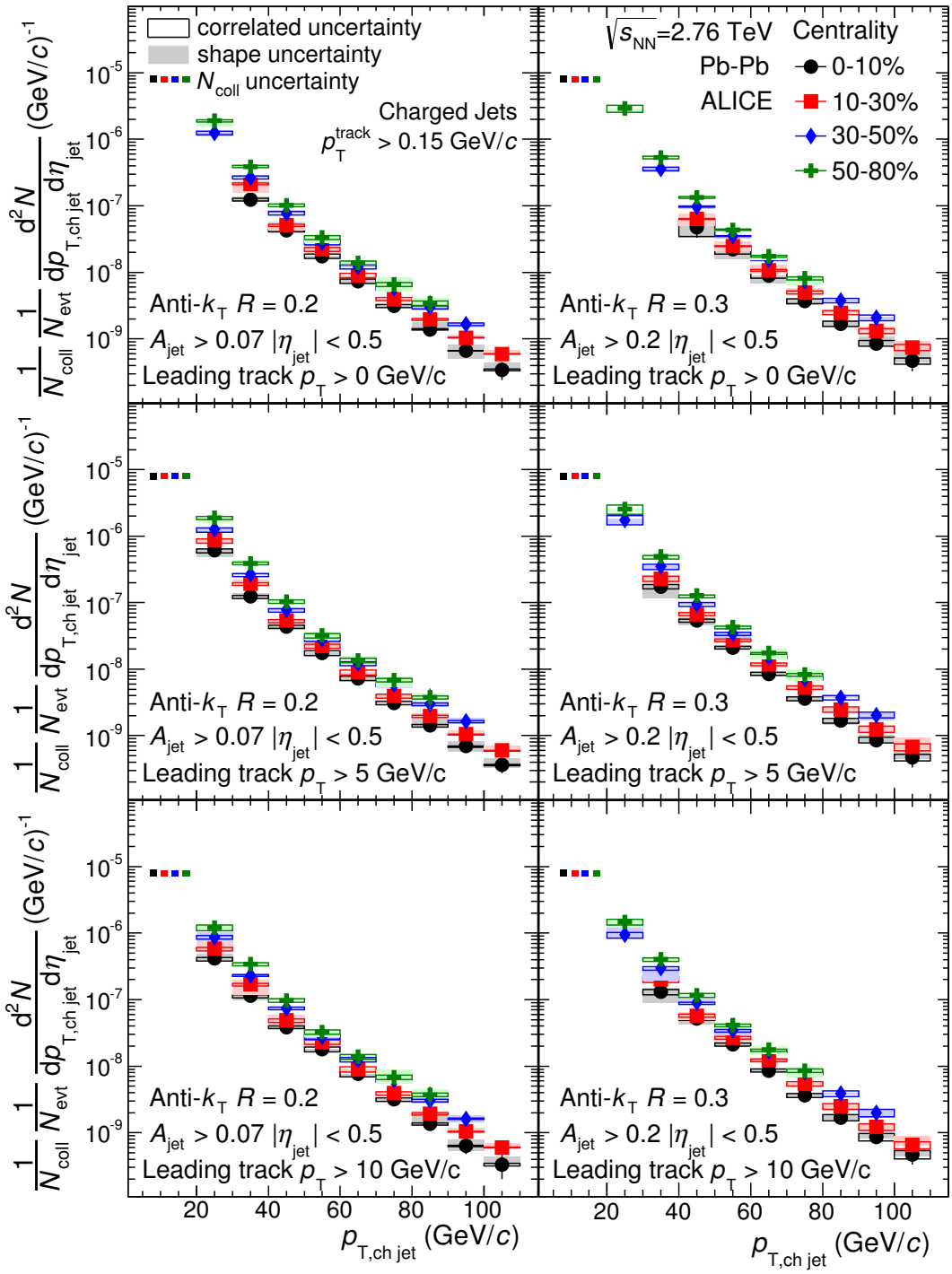

Figure 8.24: Pb–Pb jet spectra for radii $R = 0.2$ and 0.3 for no leading track requirement and jets with at least 5 and 10 GeV/c leading track.

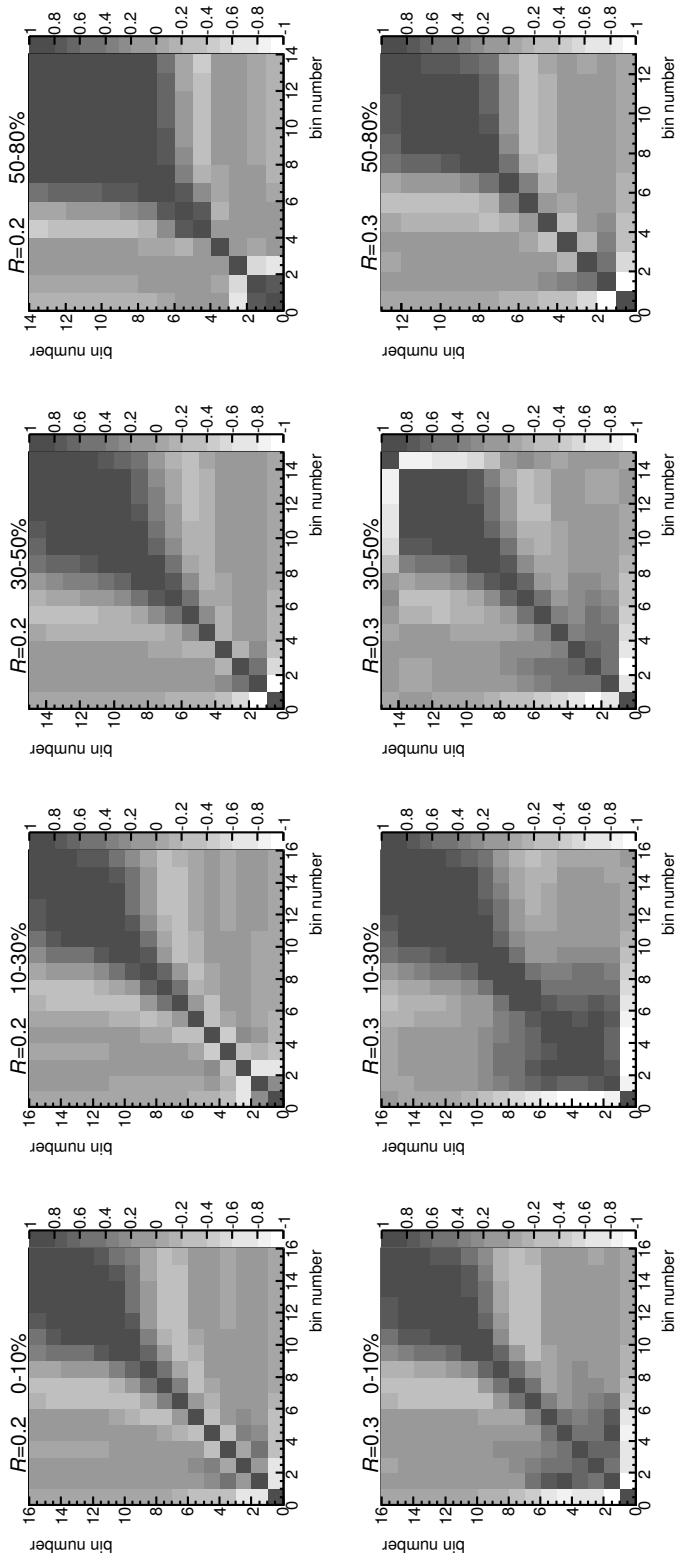

Figure 8.25: Pearson coefficients of the unfolded jet spectra without leading track selection.

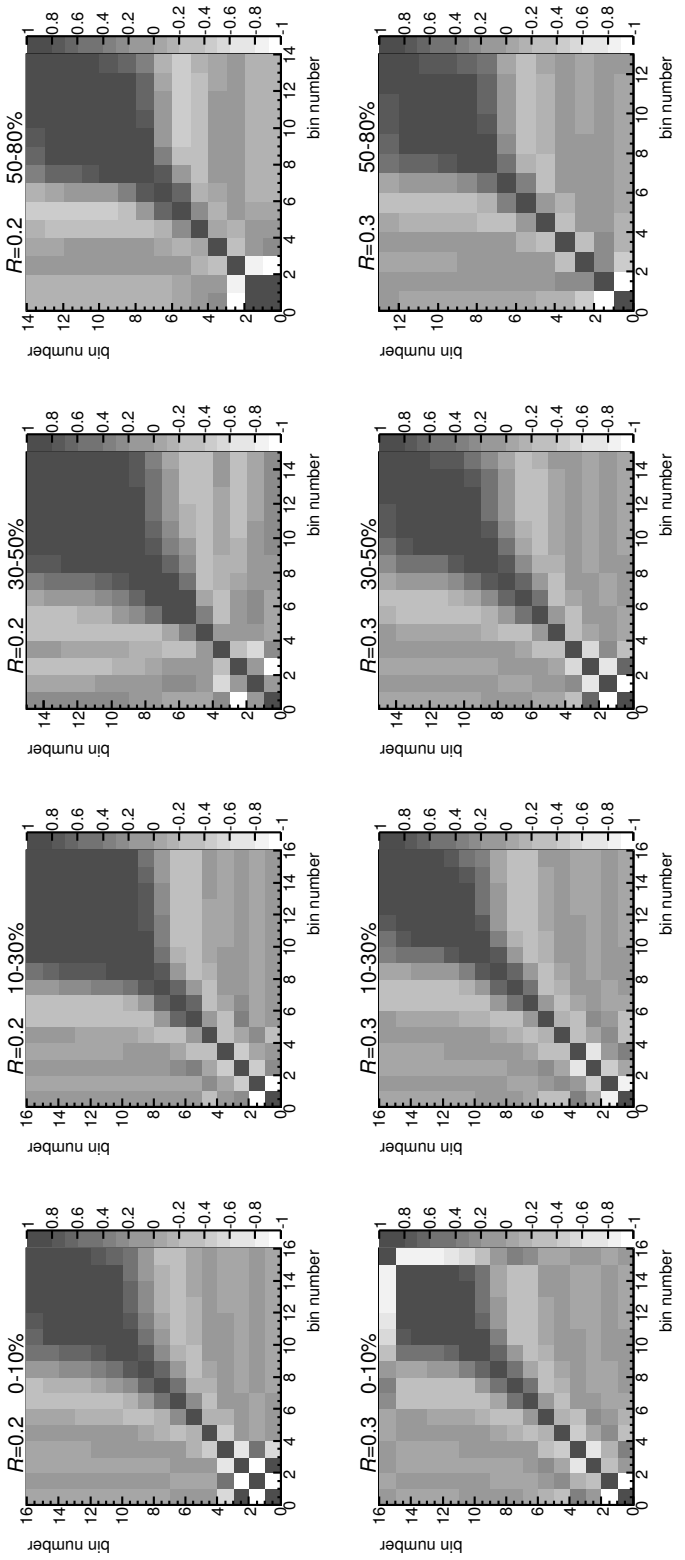

Figure 8.26: Pearson coefficients of the unfolded jet spectra without leading track selection with a 5 GeV/c leading track selection.

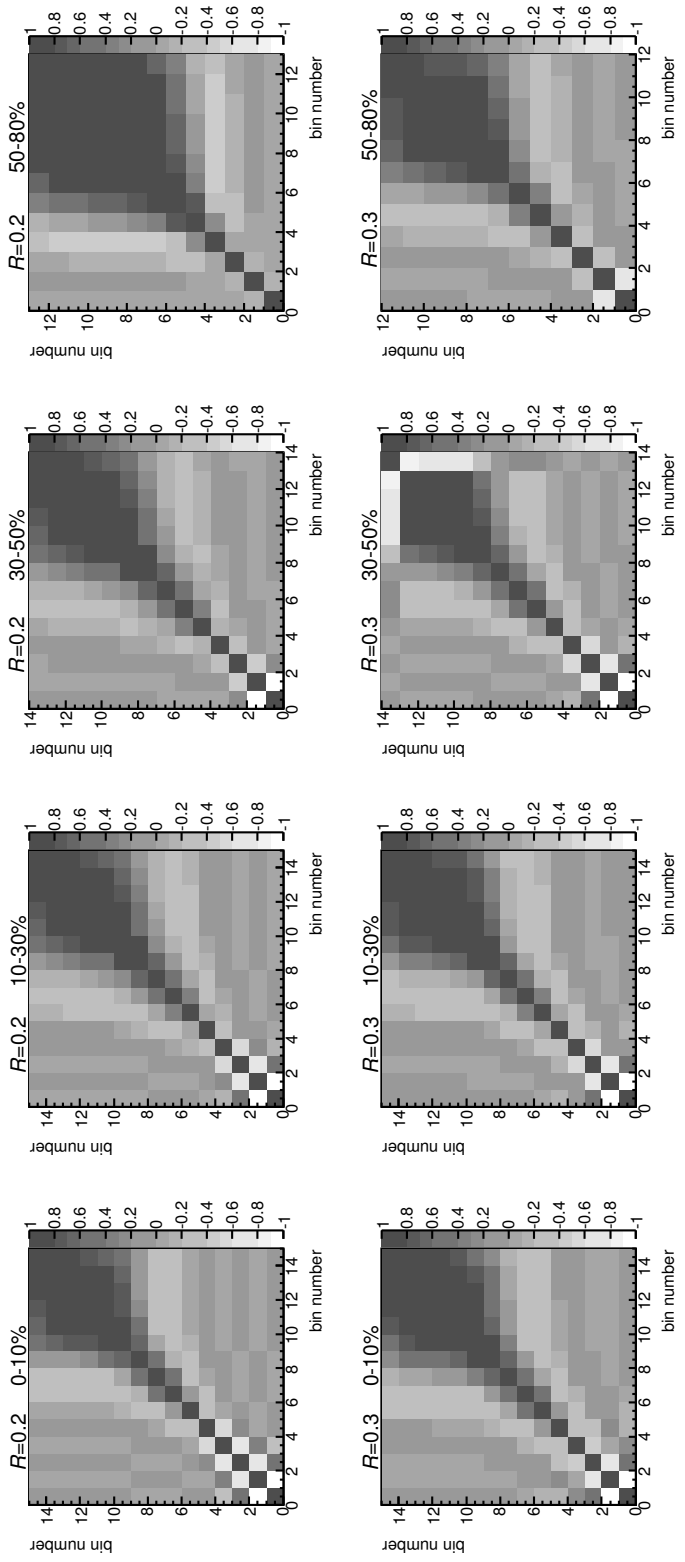

Figure 8.27: Pearson coefficients of the unfolded jet spectra with a 10 GeV/c leading track selection.

9. Results and Discussion

Inclusive charged jet spectra measured in heavy-ion events are presented in the previous chapter in Figure 8.24. Effects of jet quenching are studied by looking at the centrality dependence of the single inclusive jet p_{T} spectrum in heavy-ion collisions. In this chapter various observables following from the jet spectrum analysis in Pb–Pb with ALICE are presented and interpretations of the results are discussed.

9.1 Jet Suppression

To quantify jet quenching effects in heavy-ion collisions, the jet nuclear modification factor is calculated by taking the ratio of jet p_{T} spectra in central and peripheral collisions normalized by the nuclear overlap functions:

$$R_{\mathrm{CP}} = \frac{\dfrac{1}{\langle T_{\mathrm{AA}} \rangle} \dfrac{1}{N_{\mathrm{evt}}} \dfrac{\mathrm{d}N_{\mathrm{ch\ jet}}}{\mathrm{d}p_{\mathrm{T}}^{\mathrm{jet}}\mathrm{d}\eta}\Big|_{\mathrm{central}}}{\dfrac{1}{\langle T_{\mathrm{AA}} \rangle} \dfrac{1}{N_{\mathrm{evt}}} \dfrac{\mathrm{d}N_{\mathrm{ch\ jet}}}{\mathrm{d}p_{\mathrm{T}}^{\mathrm{jet}}\mathrm{d}\eta}\Big|_{\mathrm{peripheral}}}, \tag{9.1}$$

where $\langle T_{\mathrm{AA}} \rangle$ is the nuclear overlap function calculated with a Glauber model. If the full jet energy is recovered in the cone, and in the absence of initial state effects like parton shadowing, R_{CP} is unity by construction. If that case, the energy within the cone might still be distributed differently compared to jets in the vacuum. The jet suppression factor R_{CP} is shown in Figure 9.1 in which the open and shaded boxes representing the shape and correlated systematic uncertainty corresponding to the central values represented by the solid markers. The centrality class 50-80% is used as the peripheral reference for the jet R_{CP}. A strong jet suppression, $R_{\mathrm{CP}} \simeq 0.4$, is observed in central events while for more peripheral collisions the suppression is less, $R_{\mathrm{CP}} \simeq 0.8$ at high $p_{\mathrm{T}}^{\mathrm{jet}}$. The strong jet suppression in central heavy-ion collisions indicates that the full jet energy is not captured by the reconstructed jets. This is consistent with a scenario in which gluons are radiated out-of-cone due to the interaction of the parton with the dense medium. It can also be that jets disappear in heavy-ion collisions resulting in a jet nuclear modification factor smaller than unity. The suppression for jets with radii of $R = 0.2$ and $R = 0.3$ is observed to be similar. A mild rise

as function of p_{T} for the R_{CP} is observed at low jet energies while at high p_{T} the suppression is consistent with a constant value.

Figure 9.2 shows the jet R_{CP} at $60 < p_{\mathrm{T}}^{\mathrm{jet}} < 70$ GeV/c as function of the average number of participants. The number of participants increase with increasing centrality. A decreasing trend of the R_{CP} as function of the number of participants is observed. Figure 9.2 also compares the jet suppression of jets with a high p_{T} track bias, and it shows that there is no evidence that there is a difference in jet suppression for jets with a hard fragmentation pattern. A significant reduction of the statistical and systematic uncertainties of the measurement is needed to determine whether the jet suppression is equivalent or a small difference is present.

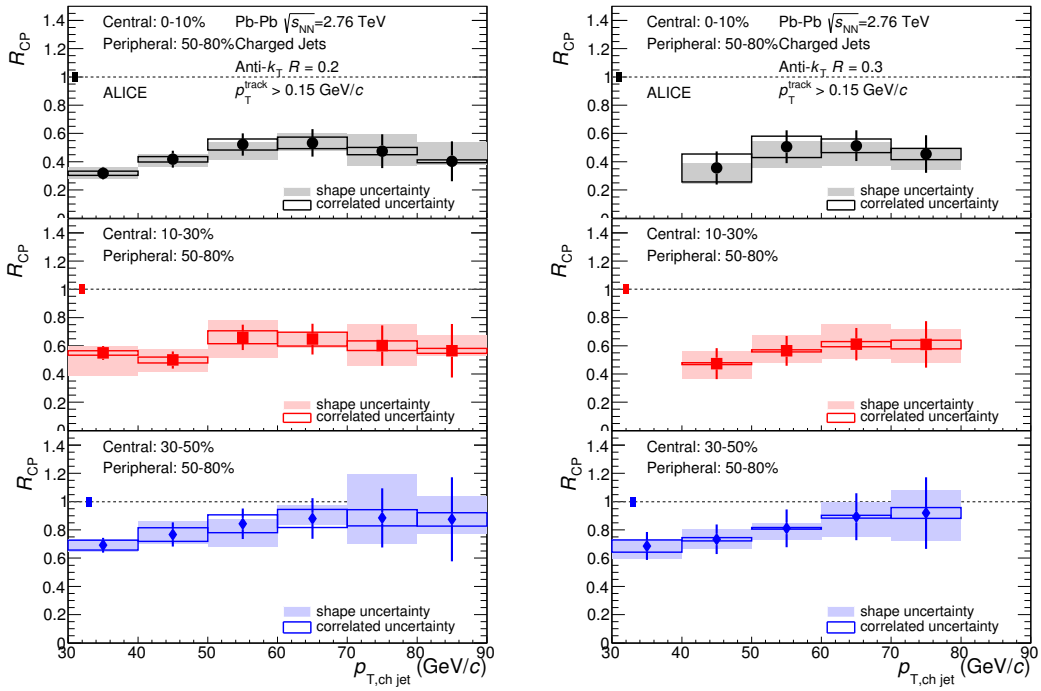

(a) R_{CP} for jets with radius $R = 0.2$.

(b) R_{CP} for jets with radius $R = 0.3$.

Figure 9.1: R_{CP} for inclusive jet spectra without a leading track selection.

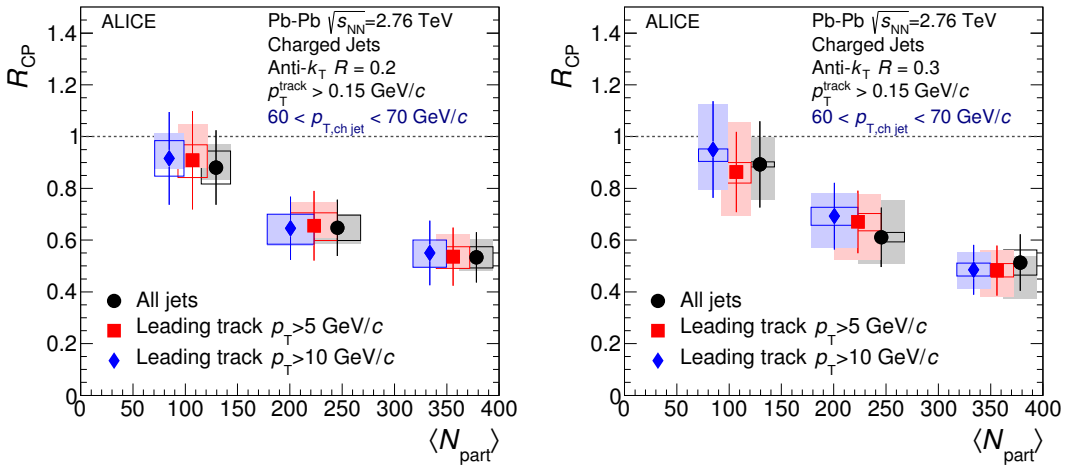

(a) $R = 0.2$. (b) $R = 0.3$.

Figure 9.2: R_{CP} for jets with $60 < p_{\mathrm{T}} < 70$ GeV/c with and without a leading track selection as function of the number of participants in the collision.

9.1.1 Comparison to Single Hadron Nuclear Modification Factor

In Figure 9.3 the jet nuclear modification factor is compared to the single particle nuclear modification factor as measured by ALICE [59]. Note that the p_{T} scale of both measurements is different. A single charged particle and jet of the same p_{T} do originate from different parton energies. Naively one expects that the jet catches some or all of the radiated energy resulting in a larger nuclear modification factor for jets compared to the nuclear modification factor for charged particles. For both measurements a p_{T} independent suppression is observed at high p_{T}. For charged jets fragmenting in the vacuum, the high p_{T} leading particle carries 70-80% of the of the corresponding jet p_{T}. The plateau region observed in the single particle suppression for $30 < p_{\mathrm{T}}^{\mathrm{track}} < 50$ GeV/c corresponds to $40 < p_{\mathrm{T,ch\ jet}} < 65$ GeV/c. The suppression for both high p_{T} observables at approximately the same parton energies is consistent.

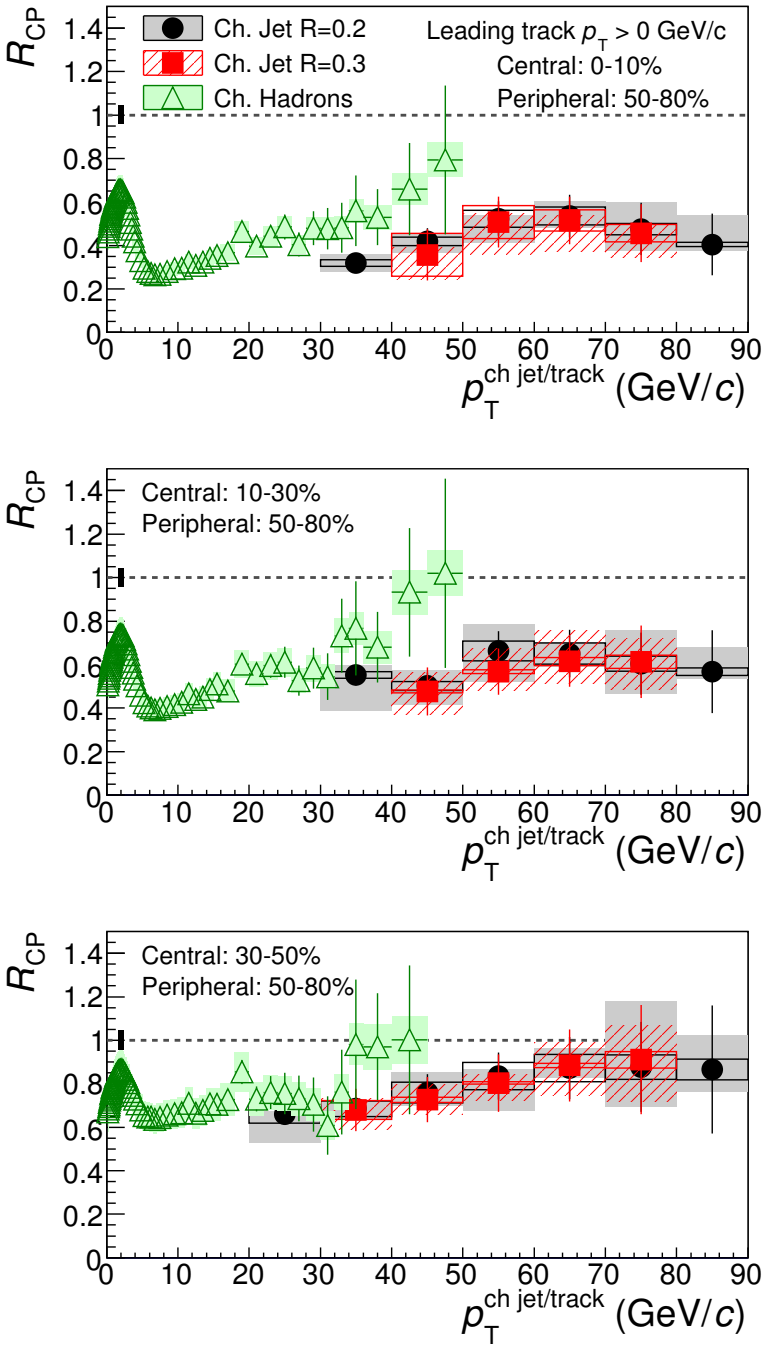

Figure 9.3: Comparison between charged particle and charged jet suppression as measured by ALICE for three centrality classes. The black boxes at $R_{CP} = 1$ indicate the uncertainty on T_{AA}.

9.1.2 Comparison to Calorimetric Jets

The jet suppression measured in ALICE is compared to calorimetric jet measurements by ATLAS [105] in Figure 9.4. Although the detector setups and reconstruction methods are different, a good agreement between the measurements is found in the overlap region $40 < p_{\mathrm{T}}^{\mathrm{jet}} < 80$ GeV/c. The p_{T}-scale for both measurements is different since the ATLAS also measures the neutral constituents of the jets in electromagnetic and hadronic calorimeters. The ALICE measurement presented in this thesis uses only charged tracks. The charged tracks are measured down to low p_{T} making the ALICE measurement more sensitive to the soft jet fragments. The agreement between the measurements suggests that low momentum fragments are not a large contribution to the jet energy with resolution parameter $R = 0.3$.

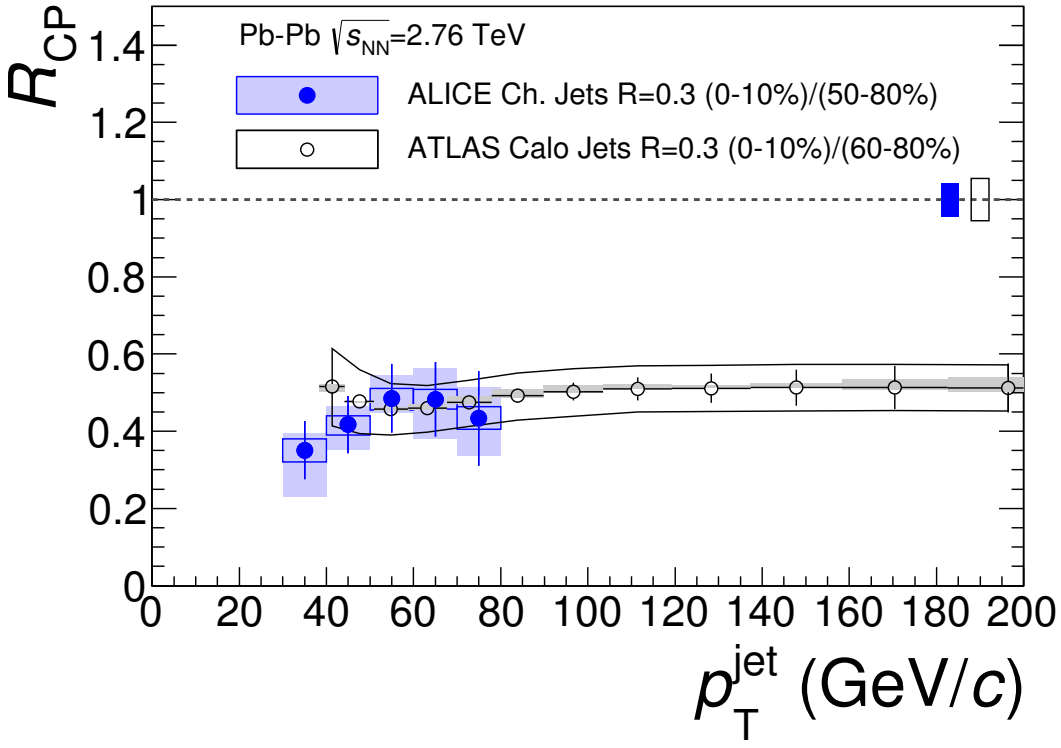

Figure 9.4: Comparison between jet suppression measured by ALICE and ATLAS. ATLAS data from [105].

9.1.3 Simplified Energy Loss Model

A selection of toy models is evaluated to quantify the jet quenching effects in terms of energy loss. The two scenarios which are considered are jets losing a constant and fractional amount of energy. The jet spectrum in the peripheral 50-80% centrality bin and a jet spectrum as produced by PYTHIA-Perugia2011

are used as a baseline. The baseline spectra are fit with a power law function: $\frac{\mathrm{d}N}{\mathrm{d}p_{\mathrm{T}}} = Ap_{\mathrm{T}}^{-n}$, with A a constant normalization factor and n the power of the power law. For the two considered baseline spectra the power n is approximately 5.5. The amount of constant energy loss needed to shift the baseline spectrum to the jet spectrum as measured in central heavy-ion collisions is estimated by fitting again a power law in which p_{T} is substituted with $p_{\mathrm{T}} = p'_{\mathrm{T}} + C$, where p'_{T} indicates the transverse momentum of the jet after energy loss and C is the p_{T} each jet loses. For the fractional energy loss scenario p_{T} is substituted with $p_{\mathrm{T}} = p'_{\mathrm{T}}/(1-\epsilon_f)$, with ϵ_f the fraction of energy each jet looses. The two modified functions used to fit to the central heavy-ion jet spectrum are:

- Constant energy loss: $A(p'_{\mathrm{T}} + C)^{-n}$;
- Fractional energy loss: $A\left(\frac{p'_{\mathrm{T}}}{1-\epsilon_f}\right)^{-n}\frac{1}{1-\epsilon_f}$;

The constants A and n are fixed to the fitted values of the baseline. For this exercise the jet spectra without a selection on $p_{\mathrm{T}}^{\text{leading track}}$ are used. The values extracted from these two toy models for 10% most central Pb–Pb events are reported in Table 9.1. The difference between the jet spectrum in the 0-10% centrality class and the considered baseline spectra can be described with a $\sim$ 20% fractional energy loss or 10-14 GeV/c constant energy loss. The χ^2 of the modified fits is always smaller for the fractional energy loss scenario. For example, the χ^2 for $R = 0.3$ with a PYTHIA baseline with a constant energy loss fit is 3.9 and for the fractional energy loss fit it is 1.0. The fractional energy loss scenario gives a better description of the measured heavy-ion jet spectrum in central collisions.

	$R = 0.2$	$R = 0.3$
	PYTHIA Baseline	
Constant (GeV/c)	11.5 ± 1.0	14.0 ± 1.5
Fractional (%)	19 ± 1	18 ± 2
	Peripheral Baseline	
Constant (GeV/c)	10.6 ± 1.2	11.8 ± 2.0
Fractional (%)	18 ± 1	19 ± 2

Table 9.1: Estimated values of jet energy loss in central heavy-ion events from toy models.

9.2 Hard Jet Fragments

A first study of the high p_{T} jet fragments is performed by comparing the leading track biased and unbiased spectra. Figure 9.5 shows the ratio between the jet spectra with a leading track p_{T} of at least 10 GeV/c and 5 GeV/c as measured in the most central Pb–Pb collisions and in PYTHIA with Perugia-2011 tune. By selecting jets with a higher momentum for the leading jet constituent, low p_{T} jets with a soft fragmentation pattern are removed from the sample. The ratio increases with p_{T} reaching 1 at $p_{\mathrm{T}}^{\mathrm{jet}} = 50$ GeV/c for $R = 0.2$ jets and at $p_{\mathrm{T}}^{\mathrm{jet}} = 60$ GeV/c for $R = 0.3$ jets. This increasing trend is compatible with the fragmentation bias observed in PYTHIA. No evidence of the modification of the hard core of the jet is observed indicating that the jet quenching mechanism does not induce frequent hard gluon radiation.

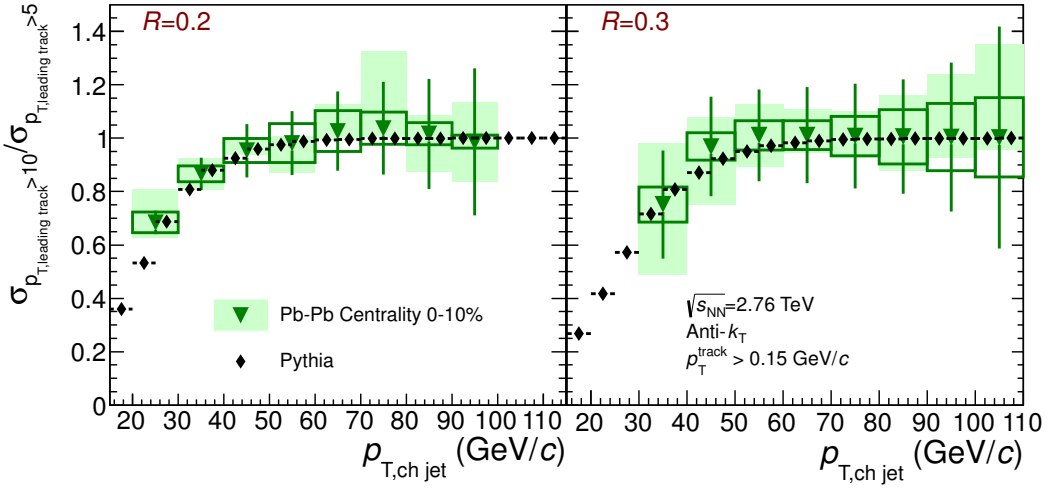

Figure 9.5: Ratio between jet spectra biased by the selection of a leading track of at least 5 and 10 GeV/c in 10% most central heavy-ion collisions and PYTHIA (Perugia-2011). Shaded boxes indicate the systematic shape uncertainty and the open boxes the correlated systematic uncertainty.

Figures 9.6 and 9.7 show a similar ratio but now with respect to the unbiased jet spectrum:
$\sigma_{\mathrm{biased}}/\sigma_{\mathrm{unbiased}}$. This ratio with a 5 and 10 GeV/c leading track is compared to the same observable in PYTHIA on particle level. For both considered jet radii the measured Pb–Pb data points are consistent with vacuum fragmentation within statistical and systematic uncertainties, both for most central (Figure 9.6), and peripheral collisions (Figure 9.7). For jets with radius $R = 0.3$, the right panel of Figure 9.6, the central value of the measured data point exceeds a value of 1 for $p_{\mathrm{T}}^{\mathrm{jet}} < 50$ GeV/c. This is unexpected since the denominator is a subset of the nominator. This effect is attributed to an over-correction for combinatorial jets during the unfolding process and is well covered by the statistical and systematic

uncertainties. The same kind of behavior is also observed in the model studies presented in section 8.7.2.

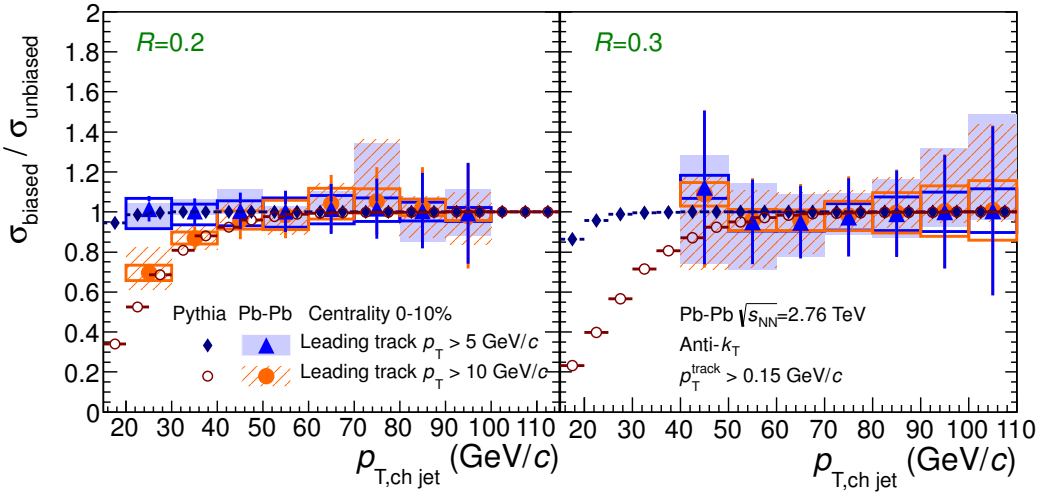

Figure 9.6: Ratio between jet spectra biased by a leading track selection and unbiased jet spectra in central Pb–Pb collisions and PYTHIA (Perugia-2011). Shaded boxes indicate the systematic shape uncertainty and the open boxes the correlated systematic uncertainty.

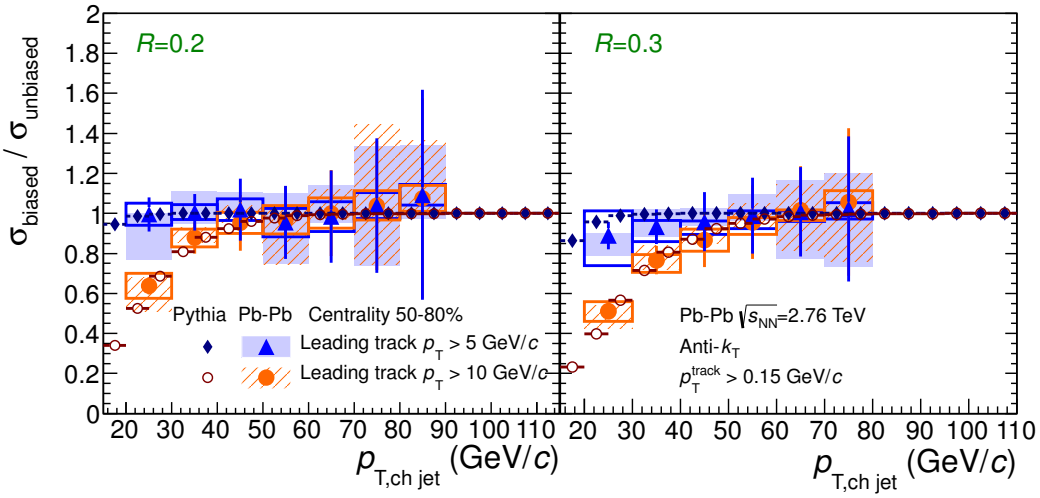

Figure 9.7: Ratio between jet spectra biased by a leading track selection and unbiased jet spectra in peripheral Pb–Pb collisions and PYTHIA (Perugia-2011). Shaded boxes indicate the systematic shape uncertainty and the open boxes the correlated systematic uncertainty.

9.3 Soft Jet Fragments

The ratio of the jet p_{T} spectra measured at different R can provide information about jet structure modifications due to redistribution of energy caused by jet quenching [5, 6]. Figure 9.8 shows the measured ratio $\sigma(R = 0.2)/\sigma(R = 0.3)$ for central and peripheral collisions. By comparing the ratio of jet p_{T} spectra in heavy-ions collisions to the equivalent observable in PYTHIA without jet quenching effects, it can be observed that the transverse jet shapes in central and peripheral collisions are consistent with jet shapes in vacuum. No sign of a modified jet structure is observed between radii of 0.2 and 0.3.

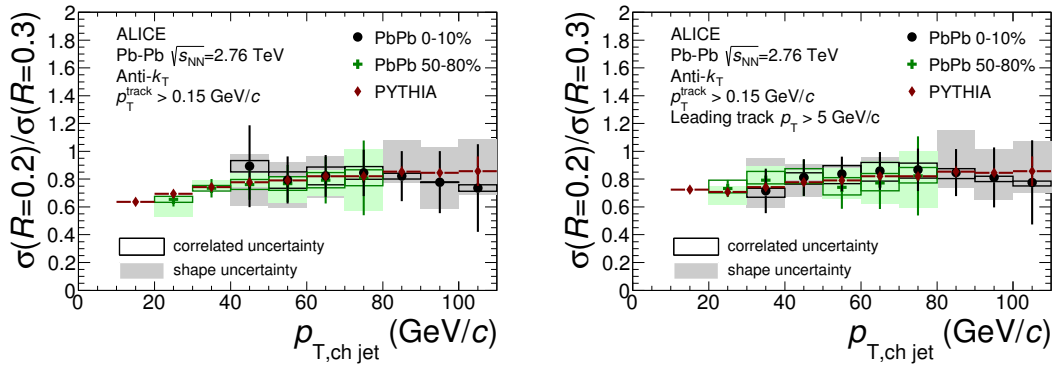

(a) No selection on leading p_{T} constituents of the jets.

(b) Jets with $p_{\mathrm{T}}^{\text{leading track}} > 5$ GeV/c.

Figure 9.8: Ratio between measured cross-section for jets with $R = 0.2$ and $R = 0.3$ in Pb–Pb collisions for central and peripheral collisions compared to particle level PYTHIA.

9.3.1 Low p_{T} jet constituents

In addition to the inclusive jet spectrum measurement with jet constituents of $p_{\mathrm{T}}^{\mathrm{track}} > 150$ MeV/c, jet spectra are also measured with a minimum p_{T} for the jet constituents of 1 and 2 GeV/c. Two types of corrections are done for these spectra. The first one is to correct only for tracks which are not measured due to tracking inefficiency. The jet spectra with a 1 or 2 GeV/c constituent cut are compared to the jet spectra with a 150 MeV/c constituent cut in Pb–Pb and `PYTHIA` events. A difference is expected since the jet p_{T}-scale changes if one removes constituents from a jet. The change in p_{T}-scale in Pb–Pb is compared to the expected change in p_{T}-scale of vacuum jets in `PYTHIA`. In the second approach, the 'unmeasured' constituents, $0.15 < p_{\mathrm{T}}^{\mathrm{track}} < p_{\mathrm{T,min}}^{\mathrm{track}}$, are corrected for based on the fragmentation model implemented in `PYTHIA`. These spectra are then again compared to the jet spectrum in which the constituents are measured with $p_{\mathrm{T}}^{\mathrm{track}} > 150$ MeV/c. If these two spectra are found to be different, it points to a modified distribution of the soft jet fragments in Pb–Pb collisions.

A study of PYTHIA events has shown that the expected contribution of fragments with $p_{\mathrm{T}}^{\mathrm{track}} < 1(2)$ GeV/c is only 4(7)% of the jet energy at $p_{\mathrm{T,ch\,jet}} = 40$ GeV/c. Figure 9.9 shows the relative diference between detector and particle level jets for the two different approaches and constituent cuts. It can be observed that the correction is larger if one corrects for the unmeasured soft constituents when a 2 GeV/c cut is applied on the tracks while with a 1 GeV/c cut only a very small difference in the correction is present.

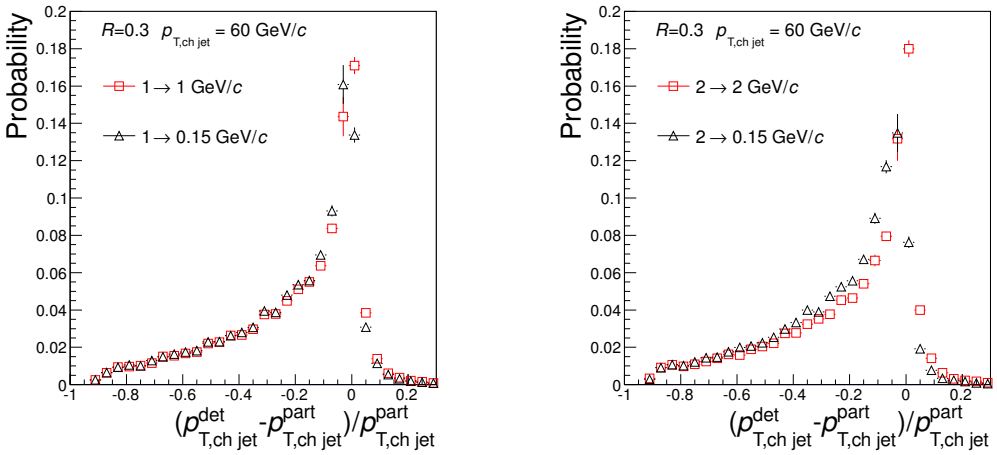

(a) Response for $p_{\mathrm{T}}^{\mathrm{track}} > 1$ GeV/c.

(b) Response for $p_{\mathrm{T}}^{\mathrm{track}} > 2$ GeV/c.

Figure 9.9: Detector response to jets with cut on p_{T} of constituents: $p_{\mathrm{T}}^{\mathrm{track}} > 1$ and 2 GeV/c.

For the correction of jet spectra with a high constituent cut, a new response matrix is build. Both p_{T}-smearing effects, background fluctuations and detector effect, change. The background fluctuations are smaller since the multiplicity of the underlying event is reduced. The detector response to jets is shown in Figure 9.9.

In the upper panels of Figure 9.10 the jet spectra with a minimum p_{T} cut on the tracks of 1 GeV/c are shown together with the jet spectra presented earlier with a minimum p_{T} of 0.15 GeV/c for the constituents. In this case no correction for the unmeasured soft particles has been applied. As can be observed in the spectra and also in the ratio between the spectra shown in the lower panels, the spectra are very similar since for small jet resolution parameters the soft constituents hardly contribute. The ratio of the spectra obtained from PYTHIA simulation at particle level is also shown and the data is compatible with the PYTHIA expectation. A statistical test with the PYTHIA ratio as hypothesis has been performed to determine the statistical significance of the observed difference between data and simulation. Observed deviations between the Pb–Pb data and PYTHIA simulation are within one standard deviation of the statistical uncertainty

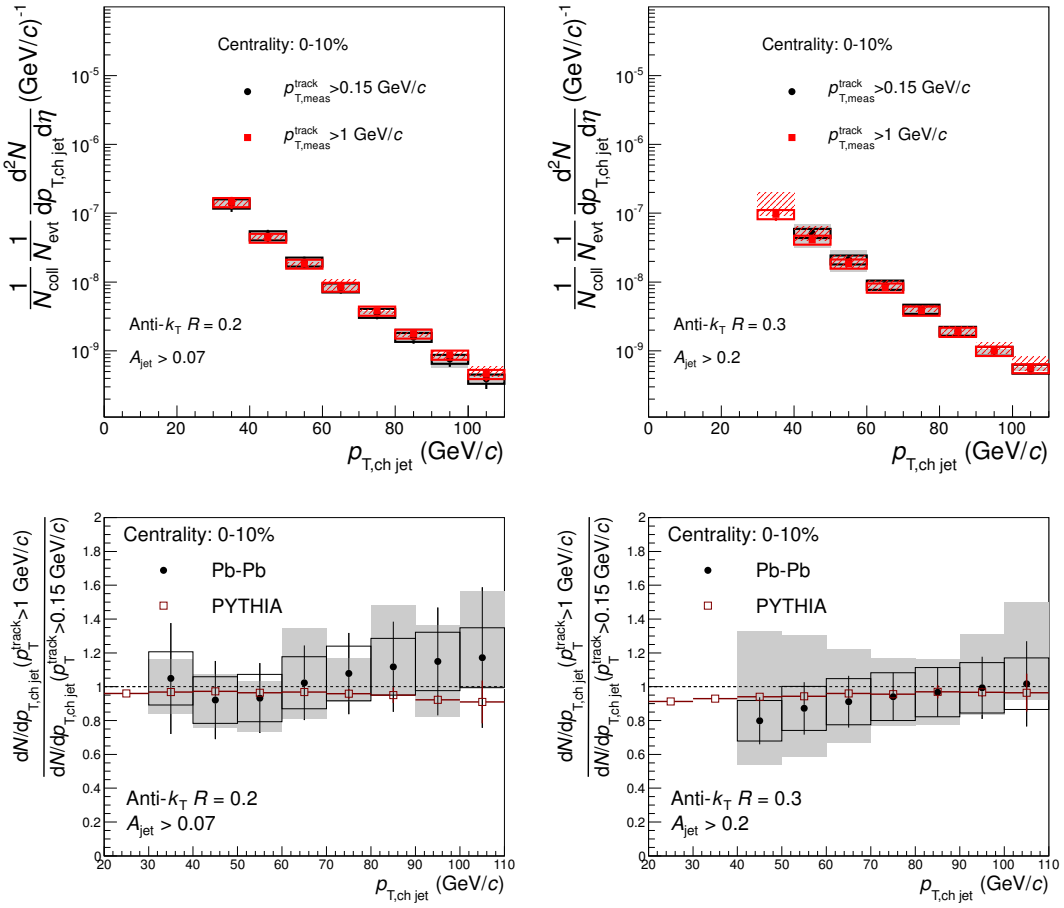

Figure 9.10: Comparison between jet spectra with measured constituents with $p_{\mathrm{T}}^{\mathrm{track}} > 0.15$ and $p_{\mathrm{T}}^{\mathrm{track}} > 1$ GeV/c for jets with resolution parameters $R = 0.2$ and $R = 0.3$ in 10% most central events. All figures are without correction for unmeasured soft tracks. Upper panels: Pb–Pb jet spectra. Lower panels: ratio between jet spectra with 1 and 0.15 GeV/c constituent cut and comparison to PYTHIA.

The contribution of constituents up to 2 GeV/c is larger. In PYTHIA a difference in the jet yield of $\sim 30\%$ is observed at $p_{\mathrm{T,ch\ jet}} = 20$ GeV/c. The reduction of the yield in Pb–Pb at a given $p_{\mathrm{T,ch\ jet}}$ is found to be similar to PYTHIA, see left panels of Figure 9.11. As a second step, the correction for the unmeasured particles with $0.15 < p_{\mathrm{T}}^{\mathrm{track}} < 2$ GeV/c is done based on the fragmentation model implemented in PYTHIA. The results are shown in the righ panels of Figure 9.11. Within the uncertainties of the measurement the ratio between the jet spectrum with measured low p_{T} constituents and the jet spectrum based on PYTHIA fragmentation are equivalent.

No significant difference of soft particle production, $p_{\mathrm{T}}^{\mathrm{track}} < 2$ GeV/c, in Pb–Pb compared to the fragmentation model in PYTHIA is observed. In this

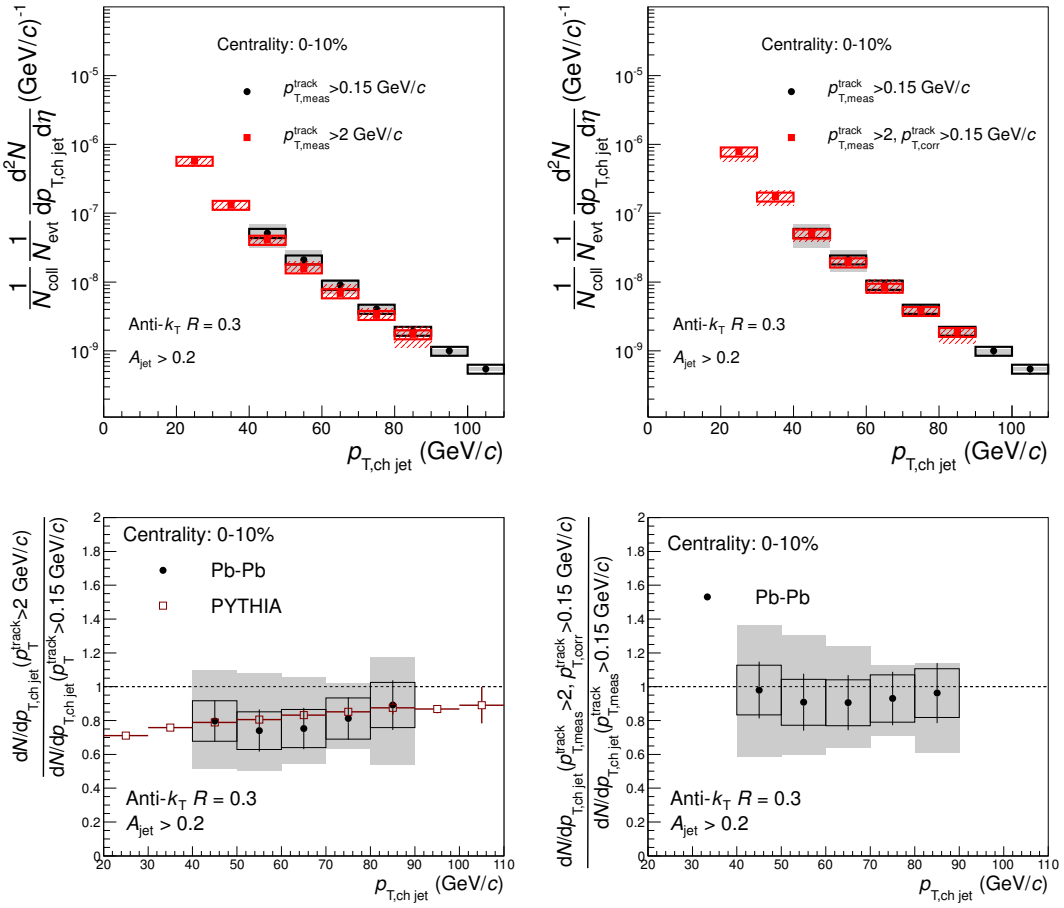

Figure 9.11: Comparison between jet spectra with measured constituents with $p_{\mathrm{T}}^{\mathrm{track}} > 0.15$ and $p_{\mathrm{T}}^{\mathrm{track}} > 2$ GeV/c for jets with resolution parameters $R = 0.3$ in 10% most central events. Upper panels: Pb–Pb jet spectra. Lower panels: ratio between jet spectra with 1 and 0.15 GeV/c constituent cut and comparison to PYTHIA. Left panels: Without correction for unmeasured soft tracks. Right panels: With correction for unmeasured soft particles.

analysis resolution parameters of $R = 0.2$ and $R = 0.3$ are evaluated. For larger cone radii which give access to gluon radiation at larger angles differences might appear.

9.4 Model Comparison

The charged jet results of ALICE are compared to the JEWEL jet quenching MC [106, 107] in Figure 9.12. JEWEL is successful in describing the observed single particle suppression at RHIC and LHC energies. A good agreement is observed between the energy loss implementation of JEWEL and the charged jet results from ALICE.

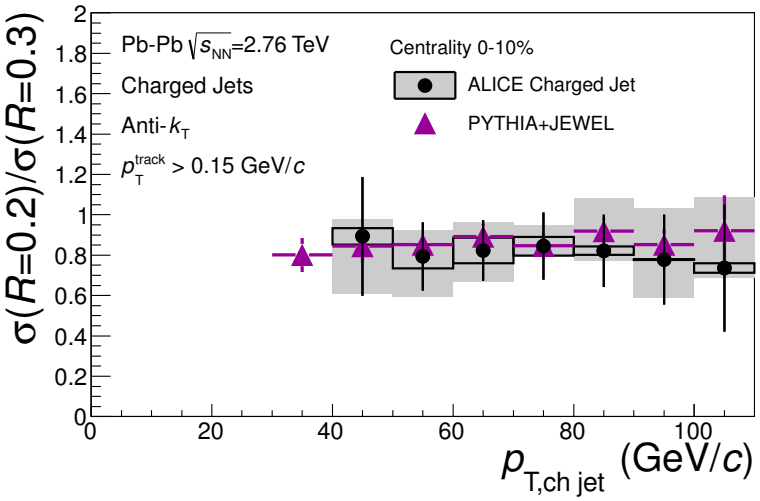

Figure 9.12: Ratio between Pb–Pb jet cross-section for jets with $R = 0.2$ and $R = 0.3$ in 10% most central collisions compared to jet quenching Monte Carlo JEWEL.

The jet suppression measured in heavy-ion events is compared to the jet suppression in JEWEL. For this comparison the ratio between the measured inclusive jet spectrum in central collisions and a jet spectrum from PYTHIA scaled by the number of binary collisions in $0 - 10\%$ centrality is calculated. This ratio is the nuclear modification factor R_{AA} with a PYTHIA reference with the Perugia-2011 tune. The measured $R_{\mathrm{AA}}^{\mathrm{Pythia}}$ is shown together with the jet R_{AA} from JEWEL in Figure 9.13. Like in data, JEWEL also shows a strong jet suppression.

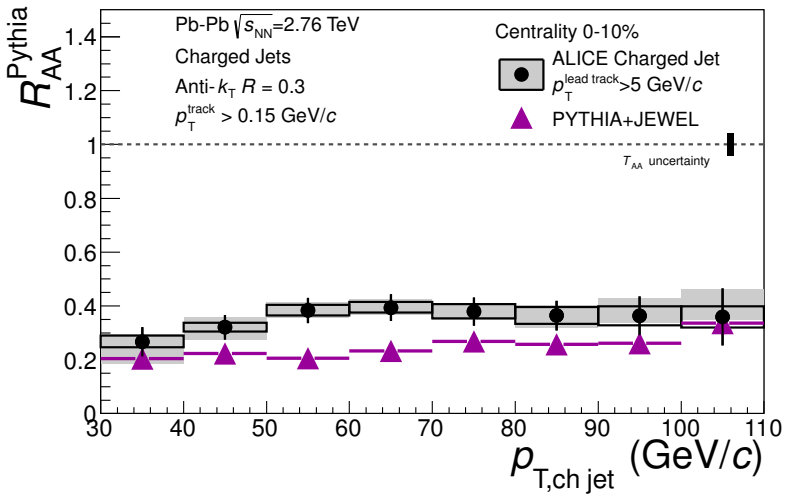

Figure 9.13: Jet suppression as measured by ALICE in central Pb–Pb collisions with a PYTHIA reference (Perugia-2011) compared to jet suppression in JEWEL.

10. Outlook

In this thesis a measurement of the inclusive jet spectrum in Pb–Pb collisions with ALICE at the LHC is presented. A strong suppression of jet production in central Pb–Pb collisions is observed. The study is performed for jets with resolution parameters $R = 0.2$ and $R = 0.3$ which both give a similar jet suppression. In addition, the ratio between the jet spectra of different radii shows the same features in central and peripheral Pb–Pb collisions, and is also similar to what is is observed with the event generator PYTHIA which does not incorporate any jet quenching effects. The same features are observed with the jet quenching Monte Carlo JEWEL, see Figures 9.12, 9.13 and [107]. A strong jet suppression at high p_{T} (> 100 GeV/c) is also observed with YaJEM, a Monte Carlo generator with a modified in-medium shower [108]. This indicates that energy is radiated outside of the measured cone at large angles with the jet axis. Detailed studies are needed to reveal how the radiated energy is redistributed in Monte Carlo implementations. The interpretation of experimental data will profit from more extensive studies comparing jet quenching Monte Carlo generators with data.

An extension of this analysis towards larger cone radii is considered for future studies. The ATLAS collaboration has measured jet spectra with as the largest considered resolution parameter $R = 0.5$ [105]. These spectra are biased by the requirement of a matching charged track jet with $p_{\mathrm{T}}^{\mathrm{jet}} > 8$ GeV/c. This selection criterion rejects jets with a soft fragmentation pattern. Nevertheless, these results indicate a decrease of the jet suppression in central events for larger cone radii at low jet p_{T}, $p_{\mathrm{T}}^{\mathrm{jet}} < 70$ GeV/c. It would be interesting to repeat this study with an unbiased jet sample.

For the analysis presented in this thesis, jets were clustered from charged particles. In an analysis including also the neutral energy measured in the ALICE electromagnetic calorimeter (EMCal) the same reduction of jet production in central events is observed for jets with resolution parameter $R = 0.2$ [109,110]. The advantage of including the neutral jet constituents as well is that the measured jet energy is closer to the parton energy.

The jet measurements suggest that the lost energy is radiated towards large angles. Theoretical studies of parton energy loss by medium induced radiation indicate that the gluon radiation could be dominated by relatively high-energy gluons emitted at small angles [25]. In the light of the recent LHC measurements, several mechanisms causing large angle radiation have been proposed.

For example, a jet collimation mechanism in which the soft fragments are separated from the jet axis by re-interactions with the medium [111]. QCD calculations of in-medium energy loss with an antenna presenting a $q\bar{q}$ pair show an anti-angular ordering of the medium-induced gluon radiation [112, 113], e.g. the medium-induced gluon radiation comes on top and at larger angles than the gluon radiation already present in the vacuum.

In the jet quenching Monte Carlo Q-PYTHIA a softening of the particle composition at large angles of the jet axis is present [114] and in agreement with the observation of the CMS collaboration [115]. Q-PYTHIA with strong jet quenching produces jets which are broadened by producing additional soft particles that are distributed over a wide range of phase space.

The unfolding strategy presented in this thesis is also applied in an ongoing analysis of jets recoiling form a high momentum hadron. Preliminary results of this analysis are available in the proceedings of the Quark Matter 2012 conference [116]. Recoil jet spectra are measured, subtracted and unfolded for the

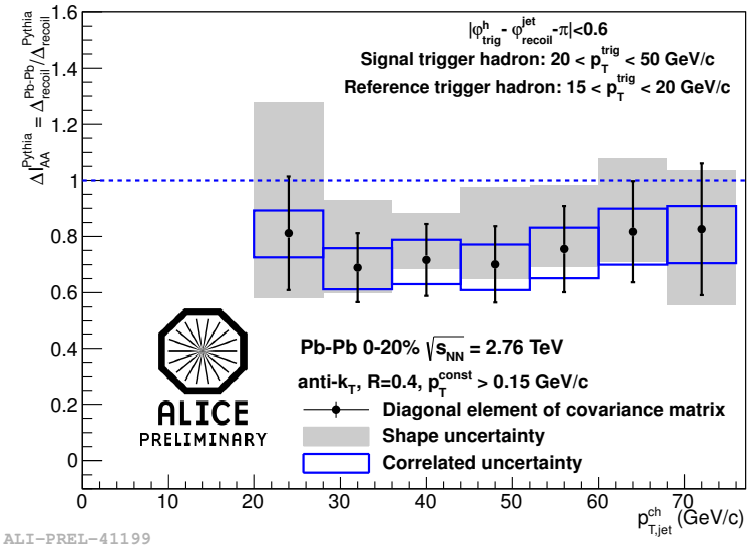

Figure 10.1: Ratio between recoil jet spectra in central Pb–Pb collisions and PYTHIA, $\Delta I_{\mathrm{AA}}^{\mathrm{PYTHIA}}$. Jets are reconstructed from charged particles with resolution parameter $R = 0.4$ and $p_{\mathrm{T}}^{\mathrm{track}} > 0.15$ GeV/c.

large underlying event background, using a technique that does not impose a fragmentation bias on the measured jets. The Pb–Pb measurements are compared to a PYTHIA reference distribution, see Figure 10.1. Comparison of these distribution does not show a large redistribution of energy within the jet cone. Similar results were also obtained for jets with a transverse momentum of at least 2 GeV/c for the constituents [116].

Samenvatting

In relativistische botsingen tussen zwaren ionen wordt een sterk interagerend medium gecreëerd. Dit medium wordt het Quark Gluon Plasma (QGP) genoemd. De verwachting is dat een dergelijk medium ook vlak na de Big Bang bestond. Heden ten dage zou een QGP ook kunnen bestaan in de kern van neutron sterren. Het QGP is een heet medium dat bestaat uit ongebonden quarks en gluonen. De faseovergang van gewone materie naar het QGP wordt bestudeerd in botsingen tussen zwaren ionen. Gewone materie bestaat uit hadronen waarin de quarks en gluonen gebonden zijn. De faseovergang van gewone materie naar een QGP wordt voorspeld door lattice berekeningen van Quantum Chromo Dynamics bij hoge dichtheden die ver boven de kritische waaarde van 1 GeV/fm^3 liggen.

De eigenschappen van het QGP kunnen worden bestudeerd met behulp van hoog energetische partonen die een wisselwerking aangaan met de quarks en gluonen in het QGP. Hoog energetische partonen worden direct na de zware ionen botsing geproduceerd wanneer twee bestanddelen van de zware ionen een grote hoeveelheid impuls uitwisselen. De gecreëerde partonen schieten door het medium waar zij een wisselwerking aangaan met de quarks en gluonen in het medium. Het gevolg is dat het parton energie verliest door gluonen af te stralen. Dit process wordt 'jet quenching' genoemd. De partonen fragmenteren uiteindelijk in hadronen die zichtbaar zijn in detectoren als een gecollimeerde verzameling van energie wat een jet wordt genoemd. De verwachting is dat het fragmentatieproces van partonen in een QGP anders is dan wanneer er geen medium wordt gevormd. Jet quenching wordt gemeten door de productie en structuur van jets geproduceerd in zware ionen botsingen te vergelijken met jets in proton-proton botsingen.

In dit proefschrift wordt een fenomenologische studie en een meting van jet quenching gepresenteerd. Een aantal parton energieverliesmodellen wordt vergeleken met een simpele uniforme geometrie en ook met een medium dat evolueert zoals in zware ionen botsingen. Metingen van hoog energetische processen bij RHIC en LHC worden vergeleken met de uitkomst van de modellen. Door diverse benaderingen in de parton energieverlies imlementaties verschillen de voorspelde medium dichtheden significant. Voor alle modellen is het lastig om meerdere observabelen tegelijk correct the beschrijven.

De productie van jets in zware ionen botsingen is gemeten met de ALICE detector bij de LHC met een botsingsenergie van $\sqrt{s_{\mathrm{NN}}} = 2.76$ TeV. Voor deze analyze worden jets gereconstrueerd van geladen deeltjes die in de centrale track-

ing detectoren (Time Projection Chamber en Inner Tracking System) worden gedetecteerd. De geladen deeltjes zijn de bestanddelen van de jets en worden zeer efficiënt tot aan hele lage transversale impuls ($p_{\mathrm{T}} > 150$ MeV/c) gemeten. De uitdaging in zware ionen botsingen is om de deeltjes afkomstig van het hoog energetische parton en de deeltjes van de onderliggende laag energetische processen te scheiden. De achtergrond van de laag energetische processen wordt voor elke botsing vastgesteld en afgetrokken van de gemeten impuls van de jet. Resterende invloed van fluctuaties in de achtergrond worden gekwantificeerd door hoog energetische signalen aan de gemeten botsingen toe te voegen. Het gemeten jet spectrum wordt gecorrigeerd voor achtergrondfluctuaties en detector effecten met unfolding algoritmes. Een sterke afname van de totale jet productie in de meest centrale botsingen wordt waargenomen voor jets met resolutie parameters van 0.2 en 0.3. Voor meer perifere botsingen ligt het aantal jets dichter bij de jet productie in proton-proton botsingen waarin geen QGP wordt gecreëerd. De gemeten afname van jet productie is vergelijkbaar met de afname van geladen deeltjes met hoge transversale impuls. Dit wijst erop dat niet de gehele energie van het parton in de jet gevangen wordt. Het jet spectrum is ook gemeten voor jets die een deeltje met hoge transversale impuls bevatten. Dit introduceert een voorkeur in de fragmentatie naar meer gecollimeerde jets. Deze voorkeur is even sterk in centrale en perifere botsingen. Dit wijst erop dat de transversale impulsverdeling binnen in de jets niet anders is wanneer er veel jet quenching plaatsvindt. De ratio tussen de jet impulsverdelingen met resolutieparameters van 0.2 en 0.3 is hetzelfde in pp en Pb–Pb botsingen wat aanduidt dat er geen sterke verbreding van het radiële jet profiel aanwezig is.

Summary

In relativistic collisions between nuclei, the creation of a strongly interacting medium, called the Quark Gluon Plasma (QGP), is expected. It is expected that such a medium also existed in the early universe just after the Big Bang. The phase transition of interest is where the dense medium of free and unbound quarks and gluons cools down to form the ordinary matter consisting of hadrons. The phase transition from ordinary matter to a Quark Gluon Plasma is predicted in lattice formulations of Quantum Chromo Dynamics at energy densities well above a critical value of 1 GeV/fm^3. At present a QGP might also exist in the dense cores of neutron stars.

Properties of the QGP can be probed by high-energy partons interacting with the constituents of the QGP. In this interaction the high-energy parton exchanges momentum with the medium. As a consequence, the parton loses energy by radiating gluons. This process is called jet quenching. High-energy partons are created in the early phase of a heavy-ion collision in hard scattering processes of the constituents of the colliding nucleons. They are a well calibrated probe since the initial parton production rates can be calculated with perturbative QCD. The scattered partons propagate through the medium and fragment into jets of hadrons. This process is expected to be modified in heavy-ion collisions compared to proton-proton collisions due to jet quenching.

In this thesis a phenomenological study as well as an experimental observable of jet quenching is presented. A selection of parton energy loss models is studied in a simplified and a realistic medium geometry. Due to different approximations in the parton energy loss implementations of the models, the predictions of the medium energy density in heavy-ion collisions differs significantly. High-p_{T} measurements at RHIC and LHC are compared to model calculations. All models have difficulties describing multiple observables simultaneously.

The production of jets in heavy-ion collisions is measured with data collected by ALICE at the LHC at $\sqrt{s_{\mathrm{NN}}} = 2.76$ TeV. For this analysis jets are reconstructed from charged particles detected in the central tracking detectors (Time Projection Chamber and Inner Tracking System) of ALICE. The charged particles are the constituents of the jets and are measured with a high efficiency down to very low transverse momenta (150 MeV/c). The challenge in heavy-ion collisions is to separate the particles originating from the hard parton and from the soft underlying event. The background from soft particle production is determined for each event and subtracted. The remaining influence of underly-

ing event fluctuations is quantified by embedding different probes into heavy-ion data. The measured jet p_{T}-spectrum is corrected for background fluctuations and detector effects by unfolding. A strong suppression in central events of inclusive jets reconstructed with jet resolution parameters of 0.2 and 0.3 with respect to peripheral events is observed. For more peripheral events the jet spectrum is less suppressed. The observed suppression for jets is found to be similar to charged hadrons, which suggests that the radiated energy captured by the jet is limited. The fragmentation bias on jets introduced by requiring a high p_{T} leading particle, which will reject jets with a soft fragmentation pattern, is equivalent for central and peripheral events. The ratio of jets with resolution parameters $R = 0.2$ and $R = 0.3$ is found to be similar in pp and Pb–Pb events, indicating no strong broadening of the radial jet structure.

A. Hybrid Track Selection Criteria

In Table A.1 a complete list of track selection criteria are listed.

		Global Standard
1	$\|\eta\|$	< 0.9
2	Reject kinks	true
3	TPC refit	true
4	Fraction shared clusters	< 0.4
5	χ^2_{ITS}	< 36
6	$\chi^2_{\mathrm{Global-TPCconstrained}}$	< 36
7	$d_{0,\mathrm{xy}}$	< 2.4
8	$d_{0,\mathrm{z}}$	< 3.1
9	$\chi^2/N^{\mathrm{iter\ 1}}_{\mathrm{clusters,TPC}}$	< 4
10	$N^{\mathrm{iter\ 1}}_{\mathrm{clusters,TPC}}$ for $p_{\mathrm{T}} < 20\ GeV/\mathrm{c}$	$> 70 + 1.5p_{\mathrm{T}}$
	$N^{\mathrm{iter\ 1}}_{\mathrm{clusters,TPC}}$ for $p_{\mathrm{T}} > 20$ GeV/c	> 100
11	ITS refit	true
12	SPD hit	at least 1

Table A.1: Hybrid track selection

A track is contrained to the primary vertex in case the track does not have an ITS refit or a hit in one of the two SPD layers (cut numbers 11 and 12).

In the jet analysis secondaries are accepted by applying loose d_0 cuts (numbers 7 and 8 from Table A.1). Rejecting tracks with a large χ^2 between the global track and the TPC constrained track (cut number 6 from Table A.1) removes efficiently *fake* tracks at high p_{T}. However it also reduces the efficiency of low momentum tracks with 10% with respect to not applying this cut. The tracks removed from the sample at low p_{T} are not fakes but mainly secondaries from

weak decays.

B. Jet R_{CP} for leading track biased jets

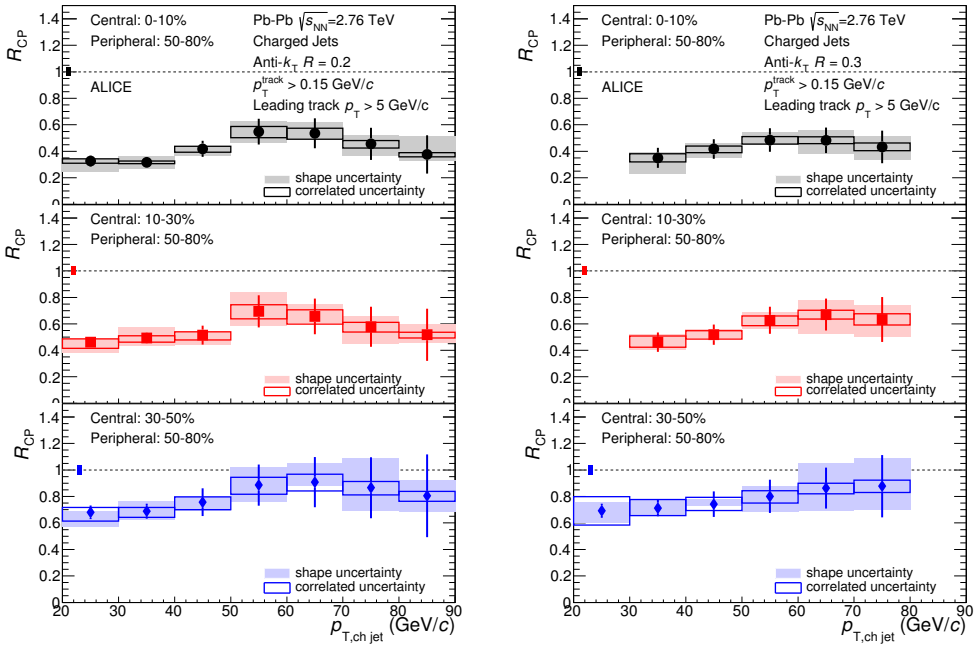

(a) R_{CP} for jets with radius $R = 0.2$. (b) R_{CP} for jets with radius $R = 0.3$.

Figure B.1: R_{CP} for inclusive jet spectra for jets with a constituent of at least $p_{\mathrm{T}} = 5$ GeV/c.

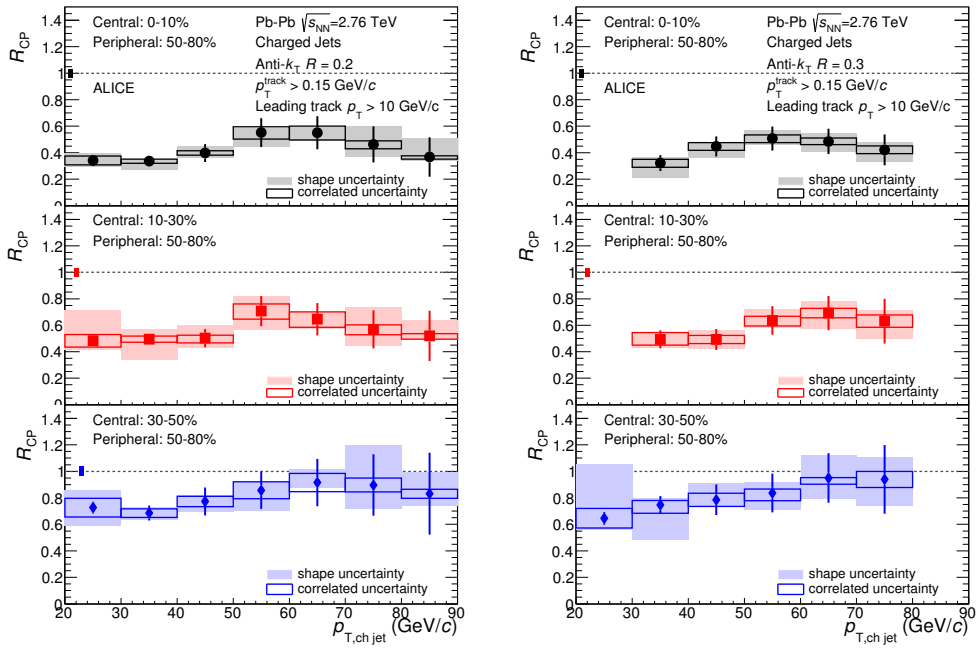

(a) R_{CP} for jets with radius $R = 0.2$. (b) R_{CP} for jets with radius $R = 0.3$.

Figure B.2: R_{CP} for inclusive jet spectra for jets with a constituent of at least $p_{\mathrm{T}} = 10$ GeV/c.

Bibliography

[1] M. Gyulassy, M. Plumer, Jet quenching in dense matter, Phys.Lett. B243 432–438.

[2] R. Baier, Y. L. Dokshitzer, S. Peigne, D. Schiff, Induced gluon radiation in a QCD medium, Phys.Lett. B345 277–286.

[3] J. E. Huth, N. Wainer, K. Meier, N. Hadley, F. Aversa, et al., Toward a standardization of jet definitions.

[4] S. D. Ellis, D. E. Soper, Successive combination jet algorithm for hadron collisions, Phys.Rev. D48 3160–3166.

[5] I. Vitev, B.-W. Zhang, S. Wicks, The Theory and phenomenology of jets in nuclear collisions, Eur.Phys.J. C62 139–144.

[6] I. Vitev, S. Wicks, B.-W. Zhang, A Theory of jet shapes and cross sections: From hadrons to nuclei, JHEP 0811 093.

[7] D. J. Gross, F. Wilczek, Ultraviolet behavior of non-abelian gauge theories, Phys. Rev. Lett. 30 (1973) 1343–1346.

[8] H. Fritzsch, M. Gell-Mann, H. Leutwyler, Advantages of the Color Octet Gluon Picture, Phys.Lett. B47 365–368.

[9] D. Gross, F. Wilczek, Asymptotically Free Gauge Theories. 1, Phys.Rev. D8 3633–3652.

[10] H. D. Politzer, Reliable perturbative results for strong interactions?, Phys. Rev. Lett. 30 (1973) 1346–1349.

[11] S. Bethke, The 2009 World Average of alpha(s), Eur.Phys.J. C64 689–703.

[12] M. Stephanov, QCD phase diagram: An Overview, PoS LAT2006 (2006) 024. arXiv:hep-lat/0701002.

[13] S. Borsanyi, Thermodynamics of the QCD transition from lattice arXiv:1210.6901.

[14] K. Ackermann, et al., Elliptic flow in Au + Au collisions at (S(NN))**(1/2) = 130 GeV, Phys.Rev.Lett. 86 402–407.

[15] K. Aamodt, et al., Elliptic flow of charged particles in Pb-Pb collisions at 2.76 TeV, Phys. Rev. Lett. 105 (25) (2010) 252302.

[16] M. Luzum, P. Romatschke, Viscous Hydrodynamic Predictions for Nuclear Collisions at the LHC, Phys.Rev.Lett. 103 262302.

[17] J. G. Milhano, Theoretical overview of jet quenching `arXiv:1211.2657`.

[18] K. Eskola, H. Paukkunen, C. Salgado, EPS09: A New Generation of NLO and LO Nuclear Parton Distribution Functions, JHEP 0904 065.

[19] K. Reygers, Characteristics of Parton Energy Loss Studied with High-p(T) Particle Spectra from PHENIX, J.Phys. G35 104045.

[20] Adams, J. et. al., Evidence from $d + \mathrm{Au}$ measurements for final-state suppression of high-p_T hadrons in $\mathrm{Au} + \mathrm{Au}$ collisions at rhic, Phys. Rev. Lett. 91 (2003) 072304.

[21] C. A. Loizides, Jet physics in ALICE `arXiv:nucl-ex/0501017`.

[22] R. Baier, Y. L. Dokshitzer, A. H. Mueller, S. Peigne, D. Schiff, Radiative energy loss of high energy quarks and gluons in a finite-volume quark-gluon plasma, Nucl. Phys. B483 (1997) 291–320.

[23] B. G. Zakharov, Fully quantum treatment of the Landau-Pomeranchuk-Migdal effect in QED and QCD, JETP Lett. 63 (1996) 952–957.

[24] R. Baier, Y. L. Dokshitzer, A. H. Mueller, D. Schiff, Medium-induced radiative energy loss: Equivalence between the BDMPS and Zakharov formalisms, Nucl. Phys. B531 (1998) 403–425.

[25] C. A. Salgado, U. A. Wiedemann, Calculating quenching weights, Phys. Rev. D68 (2003) 014008.

[26] P. B. Arnold, G. D. Moore, L. G. Yaffe, Photon emission from quark gluon plasma: Complete leading order results, JHEP 0112 (2001) 009. `arXiv:hep-ph/0111107`.

[27] P. B. Arnold, G. D. Moore, L. G. Yaffe, Photon and gluon emission in relativistic plasmas, JHEP 0206 (2002) 030. `arXiv:hep-ph/0204343`.

[28] M. Gyulassy, P. Levai, I. Vitev, Reaction operator approach to non-Abelian energy loss, Nucl. Phys. B594 (2001) 371–419.

[29] M. Gyulassy, P. Levai, I. Vitev, Jet quenching in thin quark-gluon plasmas. I: Formalism, Nucl. Phys. B571 (2000) 197–233.

[30] S. Wicks, W. Horowitz, M. Djordjevic, M. Gyulassy, Elastic, Inelastic, and Path Length Fluctuations in Jet Tomography, Nucl. Phys. A784 (2007) 426–442.

[31] U. A. Wiedemann, Gluon radiation off hard quarks in a nuclear environment: Opacity expansion, Nucl.Phys. B588 303–344.

[32] X.-N. Wang, X.-f. Guo, Multiple parton scattering in nuclei: Parton energy loss, Nucl.Phys. A696 788–832.

[33] A. Majumder, The In-medium scale evolution in jet modification `arXiv:0901.4516`.

[34] P. Arnold, W. Xiao, High-energy jet quenching in weakly-coupled quark-gluon plasmas, Phys. Rev. D78 (2008) 125008.

[35] N. Armesto, B. Cole, C. Gale, W. A. Horowitz, P. Jacobs, S. Jeon, M. van Leeuwen, A. Majumder, B. Müller, G.-Y. Qin, C. A. Salgado, B. Schenke, M. Verweij, X.-N. Wang, U. A. Wiedemann, Comparison of jet quenching formalisms for a quark-gluon plasma "brick", Phys. Rev. C 86 (2012) 064904.

[36] S. Caron-Huot, O(g) plasma effects in jet quenching, Phys. Rev. D79 (2009) 065039.

[37] S. Caron-Huot, C. Gale, Finite-size effects on the radiative energy loss of a fast parton in hot and dense strongly interacting matter, Phys.Rev. C82 064902.

[38] B. Zakharov, Radiative energy loss of high-energy quarks in finite-size nuclear matter and quark-gluon plasma, Journal of Experimental and Theoretical Physics Letters 65 (1997) 615–620. `doi:10.1134/1.567389`.
URL `http://dx.doi.org/10.1134/1.567389`

[39] W. A. Horowitz, B. A. Cole, Systematic theoretical uncertainties in jet quenching due to gluon kinematics, Phys. Rev. C81 (2010) 024909. `arXiv:0910.1823`, `doi:10.1103/PhysRevC.81.024909`.

[40] Adams, John et al., Identified hadron spectra at large transverse momentum in p + p and d + Au collisions at s(NN)**(1/2) = 200 GeV, Phys. Lett. B637 (2006) 161–169.

[41] A. Dainese, C. Loizides, G. Paic, Leading-particle suppression in high energy nucleus nucleus collisions, Eur. Phys. J. C38 (2005) 461–474.

[42] N. Armesto, M. Cacciari, T. Hirano, J. L. Nagle, C. A. Salgado, Constraint fitting of experimental data with a jet quenching model embedded in a hydrodynamical bulk medium, J.Phys. G37 025104.

[43] A. Kovner, U. A. Wiedemann, Gluon radiation and parton energy lossarXiv:hep-ph/0304151.

[44] M. Verweij, Comparison of radiative energy loss models in a hot QCD medium, Nucl.Phys. A855 359–362.

[45] I. Sarcevic, S. D. Ellis, P. Carruthers, Qcd minijet cross sections, Phys. Rev. D 40 (1989) 1446–1452.

[46] Hadron production at large transverse momentum and qcd, Physics Letters B 70 (2) (1977) 234 – 238.

[47] K. Eskola, K. Kajantie, Baryon to entropy ratio in very high-energy nuclear collisions, Z.Phys. C75 515–522.

[48] K. Eskola, Mini - jets in ultrarelativistic heavy ion collisions at future colliders, Comments Nucl.Part.Phys. 22 (1998) 185–203. arXiv:nucl-th/9705027.

[49] A perturbative qcd analysis of charged-particle distributions in hadronic and nuclear collisions, Nuclear Physics A 713 (1?2) (2003) 167 – 187.

[50] D. Stump, J. Huston, J. Pumplin, W.-K. Tung, H. Lai, et al., Inclusive jet production, parton distributions, and the search for new physics, JHEP 0310 (2003) 046. arXiv:hep-ph/0303013.

[51] B. A. Kniehl, G. Kramer, B. Potter, Fragmentation functions for pions, kaons, and protons at next-to-leading order, Nucl. Phys. B582 (2000) 514–536.

[52] A. Adare, et al., Neutral pion production with respect to centrality and reaction plane in Au+Au collisions at $\sqrt{s_{NN}}$=200 GeV arXiv:1208.2254.

[53] A. Adare, et al., Quantitative Constraints on the Opacity of Hot Partonic Matter from Semi-Inclusive Single High Transverse Momentum Pion Suppression in Au+Au collisions at $\sqrt{s_{NN}} = 200$ GeV, Phys. Rev. C77 (2008) 064907.

[54] A. Adare, et al., Suppression pattern of neutral pions at high transverse momentum in Au+Au collisions at $\sqrt{s_{NN}} = 200$ GeV and constraints on medium transport coefficients, Phys. Rev. Lett. 101 (2008) 232301.

[55] T. Renk, Constraining the Physics of Jet Quenching, Phys.Rev. C85 044903.

[56] T. Renk, Modelling jet quenching arXiv:1207.4885.

[57] Adams, J. et al., Direct observation of dijets in central au+au collisions at $\sqrt{s_{NN}} = 200gev$, Phys. Rev. Lett. 97 (16) (2006) 162301.

[58] T. Renk, H. Holopainen, U. Heinz, C. Shen, A Systematic comparison of jet quenching in different fluid-dynamical models, Phys.Rev. C83 014910.

[59] B. Abelev, et al., Centrality Dependence of Charged Particle Production at Large Transverse Momentum in Pb–Pb Collisions at $\sqrt{s_{\rm NN}} = 2.76$ TeV, Phys.Lett.B`arXiv:1208.2711`.

[60] S. Chatrchyan, et al., Study of high-pT charged particle suppression in PbPb compared to *pp* collisions at $\sqrt{s_{NN}} = 2.76$ TeV, Eur.Phys.J. C72 1945.

[61] K. Aamodt, et al., Particle-yield modification in jet-like azimuthal di-hadron correlations in Pb-Pb collisions at $\sqrt{s_{NN}} = 2.76$ TeV, Phys.Rev.Lett. 108 092301.

[62] ATLAS public pages.
URL `http://atlas.ch/`

[63] CMS public pages.
URL `http://cms.web.cern.ch/`

[64] LHCb public pages.
URL `http://lhcb-public.web.cern.ch/lhcb-public/`

[65] TOTEM public pages.
URL `http://totem-experiment.web.cern.ch/totem-experiment/`

[66] LHCf public pages.
URL `http://www.stelab.nagoya-u.ac.jp/LHCf/LHCf/index.html`

[67] G. Dellacasa, et al., ALICE: Technical design report of the time projection chamber.

[68] G. Dellacasa, et al., ALICE technical design report of the inner tracking system (ITS).

[69] G. Dellacasa, et al., ALICE technical design report of the zero degree calorimeter (ZDC).

[70] K. Aamodt, et al., Centrality dependence of the charged-particle multiplicity density at mid-rapidity in Pb-Pb collisions at $\sqrt{s_{NN}} = 2.76$ TeV, Phys.Rev.Lett. 106 (2011) 032301. `arXiv:1012.1657`.

[71] P. Cortese, et al., ALICE technical design report on forward detectors: FMD, T0 and V0.

[72] R. Brun, F. Rademakers, ROOT: An object oriented data analysis framework, Nucl.Instrum.Meth. A389 81–86.

[73] http://svnweb.cern.ch/world/wsvn/AliRoot.

[74] T. Sjostrand, S. Mrenna, P. Skands, PYTHIA 6.4 physics and manual, JHEP 05 (2006) 026. arXiv:hep-ph/0603175.

[75] P. Z. Skands, Tuning Monte Carlo Generators: The Perugia Tunes, Phys.Rev. D82 074018.

[76] X.-N. Wang, M. Gyulassy, HIJING: A Monte Carlo model for multiple jet production in p p, p A and A A collisions, Phys.Rev. D44 3501–3516.

[77] R. Brun, et al., GEANT Detector Description and Simulation Tool, CERN program library long writeup w5013 Edition (March 1994).

[78] R. Fruhwirth, Application of Kalman filtering to track and vertex fitting, Nucl.Instrum.Meth. A262 444–450.

[79] B. Alessandro, et al., ALICE: Physics performance report, volume II, J. Phys. G 32 (2006) 1295–2040.

[80] ALICE Collaboration, Performance of the ALICE Experiment at CERN LHC, to be published.

[81] M. L. Miller, K. Reygers, S. J. Sanders, P. Steinberg, Glauber modeling in high-energy nuclear collisions, Annu. Rev. Nucl. Part. Sci. 57 (2007) 205–243.

[82] B. Abelev, et al., Centrality determination of Pb-Pb collisions at sqrt(sNN) = 2.76 TeV with ALICEarXiv:1301.4361.

[83] H. De Vries, C. De Jager, C. De Vries, Nuclear charge and magnetization density distribution parameters from elastic electron scattering, Atom.Data Nucl.Data Tabl. 36 (1987) 495–536.

[84] G. P. Salam, Towards Jetography, Eur.Phys.J. C67 637–686.

[85] M. Cacciari, G. P. Salam, G. Soyez, FastJet User Manual, Eur.Phys.J. C72 1896.

[86] M. Cacciari, G. P. Salam, Dispelling the n^3 myth for the kt jet-finder, Phys.Lett.B 641 (2006) 57–61. arXiv:hep-ph/0512210.

[87] M. Cacciari, G. P. Salam, G. Soyez, The anti-kt jet clustering algorithm, JHEP 0804 (2008) 063.

[88] M. Cacciari, G. P. Salam, G. Soyez, The catchment area of jets, JHEP 04 (2008) 005. arXiv:0802.1188.

[89] M. Cacciari, G. P. Salam, Pileup subtraction using jet areas, Phys.Lett.B 659 (2008) 119–126. arXiv:0707.1378.

[90] M. Cacciari, J. Rojo, G. P. Salam, G. Soyez, Jet reconstruction in heavy ion collisions, Eur.Phys.J.C 71 (2010) 1539. arXiv:1010.1759.

[91] V. Blobel, 8th CERN School of Computing - CSC '84, Aiguablava, Spain 9–22 Sep. (1984).

[92] G. D'Agostini, Bayesian Inference in Processing Experimental Data Principles and Basic Applications arXiv:physics/0304102.

[93] T. Adye, Unfolding algorithms and tests using RooUnfold arXiv:1105.1160.

[94] A. Hocker, V. Kartvelishvili, SVD approach to data unfolding, Nucl.Instrum.Meth. A372 469–481.

[95] B. Abelev, et al., Measurement of Event Background Fluctuations for Charged Particle Jet Reconstruction in Pb-Pb collisions at $\sqrt{s_{NN}} = 2.76$ TeV, JHEP 1203 053.

[96] M. J. Tannenbaum, The distribution function of the event-by-event average p_t for statistically independent emission, Phys.Lett.B 498 (2001) 29–34.

[97] M. J. Tannenbaum, Event-by-event average p_t fluctuations in PHENIX: measurements and jet contribution simulations, J.Phys. G 30 (2004) S1367–S1370. arXiv:nucl-ex/0403048.

[98] K. Aamodt, et al., Higher harmonic anisotropic flow measurements of charged particles in Pb-Pb collisions at $\sqrt{s_{NN}} = 2.76$ TeV, Phys.Rev.Lett. 107 032301.

[99] N. Armesto, L. Cunqueiro, C. A. Salgado, Q-PYTHIA: A Medium-modified implementation of final state radiation, Eur.Phys.J. C63 679–690.

[100] P. Jacobs, Background fluctuations in heavy ion jet reconstruction arXiv:1012.2406.

[101] G. de Barros, B. Fenton-Olsen, P. Jacobs, M. Ploskon, Data-driven analysis methods for the measurement of reconstructed jets in heavyion collisions at RHIC and LHC arXiv:1208.1518.

[102] G. D'Agostini, A Multidimensional unfolding method based on Bayes' theorem, Nucl.Instrum.Meth. A362 487–498.

[103] V. Blobel, An Unfolding method for high-energy physics experiments (2002) 258–267arXiv:hep-ex/0208022.

[104] The method of reduced cross-entropy a general approach to unfold probability distributions, Nuclear Instruments and Methods in Physics Research Section A: Accelerators, Spectrometers, Detectors and Associated Equipment 340 (2) (1994) 400 – 412.

[105] G. Aad, et al., Measurement of the jet radius and transverse momentum dependence of inclusive jet suppression in lead-lead collisions at $\sqrt{s_{NN}} =$ 2.76 TeV with the ATLAS detector, Phys.Lett. B719 220–241.

[106] K. C. Zapp, F. Krauss, U. A. Wiedemann, Explaining jet quenching with perturbative QCD alone. `arXiv:1111.6838`.

[107] K. C. Zapp, F. Krauss, U. A. Wiedemann, A perturbative framework for jet quenching, JHEP 1303 080.

[108] T. Renk, The physics probed by the p_T dependence of the nuclear suppression factor`arXiv:1302.3710`.

[109] R. Reed, Full Jet Reconstruction in 2.76 TeV pp and Pb-Pb collisions in the ALICE experiment, Hot Quarks 2012 proceeding.

[110] S. Aiola, Measurement of jet spectra in Pb-Pb collisions at $\sqrt{s_{NN}}$=2.76 TeV with the ALICE detector at the LHC, Hot Quarks 2012 proceeding.

[111] J. Casalderrey-Solana, J. G. Milhano, U. A. Wiedemann, Jet Quenching via Jet Collimation, J.Phys. G38 035006.

[112] Y. Mehtar-Tani, C. Salgado, K. Tywoniuk, Jets in QCD Media: From Color Coherence to Decoherence, Phys.Lett. B707 156–159.

[113] Y. Mehtar-Tani, C. A. Salgado, K. Tywoniuk, The Radiation pattern of a QCD antenna in a dense medium, JHEP 1210 197.

[114] L. Apolinario, N. Armesto, L. Cunqueiro, An analysis of the influence of background subtraction and quenching on jet observables in heavy-ion collisions, JHEP 1302 022.

[115] S. Chatrchyan, et al., Observation and studies of jet quenching in PbPb collisions at nucleon-nucleon center-of-mass energy = 2.76 TeV, Phys.Rev. C84 024906.

[116] L. Cunqueiro, Jet structure in 2.76 TeV Pb Pb collisions at ALICE `arXiv:1210.7610`.

Acknowledgements

Ik ben trots op iedereen die op welke wijze dan ook heeft bijgedragen aan dit proefschrift. Zonder de dynamische discussies over vele onderwerpen had ik nooit zo veel plezier in dit werk gehad de afgelopen jaren. De vele borrels en etentjes hebben ook zeker een positieve bijdrage geleverd.

Marco, ik wil je bedanken voor je steun en begrip. Je was er altijd om mij door elke fase van het promotieonderzoek te begeleiden. Je enthousiasme, positieve instelling en vertrouwen zijn bewonderingswaardig. Ik ben blij dat ik met je heb mogen samenwerken en hoop dat we dat nog blijven doen.

Rene plukte mij als masterstudent uit de collegebanken. Ik begreep niet zo goed waarom maar hij stond erop dat ik onderzoek kwam doen. En daar bleek ik erg veel plezier in te hebben. Rene nam mij ook onder zijn hoede als promotiestudent. Gedurende het eerste anderhalf jaar tot aan zijn plotselinge overlijden zijn de wekelijkse besprekingen van grote waarde geweest. Zijn interesse in het onderzoek en mijn professionele en persoonlijke ontwikkeling heb ik altijd zeer gewaardeerd.

Raimond, dank voor het overnemen van het promotorschap. Plots had je een student die jet quenching deed en je had alle vertrouwen in. Bedankt daarvoor en voor de hulp met de laatste fase van het promotietraject.

Christian, you were one of the first persons within ALICE I met. It has been a pleasure collaborating with you. I would like to thank you for the support and interest in the analysis I was doing during the past years.

Leticia, ademas de compañeras de trabajo tambien nos hicimos amigas durante los ultimos años. Gracias por ser una persona en quien puedo confiar y compartir ideas y dudas.

There are many more people in ALICE which I would like to thank for the many stimulating discussions: Bastian, Oliver, Andreas, Peter, Rosi, Salvatore, Constantin, Jörn, Mateusz and many more. It has been great working with you all.

I would like to thank everybody who collaborated in the TECHQM brick effort. It was my first international research experience and it was great to discuss with all of you.

Then there is the great group of Ph.D. students and postdocs in Utrecht. This is a great group and I hope that the coffee breaks will continue. Cristian: thanks for the company at R1 and the many rides home you gave me during

the years. Marek: I'm afraid I will never understand your passion for football but thanks for the enthousiasm. Mikolaj: dank voor je nuchtere kijk op zaken. Carlos, Noami and Panos: it was great sharing the office with you at CERN. Although we were working on different topics, I learned a lot from you. Sarah: having you in the group and as a friend is fantastic. Thanks for the support and for listening to my doubts and worries towards the end of my PhD. Deepa: thanks for all the laughs and hugs. Alessandro: thanks for the help with many practical ALICE things. Raoul: je aanstekelijke lach die over de hele verdieping te horen was zal ik niet snel vergeten. Redmer: na jouw komst heb ik met een gerust hart de UU kunnen verlaten. Succes met je promotie. Ermes, Sandro, Andrea, Davide, Ante, You: thanks for sharing misery and many borrels. Misha: thanks for the vegetarian chili con carne. For all of you: good luck with your PhDs, postdocs or any other goal you decide to pursue in your lifes.

Al mijn vriendjes en vriendinnetjes: dank voor de steun en het ongekende geduld als ik weer eens onbereikbaar was. Hanne, bedankt voor het ontwerpen van de kaft.

En dan als laatste wil ik graag mijn ouders, Pilar en Adriaan, en mijn broertjes, Pablo en Jordi, bedanken voor de interesse die zij altijd hebben getoond in mijn dagelijkse bezigheden. Dankzij de vele gespreksonderpen tijdens de familiediners die rond ieders schema gepland worden, heb ik de realiteit nooit uit het oog verloren.

Curriculum Vitae

- Ph.D., Utrecht University, Institute of Subatomic Physics
  - thesis: 'Modelling and measurement of jet quenching in relativistic heavy-ion collisions at the LHC'
- M.Sc., Experimental Physics, Utrecht University, Institute of Subatomic Physics
  - thesis: 'Optimization of $D^0 \to K\pi$ detection in Pb–Pb collisions with ALICE'
- B.Sc., Physics and Astronomy, Utrecht University
- VWO, Christelijk Gymnasium Sorghvliet, Den Haag